



THE BARYON CYCLE IN THE EARLY UNIVERSE
A Multiwavelength, High Resolution View of Interstellar And
Circumgalactic Gas Emission

TESIS PRESENTADA POR
MANUEL SOLIMANO GAMBARDELLA
A LA
FACULTAD DE INGENIERÍA Y CIENCIAS

Para optar al Grado de Doctor en Astrofísica
Profesor guía: Manuel Aravena Aguirre

UNIVERSIDAD DIEGO PORTALES

Santiago, Chile

2025

©2025, Manuel Solimano Gambardella.

Se autoriza la reproducción total o parcial, con fines académicos, por cualquier medio o procedimiento, incluyendo siempre la cita bibliográfica del presente documento y su autor.

Acta de Deliberación
Defensa de Tesis Doctoral

En Santiago, el 12 de mayo del 2025 el Tribunal de Defensa de Tesis Doctoral compuesto por el Dr. Manuel Aravena (UDP), Dr. Jorge González-López (PUC, Chile), Dra. Chiara Mazzucchelli (UDP), Dr. Roberto Decarli (INAF, Italia) y Dr. Jorjyt Matthee (Institute of Science and Technology - ISTA, Austria), sobre la base del texto del proyecto, la exposición del doctorando y sus respuestas a las intervenciones de los miembros del tribunal, ha resuelto aprobar la tesis doctoral “The Baryon Cycle in the Early Universe. A Multiwavelength, High Resolution View of Interstellar and Circumgalactic Dust Emission” del doctorando Manuel Solimano.

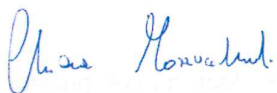
Los miembros del Tribunal firman para constancia.



Manuel Aravena
Supervisor, UDP

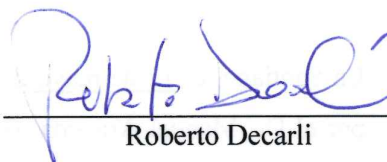


Jorge González-López
Co-supervisor, PUC



Chiara Mazzucchelli

UDP, Chile



Roberto Decarli

INAF, Italia



Jorjyt Matthee

ISTA, Austria

To my late nonno Iván, and my beloved cats Eño and Chokito

Acknowledgements

Collaboration, friendship, and mutual respect are the untaught pillars of science. In this sense, all my scientific and personal achievements rely on the contribution of wonderful people who I would wish to acknowledge.

I first want to thank my supervisors Profs. Manuel Aravena and Jorge González for guiding me through my doctoral journey. Manuel has been extremely kind and supportive, and an endless source of wisdom about academia. He taught me the fine art of knowing when to stop (worrying, analyzing data, writing telescope proposals, etc.) for my own good. Meanwhile, Jorge was my gateway to UDP, as he also supervised my undergraduate thesis project back at PUC, and introduced me both to world of ALMA and to the world of strong gravitational lensing. Since then, we have worked closely for at least three years, often under the influence of his eclectic but energizing Spotify playlist. Thanks Jorge for your unbeatable optimism, cheerful disposition, and genuine curiosity. I also want to thank both Manuel and Jorge for building a very welcoming research group with its various names and avatars: e.g., AGHATA, SGAS-SPT, CRISTAL-UDP, ORCHIDS, or MINGAL. I also thank current and former members of the group for their company and contribution to the scientific discussion: Kseniia Telikova, Ana Posses, Tanio Díaz Santos, Roberto Assef, Chiara Mazzucchelli, Meghana Killi, Devika Shobhana, Victoria Catán, Trystan Lambert, Dejene Zewdie, Belén Alcalde and Kevin Harrington.

Thank you to the Instituto de Estudios Astrofísicos (formerly the Núcleo de Astronomía) UDP for harboring a very friendly and inspiring environment. I will forever cherish the four years I spent there. Special thanks to Erika Labbé for her enthusiast dedication to outreach. She taught me many things about science communication and made me a huge fan of inclusive astronomy. I had the immense luck of working with Erika in some of her projects, most notably the “Noches de Telescopio en Tiempo Real” in which we live-streamed remote observations with a small telescope. This program was a huge success during the pandemic lockdowns, and included the challenging exercise of describing images of astronomical objects to blind or visually impaired people. In a different opportunity, Emilio and I followed Erika to a remote location in southern Chile.

There we brought interactive activities for children and had the luck of meeting Erika's parents, to whom I send my warmest greetings.

Thank you to all the friends I made among UDP students and postdocs. First, thanks to Camilo González for the piscolas, the pichangas, and for convincing me to choose UDP. Thanks to Sara Vitali for being a dear friend and companion, and for going through all the milestones of the PhD journey with me. Her lively spirit and wholesome heart were invaluable gifts to have near during these years. Thank you Sara for all the nice moments and for your unconditional support. Thanks to Florence de Almeida for her mood-lifting energy, and to the rest of the Brazilosphere (i.e., Brazilian friends from UDP and beyond): Ana and Pedro (with their king cat Morpheu), Douglas, Thallis, Tula, Priscila, Danielle, and Ana Carolina. Thank you also to Kriti, Dejene, Rosha, Trystan, Alessia, Grace, Girorgios, Keerthana, Pascal, Pablo, Emilio, Johnny, Theo, Kevin, Matthew, Alejandra, Trisha, Kurt, Scarlet, Kristy, Beyonce, Prachi, Hamideh, Tatevik, Karen, Gabriela, Suman, Mai, Yaherlyn, Elena, Arghajit, Javiera, Joshua, Regis, Anuroop, Yasna, Jacob, Sorya, and Sophie.

Thank you to Prof. Rodrigo Herrera-Camus and the entire CRISTAL collaboration. His enthusiasm and scientific vision were always an inspiration for me. I wish to one day make slides and plots as beautiful as his. Many thanks to CRISTAL members Ikki Mitsunashi, Ryota Ikeda, and Vicente Villanueva for their visits to UDP, and to everyone else who contributed to the CRISTAL survey or gave insightful comments on my paper.

I want to express my gratitude to the SPT-SMG and TEMPLATES collaborations, and especially to Kedar Pahdke for all the guidance in preparing my first successful JWST proposal. Thanks to David Vizgan, Cassie Reuter, Melanie Archipley, Prof. Joaquin Viera, Prof. Kirk Barrow, and all the folks at the Department of Astronomy of the University of Illinois for the support and friendship during my stay there. Thanks to Jane Rigby for her leadership, for her helpful comments on my paper and proposal drafts, and for being a key piece in making JWST happen.

To the Agencia Nacional de Investigación and the Chilean taxpayers for supporting me with a scholarship during the last three and a half years. I also acknowledge the Centro de Astrofísica y Tecnologías Afines for funding my multiple academic trips.

Quiero agradecer a mi familia por el apoyo constante, el cariño incondicional, y el férreo respaldo a cada una de mis decisiones. Gracias a mi madre, mi padre, a mis hermanas Clara e Isabella, a mi hermano Lucas, a La Nonna, a mis tíos, a mis primos, y por supuesto, al Mico.

Gracias a mi amigo Tomás Rojas por estar siempre disponible y por su genuino interés en mis proyectos.

Finalmente, agradezco a mi amada Catalina por traer su bella sonrisa y su cálido corazón a mi vida. Gracias a ti este último año ha sido maravilloso y lleno de alegrías, y sé que los próximos lo seguirán siendo mientras esté a tu lado.

Abstract

The baryon cycle refers to the mass transport and phase transitions of the baryonic matter in the Universe, and ultimately regulates the formation of stars and the growth of supermassive black holes (SMBHs) in galaxies across cosmic time. The processes of the baryon cycle operate on multiple spatial scales, which span three distinct realms: the interstellar, circumgalactic, and intergalactic media (ISM, CGM, and IGM, respectively). In this thesis, I address a series of questions regarding the current empirical picture of ISM- and CGM-scale gas emission at $z > 3$ and their relation to the baryon cycle. To this end, I investigate two star-forming galaxy systems at $z = 2.9$ (the lensed pair SGASJ1226) and $z = 4.5$ (the massive group J1000+0234) which exhibit extended Ly α emission. In the first project, I use state-of-the-art data from the Multi Unit Spectroscopic Explorer (MUSE) to dissect the Ly α halo of SGASJ1226. Here I demonstrate that Ly α is tracing a CGM-scale outflow, and that satellite galaxies can contribute to the luminosity of the Ly α halo. In the second project, I look at the cold gas properties of the J1000+0234 system via high-angular-resolution ALMA observations from the CRISTAL survey. The main outcome of this analysis is the detection of a 15-kpc-long plume of [C II]-emitting gas that highlights the presence of cold gas in the CGM, although its origin remains uncertain, with at least four scenarios under consideration. Finally, in the third project, I present the JWST followup of J1000+0234 which reveals the presence of two large [O III]-emitting nebulae within the system, likely powered by an obscured active galactic nucleus (AGN). This thesis presents one of the most detailed, multiwavelength views of the gas around distant galaxies to date, highlighting the complexity of the baryon cycle and the challenges in the interpretation of such exquisite datasets.

Resumen

El ciclo de los bariones comprende el transporte de masa y las transiciones de fase de la materia bariónica en el Universo, y en última instancia regula la formación de estrellas y el crecimiento de agujeros negros supermasivos (SMBHs) en galaxias a lo largo del tiempo cósmico. Los procesos del ciclo de los bariones operan en múltiples escalas espaciales, las cuales pueden agruparse en tres dominios o “medios”: el medio interestelar (ISM), el circumgaláctico (CGM) y el intergaláctico (IGM). En esta tesis, abordo una serie de preguntas sobre el panorama empírico actual de la emisión de gas en escalas del ISM y el CGM a $z > 3$ y su relación con el ciclo de los bariones. Para esto, investigo dos sistemas de galaxias con formación estelar a $z = 2.9$ (el par magnificado por lente gravitacional SGASJ1226) y a $z = 4.5$ (el grupo masivo J1000+0234) que exhiben emisión extendida de $\text{Ly}\alpha$ en sus alrededores. En el primer proyecto, utilizo datos del instrumento *Multi Unit Spectroscopic Explorer* (MUSE) que son el estado del arte para diseccionar el halo de $\text{Ly}\alpha$ de SGASJ1226. Aquí muestro que $\text{Ly}\alpha$ está trazando una efusión de gas en escala del CGM, y que las galaxias satélite pueden contribuir a la luminosidad del halo de $\text{Ly}\alpha$. En el segundo proyecto, exploro las propiedades del gas frío en el sistema J1000+0234 utilizando datos de ALMA de alta resolución angular provenientes del sondeo CRISTAL. El principal resultado de este análisis es la detección de una pluma de gas emitiendo [C II] que resalta la presencia de gas frío en el CGM, aunque la pregunta por su origen permanece abierta a al menos cuatro escenarios posibles. Finalmente, en el tercer proyecto, presento las observaciones de seguimiento de J1000+0234 realizadas con el JWST, las cuales revelan la presencia de dos grandes nebulosas de [O III] dentro del sistema. Estas nebulosas están probablemente ionizadas por la radiación de un núcleo galáctico activo (AGN) oscurecido. Esta tesis entrega una de las vistas más detalladas y en múltiples longitudes de onda del gas alrededor de galaxias distantes hasta la fecha, exhibiendo la complejidad del ciclo de los bariones y los desafíos asociados a la interpretación de datos tan ricos en información.

Contents

Acta de deliberación	i
Acknowledgements	viii
Abstract	xi
Resumen	xii
Table of contents	xv
1 Introduction	1
1.1 The Baryon Cycle	2
1.1.1 Accretion	4
1.1.2 Star formation and SMBH growth	5
1.1.3 Feedback and outflows	7
1.2 Tracers of gas emission at high redshifts	8
1.2.1 Lyman α	10
1.2.2 [C II] 158 μm	17
1.2.3 Rest-frame optical emission lines	21
1.3 This thesis	23
2 A resolved study of a strongly-lensed Lyman Alpha Halo at $z \approx 3$	25
2.1 Introduction	25
2.2 Observations and data reduction	27
2.2.1 MUSE	27
2.2.2 HST	30
2.2.3 Lens model	32
2.3 Results	34

2.3.1	Host galaxy properties	34
2.3.2	Continuum subtraction and pseudo narrowband imaging	36
2.3.3	Asymmetric Gaussian fitting	37
2.3.4	Image plane analysis	39
2.3.5	Source plane analysis	46
2.3.6	Low ionization absorption lines	58
2.4	Discussion	59
2.4.1	Kinematics of SGASJ1226	59
2.4.2	Powering mechanism	62
2.5	Conclusion	66
3	ALMA discovery of a [C II] plume in a $z = 4.54$ LAB	69
3.1	Introduction	69
3.2	The J1000+0234 system	70
3.3	Observations and data reduction	72
3.3.1	ALMA	72
3.3.2	MUSE	74
3.3.3	HST	75
3.4	Results and analysis	75
3.4.1	Adaptive masking of datacubes	75
3.4.2	Parametric morphology	78
3.4.3	Stack of HST images	81
3.4.4	Spectral properties of the [C II]-emitting plume	84
3.4.5	Symmetric difference correction of aperture #1's [C II] spectrum	88
3.5	Discussion	92
3.5.1	Conical outflow	92
3.5.2	Gas accretion	97
3.5.3	Ram pressure stripping	99
3.5.4	Gravitational interactions	101
3.6	Summary and conclusions	104

4 A hidden AGN revealed by JWST	109
4.1 Introduction	109
4.2 Observations and data reduction	112
4.2.1 JWST/NIRCam data	112
4.2.2 JWST/NIRSpec data	113
4.3 Results and analysis	114
4.3.1 Morphology and kinematics	114
4.3.2 Broad velocity component in O3-N	116
4.4 Line fitting with pPXF	118
4.4.1 Line ratio diagnostics and high-ionization species	119
4.4.2 Oxygen abundance	124
4.5 Discussion	124
4.5.1 No evidence of shocks	126
4.5.2 Constraints on AGN luminosity and obscuration	127
4.5.3 Proposed scenario and implications	129
4.6 Summary and conclusions	132
5 Concluding Remarks	135
5.1 Key Findings	135
5.2 Ongoing work	140
5.2.1 Analysis of ALMA and JWST data of SGASJ1226	140
5.2.2 J1000+0234's H α revival: the origin of the plume	144
5.3 Future directions	146
List of Figures	150
List of Tables	151
Bibliography	152

Chapter 1

Introduction

Galaxies are vast collections of stars, gas, dust, and dark matter (DM, including black holes), all bound together by the force of gravity. While DM dominates a galaxy's total mass, it is everything else—the so-called baryons—that gives off the light detected by telescopes. Despite their enormous sizes and early formation in cosmic history, galaxies are highly dynamic, evolving continuously over billions of years. These transformations give rise to the rich diversity of galaxy shapes, colors, and sizes observed in the sky. Understanding how galaxies form and evolve is thus a major goal of modern astrophysics.

In this thesis, I will seek insights into galaxy evolution by looking in detail at their different components, but specially at the gas inside and around galaxies seen more than eleven billion years ago. I will present state-of-the-art data from multiple observatories at the highest angular resolution currently available. With these data, I will explore structural and kinematic properties of the gas and its relation to star formation and feedback. This chapter sets the stage and describes the scientific background of this thesis before diving into the actual work I have developed in the past four years and published into three separate peer-reviewed journal papers.

A major outcome of galaxy evolution is the accumulation of mass in the form of stars. In the current paradigm, the stellar mass buildup is regulated by the complex interplay of internal (e.g., star formation, chemical enrichment, dust growth, feedback) and external processes (e.g., mergers, accretion, environmental quenching). A useful framework that captures most these processes and their impact on galaxy evolution is the concept of the

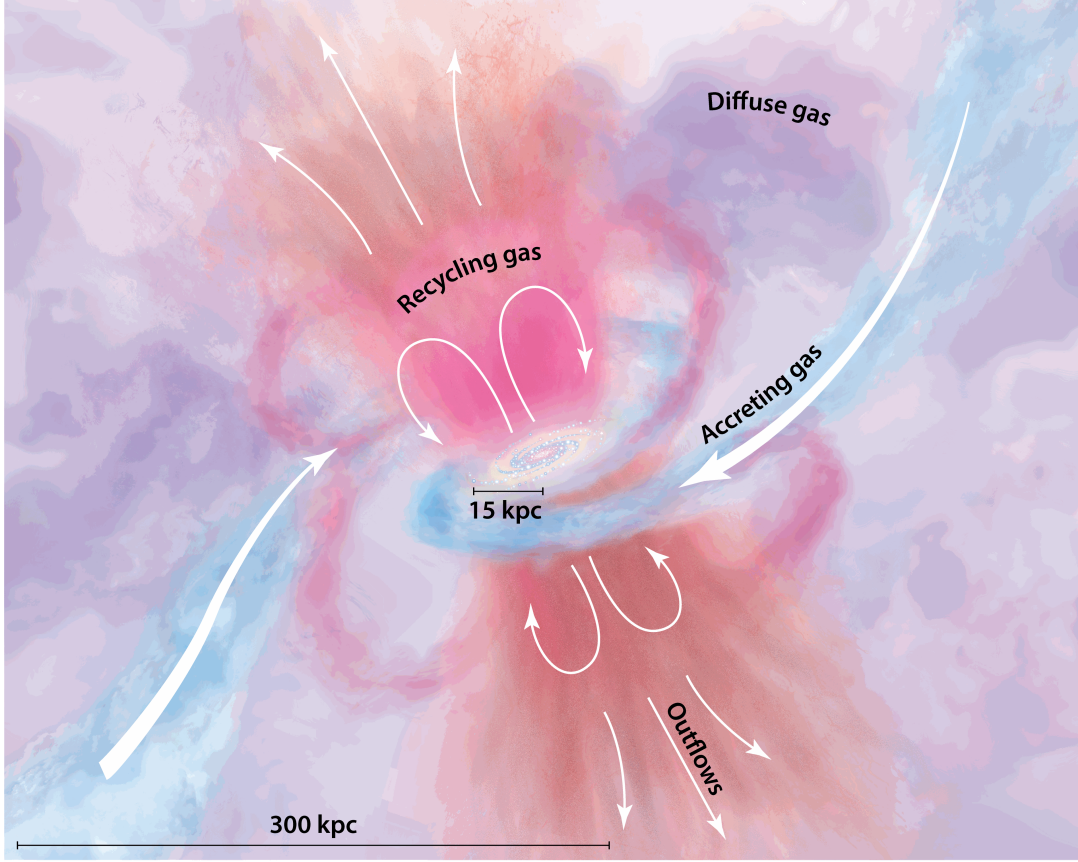
baryon cycle. It is founded on the idea that baryons (i.e., the matter that interacts with light) are constantly moving in and out of galaxies, and they transform between different phases in a potentially circular way.

In § 1.1 I give an overview of the baryon cycle including the accretion of gas onto galaxies (§ 1.1.1), how the accreted gas is consumed by star formation and the growth of supermassive black holes (§ 1.1.2), and finally how feedback returns the processed baryons back into the cycle (§ 1.1.3).

1.1 The Baryon Cycle

Before starting a discussion about the baryon cycle, I will introduce some definitions. First, I will consider the baryons not locked into stars as being exclusively gas, dust, and cosmic rays, and to be distributed in three nested “media”. The first one is the interstellar medium (ISM), which corresponds to the innermost region of galaxies and is defined as the baryons occupying the space between the stars of a galaxy (see [Draine 2011](#), for a classical textbook on the subject). Depending on the size of the galaxy, the ISM extends in scales of a few hundreds of parsecs to a few tens of kiloparsecs. Crucially, the ISM is where both star formation, evolution, and death take place: the ISM is home to molecular clouds, H II regions, planetary nebulae, and supernova remnants, among other astrophysical nebulae.

At larger scales, outside the ISM but still within the gravitational pull of the galaxy (in other words, within the virial radius), we find the circumgalactic medium (CGM; see [Tumlinson et al. 2017](#); [Péroux & Howk 2020](#); [Faucher-Giguère & Oh 2023](#); [Chen & Zahedy 2024](#), for recent reviews). The CGM is much more diffuse than the ISM, yet it fills a much larger volume, since it extends up to hundreds of kiloparsecs. Despite its low average density, the CGM of early galaxies and present-day dwarfs contains the majority of the bound baryonic mass ([Tumlinson et al. 2017](#)). Moreover, the CGM is a buffer zone hosting the main flows of matter and energy that regulate galaxy growth. The CGM is where gas outflows expand into, the site of metal mixing, and the direct recipient of inflowing gas (see [Fig. 1.1](#)).



Tumlinson J, et al. 2017.
Annu. Rev. Astron. Astrophys. 55:389–432

Figure 1.1: Artistic representation of the baryon cycle at CGM scales reproduced from [Tumlinson et al. \(2017\)](#). The isolated disk galaxy at the center holds the ISM and the star formation within it, along with potential AGN activity in the nucleus. Accretion streams coming from the IGM are shown in blue, while outflows are painted red. Fountain flows where the gas is mixed and recycled are depicted in pink.

The third and top medium in the hierarchy is the intergalactic medium or IGM. The IGM is the gas that permeates the entire Universe and is not bound to galaxies. However, the density distribution of the IGM roughly follows that of galaxies, which are located along the intricate network of gigantic filaments that make up the cosmic web. At present, the IGM mainly holds warm-to-hot (10^5 K to 10^7 K) ionized hydrogen and helium, and it is home to 50%-90% of the baryons in the Universe (e.g., [Lin & Zou 2023](#); [Khrykin et al. 2024](#)). At high redshifts ($z > 2$), the IGM hosted a larger fraction of cool neutral gas as evidenced from observations of the Lyman Alpha Forest (e.g., [Rauch 1998](#)). At even earlier times ($z \gtrsim 10$), that fraction was close to unity: the IGM was still fully neutral as

Cosmic Reionization was just beginning (e.g., [Morales et al. 2021](#); [Qin et al. 2024](#); [Kageura et al. 2025](#); [Mason et al. 2025](#)).

A key characteristic of these three astrophysical media is their multiphase nature. The gas spans a broad range of temperatures, densities and ionization states depending on local conditions such as proximity to energy sources. Some phases are particularly relevant in the context of the baryon cycle. For example, cold molecular gas has the lowest temperatures (10 – 50 K) and the highest densities ($n_{\text{H}} = 10^2 \text{ cm}^{-3}$ to 10^6 cm^{-3}), it exists almost exclusively in the ISM and represents the immediate fuel for star formation. At slightly higher temperatures, the cold neutral phase is mainly composed of atomic hydrogen and makes up the longer-term reservoir of cold gas for star formation. Next there is warm ionized gas, at temperatures of $T \gtrsim 10^4 \text{ K}$ and densities $n_{\text{H}} = 0.3 - 10^4 \text{ cm}^{-3}$. Gas reaches this phase after photoionization from hot stars or accreting black holes, therefore is a good tracer of ionizing photons. Finally, a very hot ($T \gtrsim 10^6 \text{ K}$), X-ray emitting, volume-filling phase is often present in the CGM of mature galaxies, heated by shocks and ionized by collisions.

In the next sections, I will describe the main processes involved in the baryon cycle, starting from IGM to ISM direction.

1.1.1 Accretion

Galaxies grow their mass through major mergers (violent collisions of similarly-sized galaxies that end up forming a single but larger galaxy) and through accretion. The latter is thought to sustain growth over longer timescales, and is generally smoother and less drastic than mergers. Simply put, accretion is the infall of gas from the IGM into the CGM and eventually the ISM. This gas can be either pristine (i.e., with Big Bang primordial abundances) or polluted by metals ejected from previous star formation episodes.

According to theoretical models, accretion occurs in either a cold mode or a hot mode, depending on the overall state of the IGM and the properties of the accreting halo ([Dekel & Birnboim 2006](#)). On one hand, cold-mode accretion flows along narrow streams that pierce DM halos and deliver cold gas directly to the inner CGM or even the ISM (e.g.,

Kereš et al. 2005). This mode is mainly relevant for high-redshift galaxies and present-day dwarfs. On the other hand, hot-mode accretion occurs in a more spherical way, and the gas is heated by shocks caused by the virialization of matter in the gravitational potential of the galaxy. This mode is less efficient and leads to lower mass inflow rates overall, but tends to dominate in massive galaxies and dense environments (e.g. Genel et al. 2008).

Observationally, direct evidence of accretion is scarce (e.g., Emonts et al. 2023), yet there is plenty of indirect evidence suggesting the need of continuous accretion to sustain the measured star formation rate given the available molecular gas (e.g., Béthermin et al. 2013; Conselice et al. 2013; Tacconi et al. 2013; Scoville et al. 2017; Tacconi et al. 2018; Walter et al. 2020). An often quoted consequence of accretion as a major mode of galaxy growth is the existence of a relatively tight correlation among star-forming galaxies between their SFRs and stellar masses (e.g., Brinchmann et al. 2004; Noeske et al. 2007; Elbaz et al. 2007; Daddi et al. 2007). This correlation is known as the star-forming “main sequence” (MS) and has been observed to hold up to at least $z \approx 6$ (e.g., Topping et al. 2022; Endsley et al. 2024). Star-forming galaxies that lie along the MS are deemed “normal”, while the high- and low-SFR outliers are defined as starbursts and quenched galaxies, respectively. The continuous accretion of gas, and its conversion into stars with a constant efficiency, ensures that galaxies build up steadily along the MS.

1.1.2 Star formation and SMBH growth

Once the accreted gas cools down and settles into the ISM it can suffer at least four different fates: (1) be ejected back into the CGM or IGM by a powerful wind; (2) be ionized by the ambient ionizing photons; (3) cool further down, fragment into dense molecular cores, and finally turn into stars; or (4) approach and fall into the supermassive black hole (SMBH) at the center of the galaxy. The first two options fall in the category of feedback and therefore are postponed to the next section. Here I will discuss star formation and SMBH accretion.

Star formation occurs within Giant Molecular Clouds (GMCs), which are self-gravitating structures of tens of parsecs in scale primarily composed by molecular hydrogen (H_2).

Under the right conditions, GMCs fragment and develop dense embedded cores of free-falling gas that collapse into groups or clusters of protostars. These protostars will keep accreting mass for some time, although with ever decreasing rates. At some point, the protostars contract enough for their core temperatures and pressures to trigger nuclear fusion.

The resulting group of stars will have a distribution of masses sampled from the so-called initial stellar mass function (IMF; [Salpeter 1955](#)). While there are multiple prescriptions for the IMF (see [Bastian et al. 2010](#), for a review), all of them predict a larger amount of low-mass stars than high-mass stars. This is relevant because mass is the strongest predictor of the evolutionary path a star will follow. Low-mass stars of up to $\approx 8 M_{\odot}$ will live for billions of years and eventually disperse its nucleosynthetic material back to the ISM in the form of a planetary nebula. Only a fraction of those baryons will remain locked up in the white dwarf stellar remnant. Instead, high-mass stars ($> 8 M_{\odot}$) live only for a few million years before exploding as core-collapse supernovae that inject energy, metals, and momentum into the ISM and CGM. Again, a fraction of these baryons will remain in the collapsed cores (neutron stars or black holes).

According to the IMF, low-mass stars will make up the bulk of the total stellar mass formed in a single burst, while high-mass stars will dominate the total luminosity and feedback during their brief lifetime. In fact, high-mass stars will be the main sources of ionizing photons, which will quickly carve out an ionized nebula (H II region) within the parent GMC. High-mass stars will also dominate the non-ionizing UV and optical luminosity, and therefore the heating of dust particles. The latter will re-emit this energy in the form of thermal radiation in the far-infrared (FIR), making the FIR luminosity a good tracer of the (obscured) SFR. High-redshift galaxies with $L_{\text{FIR}} > 10^{12} L_{\odot}$ form stars in excess of $100 M_{\odot} \text{ yr}^{-1}$, and are hereafter referred to as dusty star forming galaxies (DSFGs; [Casey et al. 2014](#)).

Other than star formation, the accreted gas can feed SMBH growth. For this to happen, the gas must lose a substantial amount of angular momentum so it can spiral inward and reach the proximity of the SMBH. Then, it will form an accretion disk around the SMBH and subsequently become an active galactic nucleus (AGN). Part of the gas in the

accretion disk will cross the event horizon of the SMBH and add up to its mass, locking up these baryons virtually forever. The rest of the gas will be turned into radiative energy or simply expelled outward due to feedback from the AGN.

1.1.3 Feedback and outflows

As mentioned above, only a small portion of the gas that is accreted ends up in stars or in the SMBH of a galaxy. A larger share is subject to the energetic and kinematic output of star formation and SMBH accretion.

Feedback from star formation comes mainly from the young hot massive stars. Even before the explosion of the first core collapse supernova of a newly formed batch of stars, massive stars contribute ionizing radiation and stellar winds to the environment. This helps clear out the molecular gas and the dust from the birth cloud. But when supernovae start to blow up, they inject energy and momentum into the gas. If the kick from supernovae is high enough to overcome the gravitational potential, the gas is then ejected in the form of galactic-scale outflows. This is for example what happens in nearby starburst galaxies, such as the prototypical M82. M82 is hosting a starburst that forms about a dozen of solar masses per year in a relatively compact region at the center (e.g., [O’Connell et al. 1995](#); [Förster Schreiber et al. 2003](#)). The intense rate of supernovae explosions then drive a spectacular bipolar outflow that extends to both sides of the disk and reaches CGM scales ([Shopbell & Bland-Hawthorn 1998](#); [Veilleux et al. 2005](#)).

Outflows are thus a mechanism capable of returning baryons to the CGM. Outflows will also carry newly formed metals from the supernovae ejecta, making the CGM chemically richer. Another consequence of outflows is that gas removal can suppress further star formation, leading to a sharp decrease in SFR. However, if the outflow speed does not overcome the galaxy’s escape velocity, the expelled gas can rain down back again into the ISM and become fuel for a new generation of stars, thus completing one round of the baryon cycle. Such flows are known as galactic fountains (e.g., [Fraternali & Binney 2008](#); [Fraternali 2017](#)) and represent the foremost example of gas recycling.

Feedback from SMBH accretion also has important consequences for the host galaxy.

As mentioned in the previous section, gas accretion onto SMBHs leads to a highly energetic event known as AGN (Alexander & Hickox 2012, and references therein). A defining feature of AGN is the accretion disk surrounding the SMBH, which, due to the extreme densities and orbital velocities, heats up and glows with a luminosity similar or even higher than that of the entire host galaxy. The accretion disk shines from the near-IR to the UV and produces copious amounts of ionizing radiation. Moreover, Compton up-scattering of the UV photons by a corona of hot electrons above the accretion disk gives the AGN a powerful X-ray output. AGN radiation ionizes gas closely bound to the SMBH in the so-called Broad Line Region (BLR), named after the recombination lines that are Doppler-broadened by the huge orbital velocities of this gas. But the AGN can ionize gas sitting well beyond the strong gravitational pull of the SMBH, giving rise to nebulae with narrow emission lines (i.e., Narrow Line Regions; NLR).

The sheer intensity of the radiation field can drive fast winds out of the accretion disk, which can then propagate to the ISM and CGM in a similar way to star-formation-driven outflows. In some cases, the winds get funneled into narrow collimated jets that rise perpendicular to the accretion disk and above the SMBH. These jets carry ionized particles at relativistic speeds and can propagate out to hundreds or even a thousand kiloparsecs. Such jets are routinely detected in radio frequencies due to their synchrotron radiation, and provide kinetic energy to the surrounding media. Jets are thus main examples of kinetic or “radio-mode” AGN feedback. Radiation, winds, and AGN-driven jets can remove or heat gas sufficiently to quench star formation in the ISM and even inhibit further accretion.

1.2 Tracers of gas emission at high redshifts

In this thesis, I will investigate gas emission in two $z > 3$ systems at CGM and ISM scales. For this, I will use three main emission line tracers: Lyman Alpha (§ 1.2.1), and [C II] 158 μm (§ 1.2.2), and a set of rest-frame optical emission lines such as $\text{H}\alpha$ and [O III] (§ 1.2.3). A visual summary of these lines in the context of a $z = 4$ star-forming galaxy’s spectral energy distribution is found in Fig. 1.2.

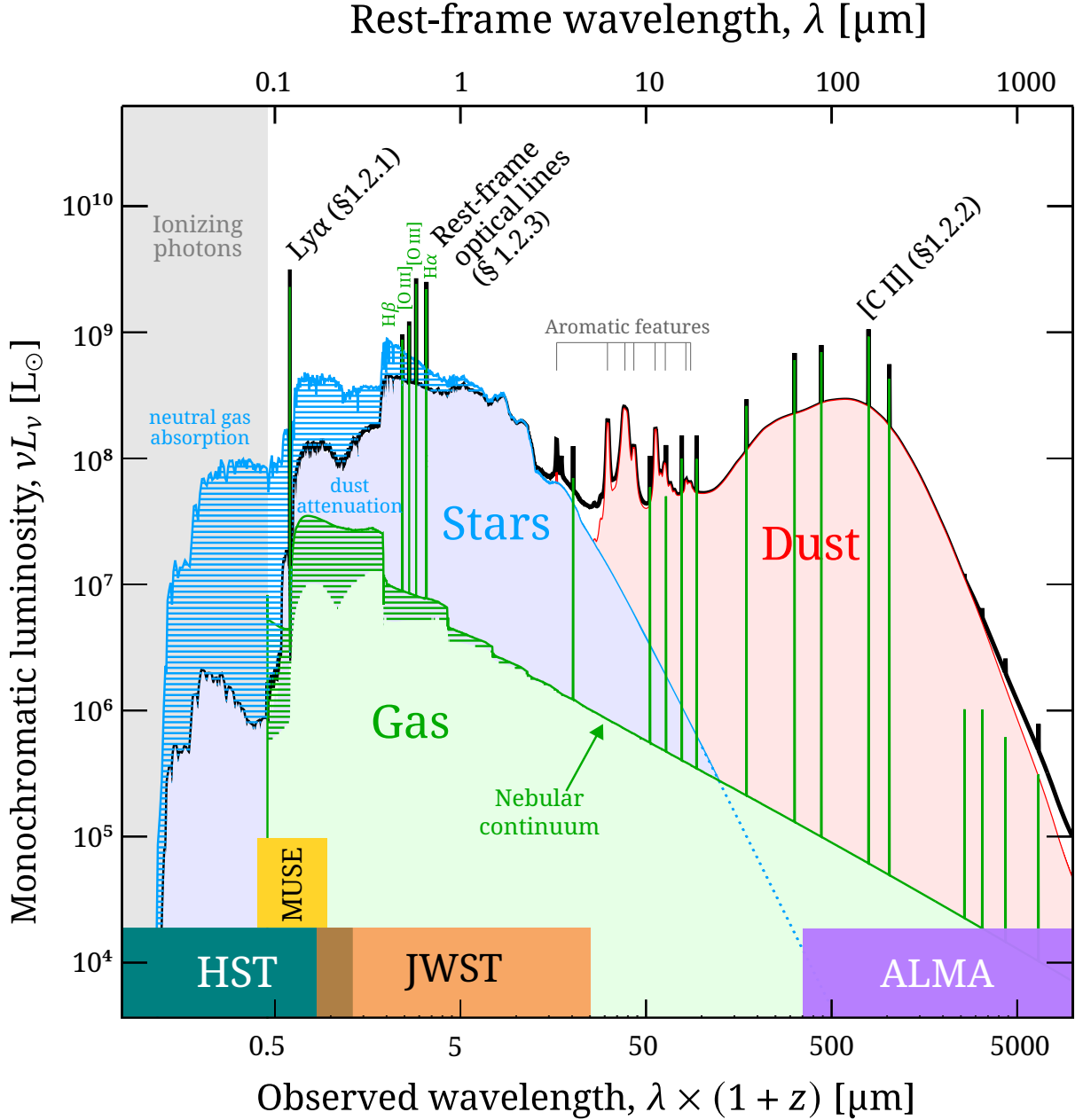


Figure 1.2: Spectral energy distribution of a star-forming galaxy at $z = 4$. Figure adapted from Galliano et al. (2018). The emitted radiative energy from stars, dust, and gas is displayed from UV to millimeter wavelengths. The three gas tracers discussed in § 1.2 are highlighted at the top: Ly α , rest-frame optical lines, and [C II] 158 μm . At the bottom, the color boxes show the spectral ranges of HST, MUSE, JWST, and ALMA.

1.2.1 Lyman α

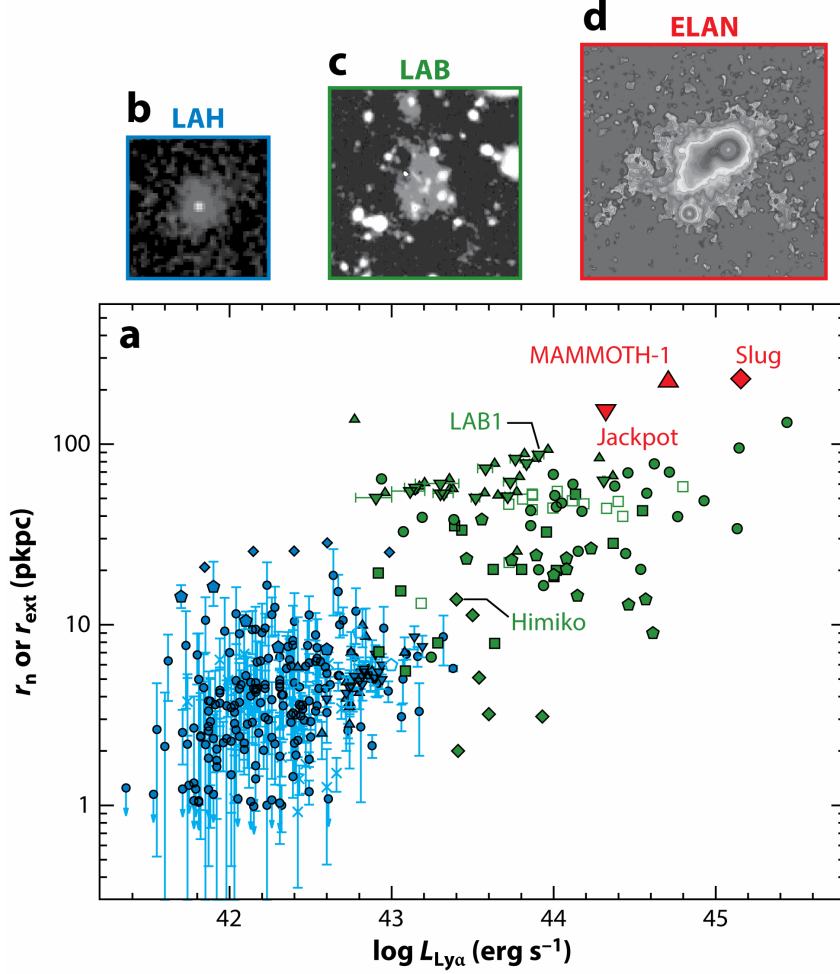
At a rest-frame wavelength of 1215.67 Å, the spectral line known as H I Lyman- α (hereafter Ly α , for short) has an undeniable relevance in modern astrophysics. Ly α is associated with the $n = 2 \rightarrow n = 1$ electronic transition of neutral hydrogen (H^0), a transition that is particularly likely to occur, either as the end result of a recombination event or after excitation by collisions. In fact, in the typical conditions found in H II regions, about two-thirds of all recombination events end up with the emission of a Ly α photon. This makes Ly α the strongest recombination line in the spectra of star-forming galaxies, which has led to the use of Ly α as an efficient redshift machine (e.g., [Cowie & Hu 1998](#); [Rhoads et al. 2000](#); [Ouchi et al. 2003](#); [Gawiser et al. 2007](#); [Adams et al. 2011](#); [Bacon et al. 2017](#)). Besides its large intrinsic brightness, Ly α can be observed from the ground at redshifts between $z \approx 2$ and $z \approx 7$, enabling the selection of high-redshift star-forming galaxies all the way from Cosmic Noon to the Epoch of Reionization (e.g., [Zitrin et al. 2015](#)).

However, the nature of the line plus the sheer abundance of hydrogen in the Universe place some obstacles between the observer and the source of a Ly α photon. First, the far-UV wavelength of the line makes it strongly susceptible to dust attenuation. For example, a dust screen producing an attenuation of one magnitude in the V band, would produce an attenuation of almost three magnitudes at $\lambda = 1215.67$ Å according to a [Calzetti et al. \(2000\)](#) attenuation law. Second, Ly α photons are absorbed by H^0 atoms just as easily as they are emitted, which leads to the so-called resonant scattering effect: as soon as a photon with a frequency close enough to the Ly α rest-frame frequency hits an H^0 atom in its ground level, it will get absorbed and then re-emitted in a random direction shortly after, due to the large transition probability. This process repeats in a sequence where the photon undergoes a random walk in both spatial and spectral dimensions. The scattering stops when the photon (1) hits a dust particle, (2) is Doppler-shifted out of the resonant frequency, or (3) does not encounter additional hydrogen atoms. Only the options (2) and (3) enable Ly α photons to escape the galaxy and eventually reach an observer on Earth. In addition, (2) explains why the peak of the Ly α line is almost always shifted from the systemic velocity of the galaxy (traced by a non-resonant line). Crucially, resonant

scattering amplifies the optical path of Ly α photons, increasing their chance of being absorbed by dust. For these reasons, the strength, visibility and spectral shape of the Ly α line is a complex function of the distribution, kinematics, and ionized fraction of hydrogen, as well as the properties, geometry and mixing of dust.

Nevertheless, it is this very complexity that makes Ly α a tool to much more than just redshift measurements. For example, quantifying the redshift evolution of the Ly α luminosity function provides constraints on the timing of the Cosmic Reionization process, since Ly α emission was suppressed when the IGM around a distant galaxy was still neutral. In fact, the number of Ly α emitters (LAEs, i.e., galaxies selected via their strong Ly α emission) becomes progressively smaller at $z > 7$ (e.g., [Goto et al. 2021](#)), and when they are detected, they are interpreted as galaxies embedded in early ionized bubbles within a neutral IGM (e.g., [Zitrin et al. 2015](#); [Hashimoto et al. 2018](#); [Witstok et al. 2025b,a](#)). Another example is the study of the Ly α line profile, which encodes valuable information about kinematics, opacity, and column density of H I gas of distant galaxies. Inferring these properties, however, requires careful radiative transfer (RT) modeling under simplifying assumptions about the geometry of the system (e.g., [Ahn 2004](#); [Verhamme et al. 2006](#); [Gronke et al. 2016](#)).

In this thesis, we will be interested in Ly α as a tracer of the CGM. Low surface brightness (SB) Ly α emission extending beyond the star-forming component of galaxies is a well-established phenomenon at high redshifts: almost all LAEs and many UV-selected galaxies exhibit diffuse emission that extends out to about ten times the size of the rest-frame UV, suggesting that Ly α does indeed trace the CGM. These regions are known in the literature as a Lyman Alpha Halos (LAHs; e.g., [Hayashino et al. 2004](#); [Steidel et al. 2011](#); [Wisotzki et al. 2016](#); [Leclercq et al. 2017](#); [Chen et al. 2021b](#); [Claeyssens et al. 2022](#)). Following the nomenclature of [Ouchi et al. \(2020\)](#), LAHs are characterized by exponential scale lengths of 1-10 kpc and luminosities of up to $L_{\text{Ly}\alpha} = 10^{43} \text{ erg s}^{-1}$. At larger scales and luminosities, [Ouchi et al. \(2020\)](#) define Ly α “blobs” (LABs; e.g., [Steidel et al. 2000](#); [Matsuda et al. 2004](#); [Shibuya et al. 2018](#)), having sizes between 10 kpc and 100 kpc, and luminosities in the $10^{43} \text{ erg s}^{-1}$ to $10^{44} \text{ erg s}^{-1}$ range, and Enormous Ly α Nebulae (ELANe; [Cantalupo et al. 2014](#); [Hennawi et al. 2015](#); [Cai et al. 2016](#)) which denote the largest ($\gtrsim 100 \text{ kpc}$)



 Ouchi M, et al. 2020.
Annu. Rev. Astron. Astrophys. 58:617–59

Figure 1.3: Ly α size versus Ly α luminosity for different types of Ly α nebulae. Figure reproduced from [Ouchi et al. \(2020\)](#). **a.** Ly α scale-length r_n or extent r_{ext} as a function of Ly α luminosity, with blue, green, and red symbols denoting LAHs, LABs and ELANes, respectively. Data is compiled from the literature ([Matsuda et al. 2011](#); [Steidel et al. 2011](#); [Cantalupo et al. 2014](#); [Momose et al. 2014, 2016](#); [Hennawi et al. 2015](#); [Borisova et al. 2016](#); [Cai et al. 2016](#); [Wisotzki et al. 2016](#); [Leclercq et al. 2017](#); [Xue et al. 2017](#)). **b-d.** Thumbnails of example members of each class: LAHs ([Leclercq et al. 2017](#)), LABs ([Matsuda et al. 2011](#)) and ELANes ([Cantalupo et al. 2014](#)).

and most luminous ($\gtrsim 10^{44} \text{ erg s}^{-1}$) objects. While LAHs are associated with single or pairs of galaxies, LABs typically host multiple galaxies, often in overdense environments ([Overzier 2016](#)). ELANes, on the other hand, always harbor one or more powerful quasars.

Ly α emission has also been proposed as a tracer of cosmic web filaments in the inter-

galactic medium (IGM), although at much fainter SB levels ($\lesssim 10^{-20} \text{ erg s}^{-1} \text{ cm}^{-2} \text{ arcsec}^{-2}$; Gould & Weinberg 1996). Such levels can only be detected in the deepest observations with 8 m-class facilities (Bacon et al. 2021).

Extended Ly α emission mechanisms

There are several mechanisms that can produce spatially extended Ly α emission, summarized in the cartoon in Fig. 1.4. Here we list only four mechanisms that are relevant to CGM-scale emission in LAHs and LABs, while other accounts in the literature may add additional mechanisms or further divide them into more specific scenarios.

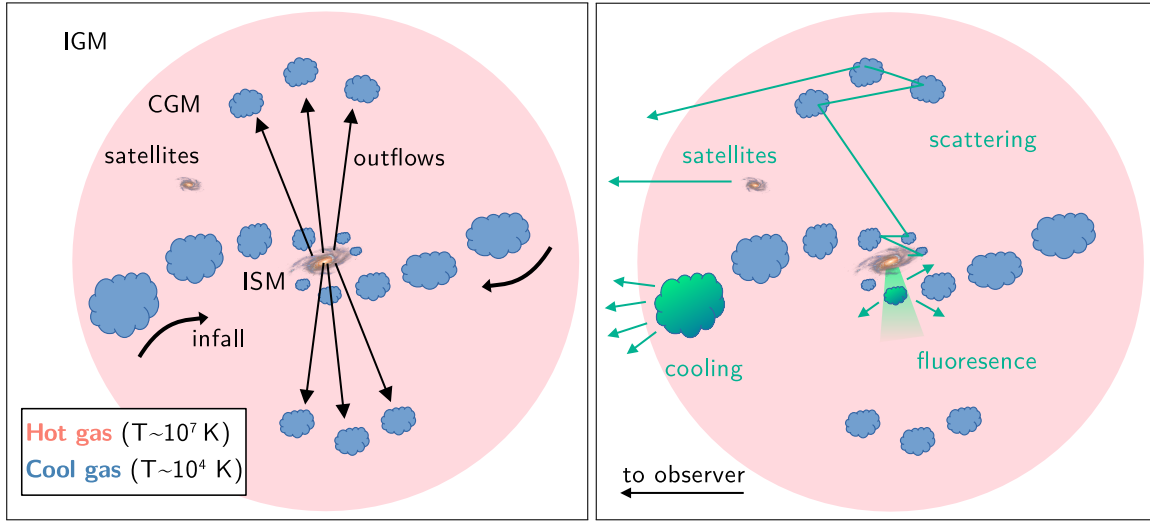


Figure 1.4: Visual summary of the CGM and its extended Ly α emission. *Left:* Simplified schematic of the CGM. The pink circle represents hot ionized gas filling the halo, while blue clouds represent denser and cooler regions (neutral phase) of the CGM. Colder and intermediate phases are not pictured. Black arrows indicate possible motions of the cool gas in the CGM: infall (accretion) from the IGM and outflows from the ISM (disk galaxy at the center). *Right:* Same as in the left panel but indicating possible mechanisms and light paths (green arrows) leading to Ly α extended emission.

1. **Resonant scattering:** If there are extended neutral hydrogen reservoirs around or near a Ly α -emitting source, resonant scattering will diffuse the photon flux out to large radial distances until it escapes the system in the direction of the observer. The efficiency of this mechanism strongly depends on the density, covering fac-

tor, clumpiness, and kinematics of the H I reservoirs, as well as the presence of dust within them. For example, large velocity gradients (e.g., from inflows or outflows) help the escape of Ly α photons through this mechanism thanks to favorable Doppler shifts.

In the resonant scattering mechanism, the observed Ly α emission is powered by a central source, where the intrinsic emission is typically associated with recombination radiation from H II regions or AGN. We thus say the Ly α emission is produced *ex situ* and then scattered, thereby tracing extended H I reservoirs.

2. **Fluorescence:** Ly α emission can also originate directly in the CGM (*in situ*). This can be achieved through the phenomenon of “fluorescence”, in which recombination emission is boosted by the exposure of the gas to ionizing radiation that comes from either internal (e.g., hot stars, AGN) or external sources (the cosmic UV background). In other words, the extended Ly α emission comes from a CGM-scale photoionized nebula which should also emit all the other recombination lines. In fact, the detection of co-spatially extended H α emission is a powerful diagnostic to confirm that this mechanism is at play (e.g., [Leibler et al. 2018](#)). Fluorescence is often invoked to explain LABs hosting unobscured quasars, because they can provide a high enough ionizing photon flux density to sustain a large-scale ionized nebula (e.g., [Borisova et al. 2016](#)).
3. **Gravitational cooling:** In this mechanism, infalling cold gas clouds or streams are heated as the gravitational binding energy is transformed into thermal energy of the gas (e.g., via weak shocks, [Haiman et al. 2000](#)). The heating is then balanced out by cooling via emission of Ly α photons *in situ*, therefore resulting in extended emission. In this case, the $n > 1$ states of H⁰ are excited by collisions with free electrons, not recombination events. The emission of Ly α photons then ‘cools’ the gas by taking kinetic energy away from the free electrons. If this mechanism is a major channel for creating LAHs and LABs, then they would represent evidence for cold-mode baryonic accretion feeding dark matter halos.
4. **Faint satellites:** Finally, a sizable contribution to extended Ly α emission is ex-

pected to come from the aggregate, unresolved emission from faint star-forming satellites or ejected H II regions populating the halo (e.g., [Momose et al. 2016](#); [Mas-Ribas et al. 2017](#); [Mitchell et al. 2021](#); [Byrohl et al. 2021](#)). Some observational evidence suggests these faint LAEs can play a significant role in sustaining the extended Ly α emission in the outskirts of LAHs (e.g., [Herrero Alonso et al. 2023](#)). However, even in the deepest HST images, the UV counterparts of this population remains undetected (e.g., [Leclercq et al. 2017](#)).

In any given LAH, the observed emission might come from a complex combination of the mechanisms described above. Disentangling what is the dominant mechanism and power source is a challenging task and an active area of research.

Resolved observations of Ly α with MUSE

Integral field spectrographs (IFS) are the most powerful tool to detect and characterize extended Ly α emission at high redshifts. These instruments are designed to obtain spectra along multiple and contiguous lines of sight toward a celestial object in a single observation. The products of these observations are spectral datacubes, that is, data containing information along two spatial dimensions (RA, Dec.) and one spectral dimension (wavelength). Therefore, they enable the joint measurement of spatial (e.g., sizes, morphologies) and spectral properties (e.g., line width, peak shift, velocity structure) of LAHs and LABs.

Among IFS instrumentation, the Multi Unit Spectroscopic Explorer (MUSE; [Bacon et al. 2010](#)) mounted on the Very Large Telescope (VLT) stands out as the most successful instrument for LAH science at $z \gtrsim 3$. Its Wide Field Mode (WFM) boasts a field of view of $1 \times 1 \text{ arcmin}^2$ (currently the largest in the optical IFS market) and a superb imaging quality (seeing-limited to a PSF FWHM $\lesssim 1''$ under typical conditions in Paranal, or $\lesssim 0''.7$ with ground-layer adaptive optics assistance). Moreover, MUSE covers almost entirely the optical wavelength range from 4650 Å to 9300 Å¹ with a nominal resolving power of $R \sim 1700$ in the blue end and $R \sim 3600$ in the red end. These features enable a full

¹Here I am quoting the extended rather than the nominal wavelength range from the ESO [website](#).

Ly α survey from $z = 2.8$ to $z = 6.7$ in a single pointing, equivalent to a comoving volume of roughly $10\,800\,\text{Mpc}^3$. Furthermore, MUSE can easily reach SB sensitivities on the order of $10^{-19}\,\text{erg s}^{-1}\,\text{cm}^{-2}\,\text{arcsec}^{-2}$ per spectral resolution element in 4h-long exposures, making the detection of extended Ly α emission a matter of routine. Such exquisite SB sensitivity can be pushed down to $10^{-20}\,\text{erg s}^{-1}\,\text{cm}^{-2}\,\text{arcsec}^{-2}$ or below with very deep exposures ($t > 100\,\text{h}$) and careful reduction techniques (e.g., [Bacon et al. 2023](#)).

The first decade of MUSE operations was marked by an explosion of extended Ly α science, primarily led by the instrument’s consortium with their wide (MUSE-Wide; [Urrutia et al. 2019](#)), deep (MUSE Hubble Ultra Deep Field; [Bacon et al. 2017, 2023](#)), and strong-lensing cluster field ([Richard et al. 2021](#); [Claeyssens et al. 2022](#)) surveys. In particular, the MUSE Hubble Ultra Deep Field (MUDF) produced some of the first individual detections of unlensed LAHs ([Wisotzki et al. 2016](#)), which were then found to be ubiquitous among high- z LAEs ([Leclercq et al. 2017](#)), to the point they cover almost the entire sky in projection ([Wisotzki et al. 2018](#)).

[Leclercq et al. \(2017\)](#) provided the first statistical sample ($N = 145$) of blindly-selected LAHs, finding that LAHs are characterized by a double exponential radial profile, with the more extended halo-like component having an exponential scale length 4 to 20 times larger than their UV counterpart, with a median of 4.5 kpc. Moreover, they find a diversity of Ly α line profiles although 90% of the sample shows a single-peaked red-asymmetric profile with FWHM ranging from $118\,\text{km s}^{-1}$ to $512\,\text{km s}^{-1}$. One noteworthy limitation of this study is the exclusion of galaxies in pairs from the LAH sample; yet, galaxy pairs and mergers are interesting since numerical simulations suggest that mergers can enhance Ly α SB by stripping dense gas into the CGM and boosting SFR-driven photoionization (e.g., [Yajima et al. 2013](#)).

Other studies leverage the angular resolution of MUSE and investigate the spatial variations of the Ly α profile within a single halo, but this can only be achieved in the brightest (e.g., [Leclercq et al. 2020](#)) and/or gravitationally lensed LAHs (e.g., [Smit et al. 2017](#); [Claeyssens et al. 2019](#); [Chen et al. 2021a](#)). One key result from these studies is that the correlation between peak shift and line FWHM found for samples of LAEs (e.g., [Verhamme et al. 2018](#)) also holds among resolved regions within individual halos, lending support

to the idea that resonant scattering is the main mechanism for producing LAHs.

Taking advantage of the enhanced angular resolution afforded by gravitational lensing, [Claeysens et al. \(2022\)](#) compiled a sample of ~ 600 LAEs resolved at subgalactic scales. In their work, they confirm that halo size is correlated to the size of the UV continuum, yet 60% of the sample shows significant spatial offsets between these two components ($\text{Ly}\alpha$ and UV). The smallest offsets can be explained by star-forming substructure within the UV continuum, while the largest offsets require resonant scattering in the CGM (mechanism 1), or emission from satellite or merging galaxies (mechanism 4).

1.2.2 [C II] 158 μm

While $\text{Ly}\alpha$ is a powerful tracer of gas in the UV, the fine structure line of singly-ionized carbon at $\nu_{\text{rest}} = 1900.5369$ GHz (hereafter [C II] 158 μm or simply [C II]) plays a similar role in the far-infrared (FIR) regime. [C II] is an important cooling channel of gas in a wide range of temperatures and densities (e.g., [Tielens & Hollenbach 1985](#); [Wolfire et al. 1990](#)), radiating out about 0.1-10% of the total FIR luminosity of a galaxy ([Stacey et al. 1991](#)), and thus an obvious target for extragalactic studies of the ISM.

Since carbon has a lower ionization potential than hydrogen (11.26 eV), C^+ can exist in the molecular (e.g., [Contursi et al. 2013](#); [Pineda et al. 2013](#)), the atomic (e.g., [Madden et al. 1993](#)) and ionized gas phases (e.g., [Heiles 1994](#)), and for this reason [C II] 158 μm is considered an “all-round” ISM tracer and a proxy of total ISM mass (e.g., [Olsen et al. 2017](#)). Most of it, however, is produced via collisional excitation within photodissociation regions (PDRs; [Stacey et al. 1991, 2010](#)), the transitional zone between ionized and cold gas at the edges of irradiated molecular clouds.

At $z \gtrsim 3$ [C II] 158 μm is shifted to atmospheric windows in the (sub)-millimeter range, and hence observable from the ground. This fact, together with the exquisite angular resolution and sensitivity of the Atacama Large Millimeter/Submillimeter Array (ALMA) has led to a new era in the exploration of the high-redshift Universe ([Hodge & da Cunha 2020](#)). [C II] is now routinely used for redshift confirmation (e.g., [Swinbank et al. 2012](#); [Bradač et al. 2017](#); [Molyneux et al. 2022](#); [Bouwens et al. 2022](#); [Endsley et al. 2023](#)), for measuring

SFRs (e.g., [Schaerer et al. 2020](#)), gas masses (e.g., [Zanella et al. 2018](#); [Dessauges-Zavadsky et al. 2020](#); [Vizgan et al. 2022](#); [Heintz et al. 2022](#); [Aravena et al. 2024](#)), and even for constraining dust temperature at $z \sim 7$ ([Sommovigo et al. 2021](#)). But where [C II] really excels is in probing the kinematics of the ISM ([Carilli & Walter 2013](#)), since it is mostly optically thin and largely unaffected by dust attenuation. With such a powerful tool, researchers have recently identified disk-like galaxies at $z > 4$ that appear to be dynamically supported by rotation, something that was unexpected at this early age of the universe (e.g., [Neeleman et al. 2020, 2021](#); [Rizzo et al. 2020, 2021](#); [Herrera-Camus et al. 2022](#); [Neeleman et al. 2023](#); [Roman-Oliveira et al. 2023](#); [Venkateshwaran et al. 2024](#); [Rowland et al. 2024](#); [Fujimoto et al. 2024](#)).

In addition, [C II] has the potential of revealing cool outflows launched in the ISM via the detection of broad velocity wings in the [C II] spectrum (e.g., [Gallerani et al. 2018](#); [Bischetti et al. 2019](#); [Ginolfi et al. 2020a](#); [Herrera-Camus et al. 2021](#)). However, since [C II] traces multiple gas phases, the signal of the broad component can be diluted if the outflowing phases are subdominant in terms of luminosity. A good example of this caveat is highlighted by [Spilker et al. \(2020\)](#), who find that none of the eleven DSFGs hosting unambiguous molecular outflows in their sample (detected as blueshifted OH 119 μm absorption) exhibits a corresponding broad component in the [C II] emission line.

In recent years, authors have begun to explore the synergies between [C II] 158 μm and Ly α for studying complementary aspects of galaxies, the two being the brightest emission lines available. For one, [C II] 158 μm overcomes some of the complexities of the Ly α line outlined in § 1.2.1: it is a good reference for the systemic velocity, allowing researchers to identify and measure velocity offsets in the Ly α line (e.g., [Maiolino et al. 2015](#)), which are key to understand the underlying scenario (e.g., [Matthee et al. 2018](#)). Moreover, when 3D observations are available for both lines, [C II] spatial and kinematic properties are very valuable to interpret complex Ly α -emitting structures such as LAHs (e.g., [Matthee et al. 2020](#)), LABs (e.g., [Umehata et al. 2021](#)), Ly α nebulae around quasars (e.g., [Drake et al. 2020](#); [Neeleman et al. 2023](#)), or Ly α nebulae in dusty protocluster environments (e.g., [Guaita et al. 2022](#); [Apostolovski et al. 2024](#)). Conversely, Ly α properties can help explain phenomena observed in the [C II] line. For example, [Fujimoto et al. \(2019, 2020\)](#)

report the detection of extended $\approx 10 - 20$ kpc “halos” of diffuse [C II] emission around normal $z = 4 - 7$ SFGs (see Fig. 1.5). In their analysis, Fujimoto et al. (2020) found that such galaxies have lower Ly α equivalent widths relative to galaxies that do not exhibit [C II] halos, thus favoring an interpretation in which the extended [C II] is coming from the neutral phase instead of the ionized phase.

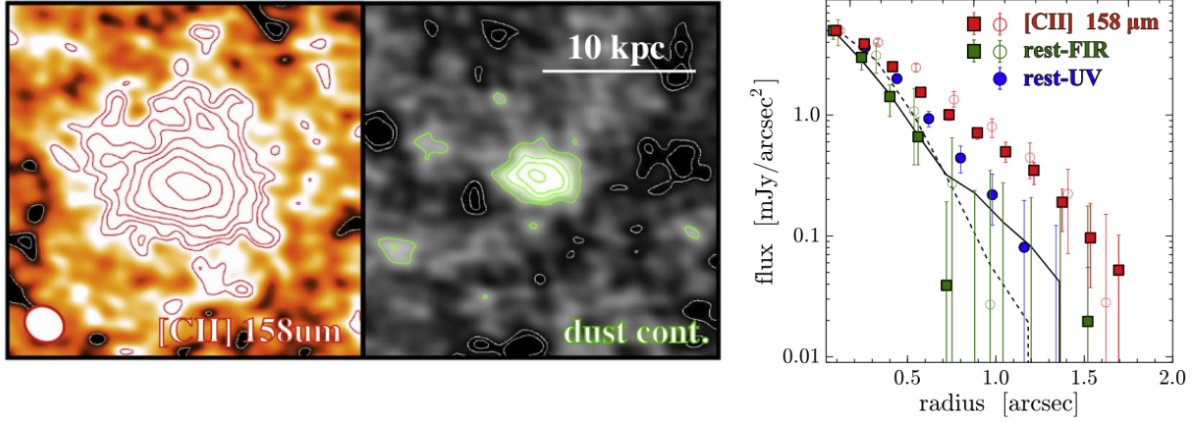


Figure 1.5: Stacked [C II] emission around distant star-forming galaxies. Figure adapted from Fujimoto et al. (2019). The left and middle panels are $4'' \times 4''$ cutouts from the ALMA stacks of [C II] and $158 \mu\text{m}$ dust emission, respectively, from a sample of 18 sources at $5 < z < 7$. The [C II] emission is about ≈ 5 times more extended than the dust continuum. The right panel shows the same data but displayed as radial profiles, also comparing with the rest-frame UV emission (blue circles).

Following the work of Fujimoto et al., extended [C II] emission has been detected in many other high- z galaxies with ALMA (e.g., Arata et al. 2020; Herrera-Camus et al. 2021; Lambert et al. 2023; Posses et al. 2023). However, the term “halo” can be misleading since, in most of the cases, the 2D morphology of the emission is well described by a single exponential profile, which only happens to be larger (in terms of effective radius) than the rest-frame UV emission (Ikeda et al. 2025, but see Akins et al. 2022)

The existence of extended [C II] emission suggests that, in some cases, [C II] $158 \mu\text{m}$ is also tracing structure at the CGM scales. However, the origin of this structure remains poorly understood. Fujimoto et al. (2019) proposed five possible scenarios for the physical origin of the [C II] halos that are closely related to the LAH mechanisms discussed in § 1.2.1: a) unresolved [C II]-emitting satellites (equivalent to mechanism 4 for LAHs,

§ 1.2.1); b) CGM-scale PDRs, where the [C II] emission arises from the neutral layer of UV-irradiated cold gas clumps in the CGM (similar to mechanism 1, § 1.2.1); c) CGM-scale H II regions, where the [C II] emission comes from cooling of photoionized gas (similar to mechanism 2, § 1.2.1); d) cold streams, where [C II] arises from the cooling of filaments of infalling gas (equivalent to mechanism 3, § 1.2.1); and e) outflows, where the [C II]-emitting material is blown away to large projected distances by a wind. Similar to LAHs, more than one scenario can be true, and the question about the origin of [C II] halos is still open. However, the outflow scenario is the one that currently has the most developed theoretical support (Pizzati et al. 2020, 2023; Muñoz-Elgueta et al. 2024).

While the scenarios above were devised for a sample of [C II] halos in isolated galaxies, the extended [C II] phenomenon also occurs among galaxies undergoing strong dynamical interactions. In the local Universe, it has been shown that extended [C II] emission arises from tidal features and shock fronts in interacting galaxies, with the shocks themselves being the powering source of the emission (e.g., Cormier et al. 2012; Appleton et al. 2013; Peterson et al. 2018). At higher redshift, authors have found diffuse emission (e.g. Ginolfi et al. 2020b; Di Cesare et al. 2024) and low-SB “bridges” between interacting galaxies (e.g. Carilli et al. 2013; Litke et al. 2019). These results underline the idea that interaction between galaxies enable the transfer of processed material and the enrichment of the CGM, as shown by simulations (e.g., Bournaud et al. 2011; Nelson et al. 2015; Anglés-Alcázar et al. 2017; Hani et al. 2018).

The ALMA-CRISTAL Large Program

The “[C II] Resolved ISM in STar-forming galaxies with ALMA” (CRISTAL) is a completed ALMA Large Program in Cycle 8 (program ID 2021.1.00280.L, PI: Herrera-Camus) designed to spatially resolve the [C II] emission of normal galaxies (i.e., within the star-forming main sequence) at $4 < z < 6$. CRISTAL targeted a subsample of 19 [C II]-detected galaxies from the “ALMA Large Program to Investigate C⁺ at Early Times” (ALPINE; Le Fèvre et al. 2020; Faisst et al. 2020) with stellar masses down to $3 \times 10^9 M_{\odot}$, and observed them at higher angular and spectral resolution with ALMA Band 7. The sample later expanded to 37 galaxies after including newly detected sources and archival data. This includes two

galaxies outside the main sequence, namely the massive DSFGs J1000+0234 (Capak et al. 2008, and Chapter 3) and CRLE (Pavesi et al. 2018).

Combined with ancillary data from HST and JWST, CRISTAL produced the first systematic census of gas, dust, and stars on kiloparsec scales when the Universe was roughly one billion years old (see Fig. 1.6). The CRISTAL survey is already building a lasting impact in the fields of galaxy kinematics (e.g., Posses et al. 2024; Telikova et al. 2024, Lee et al., submitted), morphologies (e.g., Mitsuhashi et al. 2024; Ikeda et al. 2025), feedback (Birkin et al., submitted, Davies et al., submitted), and the properties of the ISM at high redshifts (Li et al. 2024; Villanueva et al. 2024; Lines et al. 2025). A comprehensive overview of the survey is presented in Herrera-Camus et al. (2025)

1.2.3 Rest-frame optical emission lines

The optical range of the electromagnetic spectrum (roughly from 3000 Å to 9000 Å) offers a plethora of emission lines that are commonly observed in star-forming galaxies. These lines trace the warm neutral and warm ionized phases, and their intensities and ratios encode information about the temperature, ionization state, and chemical abundances of the gas. Importantly, the optical range includes the Balmer series of hydrogen recombination, which includes the second and third strongest recombination lines of hydrogen after Ly α , namely H α at 6564.6 Å, and H β at 4862.7 Å. Unlike Ly α , these lines are not resonant, therefore they are good tracers of kinematics, the rate of ionization, and consequently the SFR. Another set of strong lines is that of the forbidden oxygen lines, most notably the [O III] doublet at 4960.3 Å and 5008.2 Å, which is a key tracer of gas ionized by photons with energies above 35 eV, thus coming either from fairly massive stars or AGN.

Before the advent of the James Webb Space Telescope (JWST; Gardner et al. 2006; Menzel et al. 2023; Rigby et al. 2023), these lines were only accessible from the ground for galaxies up to $z \approx 2$, where their observation was technically difficult and thus limited to relatively bright objects. Now, JWST’s sensitive Near Infrared Spectrograph (NIRSpec, Böker et al. 2023) and Near Infrared Camera (NIRCam) Wide-field Slitless Spectroscopy (Rieke et al. 2023) have unlocked the rest-frame optical spectrum up to $z \approx 9$, and have

achieved deeper limits than ever before. In the last few years, the JWST has unleashed an avalanche of emission line spectra from early galaxies helping to uncover their redshifts (e.g., Oesch et al. 2023; Curtis-Lake et al. 2023; Carniani et al. 2024), ionization sources (e.g., Scholtz et al. 2023; Chisholm et al. 2024), nebular abundances (e.g., Curti et al. 2023; Bunker et al. 2023; Sanders et al. 2024), and their growing SMBHs (e.g., Harikane et al. 2023; Maiolino et al. 2024; Matthee et al. 2024).

Furthermore, NIRSpec’s Integral Field Spectroscopy (IFS) mode provides the opportunity of studying the gas and stars in distant galaxies in a spatially resolved way. Although the aperture of the Integral Field Unit (IFU) is only of $3'' \times 3''$, the NIRSpec IFS mode has enabled the detection of gas at CGM scales around a variety of sources (e.g., Wylezalek et al. 2022; Perna et al. 2023; Roy et al. 2024; Wang et al. 2024; Scholtz et al. 2024; Saxena et al. 2024; Vayner et al. 2024a,b; Pérez-González et al. 2024).

1.3 This thesis

As discussed in this chapter, the CGM is one of the main characters of the baryon cycle, as it mediates accretion, outflows, and metal mixing, and ultimately the cool gas supply of the ISM. While significant progress has been made in understanding the properties of the high-redshift CGM, several questions remain unsolved. In this thesis, we propose that high angular resolution observations of Ly α , [C II], and rest-frame optical emission lines can be used to fill in the missing details by addressing the following questions:

- What is the relative contribution of each mechanism to the origin of LAHs?
- What is the nature of extended [C II] emission?
- How do feedback and dynamical interactions shape the close environments of SFGs?

Here, we aim to advance toward a finer observational picture of galaxy evolution and the baryon cycle through deep, high resolution spectral imaging of the ISM and CGM at $z \gtrsim 3$. Given the difficulty and observational cost of such observations (even in the era of ALMA, MUSE, and JWST), we will limit our analysis on the following two benchmark systems, with the intention of setting a starting point for future expansion of the sample:

- SGAS J122651.3+215220 (a strongly-lensed pair of UV-selected galaxies with LAH at $z = 2.92$)
- CRISTAL-01 (also known as DEIMOS-COSMOS 842313; a massive UV-bright galaxy with LAH at $z = 4.55$ and a DSFG companion)

The content of the next three chapters was first published in peer-reviewed journals in three separate papers. In [Chapter 2](#) ([Solimano et al. 2022](#)) I present a study on the LAH of the SGASJ1226 system using state-of-the-art observations with MUSE. SGASJ1226 had been previously studied with a variety of instruments and methods, therefore represents one of the best known galaxies of its kind at $z \approx 3$. My collaborators and I investigated the properties and origin of the extended Ly α emission of SGASJ1226 for the first time. In [Chapter 3](#) ([Solimano et al. 2024](#)) I present the discovery of a 15 kpc plume of [C II]-emitting gas associated with the J1000+0234 system. This study leverages the deep, high-angular resolution ALMA-CRISTAL data to resolve the structural and kinematic properties of the plume, and shed light into its physical origin. In [Chapter 4](#) ([Solimano et al. 2025](#)) I present the discovery of another extended structure in the J1000+0234 system. This time, novel JWST observations revealed large-scale ionized clouds in the proximity of J1000+0234's DSFG. Finally, In [Chapter 5](#) I review the main findings of this thesis, present ongoing work on followup data, and conclude with a few ideas of future projects.

Chapter 2

A resolved study of a strongly-lensed Lyman Alpha Halo at $z \approx 3$

The content of this chapter was published online on August 9th 2022 as a research article in the *Astrophysical Journal*, volume 935, page 17, under the title “*Revealing the Nature of a Ly α Halo in a Strongly Lensed Interacting System at $z = 2.92$ ””, see [Solimano et al. \(2022\)](#). The article was coauthored by Jorge González-López, Manuel Aravena, Evelyn J. Johnston, Cristóbal Moya-Sierralta, Luis F. Barrientos, Matthew B. Bayliss, Michael Gladders, Leopoldo Infante, Cédric Ledoux, Sebastián López, Suraj Poudel, Jane R. Rigby, Keren Sharon, and Nicolás Tejos. Here I reproduce the full article with minor modifications intended to integrate seamlessly with the rest of the thesis. The main changes were the deletion of the first paragraphs of the introduction and a few paragraphs of the discussion to avoid redundancy with [Chapter 1](#), and the inclusion of the appendices as actual sections in the text.*

2.1 Introduction

Theoretical models and simulations show that LAHs form by several mechanisms, as reviewed in [§ 1.2.1](#). Observationally, determining which mechanisms are at play is challenging, since the spectral shape of the line can be very similar for different underlying scenarios. Fortunately, simulations also predict LAHs to have a rich spatial substructure,

featuring filaments, clumps and satellites, but also spatial variations in the spectral properties of the line (Mitchell et al. 2018; Behrens et al. 2019; Smith et al. 2019). For this reason, high angular resolution spectroscopy of LAHs is very valuable, since it can help understand the physical nature of LAHs and potentially disentangle some of the degeneracies that affect the interpretation of the Ly α line.

In this context, a growing number of studies have exploited the power of strong gravitational lensing to resolve LAHs in a great level of detail (e.g., Swinbank et al. 2007; Karman et al. 2015; Caminha et al. 2016; Patrício et al. 2016; Smit et al. 2017; Erb et al. 2018; Claeysens et al. 2019, 2022; Chen et al. 2021a). This approach was pioneered by Swinbank et al. (2007), who obtained early IFU data of a giant lensed arc corresponding to a galaxy at $z = 4.8$. With MUSE, the efficiency of this technique was enhanced, providing the first tentative evidence of spatial variations in the line profile of a few lensed LAHs (Smit et al. 2017; Erb et al. 2018). Later on, Claeysens et al. (2019) showed two examples of bright lensed LAHs with a robust measurement of the Ly α variation across the halo, finding in both cases a broader and redder line towards the outskirts of the halo. Although similar results were obtained in a handful of nonlensed halos in the MUSE *Hubble* Ultra Deep Field (hereafter UDF, Leclercq et al. 2020), the spatial scales reached with lensing remain unrivaled.

In this chapter we present MUSE observations of SGAS J122651.3+215220 (hereafter SGASJ1226), a lensed, multiply imaged pair of SFGs at $z = 2.92$. The main arc was discovered as a u -band dropout (Koester et al. 2010) and thanks to its high apparent brightness ($r = 20.6$ mag), it has been subject to several follow up observations (Wuyts et al. 2012; Saintonge et al. 2013; Malhotra et al. 2017; Rigby et al. 2018; Gazagnes et al. 2018; Chisholm et al. 2019; Solimano et al. 2021), becoming one of the best studied Lyman Break Galaxies (LBG). Here, we report the discovery of a LAH associated to this galaxy and its close companion, that thanks to the lensing effect spans $\sim 20''$ on the sky. We take advantage of its extreme magnification (between $\mu \approx 10$ and $\mu \approx 100$ across the whole system) to spatially sample the Ly α line on sub-kpc scales, thus offering a unique view of the CGM.

Throughout this chapter, we adopt a flat Λ CDM cosmology with a matter density of $\Omega_{m,0} = 0.3$ and a Hubble parameter at $z = 0$ of $H_0 = 70 \text{ km s}^{-1} \text{ Mpc}^{-1}$. Unless otherwise

specified, we will refer to physical (proper) distances rather than comoving distances. Also, all photometric magnitudes quoted in the chapter are in the AB system. When relevant, we assume a universal [Chabrier \(2003\)](#) initial mass function (IMF).

2.2 Observations and data reduction

2.2.1 MUSE

We observed SGAS J122651.3+215220 with the Multi Unit Spectroscopic Explorer (MUSE, [Bacon et al. 2010](#)) mounted at the Unit Telescope 4 (Yepun) of the Very Large Telescope (VLT). The data were taken between April 2018 and February 2019 as part of program 101.A-0364 (PI: López), using the Wide Field Mode with Adaptive Optics and extended wavelength range (WFM-AO-E). This setup provides a field of view (FoV) of $1' \times 1'$ with a pixelscale of $0''.2$, and a wavelength range of 4600 \AA to 9350 \AA with a resolving power of $R \sim 1770$ at 4800 \AA (the wavelength of $\text{Ly}\alpha$ emission at $z \sim 2.92$). A subset of these data were already presented by [Tejos et al. \(2021\)](#), and in this chapter we followed similar reduction steps. The main difference is that [Tejos et al.](#) only combined 20 exposures (six were discarded due to slightly suboptimal seeing) to create the final stacked datacube, while here we used the full set of 26 exposures to reach deeper in $\text{Ly}\alpha$ surface brightness. All exposures have an exposure time of $\sim 640 \text{ s}$, resulting in a total exposure time of $16,640 \text{ s}$ (~ 4.6 hours). We found that including these additional exposures provides a 14% reduction in the 5σ noise level of the $\text{Ly}\alpha$ pseudo narrowband image, while the PSF full width at half maximum (FWHM; $0.72'' \pm 0.03''$, see below) stays within the uncertainties of the value measured in the original cube ($0.76'' \pm 0.04''$).

The data was reduced using the MUSE pipeline ([Weilbacher et al. 2012](#)) within the ESO Recipe Execution Tool (EsoRex) environment ([ESO CPL Development Team 2015](#)), using standard procedures and calibrations. The wavelength solution was calibrated to vacuum. We measured and cleaned residual sky contamination from the standard pipeline using the Zurich Atmosphere Purge code (ZAP, [Soto et al. 2016](#)). We then aligned the WCS of the datacube to match that of the HST imaging (see below) using a bright star in the

FoV as reference. The effective PSF FWHM is $0.72'' \pm 0.03''$, as measured from a Moffat fit to the bright star in a spectrally stacked image around the wavelength of $\text{Ly}\alpha$ at $z = 2.92$.

The MUSE pipeline propagates uncertainties in the individual pixel tables during the datacube creation, yielding a “variance cube” as part of the output. However, variance cubes generated in this way are known to underestimate the true variances of the data, because the algorithm neglects the spatial correlation in the noise introduced by the dithering and the slicer patterns (e.g., [Bacon et al. 2017](#)). Since the analysis presented in this chapter requires a good knowledge of the uncertainties, we estimated the true variances following the method outlined by [Urrutia et al. \(2019\)](#) and [Weilbacher et al. \(2020\)](#), but with a small modification. While they assume the noise is spatially uniform (hence only wavelength dependent), we keep the spatial structure of the original variance cube, but scale it up according to a correcting factor. The rationale behind this choice is to account for the sources’ contribution to variance, which becomes relevant in the brightest regions of the $\text{Ly}\alpha$ halo. To obtain the correction factor, we created a new pixel table populated with noise following a Gaussian distribution (mean=0, variance=1), and then fed it to the `muse_scipost` routine in the EsoRex pipeline to produce a mock noise datacube. We then measured the variance in sky regions of the resulting datacube to be close to 0.4 (the actual value is slightly wavelength dependent, but we assume it is constant). So the correction factor is $1/0.4 = 2.5$, which is then multiplied by the original variance cube. After this correction, the S/N distribution of sky apertures is consistent with a variance of ~ 1 while without the correction such values were ~ 2 .

After visual inspection of the datacube, it became apparent that the central galaxy of the lensing cluster (hereafter BCG) contributed significantly to the background light near the arcs (see [Fig. 2.1](#)). Due to the position, orientation and angular extension of the arcs with respect to the BCG, modeling and subtracting the background contamination in apertures would have been impractical and prone to many systematic effects. Instead, we opted for the self consistent approach of modeling the BCG with a parametric light profile as a function of wavelength. We achieved this using the Bulge-Disk Decomposition of IFU data package (BUDDI, [Johnston et al. 2017](#)), which uses GALFITM ([Häußler et al. 2013](#)) to model the 2-dimensional light profile of a galaxy simultaneously across several

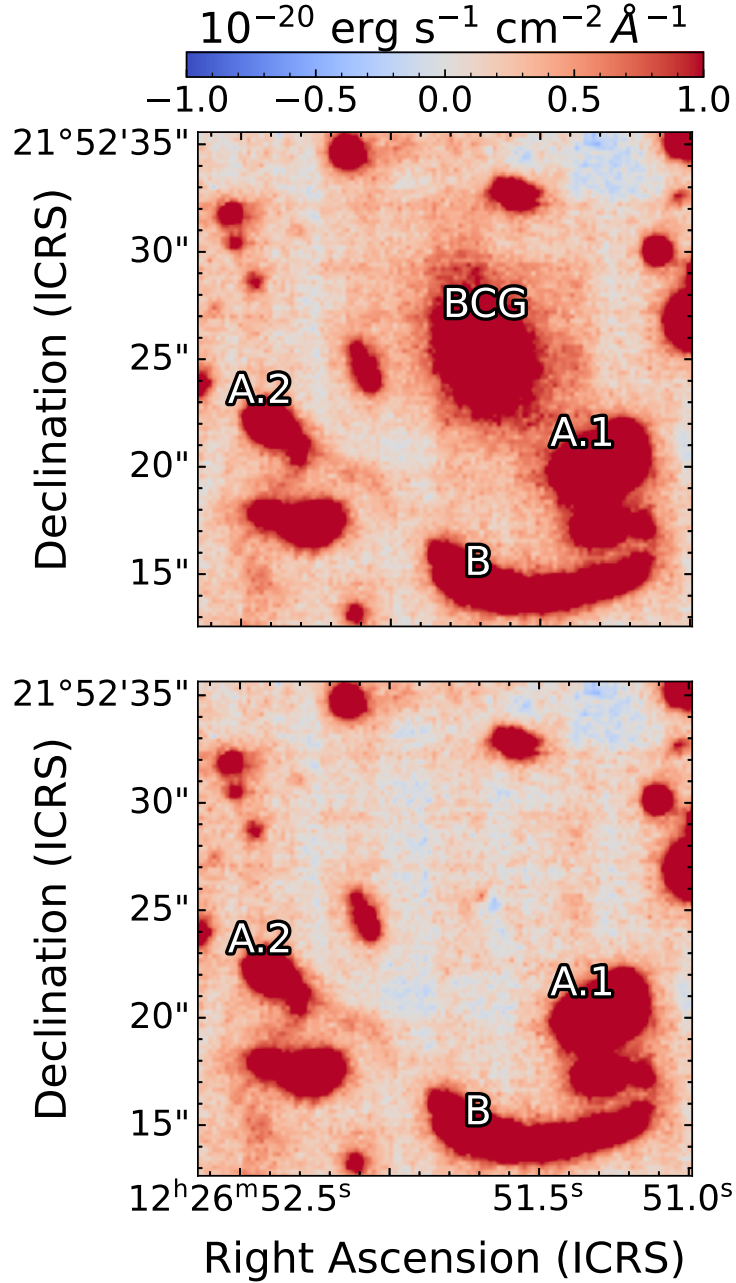


Figure 2.1: Subtraction of the BCG light model from the MUSE cube. The upper panel shows the inner $23'' \times 23''$ of an average channel map integrated from 4900 Å to 5700 Å taken from the datacube. The lower panel shows the same view but the average is obtained from the BCG-subtracted residual cube created with BUDDI. The image does not contain significant features at the position of the BCG within the colormap cuts ($\pm 7\sigma$).

wavelength slices. While BUDDI is usually used to cleanly extract the spectra of each component included in the model, it also provides a residual datacube where the light of the

target has been subtracted and the foreground and background objects can be analyzed with minimal contamination. In this case, we modeled the BCG with a single Sérsic profile plus a central PSF component after masking the arcs and other unrelated sources. After extracting the best fit model datacube, the residual datacube was obtained, in which the light of the arcs is free from contamination from the BCG (see bottom panel of Fig. 2.1). In what follows, we use this BCG-subtracted datacube to perform the Ly α analysis.

2.2.2 HST

Observations of SGAS J122651.3+215220 were taken with the *Hubble* Space Telescope (HST) with the Advanced Camera for Surveys (ACS) in the broadband filters F606W and F814W, and with the infrared channel of the Wide Field Camera 3 (WFC3) in the F110W and F160W filters, as part of the General Observer programs #12368 and #15378 respectively. We used DRIZZLEPAC’s AstroDrizzle routine to align and combine the calibrated exposures to a common grid with a pixelsize of 0''.03 using a gaussian kernel with pixfrac=0.8. The images reach 5 σ limiting magnitudes¹ at $m_{606} = 25.9$, $m_{814} = 25.4$, $m_{110} = 24.7$ and $m_{160} = 24.6$. To check the accuracy of the astrometric solution *a posteriori*, we cross-matched the point sources in the final ACS frames with the *Gaia* DR2 catalog [Gaia Collaboration et al. \(2018\)](#) and found 5 sources with a mean shift of 0''.08 and no signs of rotation nor major distortion.

A 30'' \times 20'' cutout of the ACS F606W image is shown in the upper right panel of Fig. 2.2. The multiple images and arcs are labeled using the same nomenclature as in Fig. 2.1. A.1 is the brightest (most highly magnified) component and corresponds to a two-fold, almost symmetric pair of images of galaxy A at both sides of the lensing critical curve (dotted white line). A fainter counterimage (A.2) of the same galaxy is seen $\sim 15''$ to the East. The second galaxy of the system, B, has a single known image (arc B) stretching from East to West a few arcseconds below A.1. A zoom-in view of arc B shown in the lower right panel of Fig. 2.2 reveals multiple knots of UV emission. Arc B is also the host of the unresolved 870 μ m continuum detection (purple ellipse) reported in [Solimano et al.](#)

¹With σ computed as the standard deviation of a sample of 5000 flux measurements from randomly placed 1'' apertures in blank sky regions.

(2021). Between arcs A.1 and B we indicate G1, the $z = 0.77$ foreground Mg II absorber studied in Mortensen et al. (2021) and Tejos et al. (2021).

Table 2.1: HST aperture photometry of the $z = 2.92$ lensed arcs of the SGASJ1226 system.

Filter / Image	AB Magnitude ^a		
	A.1 ^b	A.2	B.1
ACS F606W	20.62 ± 0.04	22.29 ± 0.05	21.27 ± 0.12
ACS F814W	20.47 ± 0.04	22.15 ± 0.06	21.00 ± 0.11
WFC3 F110W	20.51 ± 0.04	22.23 ± 0.08	20.94 ± 0.12
WFC3 F160W	20.13 ± 0.04	21.91 ± 0.09	20.46 ± 0.12

^a Corrected by Galactic extinction but not lensing magnification.

^b Includes both halves of the arc. The contamination from the lens perturber is not accounted for.

At $z = 2.92$ the observed filters cover the ultraviolet continuum and the Balmer break at the source rest frame, sampling the SED of the young stellar populations. The high resolution imaging also provides exquisite morphological detail on the lensed arcs, revealing numerous clumps and substructure. At the same time, it enables the identification of lensed image pairs and the positions of the cluster members that are included in the development of the lens model (Dai et al. 2020; Tejos et al. 2021).

The complex morphology of the lensed galaxies in SGASJ1226 system (see § 2.3.5) makes the standard photometric extraction techniques unsuited. For this reason, we used manually defined *ad hoc* polygonal apertures to obtain the total flux from the arcs. To assess the systematic error associated with this method, four members of the team created several apertures for each arc based on the image with the broadest PSF (WFC3-IR/F160W). The flux standard deviation derived from 20 different contributed apertures is about 10 percent, three times larger than the statistical error inferred from linear propagation. The final image plane magnitudes are reported in Table 2.1 after correction from Milky Way reddening using the Schlafly & Finkbeiner (2011) extinction tables.

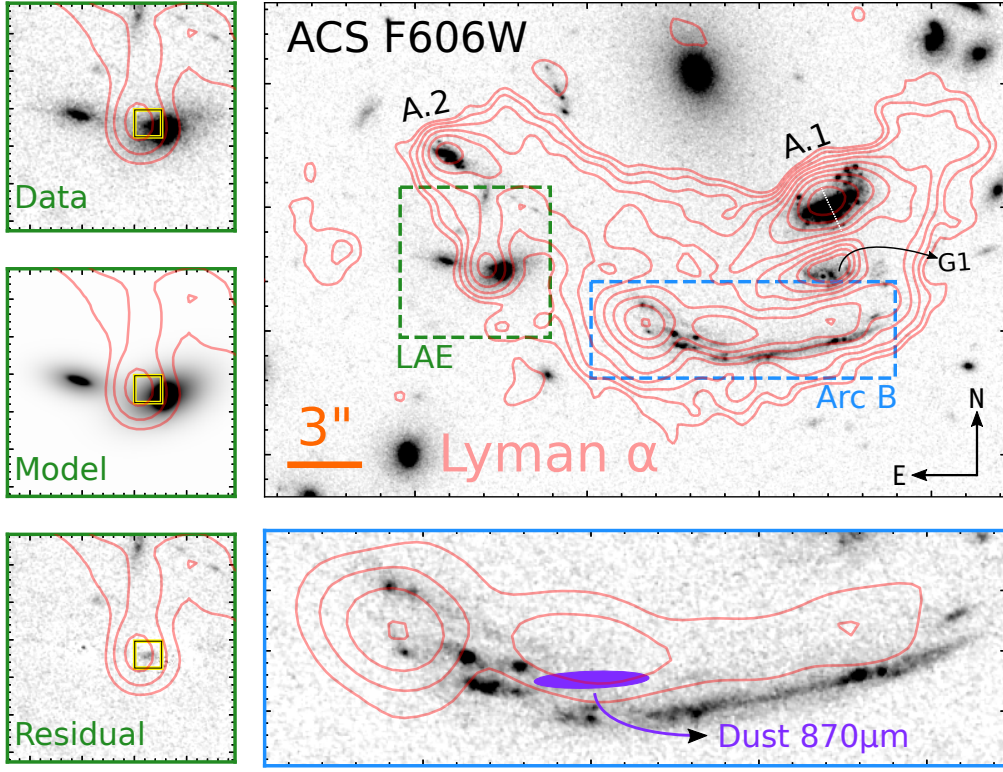


Figure 2.2: Overview and details of the image plane morphology of the SGASJ1226 system. *Upper right:* $30'' \times 20''$ cutout of the HST ACS F606W image, with MUSE Ly α contours overplotted (pale red). The contours start at the $3\sigma = 2.27 \times 10^{-18} \text{ erg s}^{-1} \text{ cm}^{-2} \text{ arcsec}^{-2}$ surface brightness level of the smoothed NB image (see § 2.3.2) and increase in powers of $\sqrt{2}$. The thin, dotted white line segment approximately divides A.1 into the two symmetric halves of the arc. *Lower right:* zoom-in view of Arc B that highlights the spatial offset between the UV and Ly α emission. For clarity, contours only show the top $12\sqrt{2}$, 24 , $24\sqrt{2}$ and 48σ levels of Ly α SB. *Top left:* $6''.1$ cutout of the ACS image centered on a local maximum of Ly α SB, with contours starting at 6σ . *Middle left:* GALFIT model of the two foreground elliptical galaxies near the local Ly α peak. *Lower left:* Residuals from the subtraction of the GALFIT model. A compact excess of continuum appears near the center of the Ly α peak. The purple ellipse shows the location and deconvolved size of the dust continuum emission at $870 \mu\text{m}$ detected with the ACA (Solimano et al. 2021)

2.2.3 Lens model

A proper measurement of the intrinsic properties of strongly-lensed galaxies requires accurate knowledge of the geometrical distortion and magnification produced by the lens-

ing cluster. Good approximations of the amount and direction of the distortion at any given position are obtained by modeling the cluster as a collection of parametric dark matter profiles and then constraining the model to predict the positions of image pairs identified in the data. In this chapter, we use the lens model presented in [Tejos et al. \(2021\)](#), therefore we refer the reader to that work for further details. Briefly, the modeling was done using the *Lenstool* software ([Jullo & Kneib 2009](#)) following the procedure described in [Sharon et al. \(2020\)](#). The model was fitted using the three images of galaxy A (two images in A.1 plus the counterimage A.2; see [Fig. 2.2](#)), with the position of individual clumps identified in the HST data serving as constraints. Both cluster-scale and galaxy-scale potentials were modeled as pseudo isothermal ellipsoidal mass distributions (PIEMD), all located at $z_{\text{lens}} = 0.43$. For galaxy-scale potentials the center of each PIEMD was held fixed to match the optical centroids of the cluster members during the fitting process. The presence of a second strong-lensing cluster at the same redshift only $157'$ to the South of SGASJ1226 motivated the addition of a cluster-scale PIEMD at that position, contributing shear to the overall lensing potential. Finally, a perturber on top of the West part of arc A.1, plus the $z = 0.77$ galaxy between A.1 and B (labeled G1 in [Tejos et al. 2021](#), see [Fig. 2.2](#)) were included as individual components. The latter was treated as belonging to the same plane as the foreground cluster.

The resulting best fit model, provides a set of deflection matrices that prescribe the angular offsets (in both R.A. and Dec. axes) induced by the lens at any given position in the image plane. This model reproduces the positions of 26 constraints with a root mean square (RMS) of $0''.08$. Throughout this chapter, we use the deflection matrices to reconstruct source plane positions and sizes.

In [Fig. 2.3](#) we plot the lensing critical curve (i.e., the locus of maximal magnification) on top of the MUSE pseudo narrowband image as a way to visualize the morphology of the lensing potential.

2.3 Results

2.3.1 Host galaxy properties

In this section we give a characterization of the host galaxies in terms of systemic velocity, mass and luminosity. A crucial step to understand the origins and kinematics of the Ly α emitting gas is to secure systemic redshifts for the galaxies within the halo. For galaxy A, numerous reports exist in the literature. Firstly, in the discovery paper [Koester et al. \(2010\)](#) use the UV absorption lines to get $z_{\text{ISM}} = 2.9233$. Later, [Wuyts et al. \(2012\)](#) obtained Keck/NIRSPEC spectroscopy which allowed the measurement of rest-frame optical nebular lines to find $z_{\text{neb}} = 2.9257 \pm 0.0004$. The difference of $\sim 200 \text{ km s}^{-1}$ between emission and absorption solutions was then suggested as tentative evidence for outflows ([Wuyts et al. 2012](#)). For galaxy B, *Gemini*/GMOS spectroscopy yielded $z_{\text{ISM}} = 2.9233$ ([Bayliss et al. 2011](#)) but no nebular redshift is available. Here, we avoid the systematic effects arising from the mix of different instruments by measuring redshifts directly on the MUSE datacube. Unfortunately, the nebular lines accessible in the MUSE wavelength range are extremely faint, so we coadded all spaxels associated with each galaxy to improve the S/N, thereby losing any information of possible spatial velocity gradients. For each galaxy, we simultaneously fit the Si II* $\lambda 1533$ and [C III] $\lambda\lambda 1906, 1908$ lines on the continuum subtracted spectrum with gaussian profiles of common width, varying only z and the line amplitudes. In this way we obtain $z_{\text{neb}} = 2.9257 \pm 0.0001$ and $z_{\text{neb}} = 2.9238 \pm 0.0002$ for A and B respectively, corresponding to a radial velocity difference between A and B of $(145 \pm 17) \text{ km s}^{-1}$. The value for galaxy A is fully consistent with prior literature measurements ([Wuyts et al. 2012](#); [Rigby et al. 2018](#)). We checked that our solutions are robust against the relaxation of the width constraint: letting Si II* to have a width parameter independent of the [C III] lines yields the same 16-50-84 percentiles as the single width run.

The general properties of the two brightest galaxies in the Ly α halo were already reported in [Solimano et al. \(2021\)](#) by the means of fitting spectral energy distribution (SED) models to the available broadband photometry. Briefly, the SED fits included photometry from the four HST bands mentioned above, *Spitzer*/IRAC 3.6 μm and 4.5 μm bands, as well

Table 2.2: Properties of the two largest member galaxies

Property	Galaxy A	Galaxy B
Redshift ^a	2.9257(1)	2.9238(2)
Average μ	7.5 ± 1.5^b	30 ± 6
$\log (M_{\text{stars}}/M_{\odot})$	9.8 ± 0.2^b	9.7 ± 0.2
SFR ($M_{\odot} \text{ yr}^{-1}$) ^c	10 ± 2^b	15 ± 4
$\log (L_{\text{UV}}/L_{\odot})$	10.80 ± 0.09^b	10.6 ± 0.1
$\log (L_{\text{IR}}/L_{\odot})^c$	< 11.5	10.9 ± 0.3
β_{UV}	-0.82 ± 0.15	-0.66 ± 0.24
$12 + \log (\text{O}/\text{H})^d$	8.2 ± 0.2	8.2 ± 0.2

^a Based on the simultaneous fit to the Si II* $\lambda 1533$ and [C III] $\lambda\lambda 1906, 1908$ nebular emission lines in the MUSE spectra.

^b Estimated from the complete lensed counterimage A.2, see § 2.2.3 and § 2.3.1. The average magnification of the arc A.1 is $\mu \approx 87$.

^c From Solimano et al. (2021).

^d From Chisholm et al. (2019) STARBURST99 fits assuming stellar metallicity equals gas phase metallicity.

as Atacama Compact Array (ACA) 870 μm continuum. The available *Herschel* bands were excluded due to severe blending and low S/N (see Saintonge et al. 2013). The magnified fluxes were then fit with the MAGPHYS (da Cunha et al. 2008, 2015) energy balance code to constrain the SFR, stellar mass and infrared luminosity. The lack of mid-infrared bands prevented the detection of continuum from dust heated by an active galactic nucleus (AGN). Here, we reproduce the best fit values and their uncertainties after demagnification in Table 2.2. The average magnification was computed as the ratio between the solid angle of the HST aperture in the image plane and the solid angle spanned by the smallest polygon that encloses all the delensed grid points in the source plane. The magnification uncertainty was fixed to 20% to account for typical systematic errors in the lens modeling (Raney et al. 2020, where statistical errors are less important). We tested this choice by

computing the actual statistical uncertainties using a set of 100 realizations of the lens model sampled from the MCMC chain. We found that for the apertures used here, the relative uncertainty in magnification is between 13% and 17%.

We also estimate the rest-frame far ultraviolet (UV) luminosity of the arcs directly from the ACS/F606W photometry tracing the stellar continuum at $\lambda_{\text{rest}} \approx 1500 \text{ \AA}$ at $z = 2.92$. As we do with all the available HST data, we divide the image plane fluxes by the average magnification factor of the most complete image. This means that despite A.1 having the largest S/N, our flux-dependent estimates for galaxy A come from the counterimage A.2 instead, since it has the largest footprint in the source plane. In this way, we use $\mu = 7.5$ for A.2 and $\mu = 30.2$ for the arc B to find $\log(L_{\text{UV}}/L_{\odot}) = \log(\lambda L_{\lambda}) = 10.80 \pm 0.09$ for galaxy A and $\log(L_{\text{UV}}/L_{\odot}) = 10.6 \pm 0.1$ for galaxy B, corresponding respectively to 1.0 ± 0.2 and 0.64 ± 0.15 times the typical UV luminosity at $z = 3$, $L^* = 6.2 \times 10^{10} L_{\odot}$ (e.g., Paltani et al. 2007; Reddy et al. 2008; Bian et al. 2013; Mehta et al. 2017).

2.3.2 Continuum subtraction and pseudo narrowband imaging

The first step in our analysis was to create narrowband Ly α images from the reduced MUSE cube. We first extracted a subcube between 4754 Å and 4810.3 Å, a range that fully includes both the Ly α emission line and 10 Å of adjacent continuum to each side. In the UV-bright regions of the arc, the continuum shows a clear break at the wavelength of Ly α . At bluer wavelengths the continuum is strongly suppressed by a combination of damped self absorption and decreased IGM transmission, while at redder wavelengths the emission is dominated by the UV power-law continuum but modulated by the H I damping wings. These effects produce an underlying continuum with a complex shape. In principle, one could model it as the superposition of the UV powerlaw, a damped Voigt profile and the break from the IGM transmission, however, the data lacks sufficient signal to noise to fit such a model on a spaxel-to-spaxel basis. Instead, we chose to model the continuum as linear ramp between the blue and red continuum levels. This scheme has been successfully applied to similar datasets (e.g., Claeysens et al. 2019). The functional form of this model is

$$f_{\lambda} = \begin{cases} f_{\text{blue}} & 4754 \text{ \AA} \leq \lambda < \lambda_1, \\ m(\lambda - \lambda_1) + f_{\text{blue}} & \lambda_1 \leq \lambda \leq \lambda_2, \\ f_{\text{red}} & \lambda > \lambda_2 \geq 4810.3 \text{ \AA}, \end{cases}$$

where $m = (f_{\text{red}} - f_{\text{blue}})/(\lambda_2 - \lambda_1)$ is the slope of the linear ramp. We estimate the mean blue (f_{blue}) and red (f_{red}) continuum levels by averaging the spectral channels to each side of the line from the subcube, at $\lambda < \lambda_1$ and $\lambda > \lambda_2$ respectively. We found that the values $\lambda_1 = 4768.8 \text{ \AA}$ and $\lambda_2 = 4788.0 \text{ \AA}$ produced robust continuum subtraction (average zero flux) at both sides of the line.

Once the continuum was extracted from every spaxel, we integrated the resulting cube between 4769 \AA and 4788 \AA (rest frame 1215.3 \AA and 1219.6 \AA at $z = 2.924$) to obtain the pseudo narrowband image of the Ly α emission. The integration limits were chosen to enclose the full spectral extent of the redshifted line. We exclude the blueshifted peak since it only appears in a limited image plane region and its contribution to the total flux is less than 1%. [Fig. 2.3](#) shows the final image after smoothing with a Gaussian kernel of $\sigma = 2$ spaxels. The smoothing is applied only for the ease of visualizing the low surface brightness structure of the object, but in the subsequent analysis we used the unsmoothed version.

2.3.3 Asymmetric Gaussian fitting

The asymmetric Gaussian (AG) profile as parameterized by [Shibuya et al. \(2014\)](#) serves as a tool to measure basic properties of typical Ly α spectra, namely the amplitude, peak shift velocity, full width at half maximum plus an asymmetry parameter that quantifies the skewness of the curve. The use of the AG profile is becoming increasingly common in the resolved LAH literature ([Claeyssens et al. 2019](#); [Leclercq et al. 2020](#); [Claeyssens et al. 2022](#)). In this chapter we fit Ly α spectra either from the integrated apertures ([§ 2.3.4](#)), from individual resolved regions ([§ 2.3.5](#)) or absorption lines ([§ 2.3.6](#)) using a standard MCMC posterior sampling scheme. For each fit, we impose a Gaussian likelihood for the residuals, which are computed from the difference between the data and the AG profile

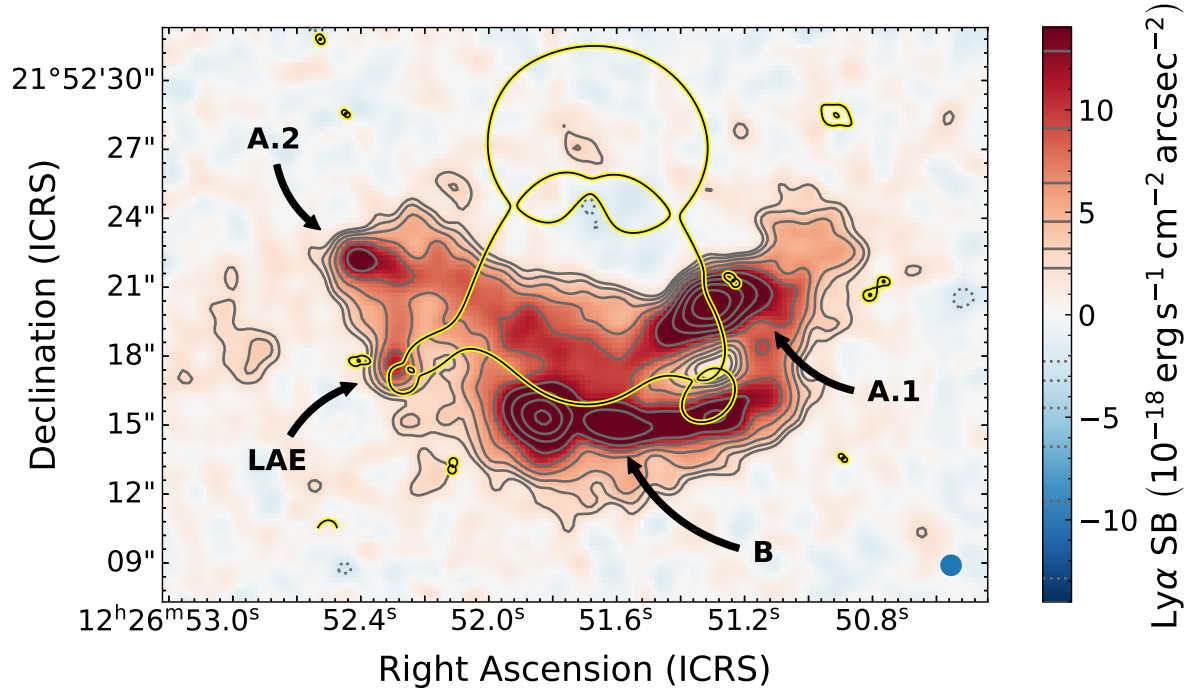


Figure 2.3: Continuum-subtracted pseudo narrowband image of the lensed Ly α halo at $z = 2.92$. The image was smoothed with a gaussian kernel of 2 spaxels' width. The blue circle at the lower right corner indicates the FWHM size of the smoothing kernel, setting the angular resolution at effective $0''.94$. Positive (negative) contours shown in gray solid (dotted) lines are the same as in Fig. 2.2 and start at the $\pm 3\sigma = \pm 2.27 \times 10^{-18} \text{ erg s}^{-1} \text{ cm}^{-2} \text{ arcsec}^{-2}$ level of surface brightness and increase (decrease) in powers of $\sqrt{2}$. The black curve with yellow outline traces the lensing critical curve, that is, the loci of maximum magnification.

convolved with the line spread function (LSF). We sample the posterior distribution using 32 walkers and 2000 steps within the `emcee` library (Foreman-Mackey et al. 2013) to obtain robust estimates of the parameter uncertainties and covariances. We set uniform priors on each of the five parameters (the four named above plus an amplitude parameter) and let them vary freely over their domain ranges. During the optimization, we also keep track of the integrated flux of the model. The value for the peak shift velocity of depends on the systemic redshift input by the user. An example of an AG fit is displayed in Fig. 2.4.

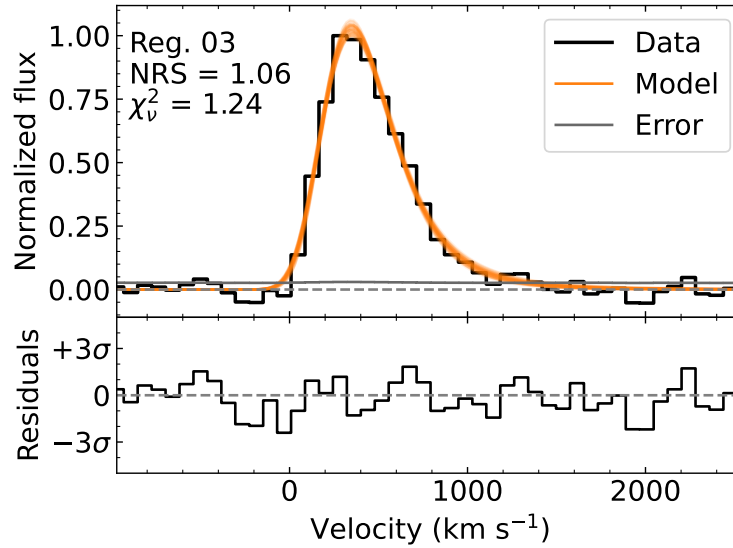


Figure 2.4: Example of asymmetric Gaussian fit to one of the extracted spectra. The solid orange curves show 50 random draws from the posterior probability distribution. The gray dashed line marks the zero flux level. In the legend in the upper left corner, NRS stands for normalized residual scatter, which is the standard deviation of the residuals weighted by the error spectrum.

2.3.4 Image plane analysis

In order to obtain insights on the spatial Ly α properties of SGASJ1226 in a way that is independent of the lens model, we start our analysis in the image plane, rather than in the source plane. The NB image in Fig. 2.3 shows at least five strong peaks of Ly α SB that stand out from the diffuse emission. For aid of comparing these features to the UV continuum, we have reproduced the Ly α SB contours of Fig. 2.3 in Fig. 2.2, placing them

on top of the ACS F606W image, the band that traces the UV continuum at $z = 2.92$. The two northernmost local peaks are associated to images A.1 (West, bright) and A.2 (East, faint) of galaxy A. Toward the South, we observe the second brightest peak of Ly α SB, that is connected to a fainter arc-like structure extending about $5''$ to the East. The arc itself has two secondary peaks at the $\approx 34\sigma$ level. We associate the peak plus the arc with Arc B in the HST image, although there is an evident offset between the bright spots in Ly α and the location of the UV-bright clumps (see lower right panel of Fig. 2.2). In particular, the bright Ly α peak at B is offset by $1''.2$ with respect to the UV centroid, which lies in the middle of the brightest knots of the arc. Also, the Ly α arc is offset by $0''.6$ on average to the North of the UV arc B. Due to the achromatic nature of lensing, offsets in the image plane between two tracers (e.g., Ly α and UV here) imply intrinsic offsets in the source plane.

The other remarkable local peak is $\sim 5''$ southward from A.2 at 17σ above the sky background (see green box in Fig. 2.2). Interestingly, this peak is centered very close to two intervening foreground cluster members. Since no emission line is expected at $\lambda_{\text{obs}} = 4471 \text{ \AA}$ at the redshift of the cluster ($z_{\text{lens}} = 0.43$), we conclude that the signal comes from the same redshift of the LAH and is likely originated in a compact Ly α Emitter (LAE) embedded in the halo (hereafter we refer to this Ly α source as SGASJ1226-LAE). Motivated by this hypothesis, we searched the HST data for a continuum counterpart, finding a candidate near the core of one of the cluster members in the F606W image. To confirm the presence of this counterpart, we employed GALFIT (Peng et al. 2002, 2010) to model the light of the two intervening galaxies with Sérsic profiles. After subtraction of the best fit model, the residuals clearly show an excess emission within $0''.2$ of the Ly α peak. The excess is also detected in the F814W image, but not in the near infrared filters. The limited spatial resolution in the F110W and F160W bands results in the contamination the expected location of the galaxy by PSF subtraction residuals, preventing us to put any constraint on its flux.

We measured the flux in the residual images with SExtractor's (Bertin & Arnouts 1996) automatic apertures with the F606W residual as the detection frame, yielding (magnified) magnitudes of $m_{606} = 25.94 \pm 0.17$ and $m_{814} = 25.82 \pm 0.30$. From these two band we infer

a UV slope of $\beta = -1.6 \pm 1.1$. A Ly α flux of SGASJ1226-LAE of $7.5 \times 10^{-17} \text{ erg s}^{-1} \text{ cm}^{-2} \mu^{-1}$ was measured by fitting an asymmetric Gaussian profile (see § 2.3.3). to the spectrum integrated in a $1''$ circular aperture. Extrapolating the continuum flux to $\lambda_{\text{rest}} = 1215.67 \text{ \AA}$ we estimate a rest-frame Ly α equivalent width of $(104 \pm 19) \text{ \AA}$, which falls in the classical definition of high-redshift LAEs (Ouchi et al. 2020). At the same redshift than the rest of SGASJ1226, this source is likely a satellite galaxy of the system. Details on the characterization of this source together with estimates of its contribution to the total Ly α luminosity are presented in § 2.4.2.

Integrated spectrum

In Fig. 2.5 we show the spatially integrated Ly α spectrum for three different apertures, one for each of the two arcs and another for the diffuse emission. To create the apertures, we first integrated the datacube at $1550 \text{ \AA} < \lambda_{\text{rest}} < 1650 \text{ \AA}$ to obtain a map of the UV continuum at $z = 2.92$ at the same resolution, pixel scale and astrometry as the Ly α NB image. Then, we applied a threshold of continuum S/N = 5 on this image to isolate the spaxels containing bright UV emission. The resulting masks were manually inspected and tweaked to remove spurious spaxels that met the SNR threshold but were associated to unrelated sources. For galaxy A, the masks includes all spaxels both from the arc A.1 and the counterimage A.2. The mask for the diffuse Ly α halo was defined as all spaxels with Ly α surface brightness above $3\sigma(\text{smooth}) = 2.2 \times 10^{-18} \text{ erg s}^{-1} \text{ cm}^{-2} \text{ arcsec}^{-2}$ in the smoothed narrowband image. Then, the continuum masks were subtracted from the diffuse halo mask to exclude spaxels with continuum emission. The three apertures and their corresponding Ly α spectra are shown in Fig. 2.5.

The three profiles show a very strong red peak with no clear blue component. Also, the line profile is markedly asymmetric in the three cases, with a sharp drop from the peak to the blue and a broad red wing. The major difference between the three spectra is the width of the line and the location of the peak. We measure line properties such as the FWHM and the shift of the peak with respect to the systemic velocity of the system by fitting an asymmetric Gaussian (AG) profile to the spectrum after taking into account the line spread function (LSF). Galaxy A shows the narrowest line, with an observed-frame

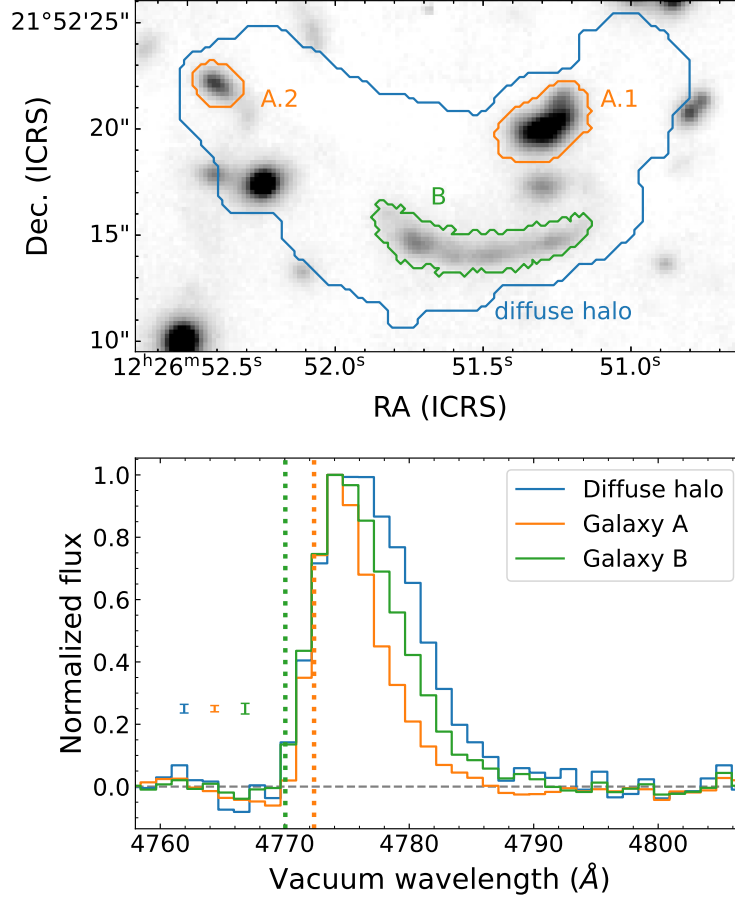


Figure 2.5: Ly α profiles extracted from global apertures. *Top:* MUSE broadband image synthesized around rest frame 1600 Å with the global image plane apertures used for extraction shown in color lines. *Bottom:* Continuum-subtracted, normalized MUSE spectra from three different image plane apertures. The blue, orange and green curves correspond to the spectra of the diffuse halo, galaxy A and galaxy B, respectively. Representative error bars are shown on the left. The dotted orange and green vertical lines indicate the wavelength of Ly α at the systemic redshifts (see § 2.3.1) of galaxy A and galaxy B, respectively.

FWHM of 4.68 ± 0.60 Å (equivalent to a rest-frame velocity of 294.2 ± 4.0 km s $^{-1}$) and a 1.72 ± 0.03 Å (108.2 ± 1.8 km s $^{-1}$) offset between the peak and the systemic redshift $z_{\text{sys}}^A = 2.9257$, indicated by a dotted orange line. The Ly α profile emitted by galaxy B is broader (FWHM = 6.84 ± 0.10 Å, 430.1 ± 6.5 km s $^{-1}$), and, despite having the same peak wavelength as galaxy A, the systemic redshift is lower ($z_{\text{sys}}^B = 2.9238$; dotted green line) and thus the velocity offset is 4.63 ± 0.06 Å (291.5 ± 3.5 km s $^{-1}$). Finally, the diffuse halo emission has

the broadest line width ($8.10 \pm 0.07 \text{ \AA}$, $509 \pm 4 \text{ km s}^{-1}$) and a peak that slightly displaced redward with respect to the peaks of A and B ($4.31 \pm 0.05 \text{ \AA}$, or $270.6 \pm 3.0 \text{ km s}^{-1}$ if we assume $(z_{\text{sys}}^A + z_{\text{sys}}^B)/2 = 2.92475$). We warn the reader that the relatively low uncertainties on the fitted parameters reflect the high S/N of the spectra, and thus do not include the systematic uncertainties arising from the unknown intrinsic profile shape.

The broader and redder line profile we observe in the diffuse halo relative to the central component agrees with previous findings by [Claeyssens et al. \(2019\)](#) for other two lensed LAHs (SMACS2031 and MACS0940) and by [Leclercq et al. \(2020\)](#) in a sample of unlensed LAHs in the UDF. In a scenario where the extended Ly α emission is explained exclusively by neutral gas scattering, the width of line is linked to the number of scatterings those photons had to experience before escaping the halo in the direction of the observer. The broader the line, the more reprocessed are the photons in the high velocity tail. In this context, our results would indicate that Ly α photons coming “down the barrel” from the star-forming galaxies are less reprocessed on average than the photons that escape from outskirts of the halo. Such effect can naturally arise if the close environments of the galaxies have a higher ionization fraction that effectively reduces the optical depth along the line of sight. However, the Ly α signal does not only depend on neutral hydrogen column density, but also on the gas kinematics.

Resolved Equivalent Width

Another important observable is the rest-frame Ly α equivalent width (EW), $W_{\text{Ly}\alpha}$, since it has been shown to correlate very strongly with the Ly α escape fraction ($f_{\text{esc}}^{\text{Ly}\alpha}$) of a galaxy (e.g., [Harikane et al. 2018](#); [Sobral & Matthee 2019](#)), defined as the ratio between observed and intrinsic Ly α luminosity. However, measuring EW is subject to some complexities when the line profile is composed by both emission and absorption components (e.g., [Kornei et al. 2010](#); [Erb et al. 2019](#)), as it is in the case of SGASJ1226. Here, we calculate the net or total EW dividing the Ly α flux by the expected continuum level at $\lambda_{\text{rest}} = 1215.67 \text{ \AA}$, which is extrapolated from a powerlaw fit to the continuum at $\lambda_{\text{rest}} \gtrsim 1270 \text{ \AA}$. Using the image plane apertures for A and B, we extracted the full MUSE spectra and fitted a powerlaw described by $f_{\lambda} \propto \lambda^{\beta}$ to all the line-free channels at $\lambda_{\text{rest}} \gtrsim$

1270 Å. We used uniform priors on β and the normalization factor. This resulted in slopes β of -1.18 ± 0.15 for the galaxy A and -0.79 ± 0.21 for the galaxy B. We use these values to extrapolate the de-magnified F606W magnitudes ($\lambda_{\text{pivot}} = 5921$ Å) to the redshift Ly α wavelength (4771 Å) continuum, finding a total (A+B) intrinsic flux level of $f_{4771} = (1.03 \pm 0.16) \times 10^{-18} \text{ erg s}^{-1} \text{ cm}^{-2} \text{ Å}^{-1}$. Then, we compute the EW by dividing the total delensed Ly α flux of the LAH, $F_{\text{Ly}\alpha} = (6.9 \pm 0.2) \times 10^{-17} \text{ erg s}^{-1} \text{ cm}^{-2}$ (see § 2.3.5), with the underlying continuum level obtained above. After propagating all uncertainties, this ratio yields $W_{\text{Ly}\alpha} = (66 \pm 10)(1+z)^{-1} \text{ Å} = (17.0 \pm 2.7) \text{ Å}$. Such value is typical of Lyman Break galaxies (e.g., Steidel et al. 2003) and, according to the empirically calibrated relation of Sobral & Matthee (2019), it implies a global $f_{\text{esc}}^{\text{Ly}\alpha} = 0.082 \pm 0.018$.

However, with the available data it is also possible to investigate spatial variations of the EW across the arcs. The distribution of EW can inform about the homogeneity of the intervening gas. For example if the EW is uniform across the source, it could mean that the Ly α signal is processed by an approximately homogeneous slab of gas. If the EW distribution is clumpy or has gradients, a more complex geometry can be in place.

We constructed a map of EW as the ratio between the Ly α NB and the extrapolated UV flux density at $\lambda_{\text{Ly}\alpha}$. To avoid discrepancies in the spatial resolution at different wavelengths, we estimated the UV slope in each spaxel by taking the ratio between PSF homogenized images at $\lambda_{\text{obs}} = 5300$ Å and $\lambda_{\text{obs}} = 7060$ Å (rest-frame 1350 Å and 1800 Å, respectively) before extrapolating to $\lambda_{\text{Ly}\alpha}$. The images were obtained by averaging over the spectral axis on a ≈ 200 Å window centered at these two wavelengths and masking the channels with line absorption or emission. We created models of the MUSE-AO PSF by fitting a circular Moffat 2D profile to a single star near the center of the field and used them to convolve all images to a common PSF with FWHM=0.72". We compute the UV slope array from the ratio between the blue and red continuum images and then use it to extrapolate the continuum flux density to the Ly α wavelength. The EW map is finally constructed from the resulting continuum image at $\lambda_{\text{Ly}\alpha}$ and the NB image (see Fig. 2.6). This operation was restricted to the same continuum apertures defined in § 2.3.4.

We observe that $W_{\text{Ly}\alpha}$ is mostly uniform towards galaxy A, with an average value of 4 Å, whereas galaxy B has values that range from 3 Å to 42 Å. The increased $W_{\text{Ly}\alpha}$ towards

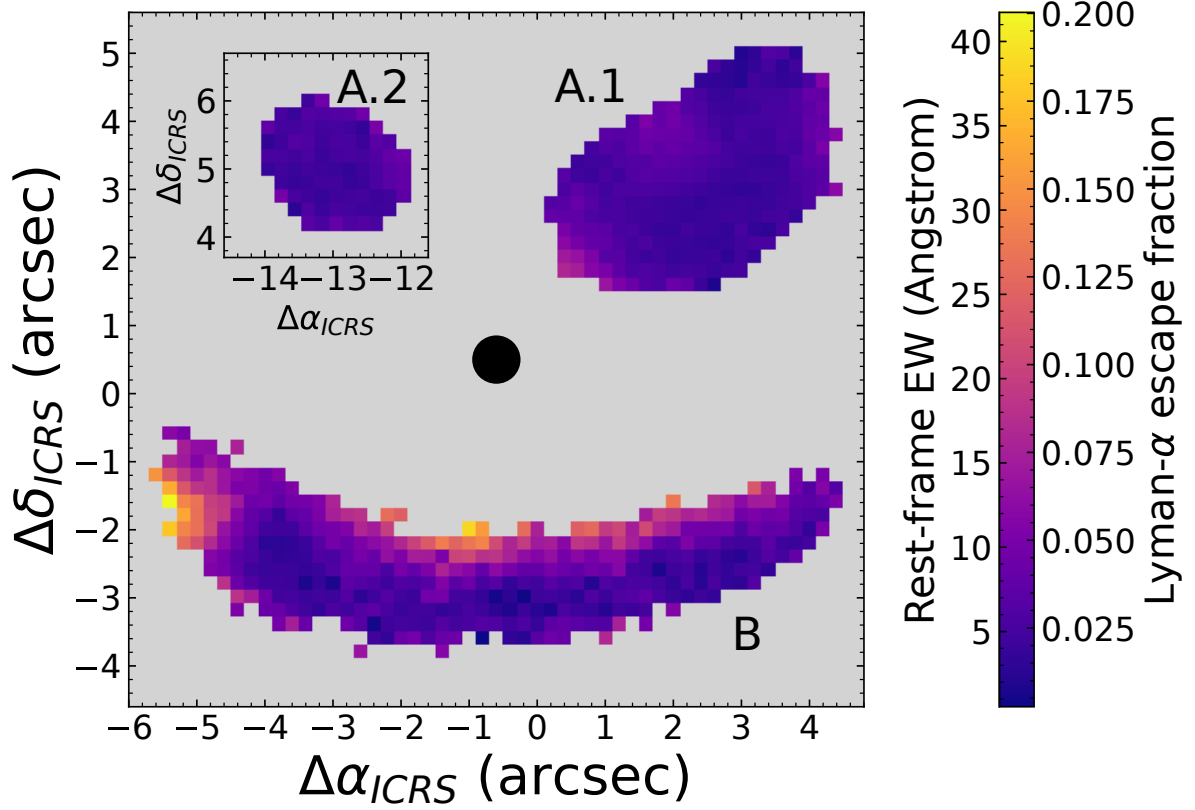


Figure 2.6: Image plane Ly α equivalent width map displaying arcs A.1, B and the counterimage A.2 (see inset panel). Spaxels without continuum were masked out. The black circle in the middle of the panel indicates the FWHM size of the effective PSF. The right axis of the EW colorbar shows the corresponding Ly α escape fraction according to the Sobral & Matthee (2019) relation.

the northern and eastern edges of the arc B can be explained by the large spatial offset between the continuum and the brightest knots of Ly α emission. As we mentioned above (§ 2.3.4), the UV arc is offset 0.6 arcseconds from the Ly α arc, and there is also a bright knot of Ly α emission to the east of the arc that has little overlap with the continuum. In Fig. 2.6 we also provide the correspondence between EW and $f_{\text{esc}}^{\text{Ly}\alpha}$ as calibrated by Sobral & Matthee (2019), but the interpretation of the EW map as a $f_{\text{esc}}^{\text{Ly}\alpha}$ map would require the relation to hold also for resolved regions.

2.3.5 Source plane analysis

Morphology

In this section we present the spatial properties of the Ly α surface brightness in the source plane. As we discussed in § 2.3.4, the NB data in the image plane already reveals that the Ly α emission is both spatially offset and more extended than the UV continuum. Qualitatively, these properties should be preserved by the lensing, but we now verify it in a quantitative way using our lens model. In what follows, we used the deflection matrices resampled to MUSE resolution (0''.2) unless otherwise specified.

We employed a Bayesian forward-modeling approach similar to the one presented in [Claeysens et al. \(2022\)](#). We modeled both the MUSE UV and Ly α data for each of the two galaxies (A and B) as Sérsic profiles and their parameter space is explored by a Markov Chain Monte Carlo (MCMC) sampling scheme using the `emcee` library ([Foreman-Mackey et al. 2013](#)). For each proposed set of parameters in the chain, the model is evaluated and traced back to the image plane according to the lens model prescription, convolved with the PSF and compared to the data under a Gaussian likelihood. For the sake of simplicity, we used a single Sérsic profile per component with all its six parameters free and set uniform priors.

We first fit the MUSE UV continuum image at $\lambda_{\text{rest}} \sim 1600 \text{ \AA}$ defined in § 2.3.4. We chose to fit the UV model in the MUSE data rather than the ACS F606W to have a more comparable data quality between the UV and Ly α datasets. After MCMC convergence we obtained a best fit Sérsic index and circularized effective radius of $n_{\text{UV}}^A = 0.57 \pm 0.04$ and $r_{50, \text{UV}}^A = (0.97 \pm 0.02) \text{ kpc}$ respectively for galaxy A, while for galaxy B, $n_{\text{UV}}^B = 1.4 \pm 0.2$ and $r_{50, \text{UV}}^B = (4.6 \pm 0.5) \text{ kpc}$. For completeness and direct comparison with [Claeysens et al. \(2022\)](#), we also quote the 90%-light radius $r_{90, \text{UV}}^A = (1.85 \pm 0.05) \text{ kpc}$ and $r_{90, \text{UV}}^B = 12.4^{+2.2}_{-1.9} \text{ kpc}$. The median distance² between the centers of A and B results in $(14.3 \pm 1.4) \text{ kpc}$.

We repeated this exercise with the Ly α NB data, finding $n_{\text{Ly}\alpha}^A = 5.18^{+0.02}_{-0.06}$ and $r_{50, \text{Ly}\alpha}^A = 9.3^{+0.3}_{-0.1} \text{ kpc}$ for galaxy A and $n_{\text{Ly}\alpha}^B = 3.73^{+0.06}_{-0.05}$, $r_{50, \text{Ly}\alpha}^B = 19.4^{+0.3}_{-0.2} \text{ kpc}$ for galaxy B. The corresponding 90%-light radii are $r_{90, \text{Ly}\alpha}^A = 65.4^{+2}_{-1} \text{ kpc}$ and $r_{90, \text{Ly}\alpha}^B = (101 \pm 1) \text{ kpc}$.

²Assumes an uncertainty of 10% associated to the square root of magnification.

In both the UV and Ly α cases the models cannot fully reproduce all of the image plane features, as revealed by the high significance residuals of the fit (see Fig. 2.7 for the UV and Fig. 2.8 for Ly α). This can be a result of the clumpy nature of the galaxies and their halos, making the Sérsic profile unsuited. A full morphological analysis of the individual clumps is outside the scope of this chapter and will be presented elsewhere. Nevertheless, the fitted Sérsic parameters can be informative of the sizes and overall light distribution of the galaxies. For example, the high Sérsic indices indicate that the sources have a very compact core and extended tails, similar to the double exponential profiles often invoked for describing LAHs (Wisotzki et al. 2016; Leclercq et al. 2017, e.g.,). The Ly α half-light radii, on the other hand, put the two sources in the top 10% of the Leclercq et al. (2017) sample and above any measurement in the Claeysens et al. (2022) sample. In this context, the size of the SGASJ1226 system approaches the lower end of the size range of Ly α blobs (Ouchi et al. 2020).

Using the centroids of the models, we computed the intrinsic spatial offsets between Ly α and the UV to be $\Delta(\text{Ly}\alpha - \text{UV})^A = (0.55 \pm 0.09)$ kpc for galaxy A and $\Delta(\text{Ly}\alpha - \text{UV})^B = (3.7 \pm 0.2)$ kpc for galaxy B. Compared to the Claeysens et al. (2022) sample, the offset of galaxy B ranks the largest at face value. However, when normalized to the size of the UV model (using the definition of “elliptical distance”, Δ_{ell} , eq. 3 of Claeysens et al. (2022)), the offsets of A and B both qualify as “internal spatial offsets” for $\Delta_{\text{ell}}^A \approx 0.06$ and $\Delta_{\text{ell}}^B \approx 0.02$ are well below unity.

Spatial distribution of line parameters

In this section we describe the procedure to extract and characterize the spectral line profile in resolved regions of the system. Following Claeysens et al. (2019), we start from our best source plane model of Ly α emission (see § 2.3.5) and evaluate it in a grid covering the delensed coordinates, at a pixel size of 0''.03. The resulting image is then fed to the VORBIN package (Cappellari & Copin 2003) which produces a tessellation of the source plane into regions of roughly equal flux.

With this method, we constructed two different tessellations. Firstly, a high-resolution tessellation of 50 bins with a median S/N of ~ 20 that we used for fitting the asymmetric

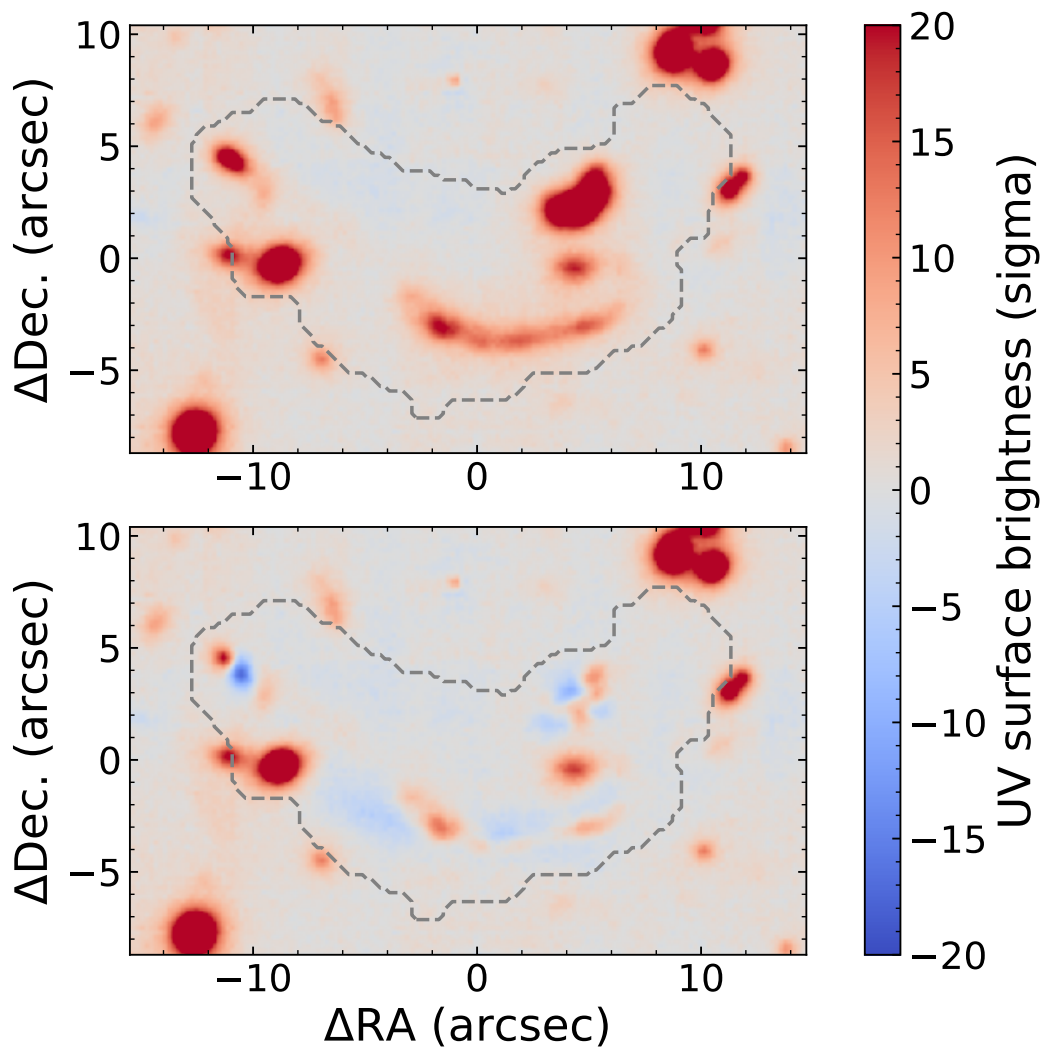


Figure 2.7: Source plane modeling of the UV emission from the central galaxies. *Upper panel:* MUSE broadband image at $\lambda_{\text{rest}} \sim 1600 \text{ \AA}$. *Lower panel:* Same as above but with the best-fit model for galaxies A and B subtracted (after convolution with the MUSE PSF). In both panels the surface brightness units are normalized to the background RMS and the dashed line indicates the “diffuse halo” aperture (see § 2.3.4).

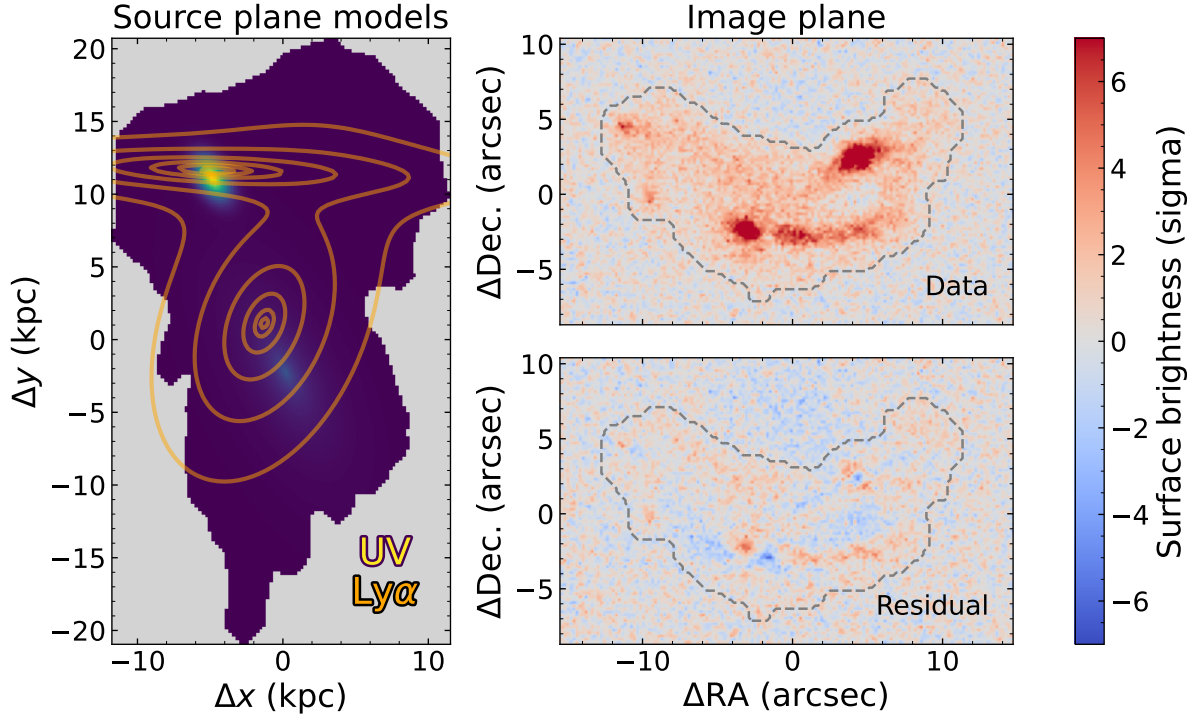


Figure 2.8: Source plane modeling of the LAH and the central galaxies. *Left:* Source plane MCMC-averaged light distribution for the UV (background image) and the Ly α emission (orange contours). The image masked borders delimit the delensed source plane area of the isophotal mask shown in dashed lines in the right panels. The Ly α model contours end at the maximum and decrease in powers of two. *Upper left:* Unsmoothed Ly α NB image in units of multiples of the background RMS. The dashed line marks the isophotal mask corresponding to the “diffuse halo” defined in § 2.3.4. *Lower right:* Residual from subtracting the best PSF-convolved Ly α model with the observed Ly α NB in units of background RMS (same as above).

gaussian profiles. And secondly, a lower resolution tessellation of 24 spatial bins with a median S/N of ~ 30 (see Fig. 2.9), used to fit the galactic wind models (see § 2.3.5) which require higher S/N for producing reliable results. Then, for a given tessellation, we extracted the spectrum from each region by combining all the image plane spaxels that trace back to it and coadded the corresponding continuum-subtracted spectra. We made sure that the traced image plane regions have at least four contiguous spaxels and they are larger than the PSF at least in one direction.

We characterized the spectral properties of the redshifted Ly α line in each bin by fitting an AG profile. An analysis of physically motivated models for the observed Ly α pro-

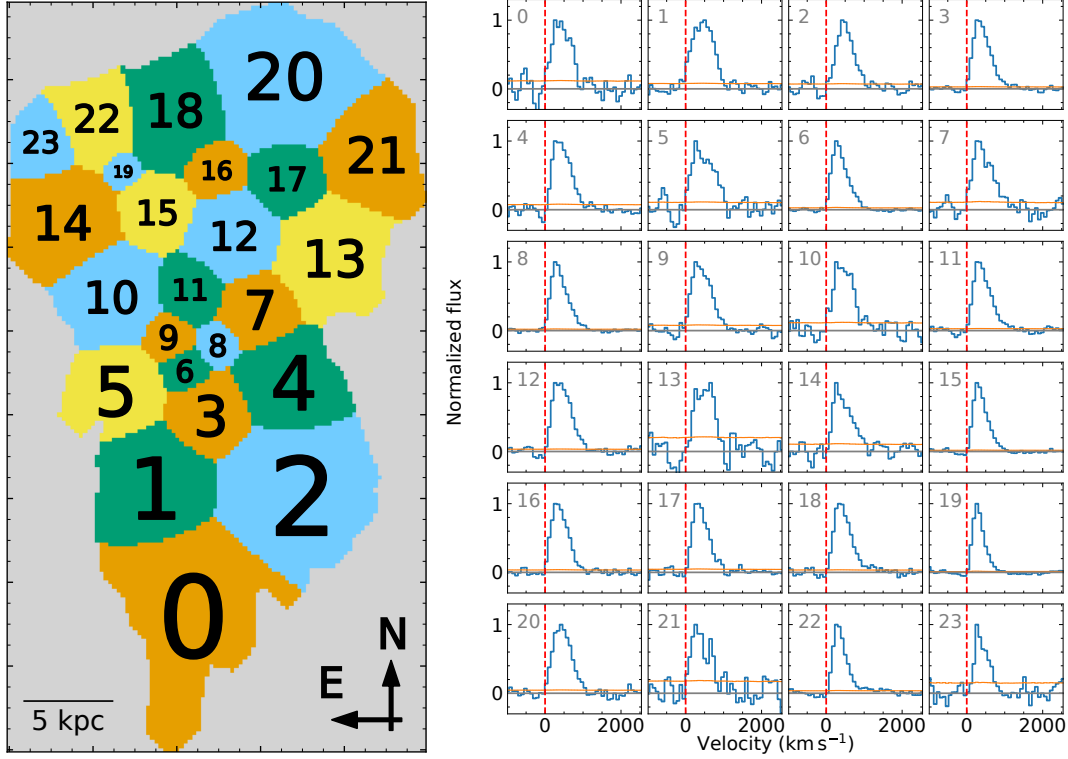


Figure 2.9: *Left:* 24-bin source plane tessellation with enumerated bins. *Right:* Extracted spectra from the tessellated bins. The dashed red vertical line indicates the zero velocity at an arbitrary $z_{\text{sys}} = 2.9236$. The orange line shows the error spectrum associated to each bin.

files is postponed to § 2.3.5.

Before fitting, each bin was assigned a systemic redshift based on its spatial overlap with UV emission of the galaxies. Bins having more than 50% of their UV flux inside the continuum masks defined in § 2.3.4 were assigned the systemic redshift of the corresponding galaxy (i.e., $z_A = 2.9257$ for galaxy A and $z_B = 2.9238$ for galaxy B). For all the other bins we set $z_{\text{mean}} = (z_A + z_B)/2 = 2.92475$.

The fit is well behaved and the marginalized posterior distributions are not multi-modal, except for a single bin of the 50-bin tessellation located at the outskirts of the halo whose spectrum did not have enough S/N for MCMC convergence. We used the integrated flux yielded by the fitted model to estimate both the intrinsic surface brightness of each bin (dividing by bin solid angle) and also the total luminosity of the system

(dividing by bin magnification³ and taking the sum). In this way, we obtained $L_{\text{Ly}\alpha} = (6.2 \pm 1.3) \times 10^{42} \text{ erg s}^{-1}$ for the whole SGASJ1226 system⁴ based on the 50-bin tessellation.

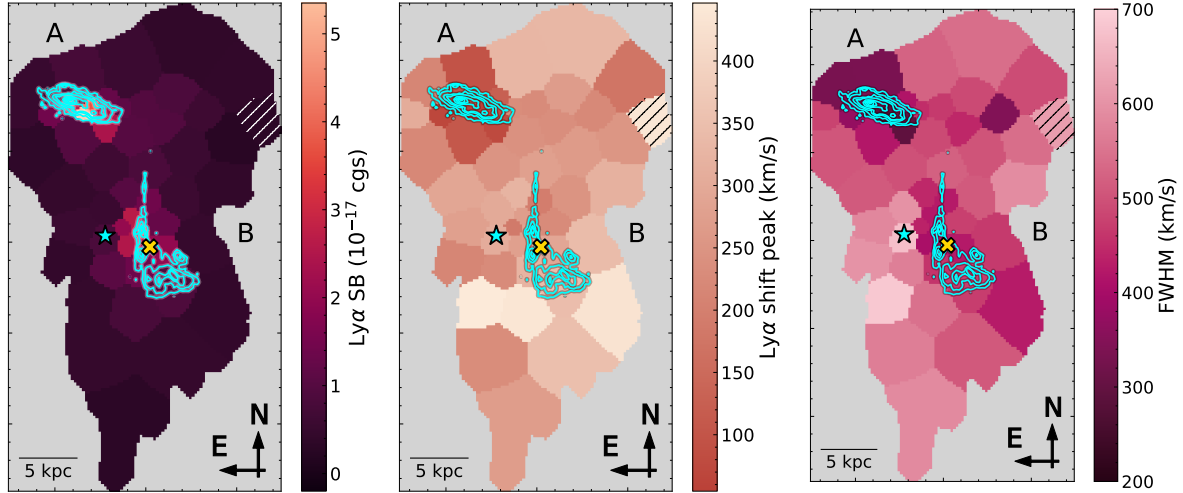


Figure 2.10: Source plane map of asymmetric Gaussian fitted parameters for the 50-bin tessellation. In all panels, the cyan contours indicate the locus of the UV continuum obtained from a pixelated source plane reconstruction of A.2 and B in the ACS F606W image, indicating the 3%, 6%, 13%, 19%, 38%, 56%, 75%, and 94% level of the maximum ($1.2 \times 10^{-20} \text{ erg s}^{-1} \text{ cm}^{-2} \text{ \AA}^{-1}$). The cross marker is the centroid of the dust continuum detected in ACA, (Solimano et al. 2021). The star symbol indicates the source plane position of the SGASJ1226-LAE. Also, we mark with hatched pattern the bin that we rejected from the analysis due to poor fitting results. *Left panel:* $\text{Ly}\alpha$ surface brightness *Middle panel:* Velocity shift of the red peak relative to the adopted systemic redshift, either 2.9257, 2.9238 or 2.9247 depending on the bin membership to A, B or the diffuse halo respectively (see § 2.3.5). *Right panel:* Full width at half maximum of the $\text{Ly}\alpha$ line.

Fig. 2.10 shows the source plane tessellation with the bins color coded according to the fitted surface brightness, peak shift velocity and line width. The leftmost panel shows the source plane distribution of surface brightness, which peaks near the position of the galaxies A and B (cyan contours) and rapidly declines toward the outskirts. However, instead of two distinct halos, the two resolved $\text{Ly}\alpha$ SB peaks are connected by a low

³Defined as the ratio between the total solid angle spanned by the image plane spaxels associated to that bin and its solid angle in the source plane.

⁴The value was corrected for a Galactic attenuation of 0.075 mag at 4771 Å, which was interpolated from the Schlafly & Finkbeiner (2011) tables. Also assumes a 20% error due to magnification.

SB “bridge” or filament. The peak velocity approximately from 50 km s^{-1} to 450 km s^{-1} across the halo, as seen in the middle panel of Fig. 2.10. The lowest values are the ones associated with galaxy A, with a uncertainty-weighted mean and standard deviation of 75 km s^{-1} and 20 km s^{-1} respectively. The highest values are instead associated to either galaxy B or to bins at the outskirts of the halo. The right panel also shows a large spread in line FWHM, spanning from 265 km s^{-1} to 690 km s^{-1} . We observe that the bins covering the UV continuum typically have lower widths than the bins of the diffuse halo, in agreement with the trends observed by Claeysens et al. (2019) and Leclercq et al. (2020). Qualitatively, the presence of this pattern seems to confirm the results obtained above for the integrated apertures (see § 2.3.4). A remarkable exception, however, is the bin covering the faint companion SGASJ1226-LAE (indicated with a cyan star in Fig. 2.10), which exhibits the second largest linewidth of the system ($\approx 670 \text{ km s}^{-1}$).

Similarities between the FWHM and peak shift maps should not come as a surprise. Recent studies have found that these two quantities are positively correlated, both among integrated measurements across different objects (Verhamme et al. 2018) and within resolved regions of individual halos (Claeysens et al. 2019; Leclercq et al. 2020). From a theoretical perspective, the relation is expected to arise as a natural consequence of resonant scattering, as confirmed by radiative transfer calculations in simple geometries (e.g., Schaerer et al. 2011; Zheng & Wallace 2014; Song et al. 2020). In contrast, the relation is not found in more complex, high resolution simulations that include full radiative hydrodynamics (Behrens et al. 2019; Mitchell et al. 2021)

In Fig. 2.11 we show the FWHM vs peak shift values for the 49 spatial bins with good fits in the 50-bin tessellation, in comparison with the Verhamme et al. (2018) empirical relation. Our data also exhibits the FWHM-shift correlation with an uncertainty-weighted Pearson’s coefficient of $r = 0.76^{+0.09}_{-0.21}$ ($p < 10^{-5}$), where the errors have been estimated with bootstrapping. Motivated by this result, we performed orthogonal linear regressions using SciPy’s odr module on the data separated in the three systemic redshift groups. The best fit lines are plotted in the left panel of Fig. 2.11 along their corresponding 68% confidence intervals. Each line is described by a slope a and a zeropoint b . We find that the slope for the diffuse halo and galaxy B bins agree at $a \approx 1.25$ within the 1σ error,

while their zeropoints differ significantly by about 120 km s^{-1} . These offsets put the resolved relations for B and the halo slightly below Verhamme et al.’s empirical relation ($a = 0.9 \pm 0.14$; $b = -34 \pm 60$), but the slopes are still consistent within 1σ . Galaxy A’s data, on the other hand, favors a much shallower relation ($a = 0.51 \pm 0.09$), which cannot be brought into agreement with Verhamme et al.’s, but is within the broad range of slopes observed by Leclercq et al. (2020) in resolved individual halos. Additionally, we investigated the effect of SB in the line profile. Just as in the two objects studied by Claeysens et al. (2019), we also observe that above a certain SB threshold, brighter bins have smaller peak velocity shifts, as shown in the right panel of Fig. 2.11.

FLaREON models

Here, we analyze the binned spectra with physically motivated models. We use the publicly available FLaREON package (Gurung-López et al. 2019) to fit template spectra for every bin. The code performs a nonlinear search in a grid of Ly α line template profiles from precomputed Monte Carlo Radiative Transfer simulations from the LYART project (Orsi et al. 2012). The simulations only include two radiative transfer effects, namely resonant scattering and dust absorption. Hence, for the interpretation of these models one has to assume that all the Ly α photons are produced in the central galaxies and then scattered away from resonance in the CGM. Other mechanisms for the production of extended Ly α emission, such as fluorescence or gravitational cooling are discussed in § 2.4.

Three geometries are currently available within FLaREON: a spherical, expanding thin shell of isothermal gas around a point source of Ly α photons (hereafter TS); a galactic wind geometry (GW), which is identical to the TS geometry except for the density distribution of the gas. While the TS assumes all the gas is concentrated in a thin shell at a fixed distance of the source, in the GW geometry the source lies in an empty spherical cavity surrounded by a spherical distribution of isothermal gas with radially declining gas density. Finally, FLaREON also offers a biconical outflow geometry, that combines an static uniform medium with a bicone of lower density, expanding gas. All geometries are governed by the same three parameters: the expansion velocity V_{exp} , the neutral hydrogen column density $\log N_{\text{HI}}$ and the pure absorption (dust) optical depth $\log \tau$.

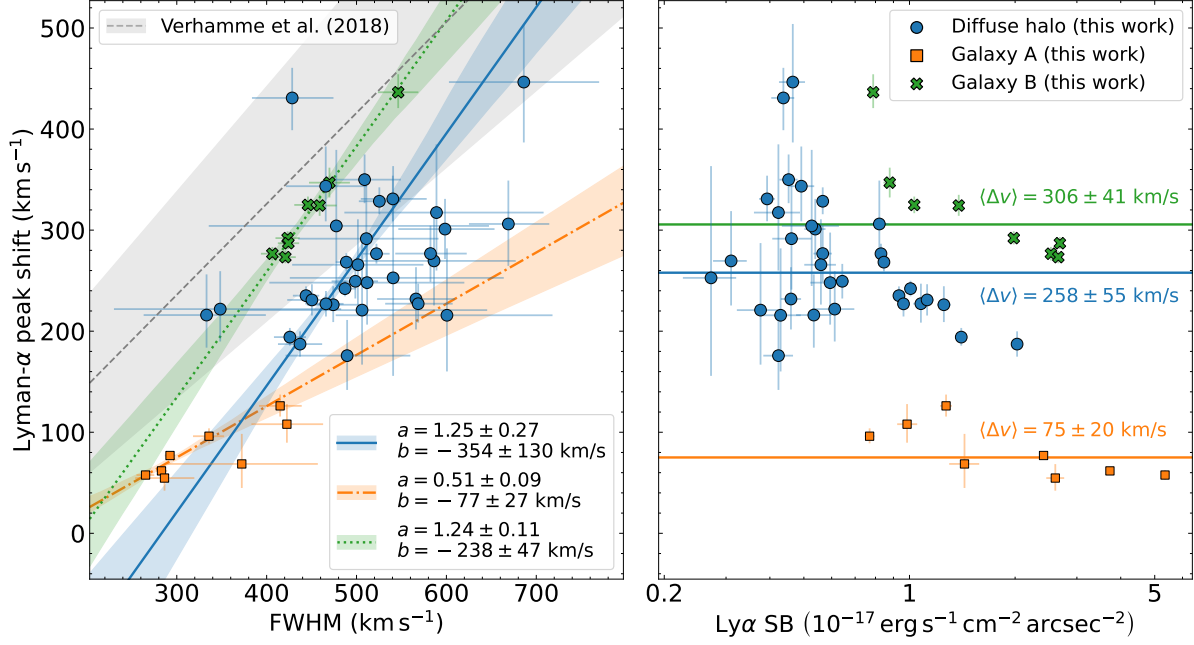


Figure 2.11: Resolved correlations of the Ly α line profile parameters. *Left panel:* Correlation between Ly α line FWHM and peak shift velocity for the individual regions of the 50-bin tessellation of SGASJ1226, obtained through parametric modeling of line as an asymmetric Gaussian profile. Marker shapes and colors separate the three components of the SGASJ1226 system, namely the cores of galaxies A (orange squares) and B (green crosses) and the halo diffuse emission (blue circles). For the latter, the systemic velocity was set to $z_{\text{mean}} = (z_A + z_B)/2 = 2.92475$. A best fitting straight line is also displayed for each of these components, along with their 68% confidence intervals shown as a shaded area around the lines. The dashed gray line traces the empirical relation found by Verhamme et al. (2018). *Right panel:* Ly α peak shift velocity versus surface brightness. Horizontal lines mark the uncertainty-weighted average peak shift velocity $\langle \Delta v \rangle$ for each of the three components.

While these models were originally developed to describe the profiles of spatially unresolved spectra of LAEs, here we use them to model individual bins of our source plane tessellation. The main caveat of this approach is that the emission source will not be, in most cases, at the center of the binned region. This means that a typical Ly α photon produced by the central galaxies will need to travel a larger distance (thus with a higher probability of absorption or scattering) to escape from any given bin than what the models imply. However, Chen et al. (2021a) proposed that if the Ly α photons do not originate inside the cloud, the problem can still be described with just the half of the expanding

sphere. Following their argument, the isotropy of the TS and GW geometries implies that the signal arising from a single hemisphere would have the same line profile as the full spectrum but with a reduction in amplitude. This property suggests that one can approximate the full halo as a collection of half expanding clouds, where now the expansion velocity is measured relative to a reference point inside each cloud along the line of sight. Since the biconical wind geometry is not isotropic, we did not try that geometry in our modeling.

The code requires the input of a systemic redshift in order to transform observed wavelengths into rest-frame wavelengths. However, the choice of systemic redshift is known to have a significant influence in the other parameters (Gurung-López et al. 2019). Due to this, one could in principle infer the systemic redshift from the Ly α profile shape alone. To explore this idea, we start by fitting FLAREON models with z_{sys} as a free parameter to the integrated spectra of galaxies A and B (see § 2.3.4), because their systemic redshifts are known and their S/N is the highest. We ran a MCMC fitting scheme similar to the one used for fitting the AG for the two isotropic geometries, TS and GW. The total number of free parameters for each model is five, since we fit an amplitude scale factor in addition to the three main parameters and the systemic redshift.

Fig. 2.12 shows the best fit GW models and residuals for the integrated spectra of A and B in the left and right panels respectively. Remarkably, the systemic redshift order ($z_A > z_B$) was correctly inferred by the models, despite the uniform priors and the fact that the line centroid of B is actually redder than A's. Moreover, the fitted redshifts $z_A = 2.9262 \pm 0.0001$ and $z_B = 2.9222 \pm 0.0001$ are only $(50 \pm 10) \text{ km s}^{-1}$ and $(-163 \pm 10) \text{ km s}^{-1}$ from the nebular redshift solution of A and B, respectively, consistent with the scatter of the different solutions (§ 2.3.1). The inferred expansion velocities and neutral column densities are $V_{\text{exp}}^A = 224.3 \text{ km s}^{-1}$, $V_{\text{exp}}^B = 187.2 \text{ km s}^{-1}$; and $\log(N_{\text{HI}}^A/\text{cm}^{-2}) = 18.9$, $\log(N_{\text{HI}}^B/\text{cm}^{-2}) = 20.3$. These two crucial parameters are constrained by the data, whereas the optical depth is not.

The best fit velocity for galaxy B is larger than the best value for galaxy A. This already gives an interpretation to the line profile being narrower in A: since the medium is moving at higher velocities, the Ly α photons need to experience on average less scatter-

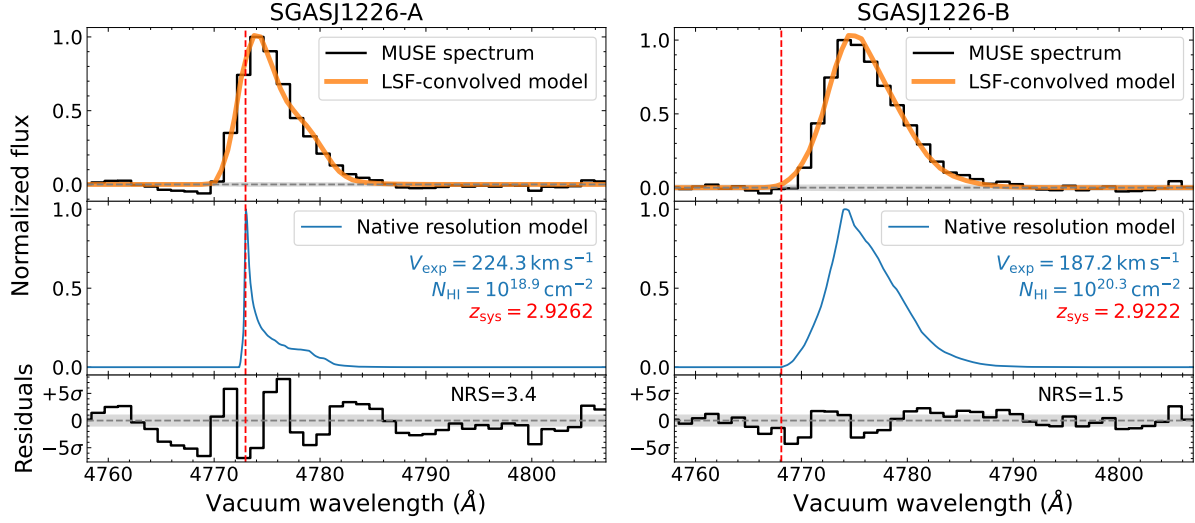


Figure 2.12: Best fit FLAREON GW models for the integrated spectra of galaxy A (left) and galaxy B (right). The top row of panels show the MUSE data (black step line) along the best fitting FLAREON model (thick orange line) convolved with the line spread function (LSF). The middle row shows the same models prior to LSF convolution (blue line). The parameters for the profiles are indicated in the inset text. The residuals are shown in the bottom row, with a legend indicating the “normalized residual scatter” (NRS), i.e., the standard deviation of the residuals weighted by the error spectrum. The gray filled area indicates the $\pm 1\sigma$ error.

ing events to shift their frequency out of resonance, because the required shift is smaller. This effect is coupled with the lower column density of neutral hydrogen in A with respect to B. A lower density of neutral hydrogen atoms reduces the number of scattering events that a photon will experience before escaping. At a fixed Doppler shift and gas velocity, a Ly α photon has higher chances of escaping if there are less atoms along its path.

We also fitted the diffuse-only spectrum in this fashion, this is, letting the systemic redshift as a free parameter. Interestingly, the best fit redshift is $z_{\text{sys}} = 2.9222$, extremely close to the best value given to B’s model. The column density inferred by the model is also similar to B’s ($N_{\text{HI}}^{\text{diffuse}} \approx 10^{20.4} \text{ cm}^{-2}$), but the expansion velocity of 198.3 km s^{-1} is in between V_{exp}^A and V_{exp}^B . These results are, however, more difficult to interpret since we have explicitly excluded the MUSE spaxels with UV continuum emission (proxy of high SFR), so there is no source of Ly α photons along the line of sight under the assumption of a pure-scattering scenario. In this sense, the high column density should be regarded

as an average integrated along the random optical paths of the escaping photons, rather than the line-of-sight between the observer and the source. This is the meaning that we will give to our subsequent results on the binned regions' spectra.

The models using the TS geometry yielded similar results, but the χ^2 was larger in the all three fits and even though the $z_A > z_B$ property was recovered, the predicted redshifts were less accurate. For this reason, plus the fact that the line shape does not vary dramatically across the halo at the MUSE resolution, we adopt the GW as our fiducial geometry to model the spectra from the individual bins.

Finally, given that our FLAREON GW model recovers the systemic redshifts reasonably well and our lack of systemic redshifts for most of the binned regions, we also let that parameter vary freely in the fitting procedure for the binned regions. Here we have used the 24-bin tessellation, since we required a higher S/N per spectrum. The source plane maps of the best fit GW parameters are shown in Fig. 2.13. Again, the dust absorption optical depth was not constrained by the data, and hence we are unable to make inferences on this parameter.

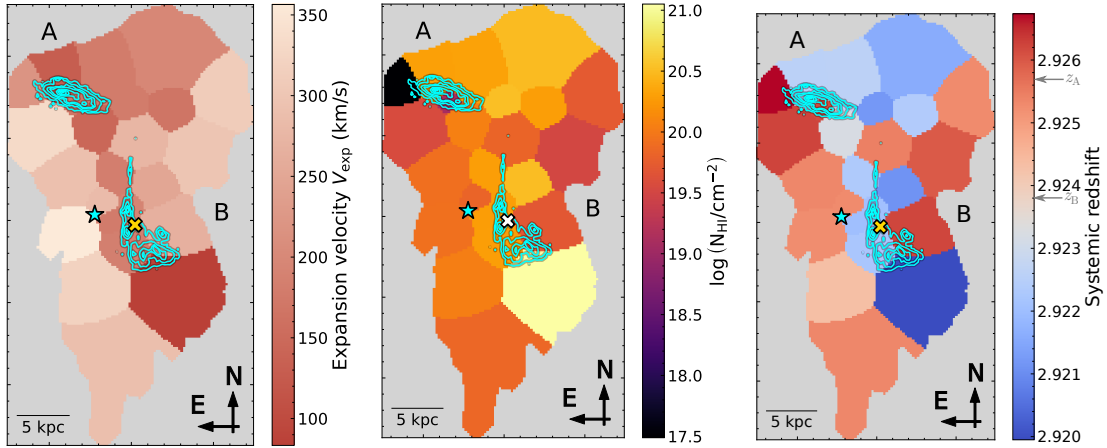


Figure 2.13: Source plane map of FLAREON GW fitted parameters. The contours and markers are the same as in Fig. 2.10. *Left panel:* Wind expansion velocity. *Middle panel:* Neutral hydrogen column density. *Right panel:* Systemic redshift inferred from the Ly α line. Nebular redshift solutions for A and B are indicated in the colormap axis.

The expansion velocities inferred by FLAREON under the GW geometry range from 80 km s^{-1} to 360 km s^{-1} , with an uncertainty-weighted average of $\langle V_{\text{exp}} \rangle = (211 \pm 3) \text{ km s}^{-1}$

and a standard deviation of $(62.5 \pm 3.0) \text{ km s}^{-1}$. Interestingly, Fig. 2.13 suggests some degree of spatial correlation between the expansion velocity values across the halo: low velocity bins are clustered along the North-South axis (vertical in the figure, and hereafter referred to as the “major axis” of the halo), including the bins associated to the continuum of the central galaxies. Similarly, high velocity bins are associated to diffuse-only regions at the outskirts of the halo, they are found on both sides of the major axis and are also clustered in the same direction. These results suggest that on halo scales the medium is not expanding isotropically, but rather with a preferred direction. In other words, they might indicate that the gas is traveling faster in a direction perpendicular to the line connecting the two galaxies (e.g., due to decreased resistance from the environment).

In terms of column density, the models distribute around $\log(N_{\text{HI}}/\text{cm}^{-2}) = 20$, with a 3σ -clipped standard deviation of 0.4 dex. After discarding 3 outlier bins ($\Delta \log N_{\text{HI}} \gtrsim 1$ dex), we find that the path-integrated column density is remarkably uniform accross the halo. Under the interpretation proposed above, this would mean that the actual column density declines as a function of the radial distance to the $\text{Ly}\alpha$ sources.

Finally, in the right panel of Fig. 2.12 we plot the systemic redshifts predicted by FLAREON for each bin. If we interpret them as the zero velocity of the reference point inside of each GW model, its complex spatial structure and a range of values exceeding differences 700 km s^{-1} would indicate that the outflow is modulated by complex underlying kinematics. Such complexity would naturally arise in a scenario where the two main galaxies are subject to dynamical interactions, for example, in a merger. Further discussion on the potential impact of the interaction between A and B is presented in § 2.4.1.

2.3.6 Low ionization absorption lines

Independent insight on the kinematics of the system can be obtained from the study of absorption features in the spectrum, although they only probe intervening gas along the line of sight to the central galaxies. As mentioned in § 2.3.1, previous studies of SGASJ1226 obtained redshift solutions based on interstellar absorption lines that are $\sim 200 \text{ km s}^{-1}$ bluer than the nebular emission based solutions (Koester et al. 2010; Wuyts et al. 2012). This re-

sult was later secured using the higher resolution Magellan Echelle (MagE) spectrum of Arc A.1 obtained as part of the MegaSaura Survey (Rigby et al. 2018). Moreover, Gazagnes et al. (2018) fitted Voigt profiles to the Lyman Series absorption lines (from $\text{Ly}\beta$ 1025.7 Å to $\text{Ly}6$ 930.8 Å), obtaining a central velocity of $(-264 \pm 21) \text{ km s}^{-1}$ (-218 km s^{-1} if we convert to our nebular redshift solution).

Here, we complement these results by measuring the absorption velocity in our MUSE data, including galaxy B. But since the Lyman Series lines lie below the MUSE wavelength cutoff, we opted for the low ionization Al 2 λ 1670 line as an alternative tracer. We extracted spatially integrated spectra from the global apertures for A and B defined in § 2.3.4. Both spectra show a very similar profile that includes an asymmetric blue tail, and thus were modeled with an absorption AG profile (see Fig. 2.14) and § 2.3.3). We find $v_A = (-197 \pm 4) \text{ km s}^{-1}$ and $v_B = (-142 \pm 13) \text{ km s}^{-1}$. Also, despite the line being narrower in A ($\text{FWHM}_A = (300 \pm 7) \text{ km s}^{-1}$ versus $\text{FWHM}_B = (373 \pm 15) \text{ km s}^{-1}$), their equivalent widths are consistent with each other, for $\text{EW}_0^A = (5.8 \pm 0.5) \text{ Å}$ and $\text{EW}_0^B = (5.6 \pm 0.2) \text{ Å}$.

The combination of blueshifted absorption lines and redshifted $\text{Ly}\alpha$ emission is very common among $z \sim 3$ LBGs (e.g., Steidel et al. 2003), and it is often interpreted as the telltale signature of (spherical) galactic outflows (Verhamme et al. 2006).

2.4 Discussion

2.4.1 Kinematics of SGASJ1226

A major goal of this chapter is to understand the physical configuration of the SGASJ1226 system, by building a picture that includes both its spatial and kinematic properties. Firstly, the lens model revealed that the UV centroids of the two main galaxies of the system are separated only by $(14.3 \pm 1.4) \text{ kpc}$ in projection (see § 2.3.5). This fact, together with the small systemic velocity offset between the two galaxies ($\Delta v \approx 145 \text{ km s}^{-1}$), suggest that they are gravitationally interacting. The interaction hypothesis is further motivated by the reconstructed source plane continuum morphology (contours in Fig. 2.10), which exhibits a very distorted galaxy B resembling the tidal tails or collisional rings seen in

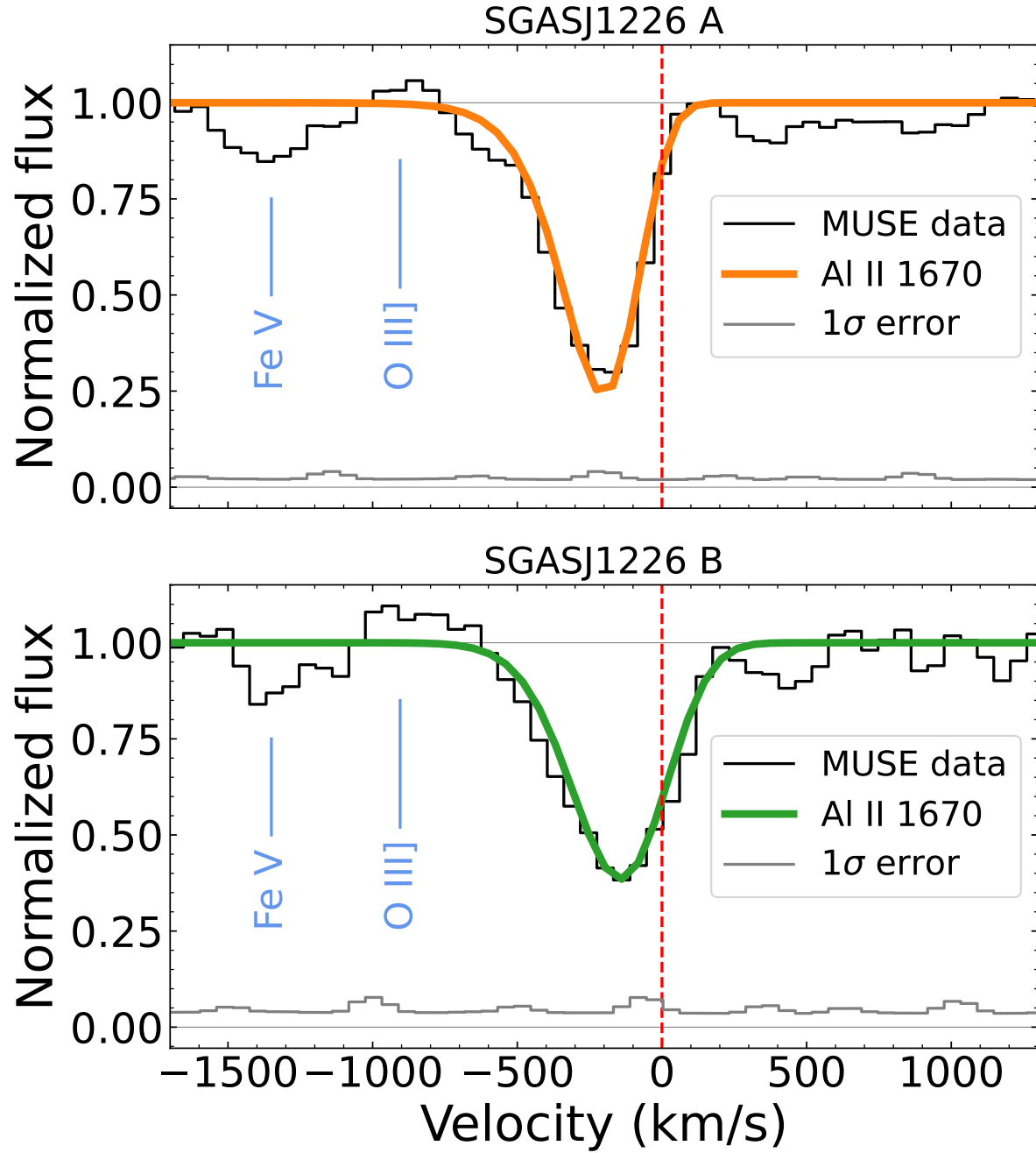


Figure 2.14: Spatially integrated Al II $\lambda 1670$ absorption spectra of galaxies A (top panel) and B (bottom panel). The solid color lines are the best fitting AG profile, while the vertical dashed line indicates the systemic velocity of each galaxy. The photospheric Fe V line and the nebular O III] line are also annotated in the figure.

galaxy interactions at low redshift (e.g., [Darg et al. 2010](#)). The source plane morphology, however, should be interpreted with care, because the distorted appearance of galaxy B can also be due to (1) strong dust attenuation in some parts of the ISM that conceal the full shape of the galaxy, or (2), geometrical artifacts that arise from the lens modeling. With the available data, we cannot distinguish whether the galaxies are experiencing a single visit flyby or the early stage of a major merger. On one hand, the lack of an ongoing starburst in both galaxies (their specific SFRs are consistent with the Main Sequence, [Solimano et al. 2021](#)) indicates that the interaction (if any) is not currently boosting the SFR, as it would be expected in some stages of a major merger (e.g., [Hopkins et al. 2008](#)). On the other hand, the extended Ly α emission implies a significant amount of gas between and around the pair of galaxies, thus favoring a merger scenario in which the interaction was able to strip gas away from the ISM into the CGM (see, for example, [Yajima et al. 2013](#)). Also, we observed in § 2.3.5 that the fitted systemic redshift map exhibits a complex morphology and a large range of values, which provides hints of complex underlying kinematics similar to the expectation for galaxy mergers (e.g., [Sparre et al. 2022](#)). But in order to confirm or reject the merger activity as a driver of the gas motions, it would be necessary to obtain resolved spectroscopy of a non-resonant line, such as H α or [C II]158 μm , to trace the internal kinematics of the ISM where the effects of a merger would be more evident.

The global kinematics of the halo are clearly dominated by outflow motions, as revealed by the characteristic redshifted and red asymmetric Ly α profile. Under simple isotropic outflow geometries such as the TS and GW considered here, RT calculations always predict an enhanced red peak with broadened red tail starting from relatively low expansion velocities. Extra evidence for outflows is seen in the absorption signature of low-ionization metal lines (see § 2.3.6), which are thought to trace the same gas phase as Ly α . The signature is seen toward the UV continuum of both galaxies, A and B, but it remains unclear whether the outflows are launched independently by each galaxy or the outflow originates preferentially in one galaxy and the absorption appears in the second galaxy by a projection effect. The first case seems to be more likely, since the two galaxies have similar stellar masses and SFR. Alternatively, the spatially coherent outflow signa-

ture could be also linked to a large stream of receding gas stripped from the galaxies by the interactions described above.

Finally, we do not find any evidence of CGM-scale rotation, although such a signal would be severely smeared by the RT effects. In fact, rotation-like gradients in the Ly α peak shift velocity of LAHs are very rare, with only one candidate out of six in the sample presented by [Leclercq et al. \(2020\)](#), the only one among the few other resolved LAHs in the literature ([Claeyssens et al. 2019](#); [Chen et al. 2021a](#)).

2.4.2 Powering mechanism

We have thus far assumed that the extended Ly α emission of SGASJ1226 is exclusively explained by resonant scattering of photons produced in the central galaxies. In this section we explore alternative mechanisms that could also drive the observed properties of SGASJ1226.

Gravitational cooling

In § 1.2.1 we introduced gravitational cooling, a mechanism in which cold gas accretion into galaxies gives rise to extended Ly α emission. In that scenario, Ly α photons are created *in situ*, and thus their peak shift should trace the line of sight velocity of the gas. Then, if there is inflowing gas between the observer and the center of the halo, the Ly α spectrum emitted from it will have a strong blueshifted peak and a blue tail (e.g., [Haiman et al. 2000](#); [Dijkstra et al. 2006](#)). Such profiles can also be produced by scattering-only scenarios (on an collapsing sphere of gas, e.g., [Verhamme et al. 2006](#)) provided that the intervening gas has a velocity opposite to the direction of propagation of the Ly α photons. In other words, the presence of an enhanced blue peak is a signature of inflowing motion, but not necessarily of gravitational cooling.

In SGASJ1226, neither the integrated (§ 2.3.4) nor the resolved spectra (§ 2.3.5) exhibit significant emission blueward of the systemic velocity. Only a few tentative blue peaks can be seen in the Ly α profiles of some halo regions (see regions 0, 2 and 5 in [Fig. 2.9](#)). The lack of blueshifted emission cannot be entirely explained by intervening absorption

in the IGM, because at $z = 2.9$ the average IGM transmission at -200 km s^{-1} from the $\text{Ly}\alpha$ rest frame wavelength is of approximately 85% (Laursen et al. 2011), high enough for a blue peak to be detectable. The caveat is that this particular line of sight can have a higher than average neutral gas column density. We therefore conclude that the presence of significant inflowing motion along the line of sight is unlikely but not completely ruled out.

Fluorescence

Another mechanism mentioned in § 1.2.1 is that of $\text{Ly}\alpha$ fluorescence, where the CGM itself is photoionized. For this mechanism to produce extended $\text{Ly}\alpha$ emission, the gas needs to be distributed in high density clumps with a low covering fraction, so the radiative transfer occurs preferentially in the surfaces of the clumps, resulting in a reduced number of scattering and absorption events with respect to the case of an homogeneous medium. In the approximation where scattering and dust absorption are negligible, this mechanism generates an intrinsic $\text{Ly}\alpha$ luminosity proportional to the production rate of ionizing photons. Here, we follow Valentino et al. (2016) to estimate the ionizing photon rate Q required to power the emission under the assumption that fluorescence is the only mechanism at play. From an observed, delensed $f_{\text{esc}}^{\text{Ly}\alpha} L_{\text{Ly}\alpha} = (6.2 \pm 0.2) \times 10^{42} \text{ erg s}^{-1}$ we obtain

$$Q = \frac{L_{\text{Ly}\alpha}}{h\nu_{\text{Ly}\alpha}\eta_{\text{Ly}\alpha}} \approx \frac{5.6 \times 10^{53}}{f_{\text{esc}}^{\text{Ly}\alpha}} \text{ s}^{-1}, \quad (2.1)$$

where $\eta_{\text{Ly}\alpha} = 0.68$ is the fraction of ionizing photons converted into $\text{Ly}\alpha$ (Spitzer 1978) and $h\nu_{\text{Ly}\alpha} = 10.19 \text{ eV}$ is the energy of a single $\text{Ly}\alpha$ photon. Since we cannot directly measure the production rate of ionizing photons (due to extreme ISM opacity at $\lambda_{\text{rest}} < 912 \text{ \AA}$) we need to rely on a longer wavelength proxy such as the far UV luminosity ($\lambda_{\text{rest}} = 1500 \text{ \AA}$). But for a given $L_{1500 \text{ \AA}}$ the actual production rate of ionizing photons Q depends on the properties of the stellar population, particularly on the luminosity-weighted age and metallicity (Steidel et al. 2001; Smith et al. 2002). Fortunately, the stellar population synthesis analysis presented by Chisholm et al. (2019) provides estimates of the

ionizing photon production efficiency, $\xi_{\text{ion}} \equiv Q/L_{1500\text{\AA}}$, for all galaxies in the MegaSaura sample including SGASJ1226’s Arc A.1. Therefore, assuming that ξ_{ion} is uniform across galaxy A and is the same for galaxy B, we can solve for Q multiplying ξ_{ion} by the total reddening-corrected UV luminosity of the system. For consistency with Chisholm et al. (2019) we apply Reddy et al. (2016)’s attenuation law with Chisholm et al. best-fit color excess $E(B - V) = 0.13$ to the total demagnified luminosity inferred from ACS F606W photometry. After dereddening we obtain a UV luminosity of

$$L_{1500}^{A+B} = (3.4 \pm 0.5) \times 10^{41} \text{ erg s}^{-1} \text{ \AA}^{-1}.$$

In Table 5 of Chisholm et al. (2019), the best fit Starburst99 model for A.1’s MagE spectrum implies a photon production efficiency of $\log \xi_{\text{ion}} = 12.74 \pm 0.16$ while the best fit BPASS model favors the slightly higher value of $\log \xi_{\text{ion}} = 13.04 \pm 0.16$. Then, the total rate of ionizing photons produced by the galaxies in SGASJ1226 is $Q = (1.9 \pm 0.7) \times 10^{54} \text{ s}^{-1}$ for the Starburst99 model and $Q = (3.7 \pm 1.5) \times 10^{54} \text{ s}^{-1}$ for the BPASS model. Taken at face value, these results imply that photoionization from young stellar populations would only account for the 20% – 60% of the total photon rate required to power the $\text{Ly}\alpha$ luminosity if we assumed $f_{\text{esc}}^{\text{Ly}\alpha} = 0.082$, the value predicted by the Sobral & Matthee (2019) empirical relation based on observed EW. Conversely, a larger escape fraction (between 0.15 and 0.30) would be needed to match the photon rates. Now, these calculations only considered young stars as the source of ionizing photons, but we cannot rule out the presence of an AGN that is obscured along the line of sight with our current data.

Also, we do not expect a significant contribution of metagalactic ionizing photons from the cosmic UV background (UVB), since the latest observational constraints imply that the UVB produces $\text{Ly}\alpha$ profiles at $z \approx 3$ with peaks at the $2 \times 10^{-20} \text{ erg s}^{-1} \text{ cm}^{-2} \text{ \AA}^{-1} \text{ arcsec}^{-2}$ SB level (Gallego et al. 2021), at least 3 orders of magnitudes fainter than the observed SB peak of SGASJ1226 on halo scales; although its contribution to the profile can become relevant at large radii, in the interface with the IGM.

In any case, we warn the reader that these ionizing photon budget considerations cannot constrain the contribution of fluorescence in the absence of an independent measure

of the escape fraction and evidence of CGM clumpiness. The most direct test for fluorescence as a major contributor to the extended Ly α emission is the concomitant presence of extended H α emission (Mas-Ribas et al. 2017). This is because under case B recombination (Osterbrock & Ferland 2006), the Ly α emissivity of the gas is 8.7 times the H α emissivity. In other words, the same regions of photoionized gas should glow in H α by a proportional amount, simultaneously solving the Ly α escape fraction and the question of *in situ* Ly α production. Promisingly, SGASJ1226 has been selected as NIRSpec IFU target for the *JWST* Early Release Science “TEMPLATES” program (Rigby et al. 2017) and thus resolved H α observations of the Arc A.1 will become available (see ??). While the FoV of the instrument will not cover the whole LAH, it will certainly tell if the H α extends beyond the ISM.

Emission from satellites and the nature of SGASJ1226-LAE

In § 2.3.4 we reported the discovery of a continuum counterpart to a local maximum of Ly α SB in the MUSE NB image labeled SGASJ1226-LAE. In this section we argue that SGASJ1226-LAE is a satellite of the main system composed of galaxies A and B, rather than another UV clump in the ISM of galaxy B. According to our best fit lens model, this source has an average magnification of $\mu = 14$ and lies ~ 3 kpc away from the UV centroid of galaxy B (see Fig. 2.10). This is approximately twice the exponential UV scale length of the continuum of galaxy B, further away than any of the UV clumps identifiable in that galaxy. Also, the candidate counterpart appears spatially resolved in the F606W image, with an exponential scale length of $250(14/\mu)^{\frac{1}{2}}$ pc, unlike the clumps of galaxy B which are all point-like. SGASJ1226-LAE has an intrinsic Ly α luminosity of $(1.0 \pm 0.2) \times 10^{41}$ erg s $^{-1}$, representing the 2% of the parent LAH luminosity. The F606W photometry implies an absolute UV magnitude of $M_{1500} \approx -16.7$, which lies at the faint end of the luminosity function of LAEs at this redshift (Ouchi et al. 2008; Kusakabe et al. 2020). In fact, the UV continuum at this luminosity is extremely difficult to detect, and only a handful of objects have been robustly detected in lensed fields (Claeyssens et al. 2022) or in deep stacks from the UDF (Maseda et al. 2018). Although with very low significance, the UV slope of this source is steeper than the mean slope of the galaxies A and B, which is an expected

property of strong LAEs due to their young ages (e.g., Nakajima et al. 2012; Hagen et al. 2014) and low dust attenuation (e.g., Stark et al. 2010; Ono et al. 2010; Kojima et al. 2017).

Theoretical models and simulations predict the presence of several satellites populating the outer parts of Ly α halos (see § 1.2.1), and some authors propose that they contribute a significant fraction of the Ly α SB at large radii ($r \gtrsim 0.25R_{\text{vir}}$) (Mas-Ribas et al. 2017; Mitchell et al. 2021). It is thus plausible that SGASJ1226-LAE is indeed a satellite of the SGASJ1226 system, made detectable by the chance alignment of the lensing caustic boosting its flux above the background.

Unfortunately, we do not detect additional lines in the MUSE spectrum of SGASJ1226-LAE due to strong contamination from the foreground galaxy light at $\lambda_{\text{obs}} \gtrsim 4800 \text{ \AA}$. Without a systemic redshift for this galaxy, interpreting the line profile becomes even more difficult. Nevertheless, the line profile shows a broad red tail, suggesting that Ly α photons coming out of SGASJ1226-LAE are also scattered in the CGM.

2.5 Conclusion

We have analyzed the spatial and spectral properties of the diffuse Ly α emission associated with a pair of lensed LBGs at $z \approx 3$. The remarkable brightness and extension of this system, together with high quality MUSE observations, allowed us to probe in detail its physical nature.

The system is composed of two main sequence galaxies (labeled A and B) of similar stellar mass ($\approx 10^{10} M_{\odot}$) and SFR ($\approx 10 M_{\odot} \text{ yr}^{-1}$) that are separated by less than 15 kpc when projected in the source plane, and by 145 km s^{-1} in the velocity space, suggesting an interacting pair. The galaxies are associated to a single Ly α halo of $L_{\text{Ly}\alpha} = (6.2 \pm 1.3) \times 10^{42} \text{ erg s}^{-1}$ which we decomposed into two Sérsic profiles in the source plane with the largest component having a circularized half light radius of 19.4 kpc. Despite its apparent Ly α brightness, the whole system has rest-frame Ly α equivalent width of only $(17.0 \pm 2.7) \text{ \AA}$. Globally, the Ly α line exhibits a redshifted peak with an asymmetric red tail, typical of CGM-scale outflows.

We find significant $\pm 200 \text{ km s}^{-1}$ spatial variations of the line FWHM and peak shift

velocity across the halo. The lowest values of FWHM and peak velocity shift are preferentially found on top of the central galaxies. We also recover a correlation between these two spectral properties, in line with recent results of resolved LAHs.

We divided the source plane emission in 24 spatial bins and fitted them with radiative transfer models in isotropic galactic wind geometries. At an average expansion velocity of $(211 \pm 3) \text{ km s}^{-1}$ and standard deviation of $(62.5 \pm 3.0) \text{ km s}^{-1}$ we find tentative evidence of structured gradients along the minor axis that suggest the outflow has a preferred direction. Also, the best fit models imply that a typical $\text{Ly}\alpha$ photon in the halo encounters a neutral column density of $\sim 10^{20} \text{ cm}^{-2}$ integrated along its path. The existence of the outflow is further confirmed by the presence of blueshifted, asymmetric absorption lines of low ionization metal species in the UV spectrum of the central galaxies. In particular, we measure the $\text{Al II } \lambda 1670$ absorption central velocity at $(-197 \pm 4) \text{ km s}^{-1}$ and $(-142 \pm 2) \text{ km s}^{-1}$ in A and B respectively, in broad agreement with the velocities inferred from the wind models. Finally, the recovered systemic redshifts for the different source plane regions show a complex structure that could be also explained by the interaction processes between the galaxies.

We explored different mechanisms that could be producing the extended emission besides the resonant scattering of photons produced in the central galaxies. $\text{Ly}\alpha$ production *in situ* by gravitational cooling is disfavored since we find no indication of infalling gas motion (e.g., dominant blue peak) assuming an average IGM transmission. However, a major contribution of fluorescent radiation is allowed by energy budget arguments but otherwise remains unconstrained due to uncertainties in the $\text{Ly}\alpha$ escape fraction and the clumpiness of the CGM. Upcoming $\text{H}\alpha$ observations with JWST will be key to establishing the contribution of extended fluorescent radiation in SGASJ1226.

The boost in spatial resolution provided by the lensing effect allowed us to detect the continuum counterpart of a faint ($M_{1500} \approx -16.7$) satellite that is a strong LAE ($\text{EW}_0 = (104 \pm 19) \text{ \AA}$) and contributes 2% of the total $\text{Ly}\alpha$ luminosity. Moreover, this source is resolved with an exponential scale length of $\approx 250 \text{ pc}$. This is one of the few observational hints that such satellites do indeed exist, and contribute to the $\text{Ly}\alpha$ luminosity.

Chapter 3

ALMA discovery of a [C II] plume in a $z = 4.54$ LAB

The content of this chapter was published online on September 10th 2024 as a research article in the *Astronomy & Astrophysics* journal, volume 689, number A145, under the title “*The ALMA-CRISTAL survey: Discovery of a 15 kpc-long gas plume in a $z = 4.54$ Lyman- α blob*”, see [Solimano et al. \(2024\)](#). The article was coauthored by J. González-López, M. Aravena, R. Herrera-Camus, I. De Looze, N. M. Förster Schreiber, J. Spilker, K. Tadaki, R. J. Assef, L. Barcos-Muñoz, R. L. Davies, T. Díaz-Santos, A. Ferrara, D. B. Fisher, L. Guaita, R. Ikeda, E. J. Johnston, D. Lutz, I. Mitsuhashi, C. Moya-Sierralta, M. Relaño, T. Naab, A. C. Posses, K. Telikova, H. Übler, S. van der Giessen, S. Veilleux, and V. Villanueva. Here I reproduce the full article with minor modifications intended to integrate seamlessly with the rest of the thesis. The main changes were the deletion of the first paragraphs of the introduction to avoid redundancy with [Chapter 1](#), and the inclusion of the appendices as actual sections in the text.

3.1 Introduction

Since the ALMA-CRISTAL program (see [§ 1.2.2](#)) targeted the massive end of its parent sample (ALPINE), it is not surprising that many of the CRISTAL sources show clear signs of multiplicity or interaction (e.g., [Posses et al. 2024](#); [Ikeda et al. 2025](#)). Among them,

CRISTAL-01 stands out due to its proximity ($\sim 1''.6$) to the well-known submillimeter galaxy AzTEC J100055.19+023432.8 at $z = 4.54$ (J1000+0234; Capak et al. 2008; Aretxaga et al. 2011). Here, we present the ALMA-CRISTAL observations of this system and report the discovery of a puzzling [C II]-emitting gas plume that extends from the center of the system.

The chapter is organized as follows: in § 3.2 we give an overview of the literature on this particular system. § 3.3 describes the observations and reduction of the new ALMA dataset and the ancillary Very Large Telescope (VLT) and HST data. In § 3.4 we detail the analysis steps and present the results characterizing the [C II] plume. Next, in § 3.5 we explore different physical scenarios that could give rise to the observed emission. Finally, § 3.6 closes with a summary and the main conclusions.

Throughout the chapter, we adopt a flat cosmology described by $H_0 = 70 \text{ km s}^{-1} \text{ Mpc}^{-1}$, $\Omega_{m,0} = 0.3$, and $\Omega_{\Lambda,0} = 0.7$. Under this assumption, $1''$ corresponds to 6.57 kpc of the proper physical scale at $z = 4.54$. When relevant, we adopted a Chabrier (2003) initial stellar mass function (IMF).

3.2 The J1000+0234 system

In this chapter, we study the core region of the J1000+0234 system at $z = 4.54$, first reported by Capak et al. (2008) as a bright submillimeter source with an associated Ly α blob. This region (see Fig. 3.1) hosts two highly star-forming galaxies within $\approx 20 \text{ kpc}$ in projection (Gómez-Guijarro et al. 2018, hereafter GG18). It is embedded in a larger scale overdensity of galaxies (Smolčić et al. 2017a; Loiacono et al. 2021), and possibly linked to the PCI J1001+0220 protocluster (Lemaux et al. 2018). One of the central galaxies, previously known as J1000+0234-South (GG18) but hereafter called CRISTAL-01a, contributes $\approx 75\%$ of the total the rest-frame UV emission of the pair, and belongs to the sample of Lyman-break galaxies (LBGs) targeted by both the ALPINE and CRISTAL surveys. The other galaxy, J1000+0234-North, lies merely $1''.6$ from CRISTAL-01a and accounts for all of the observed submillimeter flux ($S_{870 \mu\text{m}} = (7.8 \pm 0.2) \text{ mJy}$; GG18) and most of the stellar mass ($\approx 2 \times 10^{10} M_{\odot}$; e.g., Schinnerer et al. 2008; GG18). Hereafter, we also refer to

Table 3.1: Global properties of the two main galaxies in the J1000+0234 system.

Property	J1000+0234-North		CRISTAL-01a	
	Value	Ref.	Value	Ref.
[C II] redshift	4.5391	1	4.5537	2
$\log (M_{\text{stars}}) [M_{\odot}]$	10.14 ± 0.08	3	9.16 ± 0.07	3
$\log (M_{\text{dyn}}) [M_{\odot}]$	11.15 ± 0.19	1	-	-
UV slope (β_{UV})	$-1.01^{+0.39}_{-0.32}$	3	$-2.04^{+0.12}_{-0.11}$	3
SFR _{UV} [$M_{\odot} \text{ yr}^{-1}$]	52.6 ± 8.5	3	147.6 ± 7.4	3
SFR _{IR} [$M_{\odot} \text{ yr}^{-1}$]	440^{+1200}_{-320}	3	$56 \pm 35^{\text{a}}$	-
SFR _{tot} [$M_{\odot} \text{ yr}^{-1}$]	490^{+1200}_{-320}	3	204 ± 35	-

(1) [Fraternali et al. \(2021\)](#)(2) [B  thermin et al. \(2020\)](#)(3) [GG18](#)^a Estimated from the IRX- β_{UV} relation ([Meurer et al. 1999](#)) assuming an SMC attenuation law ([Bouchet et al. 1985](#)).

it as “the DSFG” (dusty star-forming galaxy). The global properties of each galaxy are extracted from the literature and listed in Table 3.1.

Multiple follow-up studies have targeted J1000+0234 as one of the brightest and most extreme non-quasar systems known at $z \gtrsim 4$. Until recently, the general picture depicts CRISTAL-01a and the DSFG undergoing a merger event, which potentially drives the elevated SFRs ([Capak et al. 2008](#); [Schinnerer et al. 2008](#); [Smol     et al. 2015](#); [GG18](#)). Yet ALMA observations of the [C II] line later revealed that the DSFG rotates fast at $V_{\text{rot}} \approx 500 \text{ km s}^{-1}$ with $V/\sigma \gtrsim 9$, suggesting a dynamically cold gas component ([Jones et al. 2017](#); [Fraternali et al. 2021](#)). In other words, the merger is either not massive enough or has not had time to dynamically disrupt the internal kinematics of the DSFG. This is consistent with spectral energy distribution (SED) models that put the stellar mass ratio between CRISTAL-01a and the DSFG at $\sim 1:10$ ([GG18](#)).

Current Chandra pointings do not detect X-rays from J1000+0234, putting an upper limit on luminosity of about $1.3 \times 10^{43} \text{ erg s}^{-1}$ in the 0.5-2 keV band ([Smol     et al. 2015](#)). This value is considerably higher than the $10^{42} \text{ erg s}^{-1}$ traditional threshold for AGN iden-

tification (e.g., Szokoly et al. 2004). Moreover the DSFG’s radio emission is weak (Carilli et al. 2008), and consistent with the infrared-radio correlation (Smolčić et al. 2015). However, Jiménez-Andrade et al. (2023, hereafter J23) recently obtained VLT/MUSE observations of J1000+0234, that yielded not only a very high fidelity 3D IFU map of the LAB in which J1000+0234 is embedded, but also the detection of spatially extended C IV and He II emission. The authors argue that the high C IV/Ly α and He II/Ly α ratios can be explained by the presence of an AGN in the DSFG. While this claim still needs confirmation, J23 provided a first view of the complex CGM of J1000+0234, as well as spectroscopic evidence for the overdensity, after identifying five Ly α emitters within the MUSE field of view (1×1 arcmin²).

In parallel to the studies focusing on the massive DSFG, CRISTAL-01a was independently targeted by the ALMA ALPINE survey of [C II] emission in bright LBGs (Le Fèvre et al. 2020, therein labeled as DEIMOS-COSMOS 842313). A successful detection of the line provided the first systemic redshift of this source at $z = 4.5537$ (Béthermin et al. 2020), closely matching the previously reported Ly α redshift ($z = 4.5520$; Hasinger et al. 2018). In the next section, we describe the high-angular resolution ALMA observations obtained by CRISTAL, along with the rest of the observations used in this article.

3.3 Observations and data reduction

3.3.1 ALMA

We use CASA (version 6.5.2, CASA Team et al. 2022) to combine ALMA observations of the redshifted [C II] 158 μ m line targeting J1000+0234 from three different programs, namely the ALPINE survey (Le Fèvre et al. 2020), the CRISTAL survey (Herrera-Camus et al. 2025), and an archival dataset from project 2019.1.01587.S (PI: F. Lelli). The ALPINE observations were carried out with the most compact configuration (C43-1), tuned to cover the line at 349.1 GHz with a velocity resolution of 40 km s⁻¹ and a natural weighting beam size of $1.25'' \times 0.78''$ (Béthermin et al. 2020). The CRISTAL data, on the other hand, include deeper integrations in two antenna configurations, namely C43-1 and C43-4, and

with a higher spectral resolution (10 km s^{-1} per channel) than that of the ALPINE data. These observations were designed to resolve the [C II] emission with a beam of $\sim 0.25''$, equivalent to 1.65 kpc at $z = 4.54$. Finally, the 2019.1.01587.S dataset was observed using a longer baseline configuration (C43-6), providing a nominal resolution of $0''.06$. However, the spectral windows were tuned around the DSFG’s rest-frame velocity, so the frequency overlap with previous data is partial and only covers the red half of CRISTAL-01a’s emission line. We do not include data from the Cycle 2 program 2012.1.00978.S (PI: A. Karim; Jones et al. 2017; Fraternali et al. 2021) into the combined dataset, because its shallower depth plus the complexities of weighting data that was processed with old versions of the pipeline¹ would have resulted in a marginal improvement.

In addition, thanks to the brightness of the DSFG we performed self-calibration on the continuum visibilities of both ALPINE and CRISTAL datasets before combination. This was done in two “phase-only” rounds for each observation, the first one combining spectral windows and scans, and the second one only the scans (of average length $\approx 180 \text{ s}$). This process resulted in a $\approx 11\%$ decrease in continuum rms and the mitigation of patchy patterns in the noise.

Finally, the self-calibrated and combined measurement sets were processed with CRISTAL’s reduction pipeline as described in Herrera-Camus et al. (2025). Briefly, it starts by subtracting the continuum on the visibility space using CASA’s `uvcontsub` task. After that, it runs `tclean` with automasking multiple times, producing cubes with different weightings and channel widths. In all cases the data are cleaned down to 1σ . In this chapter, we use datacubes with 20 km s^{-1} channel width and either natural or Briggs (`robust=0.5`) weighting.

Since the data combines different array configurations, it is important to measure and apply the “JvM” correction (Jorsater & van Moorsel 1995). We do this by following the method of Czekala et al. (2021). This correction takes into account the significant deviations from Gaussianity that the core of the dirty beam can have in multi-array observations and ensures that both the convolved CLEAN model and the residuals have compatible units. While the CRISTAL pipeline provides JvM-corrected products, it uses a

¹<https://casaguides.nrao.edu/index.php/DataWeightsAndCombination>

single correction factor per spectral window. Since we combine multiple datasets from different projects, the uv coverage has significant variations within a spectral window. For this reason, we compute and apply the correction in channel ranges with similar beam properties. We find a mean multiplicative correction factor of $\epsilon \approx 0.37$ in the channels covering the [C II] line emission when using Briggs weighting, and $\epsilon \approx 0.31$ when using natural weighting.

3.3.2 MUSE

We retrieved observations of the J1000+0234 field from the ESO archive taken with the Multi Unit Spectroscopic Explorer (MUSE) instrument mounted on the Very Large Telescope (UT4-Yepun) using ground-layer adaptive optics and the Wide Field Mode. These observations, comprising 16 exposures of 900 s (total 4 h), were taken as part of ESO GTO programs 0102.A-0448 (PI: S. Lilly) and 0103.A-0272 (PI: S. Cantalupo) under good weather conditions with average seeing of 0.9'' and airmass below 1.4. Here we use an independent reduction from that of J23, but we refer the reader to their work for further details about the observations.

The standard calibrations and procedures are performed using the MUSE pipeline (version 2.8.3; Weilbacher et al. 2020) within the ESO Recipe Execution Tool (EsoRex) environment (ESO CPL Development Team 2015). The wavelength solution is set to vacuum. We then apply the Zurich Atmosphere Purge (ZAP, version 2.1; Soto et al. 2016) post-processing tool to further remove sky line residuals. As described by J23, half of the exposures were affected by intra-dome light contamination, resulting in excess counts between 8000 Å and 9000 Å. We decided to use all the exposures in the combined datacube regardless, since the issue does not affect wavelengths near the Ly α emission at 6742 Å. We then follow the steps described in Solimano et al. (2022) to scale the variance cube and match the observed noise levels. Finally, we apply a simple 2D translation to the WCS to match the positions of the two Gaia DR2 (Gaia Collaboration et al. 2018) sources in the field. We check the alignment of the cube with respect to HST by producing pseudo broadband image from the ACS/F814W filter curve. Matching sources in the

MUSE pseudo-F814W image and the ACS/F814W image yield an astrometric rms of 220 mas, or about one MUSE pixel.

The resulting datacube yields a 1σ noise level of $\approx 10^{-19}$ erg s $^{-1}$ cm $^{-2}$ arcsec $^{-2}$ per spectral layer around 6750 Å, computed from randomly placed apertures of 1 arcsec 2 area. The datacube is sampled at pixel scale 0".2 and spectral layers have a width of 1.25 Å. We fit a Moffat profile to an $r = 19$ mag G-type star in the field and find a point spread function (PSF) FWHM of 0".6 around 6750 Å. At this wavelength, the instrument yields a resolving power of $R = 2538$.

3.3.3 HST

We retrieved from MAST² all the available HST data for the J1000+0234 field. We found observations in the ACS/F606W, ACS/F814W, WFC3/F105W, WFC3/F125W and WFC3/F160W bands, covering 1000 Å to 3200 Å in the rest-frame at $z = 4.54$. Images were processed using the standard pipeline, co-added and aligned to Gaia DR2 (Gaia Collaboration et al. 2018). All images were then drizzled with a square kernel and a pixel fraction of 0.5 using the ASTRODRIZZLE routine from DRIZZLEPAC (STSCI Development Team 2012; Hack et al. 2021), executed within the GRIZLI pipeline (Brammer 2023). ACS images were drizzled to a common pixel size of 0".03 while for WFC3/IR images we used a pixel size of 0".06.

3.4 Results and analysis

3.4.1 Adaptive masking of datacubes

Extracting the total flux and spatial extent of the different types of emission considered here, requires taking into account the contributions of faint and diffuse components. Now, given the complexity and spatial variations of the Ly α and [C II] profiles in the J1000+0234 system, a simple pseudo-narrowband “collapse” around the line will hide narrow and low surface brightness (SB) features below the noise level. Instead, we adopt an adaptive approach based on the “matched filtering” technique. This involves creating

²<https://mast.stsci.edu/portal/Mashup/Clients/Mast/Portal.html>

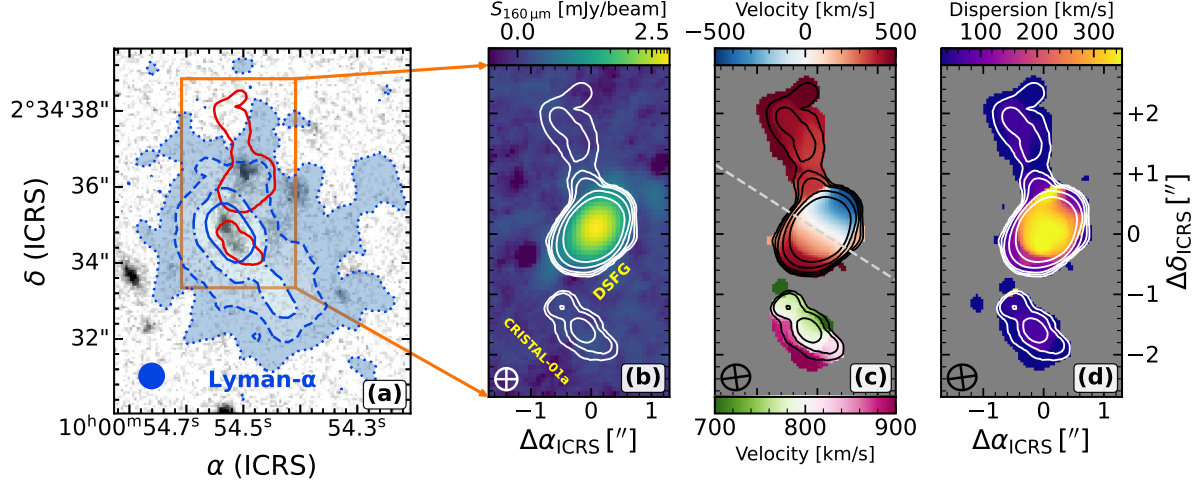


Figure 3.1: HST, Ly α , and [C II] morphologies. **(a).** $10'' \times 6''$ cutout of the WFC3/F160W image in grayscale. The blue-filled contours represent $\{1, 5, 16, 30\} \times 10^{-18} \text{ erg s}^{-1} \text{ cm}^{-2} \text{ arcsec}^{-2}$ levels of Ly α surface brightness based on the adaptive narrowband image described in the main text. The diameter of the blue circle represents the FWHM= $0''.67$ of the PSF of the VLT/MUSE observations. The orange box outlines the $2''.5 \times 5''$ zoom-in region displayed in the next panels. **(b).** ALMA Band 7 continuum image in logarithmic stretch. The white contours follow [C II] emission at $\{0.01, 0.03, 0.07, 0.2, 0.5\} \times \text{Jy km s}^{-1} \text{ beam}^{-1}$, and highlight the non-detection of dust continuum in either CRISTAL-01a or the plume. **(c).** Adaptively masked [C II] velocity field (moment-1). A single colormap is assigned separately to the DSFG and CRISTAL-01a. The midpoint of the colormaps matches their corresponding systemic velocity, with the zero set at the redshift of the DSFG, $z_{[\text{C II}]} = 4.5391$. Again, overlaid contours show increasing levels of [C II] SB. The dashed line indicates the projected rotation axis at a PA = $57^\circ.4$ through the [C II] kinematic center of the DSFG. **(d).** Adaptively masked [C II] velocity dispersion map (moment-2), with [C II] SB contours.

a 3D mask that takes into account the line morphology. For the MUSE data, we used the off-the-shelf software LSDCAT (Herenz & Wisotzki 2017), while for the ALMA cubes we used a custom script.

LSDCAT works by building an optimized S/N detection derived from the cross-correlation of the data with a template signal. Here, we first removed the continuum emission by running a median filter over the spectral axis across the full wavelength range of the cube, using the default window width of 151 spectral pixels (188.75 \AA). This step yields a continuum-only datacube which is then subtracted from the original cube. The next

step is optimized for our blind search of Ly α emitters in the cube, but it also performs well on enhancing the low SB features. The results of our search and the subsequent characterization of the detected objects will be presented in a separate paper.

Following [Herenz & Wisotzki \(2017\)](#) we built our template as a point-like source with a Gaussian spectral profile of $\text{FWHM} = 250 \text{ km s}^{-1}$, a choice that maximizes sensitivity to faint and compact line emitters. After convolving the continuum-subtracted cube by the PSF (spatial filter), we convolved the resulting cube with a 250 km s^{-1} Gaussian kernel (spectral filter) to construct the 3D matched filter output. We took into account the wavelength dependence of the PSF by fitting 2D Moffat profiles to an isolated bright star in the original cube, using 20 wavelength bins. We simultaneously fit the Moffat parameters' dependence on wavelength using 3rd and 2nd order polynomials, for the FWHM and power index parameters, respectively. These polynomials were then used to interpolate the PSF to all the channels of the cube. Then, we computed the detection S/N cube as the voxel-by-voxel ratio between the filtered datacube and the square root of the propagated variances.

Finally, we selected all voxels with $\text{S/N} \geq 2$ between 6729 \AA and 6776 \AA (equivalent to a velocity range of $[-947 \text{ km s}^{-1}, 1135 \text{ km s}^{-1}]$). To refine the selection, we exclude spaxels in which less than three voxels are above the S/N threshold. Furthermore, we create a 2D mask of the spaxels that satisfy these conditions and subsequently prune the regions with less than 55 connected spaxels. We find that this number successfully masks any remaining spurious signal. After we remove the corresponding voxels, we apply the resulting 3D mask to the data, and integrate along the wavelength axis. The result is shown in [Fig. 3.1a](#) as filled contours overlaid on top of an HST image. We recover an irregular and extended Ly α morphology down to $10^{-18} \text{ erg s}^{-1} \text{ cm}^{-2} \text{ arcsec}^{-2}$, in agreement with [J23](#). The highest SB emission is centered on CRISTAL-01a, but extends to a secondary peak $\sim 1''.5$ to the southwest.

We applied a similar procedure to the [C II] cube. Starting from the naturally weighted cube binned in 20 km s^{-1} channels, we convolved with a $\sigma = 30 \text{ km s}^{-1}$ Gaussian kernel along the velocity axis, and a $\sigma = 0''.1$ 2D Gaussian kernel in the spatial axes. We then measured the rms in the signal-free regions of the convolved cube. Finally, we split cells

above and below a $2 \times \text{rms}$ threshold into a 3D mask, which we then fed to CASA task `immoments` to obtain the intensity, velocity, and velocity dispersion maps from the original cube (as shown from panels b to d in Fig. 3.1).

This approach recovers the bright [C II] emission from the DSFG but also reveals faint and extended emission in CRISTAL-01a, and most notably, in a $2''.4$ -long plume extending north of the DSFG. We note, however, that this elongated diffuse emission was already apparent in the individual channels of our cubes, as will be discussed in § 3.4.4. The intensity map spans more than two orders of magnitude in SB, from $0.01 \text{ Jy km s}^{-1} \text{ beam}^{-1}$ (outermost contour in Fig. 3.1b-d) to $2.5 \text{ Jy km s}^{-1} \text{ beam}^{-1}$ at the center of the DSFG, equivalent to $5 \times 10^5 L_{\odot} \text{ kpc}^{-2}$ and $1.25 \times 10^8 L_{\odot} \text{ kpc}^{-2}$ respectively at $z = 4.54$. If we take the [C II] SB as a tracer of SFR surface density, according to the local $\Sigma_{[\text{CII}]} - \Sigma_{\text{SFR}}$ relation (Herrera-Camus et al. 2015), the lower limit would correspond to $\Sigma_{\text{SFR}} = 0.01 M_{\odot} \text{ yr}^{-1} \text{ kpc}^{-2}$, which is well within the regime of normal star-forming galaxies in the Local Universe from the KINGFISH sample (Kennicutt et al. 2011).

In the velocity space, significant [C II] emission spans from -500 km s^{-1} to 850 km s^{-1} across smooth gradients (see Fig. 3.1c). The main gradient goes along the major axis of the DSFG, as previously found by Jones et al. (2017) and Fraternali et al. (2021). Interestingly, the plume displays a gradient along its long axis, with a mild increase in velocity as one moves away from the DSFG. While the plume meets the DSFG in the approaching side, the velocity of the plume overlaps with that of the receding side of the DSFG. Finally, CRISTAL-01a’s [C II] emission is centered at $v \approx 800 \text{ km s}^{-1}$, and shows a more irregular gradient approximately aligned with the minor axis.

The velocity dispersion (Fig. 3.1d), on the other hand, is largest at the center of the DSFG, with the other structures showing low values ($\sigma \lesssim 100 \text{ km s}^{-1}$) and little to no variation.

3.4.2 Parametric morphology

In this section we study the morphological parameters of the two galaxies, CRISTAL-01a and the DSFG, in the J1000+0234 system. To this end, we make use of 2D light profile mod-

eling code PYAUTOGALAXY (Nightingale et al. 2023) built on top of the PYAUTOFIT (Nightingale et al. 2021) probabilistic programming framework. While PYAUTOGALAXY is capable of directly fitting the interferometric visibilities, in this chapter we used the image-based fitter for a faster workflow. We account for the noise correlation in the images by feeding the full covariance matrix into the calculation of the likelihood. The covariance matrix is estimated in source-free regions of the image using the method and the code³ presented by Tsukui et al. (2023b).

We start by modeling the DSFG, which shows a regular and almost symmetric shape. For this reason, we choose to fit a single 2D Sérsic profile (Sersic 1968), with a total of seven free parameters.

We performed two independent fits. One for the rest-frame 160 μm continuum map shown in panel b of Fig. 3.1, and the other for the [C II] integrated intensity map. However, we refrained from using the adaptive intensity map, since the noise properties are not well defined after the masking procedure. Instead, we used regular, unmasked intensity maps integrated within a given velocity range. For the DSFG, we integrated between 342.293 GHz and 344.006 GHz, corresponding to a bandwidth of 1492.7 km s^{-1} . For the center coordinates and the effective radius, we adopted broad Gaussian priors centered on previously published values (Fraternali et al. 2021). For the intensity parameter we adopted a uniform prior between 0 and the maximum surface brightness of the image. Finally, based on previous work that characterized this source as a disk (e.g. Jones et al. 2017), we adopt a Gaussian prior for the Sérsic index centered at $n = 1$ (exponential disk) with a $\sigma = 1$, but allowed n to vary between 0.2 and 10.

The parameter space was explored using the DYNESTY (Speagle 2020; Koposov et al. 2022) nested sampler backend with 50 live points. Table 3.2 lists the results of fitting with the parameters values and uncertainties drawn from the Bayesian posterior probability distribution.

Our analysis reveals that the [C II] and dust morphologies are slightly different in the DSFG. The effective radius of the gas component is approximately 1.5 times larger than that of the dust, while the axis ratio is smaller. However, since the Sérsic indices and the

³ESSENCE, Tsukui et al. 2023a

Table 3.2: Results of the parametric 2D fitting of exponential profiles to the 160 μm continuum and [C II] line maps of the DSFG.

Property	Value
<i>160 μm continuum</i>	
Center (RA)	$10^{\text{h}}00^{\text{m}}54.49129^{\text{s}} \pm 0.00002^{\text{s}}$
Center (Dec.)	$2^{\circ}34'36''.120 \pm 0''.0002$
R_{eff} [pkpc]	0.740 ± 0.003
Sérsic index (n)	1.29 ± 0.01
Axis ratio (minor/major)	0.400 ± 0.002
Flux density [mJy]	8.03 ± 0.03
PA [degrees]	57.8 ± 0.1
<i>[C II] emission</i>	
Center (RA)	$10^{\text{h}}00^{\text{m}}54.4904^{\text{s}} \pm 0.0003^{\text{s}}$
Center (Dec.)	$2^{\circ}34'36''.140 \pm 0''.0005$
R_{eff} [pkpc]	1.13 ± 0.04
Sérsic index (n)	0.71 ± 0.08
Axis ratio (minor/major)	0.34 ± 0.01
Integrated flux [Jy km s^{-1}]	7.8 ± 0.3
PA [degrees]	57.4 ± 0.8

S/N are not equal between [C II] line and 160 μm continuum, we refrain from claiming the gas is more extended than the dust. Assuming instead that the dust and gas both have disk-like geometries, share the same inclination, and are optically thin, the difference in axis ratio suggests that the dust component is thicker in the polar direction relative to the gas component. The higher Sérsic index also indicates that dust is more centrally concentrated, yet the residual continuum map shows significant features that extend beyond the central region and do not follow axial symmetry (see middle row of Fig. 3.2).

Next, we move to CRISTAL-01a and fit only the [C II] emission, since the continuum was not detected. We construct the unmasked intensity map by integrating the cube be-

tween 342.088 GHz and 342.454 GHz, which encloses only 85% of the total line flux but maximizes the S/N of the map. The source clearly breaks into two subcomponents, resembling the rest-frame UV morphology, albeit offset $\approx 0''.3$ to the southwest. We thus model the emission with two independent profiles, an elliptical 2D Sérsic for the brighter component (hereafter SW clump) and a circular Gaussian profile for the fainter component (hereafter NE clump). This model has a total of 11 free parameters. For the SW clump we use the same prior on the Sérsic index as before. For the rest of the quantities we use either broad uniform or Gaussian priors covering reasonable limits in the parameter space.

The best-fit parameters and uncertainties from this fit are listed in Table 3.3. The right panel of Fig. 3.2 shows the 2D residuals. Notably, the SW clump alone has twice the effective radius of the DSFG’s [C II] emission and more than three times the radius of its dust emission. This size is comparable to previous measurements performed on the F814W imaging (Fujimoto et al. 2020). If we were to associate the [C II] clumps to the two UV clumps seen by HST, we notice the brightness order is inverted. The SW clump’s [C II] line flux density is about ten times that of than the NE clump. Yet in the UV, the NE clump is brighter. This discrepancy could be attributed to differences in dust attenuation. In fact, GG18 provided maps of the rest-frame UV β_{UV} slope based on the HST imaging, and they show that the southern part of CRISTAL-01a is slightly redder ($\beta_{UV} \approx -2.0$) than the northern part ($\beta_{UV} \approx -2.2$).

3.4.3 Stack of HST images

In this section we present the stack of HST imaging in the F105W, F125W, F140W and F160W filters. We converted the image units to nJy per pixel, and then computed a pixel-by-pixel weighted sum. The weights correspond to the inverse variance of the full frames. We then measure fluxes in 5000 random apertures of 1 arcsec^2 area, and obtain a 5σ depth of $26.2 \text{ mag arcsec}^{-2}$. Fig. 3.3 shows the result of the stacking in the region close to the J1000+0234 system, and reveals two tentative sources near the [C II] plume that were not detected in the individual images.

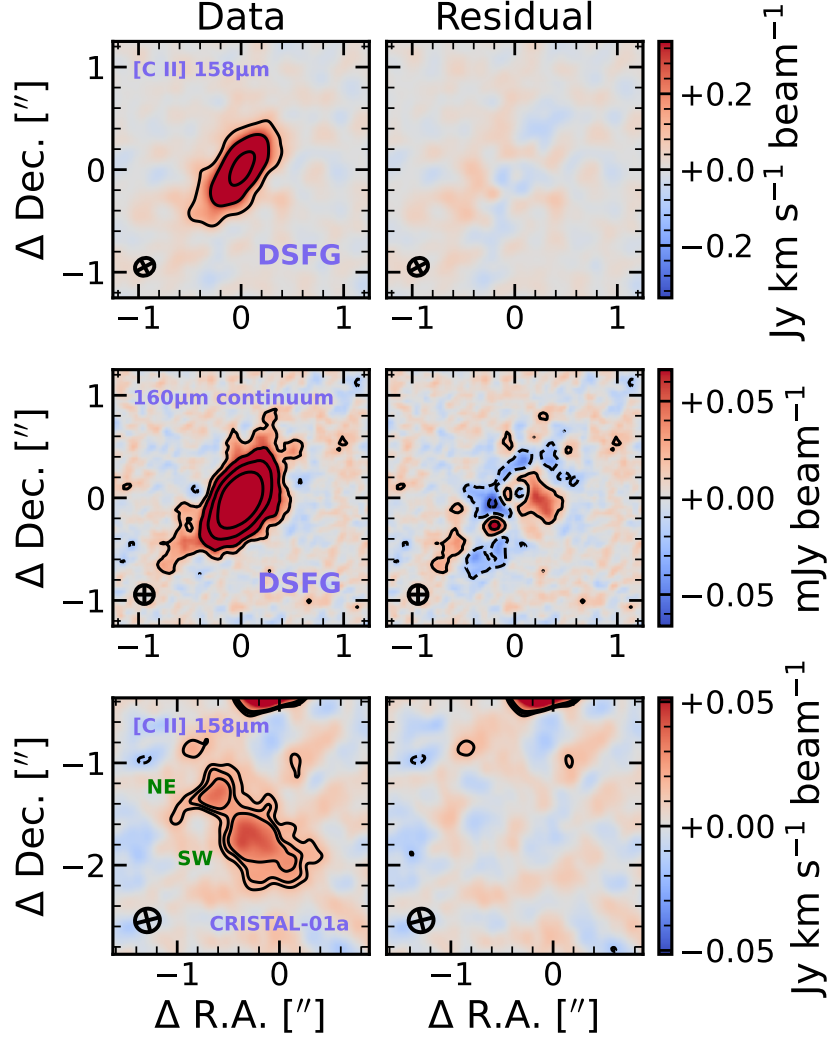


Figure 3.2: Results from parametric 2D modeling with PyAutoGalaxy. Each row shows a different source and/or image. Left column displays the observed emission, while the right column shows the residuals after subtracting the maximum likelihood model. The first and second rows show the modeling of the DSFG’s [C II] emission and 160 μm dust continuum, respectively. Black contours represent the $\pm 3, 9, 27$ and 81σ levels. Results for the [C II] emission of CRISTAL-01a (CRISTAL-1) are shown in the third row. Here, the contours only trace $\pm 3, 4$ and 5σ levels.

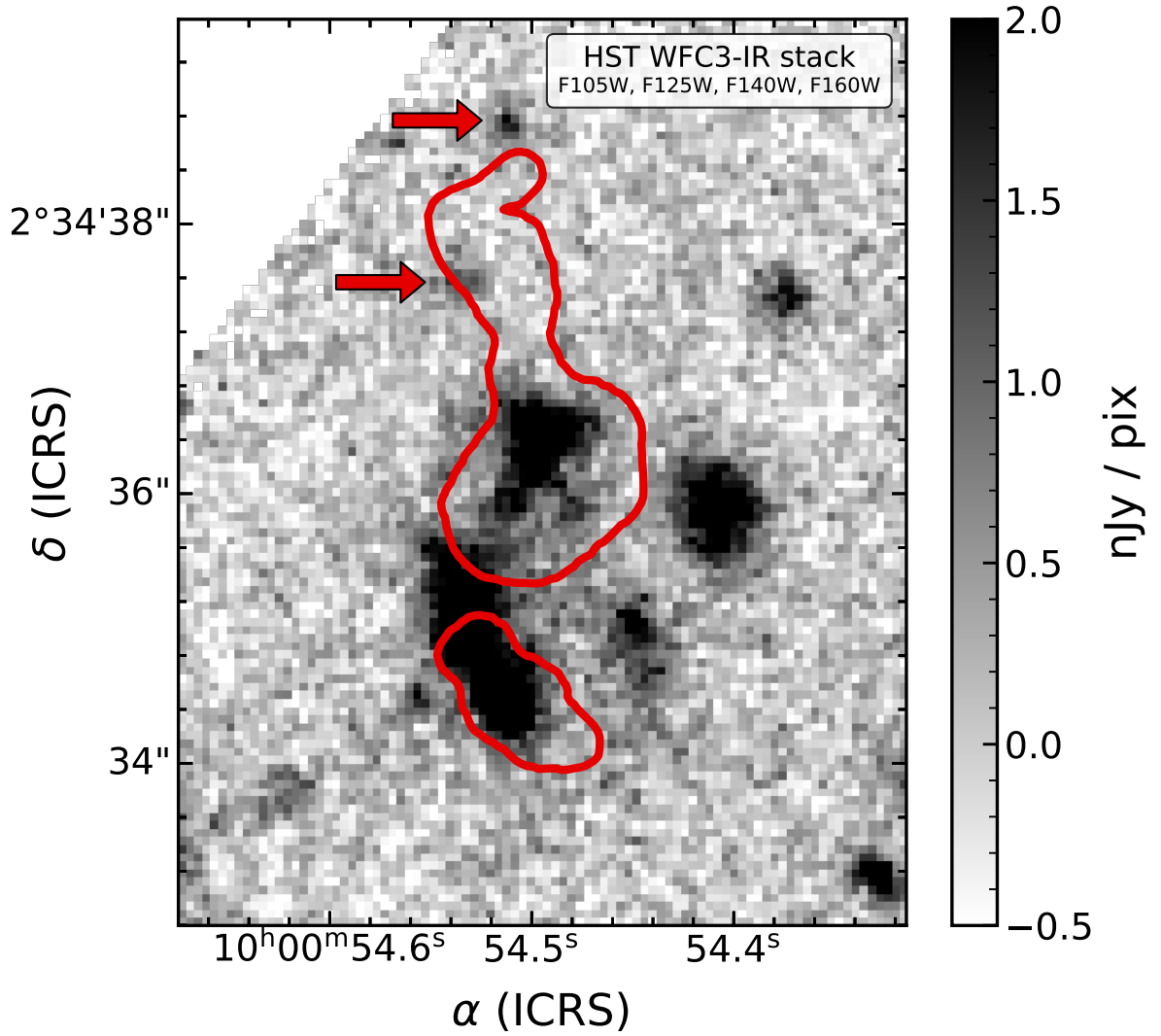


Figure 3.3: Stack of HST/WFC3-IR imaging of J1000+0234 with the outline of the [C II] emission in red. Arrows indicate the positions of the two sources potentially associated with the plume.

Table 3.3: Results of the parametric 2D fitting to the [C II] line map of CRISTAL-01a.

Property	Value
<i>SW clump</i>	
Center (RA)	$10^{\text{h}}00^{\text{m}}54.505^{\text{s}} \pm 0.003^{\text{s}}$
Center (Dec.)	$2^{\circ}34'34''.34 \pm 0''.02$
R_{eff} [pkpc]	2.4 ± 0.4
Sérsic index (n)	1.0 ± 0.3
Axis ratio (minor/major)	0.82 ± 0.09
Integrated flux [Jy km s^{-1}]	0.39 ± 0.08
PA [degrees]	175 ± 45
<i>NE clump</i>	
Center (RA)	$10^{\text{h}}00^{\text{m}}54.537^{\text{s}} \pm 0.02^{\text{s}}$
Center (Dec.)	$2^{\circ}34'34''.75 \pm 0''.03$
R_{eff} [pkpc]	0.8 ± 0.3
Integrated flux [Jy km s^{-1}]	0.03 ± 0.02
Total flux ^a (SW + NE)[Jy km s^{-1}]	0.5 ± 0.2
Centroid separation [arcsec]	0.63 ± 0.06

^a Flux has been corrected by a factor 1.17 to account for emission outside the velocity integration range.

3.4.4 Spectral properties of the [C II]-emitting plume

While the adaptive masking scheme described in Sect. 3.4.1 helped us identify all the [C II] signal present in the cube and unveil the general kinematic trends, the noise properties of the masked maps in Fig. 3.1 remain undefined. Moreover, since our data display a large dynamic range in both surface brightness and velocity dispersion, the details of the plume are partly outshined by the DSFG. In order to get a clearer picture of the plume, Fig. 3.4 displays eight consecutive channel maps of 40 km s^{-1} width, covering from 200 km s^{-1} to 480 km s^{-1} relative to the systemic velocity of the DSFG.

The limits of the colormap in Fig. 3.4 were chosen to highlight the faint extended emis-

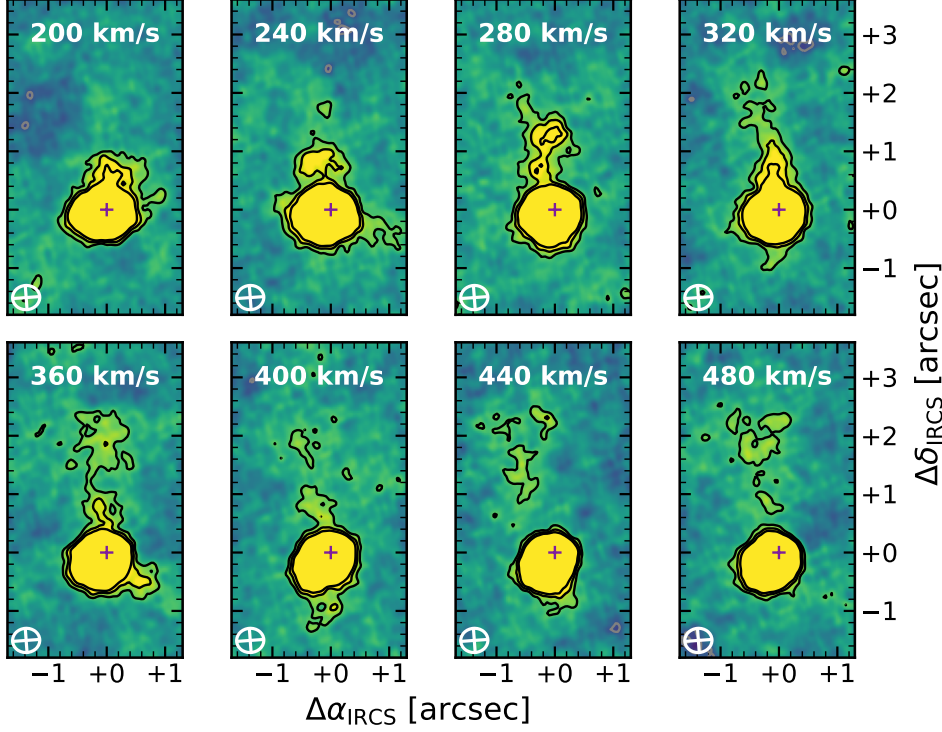


Figure 3.4: Selected channel maps from the low-resolution [C II] datacube binned to 40 km s^{-1} . Black contours represent 3, 5 and 7 times the JvM-corrected noise rms level, while the gray contours show the negative $3 \times \text{rms}$ level. The purple cross in each channel indicates the origin of the coordinates, at $\alpha_{\text{ICRS}} = 150^{\circ}227\,063$, $\delta_{\text{ICRS}} = 2^{\circ}576\,679$.

sion and to give a visual reference of the noise amplitude. On top of it, we show contours at different levels of statistical significance. All eight channel maps exhibit large patches of $\geq 3\sigma$ emission distributed between $0''.2$ and $2''.5$ northward from the DSFG kinematic center (purple cross). In the first row of panels we can see that the plume grows longer at higher velocities, reaching a maximum isophotal extent of $\approx 2''.1 = 13.8 \text{ kpc}$ at 360 km s^{-1} (bottom left panel). In the subsequent channels, the plume becomes fainter and clumpy in appearance, possibly due to the lower S/N. We note that the DSFG centroid shifts coherently to the southeast as a result of rotation.

We now want to quantify the spatial variations of the spectral profile along the plume with a proper treatment of the noise. To this end, we place six adjacent rectangular $0''.4 \times 0''.9$ apertures covering the full extent of the plume as seen in Fig. 3.5, oriented with a position angle of 14° east of north. We extract the spectra from the Briggs-weighted (ro-

bust=0.5) datacube without continuum subtraction. With this weighting, the synthesized beam ($0''.25 \times 0''.23$) fits comfortably within each aperture, making them independent.

We then fit each extracted spectrum independently with a single 1D Gaussian, except for the first two apertures, where we include a first-order polynomial to model the continuum from the DSFG. In these apertures we also mask emission from -700 km s^{-1} to 0 km s^{-1} to avoid contamination from the approaching side of the DSFG.

Once again, we use PyAutoFit with the DYNESTY (Speagle 2020; Koposov et al. 2022) static nested sampler as a backend. We assume a Gaussian likelihood for the sum of the rms-weighted residuals (data minus model). For every channel (of width 20 km s^{-1}), we measure the rms as the 3σ -clipped standard deviation of the flux densities of 300 random apertures with the same size and orientation as the extraction apertures. We adopt uniform priors for the three fitted parameters, namely the velocity center between -200 km s^{-1} and 1000 km s^{-1} ; the FWHM between 60 and 1000 km s^{-1} ; and the total flux between 0 and 1.0 Jy km s^{-1} .

Figure 3.5 and Table 3.4 show the results of these fits as a function of the distance of each aperture from the center of the DSFG. We recognize radial trends in all the three parameters, and a large gap between apertures #1 and #2. This apparent discontinuity could be due to additional contamination in aperture #1’s spectrum at positive velocities. For this reason, we subtract a velocity-inverted spectrum from an aperture that mirrors aperture #1 by the projected rotation axis (dashed line in Fig. 3.5) and repeat the fit. After this correction, we find both lower fluxes and FWHM, but a consistent central velocity, as shown by the white-filled markers in Fig. 3.5. These differences illustrate the systematic uncertainties associated with aperture #1, that make flux and FWHM less reliable.

Regardless of which fit we consider for the first aperture, we identify a radially decreasing trend for the flux density (or surface brightness). From 5 kpc to 15 kpc the flux drops almost exponentially, with an excess at $\approx 13 \text{ kpc}$. Summing apertures from #2 to #6 yields a total flux of $(0.50 \pm 0.04) \text{ Jy km s}^{-1}$, which closely matches CRISTAL-01a’s total flux (Table 3.3) and amounts to a [C II] luminosity of $(3.10 \pm 0.25) \times 10^8 L_{\odot}$. Adding aperture #1 will raise this number by a factor of 2.53 under the original fitting scheme, and by a factor of 1.61 with the corrected fit.

In the middle panel of the left row we can see a decrease in the line width as one moves further out in the plume. Starting from $400 - 600 \text{ km s}^{-1}$ at 2.5 kpc, the plume narrows down to $180^{+64}_{-38} \text{ km s}^{-1}$ in the outermost aperture. We note that at low S/N the fits tend to bias the FWHM to larger values, hence the intrinsic FWHMs of the outermost bins might be even lower than depicted here.

Our aperture-based measurements recover the velocity gradient that we had seen in the velocity map in Fig. 3.1c. Here, both methods to extract the spectrum of aperture #1 yield consistent central velocities at $v_{\text{cen}} \approx 180 \text{ km s}^{-1}$. The next aperture (#2) is already at 300 km s^{-1} , suggesting a steep velocity gradient between apertures #1 and #2. In the subsequent apertures, the increase in velocity is less abrupt, going from $\approx 300 \text{ km s}^{-1}$ to $\approx 400 \text{ km s}^{-1}$ in the outer 10 kpc.

In addition, we create custom intensity maps for each aperture, integrating over a velocity window of size 1.1 times the best-fit spectral FWHM for maximal S/N. On these maps we obtain 1D spatial profiles along the long side of the corresponding aperture, but extended to ± 3 arcsec. We then fit a Gaussian to these profiles to obtain the transversal (spatial) FWHM of the plume. After deconvolving the beam width, we obtain FWHMs between $0''.4$ and $0''.8$ with an average of $0''.6$, but no clear radial trend.

Finally, we put upper limits on the FIR luminosity surface density of each aperture based on the continuum depth. To this end, we randomly placed 600 rectangular apertures of size $0''.9 \times 0''.4$ on the rest-frame $160 \mu\text{m}$, $\text{robust}=0.5$ continuum map (without JvM correction). We obtain a distribution of flux densities with σ -clipped standard deviation of $\sigma = 38.8 \mu\text{Jy}$. Taking 5σ as the detection limit, we convert the flux density into FIR luminosity⁴ assuming an underlying $T_{\text{dust}} = 45 \text{ K}$ modified blackbody dust SED, with a dust emissivity index $\beta_{\text{dust}} = 1.5$ (a choice that roughly describes the average SED of star-forming galaxies at $z > 4$, e.g., Béthermin et al. 2020). Such an SED gives the ratio $\nu L_{\nu}(158 \mu\text{m})/L_{\text{FIR}} = 0.185$. After correcting for primary beam gain decrement, we quote the resulting limits in Table 3.4, except for aperture #1 where emission from the DSFG dominates. We note, however, that these values depend on the assumed temperature. For example, choosing $T_{\text{dust}} = 55 \text{ K}$ and $T_{\text{dust}} = 65 \text{ K}$ produce $1.7\times$ and $2.4\times$ higher L_{FIR}

⁴Defined as the integral of the rest-frame SED between $42 \mu\text{m}$ and $122 \mu\text{m}$.

limits, respectively. In any case, these measurements allow us to estimate the [C II]/FIR diagnostic, which informs about the heating mechanism of the gas. At $T_{\text{dust}} = 45$ K we obtain lower limits on the [C II]/FIR ratio between $\approx 0.2\%$ (aperture #6) and $\approx 0.6\%$ (aperture #2). Unfortunately, these lower limits are not high enough to rule out UV photoelectric heating, characteristic of photodissociation regions (PDRs; with typical [C II]/FIR ratios between 0.01% and 2%, e.g., [Herrera-Camus et al. 2018](#)), in favor of other mechanisms such as shock heating ($\gtrsim 4\%$, e.g., [Appleton et al. 2013](#); [Peterson et al. 2018](#)). Only at the coldest possible temperatures, $T_{\text{dust}} \lesssim 20$ K ($T_{\text{CMB}} = 15$ K), the highest limit becomes [C II]/FIR $> 6.8\%$, and thus harder to explain with UV photoelectric heating alone.

Table 3.4: Extracted quantities from the apertures in [Fig. 3.5](#).

Aperture #	Flux density Jy km s^{-1}	v_{cen} km s^{-1}	FWHM km s^{-1}	$\Sigma_{[\text{CII}]}$ $10^6 L_{\odot} \text{ kpc}^{-2}$	$\Sigma_{\text{FIR}}^{\text{b}}$ $10^{10} L_{\odot} \text{ kpc}^{-2}$	v_{out} km s^{-1}	M_{out} $10^7 M_{\odot}$	\dot{M}_{out} $M_{\odot} \text{ yr}^{-1}$
1 ^a	$0.27^{+0.05}_{-0.03}$	166^{+31}_{-54}	454^{+65}_{-81}	$10.6^{+2.1}_{-1.3}$	-	551 ± 75	25 ± 3	83 ± 18
2	$0.18^{+0.03}_{-0.02}$	297^{+19}_{-17}	377^{+73}_{-59}	$7.3^{+1.0}_{-0.9}$	< 1.3	617 ± 56	17 ± 2	64 ± 11
3	$0.10^{+0.02}_{-0.02}$	318^{+27}_{-23}	306^{+86}_{-58}	$4.0^{+0.7}_{-0.7}$	< 1.3	578 ± 66	9 ± 2	32 ± 7
4	$0.08^{+0.01}_{-0.01}$	336^{+17}_{-25}	228^{+40}_{-42}	$3.1^{+0.5}_{-0.4}$	< 1.3	530 ± 41	7 ± 1	23 ± 4
5	$0.09^{+0.01}_{-0.01}$	379^{+15}_{-18}	210^{+36}_{-32}	$3.5^{+0.5}_{-0.6}$	< 1.3	558 ± 33	8 ± 1	28 ± 4
6	$0.05^{+0.01}_{-0.01}$	409^{+27}_{-24}	180^{+64}_{-38}	$2.0^{+0.5}_{-0.5}$	< 1.4	561 ± 50	5 ± 1	16 ± 4

^a Values in this row were extracted from the spectrum corrected via the symmetric difference scheme (white filled circles in [Fig. 3.5](#), see [§ 3.4.5](#)).

^b Limits on the far-infrared luminosity were estimated from the 5σ depth of the rest-frame $160 \mu\text{m}$ continuum map, and assuming a modified blackbody SED of $T_{\text{dust}} = 45$ K and $\beta_{\text{dust}} = 1.5$, which yields $\nu L_{\nu}(158 \mu\text{m})/L_{\text{FIR}} = 0.185$.

3.4.5 Symmetric difference correction of aperture #1’s [C II] spectrum

As described in [§ 3.4.4](#), the aperture #1 in [Fig. 3.5](#) contains significant emission from the dust continuum and the approaching side of the DSFG rotator. To mitigate the contamination, we performed continuum subtraction and masked negative velocities before fitting the line, yet the resulting 1D Gaussian parameters deviate significantly from the parameters of the line in the subsequent apertures, suggesting additional contamination at positive velocities. Motivated by this, we attempt in this section to remove the additional emission before repeating the Gaussian fit.

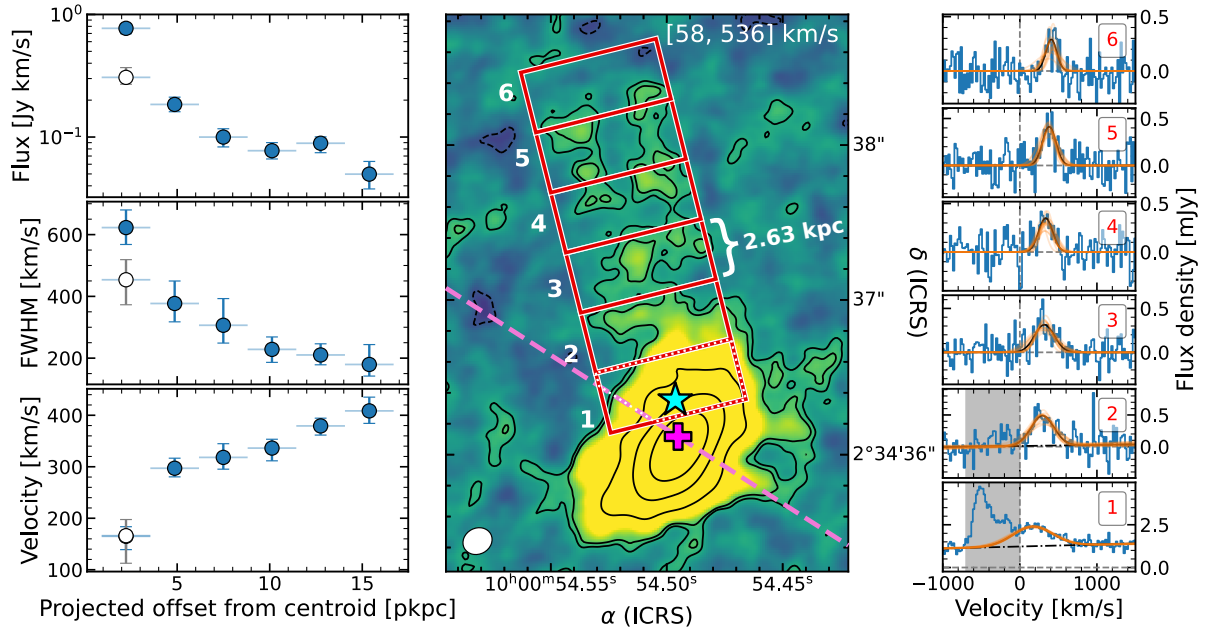


Figure 3.5: Spatial variation of spectral properties of the [C II] plume. *Left:* Radial profiles of fitted 1D Gaussian parameters in six apertures along the plume, as a function of projected distance from the kinematic center of the DSFG. The parameters shown are the integrated flux (top), the line FWHM (middle) and velocity centroid (bottom). White-filled markers in the first bin indicate best-fit values for the innermost spectrum after reducing contamination with our symmetric difference method. *Center:* [C II] intensity map integrated from 58 km s⁻¹ to 536 km s⁻¹, with black contours at the $\{\pm 2, 3, 15, 50, 150\} \times \sigma$ SB level. Red rectangles numbered from 1 to 6 delineate the extraction apertures along the plume. The cyan star and pink cross mark the position of the rest-UV and the [C II] kinematic centroids, respectively. The dashed line extrapolates the minor axis of the DSFG’s [C II] integrated emission at a PA=57°:4 (see § 3.4.2). The line intersects the first rectangular aperture, defining a polygonal subregion where we extract the spectrum for symmetric difference analysis (see § 3.4.5). *Right:* Extracted spectra from the six rectangular apertures, with their number labeled in red. The black solid line in each panel shows the maximum likelihood fit, while the orange lines are random samples from the posterior probability distribution. In panels 1 and 2 the shaded area indicates the velocity range excluded from the fit. The dash-dotted line shows the best-fit continuum component.

If the DSFG rotator is axially symmetric, we expect any aperture-extracted spectrum from one side of the DSFG to be similar—although with inverted velocities—to a spectrum extracted from a mirrored aperture, reflected with respect to the projected rotation axis. So in principle, differences in these spectra will uncover asymmetric emission in the cube, such as the plume we are studying.

Here, we take the projected rotation axis to be parallel to the minor axis of the DSFG’s [C II] emission (see dashed line in Fig. 3.5) and crossing the position of the steepest velocity gradient. In practice, we choose the point where the 2nd moment (velocity dispersion) is maximal. Once we have defined the axis, we calculate the geometrical reflection of aperture #1. However, the rotation axis crosses through the aperture, which would lead to an overlapping region between the aperture and its mirrored version. To avoid this, we crop the corner of aperture #1 that goes over the eastern side of the axis before the reflection.

We then extract the [C II] spectrum from the `robust=0.5`, 20 km s^{-1} channel width cube without continuum subtraction, from both the cropped aperture #1 and its reflection. We then apply a simple continuum subtraction by fitting a first-order polynomial to channels between $\pm 1330 \text{ km s}^{-1}$ and $\pm 1000 \text{ km s}^{-1}$ independently for each spectrum. We show the resulting spectra in Fig. 3.6.

After flipping the mirrored spectrum in velocity space and comparing it with the original, we find the horns have different peak heights and are offset by $\approx 47 \text{ km s}^{-1}$, but have similar overall shape. We thus shift and scale the mirrored spectrum to match the peak of the original and then perform the subtraction. The resulting spectrum is shown in the lower panel of Fig. 3.6. The difference is mostly consistent with zero, except for a strong but narrow negative difference around -250 km s^{-1} and a broad positive difference between 0 km s^{-1} and 400 km s^{-1} . The former arises from an excess or quirk in the spectrum from the mirrored aperture at 250 km s^{-1} , while the latter we assume to be associated with the [C II] plume.

Finally, we model the difference spectrum with the method described in Sec. 3.4.4. This is, we fit a 1D Gaussian using `PyAutoFit`. Once again, we mask the negative velocities down to -700 km s^{-1} to avoid fitting the residual negative feature. Compared to

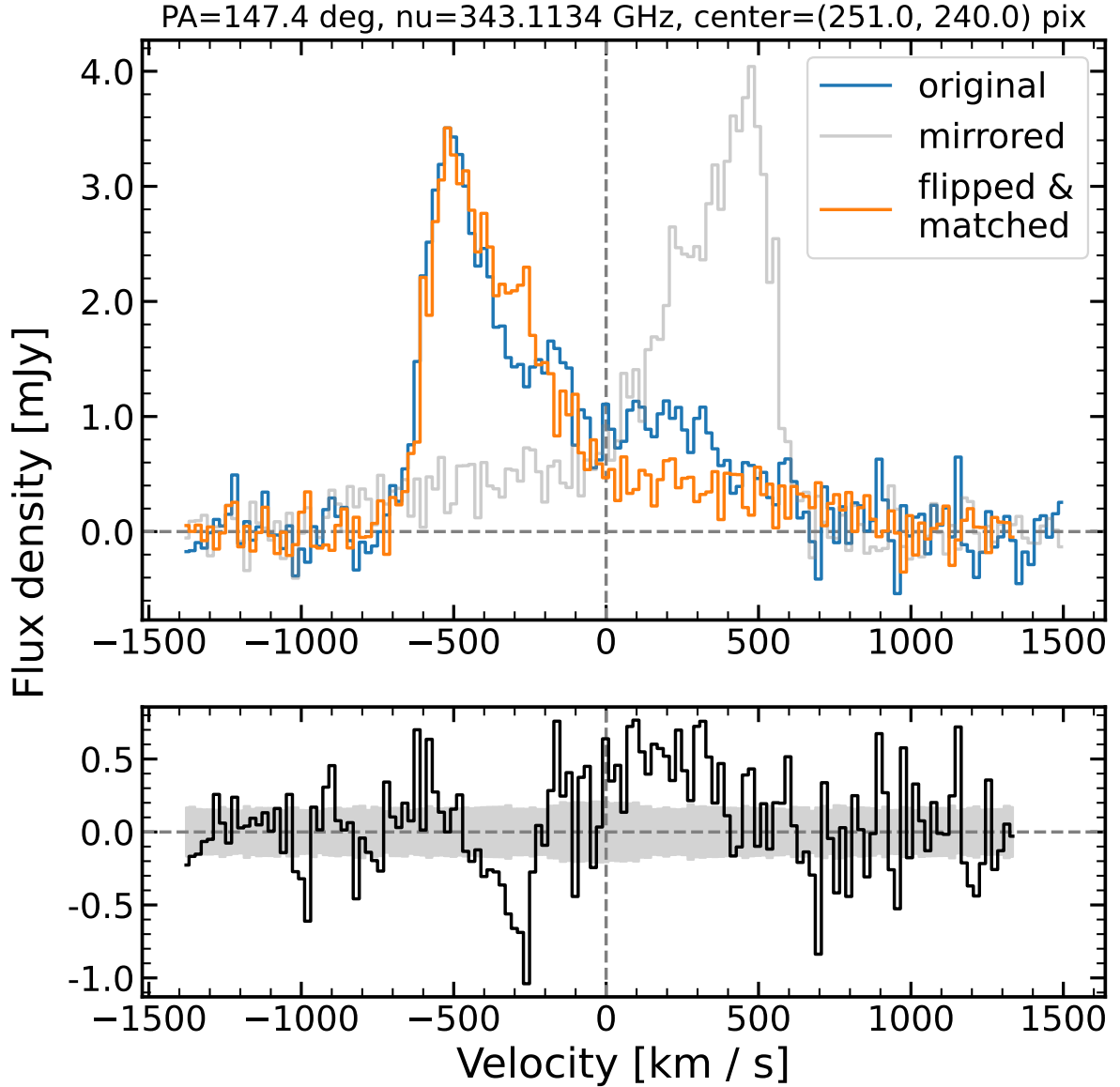


Figure 3.6: Symmetric difference analysis for aperture #1. *Upper panel:* [C II] spectra of the cropped aperture #1 (blue), its mirrored version (gray), and the mirrored version but velocity-inverted (flipped), shifted and matched to the original peak (orange). *Lower panel:* Residuals from the difference between the original and the flipped-and-matched spectra.

our fiducial method, this fit yields a significantly lower flux ($\approx 0.3 \text{ Jy km s}^{-1}$) and FWHM ($\approx 420 \text{ km s}^{-1}$), although the central velocities are consistent. In conclusion, both the flux and FWHM in aperture #1 are affected by contamination from the host, but the central velocity is not.

3.5 Discussion

The main question we want to answer in this chapter is what caused the [C II] plume in the J1000+0234 system. In this section we discuss possible scenarios such as outflows, inflows, ram pressure stripping, and tidal interactions.

3.5.1 Conical outflow

A first hypothesis on the nature of the [C II] plume is to interpret it as a collimated outflow launched by the DSFG. In this scenario, the extended [C II] emission arises from a large-scale conical wind, probably from cold gas clumps entrained in it, or from the ionized walls of the cone (see cartoon in [Fig. 3.7](#)). The specific distribution of the emission will depend on the relative mix of gas phases [C II] is tracing (molecular, neutral, and ionized), and on the type of source powering the outflow.

Galactic-scale outflows are primarily driven by either AGN activity or stellar feedback (see [§ 1.1.3](#)). Since the latter is dominated by young massive stars, outflows powered by stellar feedback (which includes stellar winds, radiation pressure, and supernova explosions) are also known as starburst-driven outflows. Theoretical and observational evidence suggests that starburst-driven outflows escape along the minor axis of disk galaxies, because it is the path of least resistance, leading to (bi-)conical structures that extend perpendicular to the disk, with M82 ([Bland & Tully 1988](#)) and NGC 1482 ([Veilleux & Rupke 2002](#)) being archetypal examples in the Local Universe. In these two cases and in other local SFGs, the wind exhibits a wide opening angle ($\theta \gtrsim 60^\circ$; e.g., [Hjelm & Lindblad 1996](#); [Veilleux et al. 2001](#); [Seaquist & Clark 2001](#); [Westmoquette et al. 2011](#); [Rubin et al. 2014](#)). Wide opening angles are also a common feature of simulated starburst-driven outflows (e.g., [Cooper et al. 2008](#); [Nelson et al. 2019](#); [Schneider et al. 2020](#)).

In contrast, AGN-driven outflows do not show a preferential alignment with the host minor axis (e.g., [Schmitt et al. 2003](#); [Ruschel-Dutra et al. 2021](#)) and can have very narrow opening angles ($\theta \lesssim 20^\circ$, e.g., [Sakamoto et al. 2014](#); [Aalto et al. 2020](#)). Starburst- and AGN-driven outflows also differ on the velocities the gas can reach and the amount of mass they carry. For example, the outflow velocity in a starburst-driven wind scales with

the SFR surface density (e.g. [Davies et al. 2019](#)), and ranges between $\approx 20 \text{ km s}^{-1}$ and $\gtrsim 2000 \text{ km s}^{-1}$ ([Veilleux et al. 2005](#)), whereas in AGN winds the velocity will be a function of the bolometric luminosity (e.g. [Fiore et al. 2017](#)) and can be exceptionally fast, up to half of the speed of light (e.g., [Chartas et al. 2021](#)).

Outflows accelerate strongly in the regions close to the energy/momentum source, but the acceleration fades once the gas reaches a certain distance. As a consequence, resolved outflows are expected to show a steep velocity gradient at small radii, followed by an asymptotic approach to a terminal velocity at large radii ([Veilleux et al. 2005](#)).

In what follows, we assume that the [C II] plume is tracing a conical outflow, and argue that most of the emission comes from the neutral phase. Then we quantify some key outflow properties, and compare them to literature values to assess how likely is this scenario and what would be the most probable energy source.

Since [C II] is the only line available, the dominant gas phase producing the emission remains unknown. One possibility is that most of the [C II] flux arises from a population of clumps of cold (molecular and/or atomic) gas entrained in the hot outflowing plasma, as illustrated in the upper left panel of [Fig. 3.7](#). Such arrangement of the cold medium is predicted by the theory (e.g., [Schneider et al. 2020](#); [Kim et al. 2020](#); [Fielding & Bryan 2022](#)) and validated by a large set of observations ([Shapley et al. 2003](#); [Rubin et al. 2014](#); [Pereira-Santaella et al. 2016, 2018](#)). Yet only a few studies exist reporting [C II] outflows at a high- z . On one hand, high-velocity wings have been detected in individual ([Herrera-Camus et al. 2021](#)) and stacked spectra of main sequence galaxies ([Gallerani et al. 2018](#); [Ginolfi et al. 2020a](#)), and QSO hosts (e.g., [Bischetti et al. 2019](#)), but they usually come without any constraint on the state of the emitting gas. On the other hand, [Spilker et al. \(2020\)](#) showed that seven out of a sample of eleven lensed DSFGs host unambiguous molecular outflow signatures in the form of blueshifted OH $119 \mu\text{m}$ absorption, yet none of these galaxies display broad [C II] emission. These results led [Spilker et al. \(2020\)](#) to conclude that [C II] line is an unreliable tracer of molecular outflows. Since the DSFG has similar intrinsic properties as the sources in the [Spilker et al. \(2020\)](#) sample, we argue that it is unlikely for [C II] to be tracing molecular gas in the plume. Therefore, the gas clumps might be composed of mainly atomic hydrogen.

Alternatively, the emission is dominated by ionized ($T \gtrsim 10^4$ K) gas and we are seeing the outflow cone walls from the side, similar to what optical nebular lines show in low-redshift edge-on outflows. When sufficient spatial resolution allows it, such cases exhibit a hallmark limb-brightening effect near the edges of the cone (e.g., [Strickland et al. 2004](#); [Westmoquette et al. 2011](#); [Venturi et al. 2017](#); [Rupke et al. 2019](#); [Herenz et al. 2023](#)). Here, the plume is resolved in the transverse direction, but the S/N is too low to draw any conclusion about the structure. Nevertheless, [J23](#) detected C IV at the position of the DSFG, with a velocity shift comparable to what we measure in the plume ($\sim 300 \text{ km s}^{-1}$). This would support the idea of a physical association of the [C II] plume with warmer gas and hence a with a more energetic origin.

To explore what is the energy source of our putative outflow, we start by quantifying its observed geometry. First, we note the [C II] plume diverges from the DSFG’s minor axis by $\sim 40^\circ$ clockwise. In other words, it is not aligned with the polar direction of the disk, thus favoring an AGN origin. Furthermore, the plume width remains narrow (transversal FWHM of $\approx 0''.6$, see § 3.4.4) along its full extent, showing little to no broadening toward the top (north). In aperture #6 of [Fig. 3.5](#), the transversal FWHM is $0''.8$. Taking that as the opening of the cone at a distance of $2''.4$ of its vertex at the center of the DSFG, we derive a projected angle of $\theta_p = 2 \arctan(0.4/2.4) \approx 19^\circ$, which is a projection of the true angle $\theta = 2 \times \arctan[\sin(i) \times \tan(\theta_p/2)]$. Using the expectation value for a random uniform distribution of inclination angles, $\langle \sin i \rangle = 0.79$ (see the derivation in [Law et al. 2009](#)), we estimate $\theta \approx 15^\circ$. This angle falls short of typical outflow opening angle observed in low redshift starbursts ($\gtrsim 60^\circ$, see references above). This again favors AGN as the driver of the outflow, although a high gas density surrounding a central starburst can also lead to a strong collimation effect, especially in the cold phases (e.g., [Pereira-Santaella et al. 2016](#)).

On a side note, the fact we see only one cone instead of a symmetric bi-cone could be explained by power source being located above the midplane of the disk. In that case, the outflow would need to be much stronger to blow out into the other side.

Now we estimate the mass of the plume enclosed in each of the apertures of [Fig. 3.5](#) from the measured [C II] fluxes. In the optically thin limit, and assuming negligible background emission, the gas mass in each aperture is $M_{\text{out}} = \kappa_{[\text{CII}]} \times L_{[\text{CII}]}$, where the conver-

sion factor $\kappa_{[\text{CII}]}$ depends strongly on the temperature, density, and carbon abundance of the gas. Following [Herrera-Camus et al. \(2021\)](#), we assume the collisions are dominated by atomic hydrogen and adopt $\kappa_{[\text{CII}]} = 1.5 M_{\odot} L_{\odot}^{-1}$ which corresponds to maximal excitation ($T \gg 90 \text{ K}$, $n \gg n_{\text{crit}} \sim 10^3 \text{ cm}^{-3}$), and solar abundance patterns. Since lower densities, temperatures and abundances yield higher values of $\kappa_{[\text{CII}]}$, the masses we derive will effectively represent lower limits. For example, $\kappa_{[\text{CII}]}$ becomes $3\times$ and $27\times$ larger when the metallicity drops to half solar, and one-tenth solar, respectively (see discussion in [Herrera-Camus et al. 2021](#)).

In this way, we measure gas masses from $5 \times 10^7 M_{\odot}$ in the outermost aperture (#6) to $2.5 \times 10^8 M_{\odot}$ in the innermost aperture (#1, corrected by symmetric difference method). The sum of all the apertures gives $(7.1 \pm 0.4) \times 10^8 M_{\odot}$. We now exploit the spectral information to derive mass outflow rates as $\dot{M}_{\text{out}} = M_{\text{out}} \times v_{\text{out}} \times \tan(i)/R$, where v_{out} represents the projected maximum outflow velocity and $R = 2.63 \text{ kpc}$ is the projected length of the aperture in the short side (parallel to the flow). For the maximum outflow velocity we use the prescription of [Genzel et al. \(2011\)](#) for outflows detected as broad emission components with Gaussian profile width σ_{broad} and velocity offset of $|\Delta v|$ with respect to the narrow component: $v_{\text{out}} = |\Delta v| + 2\sigma_{\text{broad}}$. Since we only detect a single spectral component along the plume, we take $|\Delta v| = v_{\text{cen}}$ as the velocity centroid relative to the DSFG’s systemic velocity. Both v_{out} and M_{out} values are listed in Table 3.4.

Assuming $\langle i \rangle = 57^\circ.3$, we obtain mass outflow rates between $15 M_{\odot} \text{ yr}^{-1}$ and $85 M_{\odot} \text{ yr}^{-1}$ (see last column of Table 3.4). At face value, such an outflow will take several hundreds of mega-years to deplete the DSFG’s gas reservoir of $\approx 10^{11} M_{\odot}$ ([Fraternali et al. 2021](#)), and hence it is unlikely to quench the observed SFR anytime soon. We stress, however, that [C II] conditions that differ from maximal excitation and solar abundance would drastically increase the inferred mass outflow rates.

Mass outflow rates in starburst-driven winds scale with the SFR, and typically share the same order of magnitude ([Veilleux et al. 2020](#)). When taken as lower limits, our fiducial mass outflow rates are roughly consistent with the DSFG’s SFR given its large uncertainties. We ask whether these values are consistent with AGN-driven outflows. Recalling that the X-ray luminosity of the DSFG is $L_{2-10\text{keV}} < 1.3 \times 10^{43} \text{ erg s}^{-1}$ ([Smolčić et al. 2015](#)),

we estimate a bolometric luminosity of $L_{\text{bol}} < 1.3 \times 10^{44} \text{ erg s}^{-1}$ assuming a bolometric correction of 10, appropriate for low-luminosity broad line AGN (Vasudevan & Fabian 2007). According to the AGN wind scaling relations presented by Fiore et al. (2017), our adopted L_{bol} upper limit allows for cold outflows with mass outflow rates of up to $100 \text{ M}_{\odot} \text{ yr}^{-1}$ and maximum velocities of $\approx 400 \text{ km s}^{-1}$. In contrast, ionized outflows yield mass outflow rates of $\lesssim 0.1 \text{ M}_{\odot} \text{ yr}^{-1}$. In summary, our mass outflow rates are consistent with the scaling relations for cold outflows in both starbursts and AGN.

The main caveat of the outflow interpretation is that it struggles to explain the kinematic structure of the [C II] plume. While the velocity increases as expected along the plume (although without reaching a terminal velocity), the puzzle lies in the velocity dispersion. Specifically, most spatially resolved observations of galactic-scale outflows find a high velocity dispersion ($\text{FWHM} \gtrsim 600 \text{ km s}^{-1}$) with a flat, if not increasing, radial profile (e.g. Venturi et al. 2018; Bao et al. 2019; McPherson et al. 2023). This is also true in idealized high-resolution simulations such as the one presented by Schneider et al. (2020), since outflows that start as laminar, low-turbulence flows can develop and maintain instabilities as they interact with the CGM, thus increasing the velocity dispersion. These examples contrast with our measurement of radially decreasing line widths (middle panel of left row in Fig. 3.5). Also, if the emission is optically thin, the dispersion must increase with radius because the volume of the cone slice probed by the beam gets bigger, and thus includes a larger range of projected kinematic components. In other words, the dispersion should increase due to beam smearing even if the turbulence remains low.

In conclusion, the outflow scenario is a natural explanation for the observed [C II] plume, as it fits some of the expected properties an outflow would have given the nature of the DSFG. Future observations will be essential to rule out or confirm this scenario. For example, upcoming JWST/NIRSpec IFU observations will tell if there is any broad $\text{H}\alpha$ emission—tracer of ionized gas and a better-established indicator of outflows—associated with the [C II] plume. In addition, deep rest-frame UV spectroscopy is needed to probe absorption by low-ionization metal species against the UV-bright regions of the system. Blueshifted lines will then unambiguously confirm the presence of cold outflows.

3.5.2 Gas accretion

We now consider a different possibility: the [C II] plume traces a filament of inflowing gas. In this scenario, a stream of C⁺-bearing gas falls into the galaxy from the CGM, and simultaneously cools down via [C II] line emission.

Cosmological simulations have long predicted that such streams can deliver gas to the center of massive halos at a high-*z* (e.g., Dekel et al. 2009, also see § 1.1.1). The main requisite for these gas flows to survive shock heating and reach the inner parts of the halo is that the cooling timescale needs to be shorter than the free fall time, hence the name “cold streams” (Dekel & Birnboim 2006). Simulations also predict cold streams to be narrow (widths of a few kpc; Mandelker et al. 2018; Padnos et al. 2018), and have very low metallicities, since they bring gas from the pristine intergalactic medium. Moreover, if the galaxy at the center of the halo is a rotating disk, it is expected that cold streams reach the ISM along its minor axis. If the accretion is corotating with the disk, the disk structure is reinforced, whereas in the opposite case the disk might be disrupted (e.g., Danovich et al. 2015). However, direct observational evidence of cold streams having all these features is yet to be found.

As pointed out in § 3.4.1, we observe that the [C II] plume meets the DSFG at the receding end of the rotation, although it overlaps with the opposite side in the intensity map. This would support the idea of prograde gas accretion (see upper right panel of Fig. 3.7). Regarding the velocities, cold streams flow in with a relatively uniform speed that is comparable to the virial velocity (Goerdt & Ceverino 2015). Following the estimation of Fraternali et al. (2021) for the J1000+0234 system, we assume a virial mass of $M_{\text{vir}} = 2 \times 10^{12} M_{\odot}$ and virial radius of $R_{\text{vir}} = 70 \text{ kpc}$, yielding a virial velocity of $V_{\text{vir}} = \sqrt{M_{\text{vir}} G / R_{\text{vir}}} \approx 350 \text{ km s}^{-1}$. Goerdt & Ceverino (2015) found that halos of similar mass at $z \sim 4$ accrete at $V_{\text{stream}} \approx 0.9 V_{\text{vir}}$, so for the DSFG we would expect $V_{\text{stream}} = 315 \text{ km s}^{-1}$ which is excellent agreement with our measured [C II] velocities at 5-10 kpc. Now, since these velocities are projected into the line of sight, the actual transversal speed could be much higher, depending on the inclination of the stream. Using again the average inclination for a random distribution of viewing angles, $\langle \sin i \rangle = 0.79$, we obtain

$v/\langle \sin i \rangle \approx 400 \text{ km s}^{-1}$. This implies that the gas is moving faster than expected for a cold inflow stream. We caution, however, that [Goerdt & Ceverino](#)’s simulations only track gas down to $0.2R_{\text{vir}}$, while the gas plume discussed here appears projected into smaller radii, from roughly zero to $0.2R_{\text{vir}}$, thus preventing a direct comparison.

If the gas retains or gradually loses angular momentum, it will follow a curved path as it falls. In that case, the observed velocity gradient can be due to a projection of a filament with relatively uniform gas inflow speed (see [Rose et al. 2024](#), for a similar argument applied to the Abell 2390 central plume). But we observe the plume being approximately straight, so either the curvature is parallel to the line-of-sight or the gas is truly following a straight path. The latter seems more likely since it does not require a special orientation. So, if we assume the gas is falling straight into the galaxy, the positive velocity gradient we observe implies the gas is slowing down. This is contrary to the expectation of a free fall, where the gas will accelerate toward the center of the potential, but it is a plausible hydrodynamic effect where the pressure in the immediate vicinity of the DSFG exerts a force against falling gas.

Since we detect the plume in [C II], the gas cannot be pristine but must have a significant mixture of processed material, even if the exact amount is not possible to constrain with the data in hand. While this is the strongest caveat of the cold stream interpretation, it can be explained in at least three ways: (1) enrichment occurs by mixing of the infalling gas with the metals already present in the CGM thanks to past outflow activity. (2) the gas is being enriched by star formation occurring in situ. And (3), the gas is recycled ISM from a “galactic fountain.”

Case (1) is a natural consequence of the mixing that occurs in the outer layers of cold streams, arising from Kelvin-Helmholtz instabilities (e. g., [Mandelker et al. 2016](#)). Yet is unclear how efficient this process can be.

Case (2) is supported by some cosmological simulations in which cold streams carry dwarf galaxies and star-forming clumps along them, and hence produce stars that pollute the surrounding gas (e.g., [Dekel et al. 2009](#); [Ceverino et al. 2010](#); [Fumagalli et al. 2011](#); [Mandelker et al. 2018](#)). This idea has been recently proposed to explain the 100 kpc filament of gas that feeds the massive radio-galaxy 4C 41.17, detected via its [C I] emission

(Emonts et al. 2023). To test this scenario we stacked the HST images from the four WFC3-IR filters available to search for associated UV sources (see § 3.4.3). We find two faint compact sources: one of them lies slightly outside the plume’s [C II] footprint to the north, while the other falls within the footprint at the eastern edge of aperture #4, but only at $S/N \approx 3$ (see Fig. 3.3). For this reason, we deem it a tentative detection and refrain from claiming a physical association with the plume. Otherwise, we do not detect UV emission in the HST images at a stacked 5σ depth of $26.2 \text{ mag arcsec}^{-2}$. This corresponds to an unobscured SFR density limit of roughly $2.7 \text{ M}_{\odot} \text{ yr}^{-1} \text{ kpc}^{-2}$, assuming the Kennicutt (1998) prescription scaled to the Chabrier (2003) IMF.

Finally, case (3) invokes the process of gas recycling, which is a well established phenomenon of galaxy evolution. Yet, in cosmological simulations, previously ejected gas typically rains down in the outer parts of the disk, rather than in a collimated stream onto the center (e.g., Anglés-Alcázar et al. 2017; Grand et al. 2019).

In summary, interpreting the [C II] plume as a cold accretion filament is qualitatively sound, although it requires some mechanism to slow down the gas as it falls, and a significant degree of metal enrichment. Theoretical predictions for the behavior of cold streams in the inner part of halos (below $0.2R_{\text{vir}}$) will enable stronger conclusions.

3.5.3 Ram pressure stripping

In this section we discuss a scenario where the [C II] plume is the stripped ISM of a satellite galaxy crossing the DSFG’s CGM (see lower left panel of Fig. 3.7). The interloping galaxy encounters a dense medium at high relative velocity, experiencing a drag force from the ram pressure acting on its ISM gas. If the drag force exceeds that of gravity, the gas becomes unbound. Known as ram pressure stripping (RPS; Gunn & Gott 1972) this process is one of the main ways disk galaxies quench their star formation in galaxy clusters, but it can also be an efficient quenching mechanism for dwarf satellites around groups or individual massive galaxies (Boselli et al. 2022). RPS in action is responsible for the existence of “jellyfish” galaxies, identifiable by their one-sided tails of stripped gas (e.g., Chung et al. 2009; Bekki 2009; Smith et al. 2010; Ebeling et al. 2014; Poggianti et al. 2017).

However, RPS needs special conditions to be effective. Since the drag force is proportional to the density and the square of the relative velocity (e.g., [Gunn & Gott 1972](#)), the medium has to be dense, volume-filling, and fast-moving. Galaxy clusters are thus the ideal environment for RPS, since they are filled with a hot dense plasma (the intracluster medium, ICM, e.g., [Sarazin 1986](#)), and their huge gravitational potential allows members to acquire large orbital velocities.

According to [Gunn & Gott \(1972\)](#), the requirement of ram pressure force being larger than the force holding the ISM of the satellite translates into the criterion for the ICM/CGM density ρ_{CGM} and relative velocity V ,

$$\rho_{\text{CGM}} V^2 > \frac{\Sigma_{\text{gas}} v_{\text{rot}}^2}{R_{\text{gal}}}, \quad (3.1)$$

where Σ_{gas} , v_{rot} , and R_{gal} are the gas surface density, rotational velocity, and effective radius of the satellite, respectively, assuming a thin stellar disk structure.

The main evidence supporting this scenario is that the innermost tip of the plume closely matches the position of the UV-bright spot in the DSFG. While this light could be escaping through an opening in the dusty ISM of the DSFG (as suggested by its redder UV slope, $\beta_{\text{UV}} \approx -1$; cf. Table 3.1), without a redshift measurement independent of [C II] we cannot rule out it belongs to a separate smaller galaxy currently orbiting the DSFG. In this interpretation, the UV-bright region plus the [C II] tail would represent the farthest example yet of a jellyfish galaxy.

We can now use Equation 3.1 to estimate the minimum density of the CGM of the DSFG for effective RPS. Using the inferred gas mass and aperture area of aperture #1 (Table 3.4), we adopt $\Sigma_{\text{gas}} = 1.6 \times 10^7 \text{ M}_{\odot} \text{ kpc}^{-2}$. Then, taking $v_{\text{rot}} = 100 \text{ km s}^{-1}$, $R_{\text{gal}} = 200 \text{ pc}$ and $V = 166 \text{ km s}^{-1}$, we obtain $n_{\text{CGM}} = \rho_{\text{CGM}}/m_H \gtrsim 1 \text{ cm}^{-3}$. This is three to four orders of magnitude denser than typical ICM densities, and is comparable to the densities of H II regions and the warm neutral medium in the Milky Way ([Draine 2011](#)). On one hand, these gas phases are normally clumpy in the Local Universe, so they would not fill enough volume to sustain effective RPS along 15 kpc. On the other hand, we know little about the structure of the high redshift CGM, so this concern may not apply. We note, for example,

that J23 reported extended He II and C IV emission around the DSFG, with ratios (relative to Ly α) that suggest strong ionization induced by AGN. The gas is then arguably warmer than $T = 10^4$ K, increasing the cross section for a strong RPS interaction in a fast-passing satellite.

The RPS scenario, however, is at odds with our observation of a decreasing linewidth as a function of distance along the plume. In the context of galaxy clusters, evidence suggests that stripped cold gas interacts with the hot ICM either heating it or inducing instabilities that build up turbulence with time. This effect is most clearly observed in ESO 137-001, a nearby edge-on jellyfish galaxy with a 40 kpc H α tail (Sun et al. 2007). MUSE observations resolve the trailing diffuse H α emission into three almost parallel tails, and all of them show a mild but significant increase in velocity dispersion in the direction away from the disk in the first 20 kpc (Luo et al. 2023; Li et al. 2023). Beyond that distance the dispersion remains more or less uniform. RPS in idealized numerical simulations generally reproduce this behavior, regardless of whether cooling (e.g., Roediger & Brüggen 2008; Tonnesen & Bryan 2010) and/or magnetic fields are included (e.g., Tonnesen & Stone 2014).

In conclusion, RPS requires special hydrodynamic conditions and is not well supported by our kinematic data. However, an independent redshift measurement of the putative satellite will be needed to fully rule out this scenario.

3.5.4 Gravitational interactions

Finally, we consider the scenario where the plume is formed as the result of a gravitational disturbance. We know that J1000+0234 is a complex multiple system (see Section 3.2), so we expect frequent interactions among its members. It is thus very plausible that a close encounter with the massive DSFG at the center of the group induced the formation of a tidal tail. This explanation is simpler than the RPS scenario, as it does not require special hydrodynamic conditions but only gravity.

Here we present a qualitative discussion of three different ways this interaction could have happened. First, we consider the case where CRISTAL-01a made a flyby close to the

DSFG. Second, we assume the progenitors already merged and the plume is the lasting debris of such encounter. And third, we consider the plume as a separate dwarf galaxy altogether, currently in the process of being stripped by the tidal forces exerted by the DSFG.

The idea that CRISTAL-01a and the DSFG are interacting was already suggested by several authors (e.g., [Capak et al. 2008](#); [Schinnerer et al. 2008](#); [GG18](#); [J23](#)), although it was mostly based on the short projected distance between the two objects. [J23](#) also took the UV and Ly α elongated morphologies of CRISTAL-01a as evidence of ongoing tidal effects. With reliable [C II]-based redshifts at hand, we now know CRISTAL-01a moves at a projected speed of 800 km s^{-1} relative to the DSFG, exceeding by a factor of 2.5 the escape velocity at a proper distance of 10 kpc (314 km s^{-1} ; assuming a point mass of $M_{\text{dyn}} = 2.3 \times 10^{11} M_{\odot}$ located in the center of the DSFG, [Fraternali et al. 2021](#)). This implies CRISTAL-01a is not gravitationally bound to the DSFG, indicating that if CRISTAL-01a actually interacted with the DSFG, it was in a high-speed flyby.

The main issue with this first tidal scenario is the mass ratio between CRISTAL-01a and the DSFG. Decades of work on numerical simulations of galaxy collisions have found that the largest and longest-lived tails are produced in “major” interactions (i.e., where the progenitor mass ratio is 1:3 or lower; see [Duc & Renaud 2013](#), for a review). In contrast, the stellar mass ratio here ($\sim 1 : 10$, [GG18](#)) belongs to the “minor” regime. Tidal features tend to be more prominent when the encounter occurs at low speeds, although it has been shown that high-speed flybys can also lead to the formation of gas-rich tails, provided the progenitors are both massive (cf. the case of the VIRGOHI21 cloud in the Virgo cluster; [Bekki et al. 2005](#); [Duc & Bournaud 2008](#)). In conclusion, even if CRISTAL-01a shows some evidence of ongoing interaction with the DSFG, its relatively low mass make it an unlikely candidate to be responsible for the [C II] plume.

Based on these considerations, we now discuss the second scenario, where two massive progenitors already merged into the DSFG, ejecting the [C II] plume as a tidal tail. The fact that the DSFG is rotation-supported does not necessarily rule out a merger origin, since simulations have shown that is possible for two massive galaxies to collide and result in a disk, provided they have high gas fractions (e.g., [Springel & Hernquist](#)

2005; Peschken et al. 2020). In fact, this type of merger is expected to trigger very intense starbursts, just as the one we see in the DSFG. We ask whether the merger had time to coalesce into a disk while still exhibiting a tidal tail. To answer this we need to estimate the dynamical age of the tail. To first order, we divide the length of the plume by the velocity difference between its two ends. In practice, we only consider apertures from #2 to #6, where the radial velocities are reliable. In this way we get $\tau_{\text{dyn}} = 13.15 \text{ kpc} / 112 \text{ km s}^{-1} = 115 \text{ Myr}$. On the other hand, the DSFG has a maximum rotation velocity of 550 km s^{-1} at a radius of 3.5 kpc (Fraternali et al. 2021), translating into a dynamical timescale of merely $\approx 40 \text{ Myr}$. Since the age of the plume is almost three times this value, we deem plausible that the tail persists after the merger has settled.

Tidal tails in the Local Universe usually come in pairs, as in the well-known examples of the Antennae Galaxies or the Mice (e.g., Toomre & Toomre 1972). In contrast, the DSFG only shows one. While some examples of one-sided tails in late-stage mergers exist (e.g., Mrk 273, Sanders et al. 1988), their formation involves highly inclined encounters (Howard et al. 1993). However, those configurations are not well suited for the survival of disks (e.g., Cox et al. 2006; Hopkins et al. 2013).

Finally, we consider the case of extreme tidal stripping of a satellite of the DSFG. In this picture, a dwarf galaxy orbiting the DSFG passes too close to the center, where tidal forces are strong enough to disrupt the intruder’s ISM into a long stream of gas. Depending on the central density of the intruder, it may not be totally disrupted, leaving its core relatively intact. If that is the case, the UV-bright region near the DSFG would be a natural candidate for the remnant, as it appears connected to the bottom of the plume. This idea could be tested with upcoming spectroscopy from JWST/NIRSpec.

Since gravity also acts on the stars, the three cases discussed here should produce a stellar stream associated with the plume, similar to those that populate the Milky Way halo (e.g. Malhan et al. 2018) or the surroundings of nearby massive galaxies (e.g., Martínez-Delgado et al. 2023). Here, as mentioned in § 3.5.2 we do not detect stellar emission from the plume in the HST images at a 5σ depth of $26.2 \text{ mag arcsec}^{-2}$, corresponding to an intrinsic SB of $18.8 \text{ mag arcsec}^{-2}$ after correcting for cosmological dimming. However, typical stellar streams in the Local Universe are much fainter, and only become

detectable at sensitivities of $\approx 28.5 \text{ mag arcsec}^{-2}$ or higher (e.g., [Bullock & Johnston 2005](#); [Martínez-Delgado et al. 2010](#)). In addition, our HST filters probe the rest-frame UV emission, and hence only trace young stars and not the bulk of the stellar mass. Upcoming JWST/NIRCam observations will be significantly deeper, and trace the rest-frame optical light. But even then, a detection would need the tail or stream to be remarkably bright.

We conclude that gravitational interactions are more than capable of creating extended gas structures such as the [C II] plume we observe, although the details are very uncertain. In fact, the three tidal scenarios presented here are only illustrative, and do not pretend to exhaust all the possible interactions that might produce a [C II] plume. A more systematic approach would involve a series of numerical experiments to constrain the parameters that best reproduce the observed morphology and kinematics, but that goes beyond the scope of this chapter.

3.6 Summary and conclusions

We have presented new ALMA Band 7 observations of the inner region of the J1000+0234 system at $z = 4.54$ located at the center of a bright $\text{Ly}\alpha$ blob. These observations are part of the ALMA-CRISTAL Large Program, targeting [C II] $158 \mu\text{m}$ emission and the underlying dust continuum in a sample of 25 star-forming galaxies at $4 < z < 6$. The high sensitivity and angular resolution of these data reveal the detailed structure of the star-forming galaxies in the J1000+0234 system. We report the discovery of a faint and diffuse [C II]-emitting plume extending up to $2''.4$ ($\approx 15 \text{ kpc}$) from the central massive DSFG (J1000+0234-North). Complemented with archival MUSE and HST data, we analyzed the spatial and spectral properties of the plume and the two main galaxies of the system. Our main findings can be summarized as follows:

1. The DSFG is detected in both [C II] and dust continuum, and it shows a compact disk-like morphology. On one hand, dust emission is fitted by a single 2D Sérsic profile with circularized effective radius of $R_{\text{eff}} \approx 0.74 \text{ kpc}$, Sérsic index $n \approx 1.29$ and axis ratio ≈ 0.4 . On the other hand, the [C II] emission is fitted by 2D Sérsic profile of $R_{\text{eff}} \approx 1.13 \text{ kpc}$, $n \approx 0.7$ and axis ratio ≈ 0.34 .

2. CRISTAL-01a sits at a projected distance of $1''.6$ from the DSFG, and recedes 800 km s^{-1} faster. It is detected in [C II] emission but not in dust continuum, and its [C II] morphology resembles that of the rest-frame UV emission. This means it is elongated and resolved into two clumps, although they are offset by $0''.3$ from the corresponding UV-bright clumps. We model the northeastern clump with a circular exponential profile of $R_{\text{eff}} \approx 0.8 \text{ kpc}$, and the southwestern clump with an elliptical exponential of $R_{\text{eff}} \approx 2.4 \text{ kpc}$ and axis ratio ≈ 0.82 .
3. The [C II] plume starts at the center of the DSFG and extends northward with a position angle that is offset by 40° clockwise from the DSFG's minor axis. The [C II] surface brightness declines rapidly along the plume, becoming undetected at $\approx 15 \text{ kpc}$ from the center of the DSFG. In the transverse direction we measure an average FWHM extent of $\approx 4 \text{ kpc}$.
4. The plume exhibits a clear velocity gradient, increasing the line central velocity as a function of radial distance from 180 km s^{-1} to 400 km s^{-1} , relative to the DSFG's systemic velocity. Moreover, the line FWHM also evolves with radius, showing a smooth drop from 450 km s^{-1} at the center of the DSFG to 190 km s^{-1} at the farthest measured point.
5. We detect no dust continuum at rest-frame $160 \mu\text{m}$ from the plume down to $5\sigma = 194 \mu\text{Jy}$ per $0''.9 \times 0''.4$ aperture. At an assumed dust temperature of $T_{\text{dust}} = 45 \text{ K}$, we obtain lower limits on the [C II]/FIR ratio between $\approx 0.2\%$ and $\approx 0.6\%$, consistent with UV photoelectric heating of the gas.
6. We estimate a minimum total mass for the plume of $(7.1 \pm 0.4) \times 10^8 M_\odot$, assuming a conversion factor $\kappa_{[\text{CII}]} = 1.5 M_\odot L_\odot^{-1}$ that corresponds to the limit of maximal excitation of the line in a medium dominated by atomic hydrogen, with solar-like carbon abundance.

We discuss four scenarios to explain the results outlined above: (1), the plume is a conical outflow. (2), the plume traces a filament of inflowing gas. (3), the plume is a

ram-pressure stripped tail of an infalling satellite. (4), the plume is tidal debris from past gravitational interactions.

In the first scenario (1), we infer resolved mass outflow rates between $16 M_{\odot} \text{ yr}^{-1}$ and $83 M_{\odot} \text{ yr}^{-1}$. The maximum outflow velocities across the plume range from 530 km s^{-1} to 620 km s^{-1} . These values are roughly consistent with literature scaling relations for SFR and L_{bol} in the case of starburst-driven and AGN-driven outflows, respectively. Given the very low ($\theta \approx 15^{\circ}$) opening angle we derive under the assumption of a simple conical geometry, plus the 40° misalignment with the DSFG’s minor axis, the putative outflow appears more likely to have originated in a central AGN. However, the observed kinematic radial trends are in mild tension with the expected properties of an outflow.

Scenario (2) is qualitatively consistent with theoretical expectations for cold accretion streams, except for our inference of a slow-down of the gas as it falls, although this can be accommodated by pressure gradients in the CGM. Moreover, the fact the putative stream emits in [C II] rules out a chemically pristine gas composition. Still, simulations suggest that gas enrichment can happen concurrently during the inflow, either by gas mixing in the CGM or by in situ star formation.

Scenario (3) requires the UV-bright region of the DSFG to be a satellite galaxy that is crossing the DSFG’s CGM. In addition, the CGM must be dense ($\gtrsim 1 \text{ cm}^{-3}$) in order to exert a significant ram pressure capable of stripping off the satellite’s ISM. Moreover, observations and simulations of ram pressure stripping predict an increase of velocity dispersion along the stripped tails, contrary to what we observe in J1000+0234.

Finally, scenario (4) is motivated by the fact J1000+0234 is an overdense environment and close interactions must be frequent. We explored three possible ways a gravitational interaction can lead to the formation of a one-sided tidal tail. Namely, a high-speed flyby of CRISTAL-01a, a late-stage major merger in which the [C II] plume is its remaining debris, and the tidal stripping of a minor satellite in a radial orbit. While a proper assessment of these configurations using tailored numerical simulations remains pending, heuristic arguments slightly disfavor the first two.

Besides scenario (3), which requires very special hydrodynamic conditions, outflows, inflows and tidal tails all have their pros and cons. Further observations and modeling

are needed to discriminate between them. Promisingly, upcoming JWST/NIRCam and JWST/NIRSpec observations will deliver a high angular resolution view of the rest-frame optical morphology and spectral properties. For example, narrow $H\alpha$ spectral imaging with NIRSpec IFU will constrain the star formation rate density in the [C II] plume. In addition, the detection of a broad $H\alpha$ component would support the outflow scenario. At the same time, NIRCam broad band observations will uncover the obscured regions of the DSFG and potentially discover a diffuse stellar stream associated with the [C II] plume, providing further evidence to the tidal tail scenario.

Our results highlight the power of ALMA for characterizing the cold CGM in emission at high redshift, but also the difficulty of their interpretation. Disentangling the physical mechanisms that produce a given [C II] observation is nevertheless very important for understanding how galaxies and their surroundings evolve.

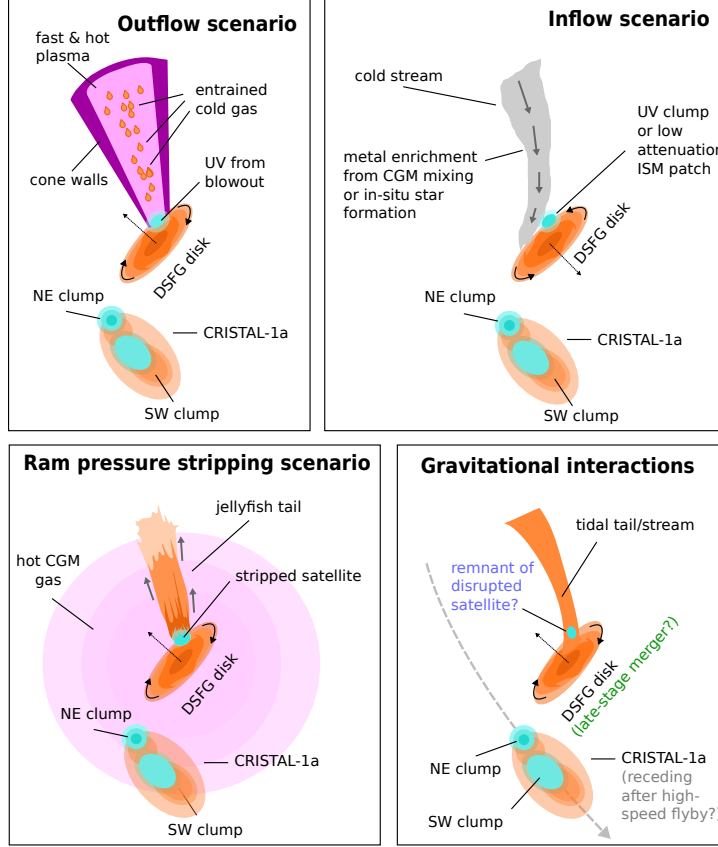


Figure 3.7: Cartoon representations of the four possible scenarios to explain the [C II] plume. In all panels the DSFG is depicted as an inclined rotating disk, with arrows showing the rotation. The spiral arms and the normal vector are only intended to show the orientation of the disk, although we cannot determine it from the data. *Upper left:* In the outflow scenario the extended [C II] emission arises from clumps of cold gas entrained within a large-scale, off-axis conical wind. Alternatively, [C II] could be tracing ionized gas in the cone walls. Here, the ISM at the launching site is blown out by the wind, allowing the escape of UV photons. *Upper right:* In the inflow scenario, a C^+ -bearing stream of gas falls from the north into the receding side of the disk. Here we depict the disk orientation inverted so that the inflow arrives in the near side of the disk. *Lower left:* In the ram pressure stripping scenario, the UV-bright clump in the DSFG is a satellite galaxy falling through a hot and dense halo around the system. Ram pressure stripping of the satellite’s ISM then produces the [C II] plume in the form of a “jellyfish” tail. *Lower right:* In the gravitational interactions scenario, the plume is a tidal tail from a past gravitational interaction between the DSFG and (possibly) CRISTAL-01a. This cartoon summarizes the three cases discussed in the main text: a high-speed flyby of CRISTAL-01a (gray), a late-stage major merger (green), and the tidal disruption of a minor satellite (purple). The dashed gray arrow qualitatively describes a possible orbit for CRISTAL-01a in the first case, that aligns with its morphological major axis.

Chapter 4

A hidden AGN revealed by JWST

The content of this chapter was published online on January 3rd 2025 as a research article in the *Astronomy & Astrophysics* journal, volume 693, number A70, under the title “*A hidden active galactic nucleus powering bright [O III] nebulae in a protocluster at $z = 4.5$ revealed by JWST*”, see [Solimano et al. \(2025\)](#). The article was coauthored by J. González-López, M. Aravena, B. Alcalde Pampliega, R.J. Assef, M. Béthermin, M. Boquien, S. Bovino, C.M. Casey, P. Cassata, E. da Cunha, R.L. Davies, I. De Looze, X. Ding, T. Díaz-Santos, A.L. Faisst, A. Ferrara, D.B. Fisher, N.M. Förster-Schreiber, S. Fujimoto, M. Ginolfi, C. Gruppioni, L. Guaita, N. Hathi, R. Herrera-Camus, E. Ibar, H. Inami, G.C. Jones, A.M. Koekemoer, L. Lee, J. Li, D. Liu, Z. Liu, J. Molina, P. Ogle, A.C. Posses, F. Pozzi, M. Relaño, D.A. Riechers, M. Romano, J. Spilker, N. Sulzenauer, K. Telikova, L. Vallini, K.G.C. Vasan, S. Veilleux, D. Vergani, V. Villanueva, W. Wang, L. Yan and G. Zamorani. Here I reproduce the full article with minor modifications intended to integrate seamlessly with the rest of the thesis. The main changes was the inclusion of the appendices as actual sections in the text.

4.1 Introduction

In the current paradigm of galaxy formation, the densest structures form in the most massive halos at high redshifts ($z > 2$), at the junctures of cosmic web filaments of galaxies and neutral gas. These structures are known as protoclusters, as they eventually evolve into massive galaxy clusters at $z < 1$ (e.g., [Baugh et al. 1998](#)). Protoclusters are sites where

active star formation, supermassive black hole (SMBH) accretion, and dynamical interactions trigger powerful feedback processes at large scales (Overzier 2016). The central regions of protoclusters can harbor dozens of galaxies within $\lesssim 100$ kpc (e.g., Oteo et al. 2018; Miller et al. 2018; Hill et al. 2020), with several of them hosting active galactic nuclei (AGN) and/or starbursts, leading to dramatic effects on the surrounding gas in the form of outflows, shocks, tidal debris, and ionized nebulae.

Protoclusters undergoing their most rapid phase of growth are commonly (though not always) signaled by a luminous quasar (QSO; e.g., Shen et al. 2007; Hennawi et al. 2015; Decarli et al. 2019), a high-redshift radio galaxy (HzRG; e.g., Venemans et al. 2007; Miley & De Breuck 2008; Wylezalek et al. 2013; Noirod et al. 2018), and/or one or more submillimeter-bright dusty star-forming galaxies (DSFGs; e.g., Riechers et al. 2014; Casey 2016; Hill et al. 2020; Wang et al. 2021). These sources are often embedded in giant H I Lyman- α (Ly α) nebulae, which in some cases reach scales of hundreds of kiloparsecs (e.g., McCarthy et al. 1987; Reuland et al. 2003; Borisova et al. 2016; Swinbank et al. 2015; Kikuta et al. 2019; Guaita et al. 2022; Apostolovski et al. 2024).

The gas in such environments is known to be multiphase, and hence the extended emission is not restricted to Ly α . Recent detections of extended CO, [C I] and [C II] emission imply the existence of cold gas reservoirs tracing widespread star formation and accretion (e.g., Emonts et al. 2018, 2023; Umehata et al. 2021). Similarly, He II-, C IV-, and [O III]-emitting ionized nebulae, are typically found to trace outflows and photoionization by AGN (e.g., Overzier et al. 2013; Cai et al. 2017). [O III] nebulae are particularly common around HzRGs, where kinetic feedback also plays a role, as suggested by their alignment with the radio jets (e.g., Nesvadba et al. 2017).

The James Webb Space Telescope (JWST) is becoming an important tool to understand ionized nebulae within protoclusters, since it has opened access to the diagnostic-rich rest-frame optical spectrum at $z > 3$. The Near-Infrared Spectrograph’s Integral Field Unit (NIRSpec IFU), in particular, has allowed the community to identify and characterize extended [O III] nebulae around quasars (e.g., Wylezalek et al. 2022; Perna et al. 2023; Decarli et al. 2024), HzRGs (e.g., Saxena et al. 2024; Roy et al. 2024; Wang et al. 2024), and DSFGs (e.g., Pérez-González et al. 2024) in protoclusters or dense groups at high z .

In this chapter, we present NIRSpec IFU observations of J1000+0234, a well-known $z = 4.54$ galaxy group in the COSMOS field (e.g., Capak et al. 2008; Smolčić et al. 2017a) hosting a massive DSFG ($M_* = 8.7 \times 10^{10} M_\odot$, Smolčić et al. 2015) and a luminous Lyman-break galaxy (LBG, $M_{UV} \approx -24.2$; Gómez-Guijarro et al. 2018) called CRISTAL-01a (hereafter C01) within the inner 20 kpc. This system resides in the center of a $z_{\text{phot}} \approx 4.5$ overdensity of LBGs at both small ($< 2'$) and large ($> 2'$) scales (Smolčić et al. 2017a; Jiménez-Andrade et al. 2023), and has been linked to the $z_{\text{spec}} = 4.57$ Taralay protocluster (also known as PCI J1001+0220, Lemaux et al. 2018; Staab et al. 2024). Furthermore, Jiménez-Andrade et al. (2023) observed J1000+0234 using the Multi Unit Spectroscopic Explorer (MUSE) mounted on the Very Large Telescope (VLT), and found a $L_{\text{Ly}\alpha} \approx 4 \times 10^{43} \text{ erg s}^{-1}$ Ly α blob (LAB) and a handful of lower-mass Ly α emitters distributed around the DSFG. Moreover, the authors confirm the results of Smolčić et al. (2017b) using the COSMOS2020 catalog (Weaver et al. 2022), and find an overdensity of $\delta_{\text{gal}} = 6 \pm 1$ within a comoving volume of 15 Mpc^3 .

Three puzzling observations make J1000+0234 an interesting case to study: first, the DSFG is detected at radio frequencies with $L_{1.4 \text{ GHz}} = (5.1 \pm 1.2) \times 10^{24} \text{ W Hz}^{-1}$ (Carilli et al. 2008; Capak et al. 2008; Jiménez-Andrade et al. 2023) that are possibly attributed to an AGN, yet have no X-ray counterpart. Secondly, the LAB is spatially and spectrally offset from the DSFG, but is coincident with the nearby LBG C01 (Jiménez-Andrade et al. 2023). Finally, Solimano et al. (2024, see Chapter 3) find a plume of [C II] 158 μm line emission of 15 kpc in length toward J1000+0234 using deep ALMA observations, indicating a dynamically complex system, although its physical origin remains unclear. The observations presented here reveal additional features that bring us closer to obtaining a full picture of the baryonic cycle around J1000+0234.

Throughout the chapter, we assume a flat cosmology described by $H_0 = 70 \text{ km s}^{-1} \text{ Mpc}^{-1}$, $\Omega_{m,0} = 0.3$, and $\Omega_{\Lambda,0} = 0.7$. At $z = 4.54$, the physical scale is $6.578 \text{ kpc arcsec}^{-1}$.

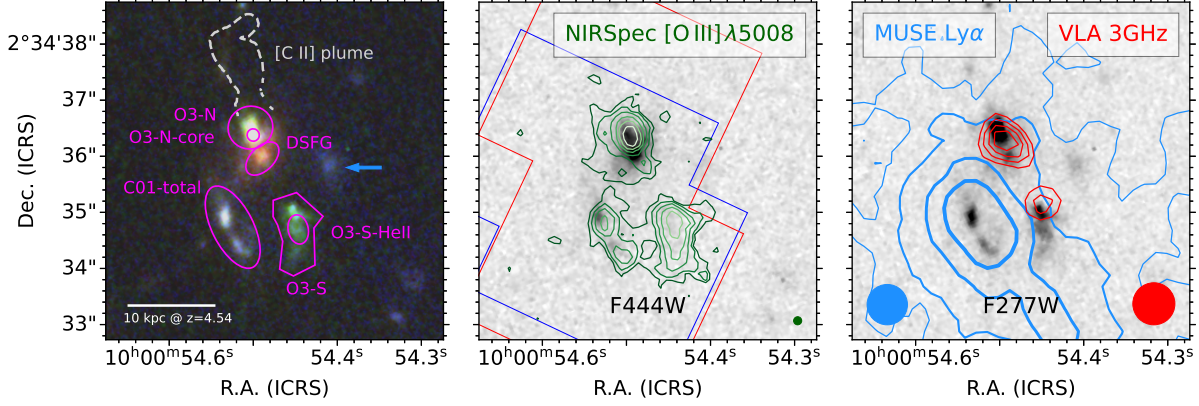


Figure 4.1: Multiwavelength view of the J1000+0234 system at $z = 4.54$. *Left panel:* Color composite image of the J1000+0234 system as seen by JWST/NIRCam. The filters F356W, F277W, and F200W are mapped to the red, green, and blue channels, respectively. The F277W filter captures the $H\beta + [O III]$ emission at $z = 4.54$. Magenta regions indicate the apertures used in this chapter. The gray dashed contour delineates the [C II] plume detected with ALMA (Solimano et al. 2024). The blue arrow points to a foreground galaxy at $z_{\text{spec}} = 1.41$ (Capak et al. 2008). *Middle panel:* NIRCcam F444W image with contours of the [O III] emission detected in the NIRSpec G235M observations. Contours start at $2\sigma = 3.3 \times 10^{-17} \text{ erg s}^{-1} \text{ cm}^{-2} \text{ arcsec}^{-2}$ and increase as integer powers of 2. The blue and red solid regions show the footprint of the observations obtained with G235M and G395H gratings, respectively. The green circle in the bottom right corner indicates the angular resolution element. *Right panel:* NIRCcam F277W image with $\pm 3, 4, 5$, and 6σ contours from Very Large Array (VLA) S-band continuum (red), and $\{1, 5, 16, 30\} \times 10^{-18} \text{ erg s}^{-1} \text{ cm}^{-2} \text{ arcsec}^{-2}$ contours of $\text{Ly}\alpha$ emission (blue) from VLT/MUSE (Jiménez-Andrade et al. 2023; Solimano et al. 2024). Blue and red circles indicate the angular resolutions of the MUSE and VLA datasets, respectively.

4.2 Observations and data reduction

4.2.1 JWST/NIRCam data

Multiband NIRCam imaging data of the J1000+0234 system comprise a total of six broad-band filters. Images using the F115W, F150W, F277W, and F444W filters were taken as part of the public Cosmos-Web survey (GO-1727, PI: Kartaltepe & Casey, Casey et al. 2023) using integration times of 515 s per filter at the position of J1000+0234, while the F200W and F356W bands were observed for 1074 s as part of GO-4265 (PI: González-López). At

the redshift of our source, the F277W and F356W filters cover the [O III]+H β and H α emission lines, respectively.

We reduced these data using the CRAB.Toolkit.JWST¹ wrapper of the JWST pipeline (version 1.10.0, pmap=1075) with highly optimized parameters. In addition, we followed Bagley et al. (2023) for $1/f$ noise mitigation, applied background subtraction via the sky-match method of the standard pipeline, removed wisp artifacts using published templates (Bagley et al. 2023), and finally aligned our images to the COSMOS2020 catalog (Weaver et al. 2022). The combined images are drizzled to a common grid with a pixel size of 0''02.

4.2.2 JWST/NIRSpec data

In this work, we used JWST/NIRSpec IFU data from programs GO-3045 (PI: Faisst) and GO-4265 (PI: González-Lopez) that target the J1000+0234 system with the G235M ($1.7\ \mu\text{m} < \lambda < 3.2\ \mu\text{m}$, $R \sim 1000$) and G395H ($2.9\ \mu\text{m} < \lambda < 5.3\ \mu\text{m}$, $R \sim 2700$) gratings, respectively.

The G235M dataset was taken using two 1080 s dithered exposures with overlap at the location of C01. The G395H dataset was set up as a two-tile mosaic covering both C01 and the [C II] plume reported by Solimano et al. (2024). Each tile was observed for 5974 seconds.

The data were reduced with the standard JWST pipeline (version 1.12.5, pmap=1234) plus some additional tweaks. Briefly, we followed the scripts provided by Rigby et al. (2025)² but implemented improved snowball removal in Stage 1, and additional bad pixel flagging after Stage 1. Also, we switched on the outlier-rejection step in Stage 3, and turned off the master background subtraction. Instead, background subtraction was performed as a post-processing step, together with stripe mitigation and astrometric alignment to NIRCcam. A more detailed description of the reduction is presented elsewhere (Fujimoto et al., in prep.).

¹<https://github.com/1054/Crab.Toolkit.JWST>

²Available at [10.5281/zenodo.10737011](https://zenodo.org/record/10737011)

4.3 Results and analysis

The NIRC*am* images reveal significant emission from several sources that were faint in previous Hubble Space Telescope (HST) imaging (Gómez-Guijarro et al. 2018; Solimano et al. 2024). For example, the DSFG starlight is now clearly detected in the long-wavelength filters. Interestingly, two other sources dominate the emission in the F277W and F356W filters (appearing green in Fig. 4.1), indicating the possibility of high-equivalent-width [O III], H β , and H α emission lines. The first of these sources is just 0".5 north of the DSFG, at the same location as an HST source (J1000+0234-North in Gómez-Guijarro et al. 2018, O3-N hereafter). The other is located south of the DSFG (hence O3-S), and has a projected extent of 1".3 = 8.55 kpc, and extremely faint HST magnitudes ($m_{F125W} \approx 26$ AB).

JWST/NIRSpec observations confirm the presence of strong [O III] emission at the locations of O3-N ($EW_0 = (1780 \pm 80) \text{ \AA}$) and O3-S ($EW_0 = (5100 \pm 1000) \text{ \AA}$)³ and, more importantly, at the same redshift as J1000+0234, therefore confirming their physical association (see the middle panel of Fig. 4.1). The nebulae also seem to be co-spatial with the 3 GHz radio detections, but they are offset from the Ly α peak surface brightness (SB; see the right panel of Fig. 4.1).

In the following subsections, we use apertures to extract and explore the spectroscopic properties of the two [O III] nebulae. The labeled apertures in Fig. 4.1 were manually defined based on the RGB NIRC*am* image and the [O III] map. For the DSFG we used an aperture significantly smaller than the full extent of the source to avoid contamination from O3-N. We also defined two sub-apertures within the [O III] nebulae that either enclose the peak of [O III] emission (O3-N-core) or maximize the signal-to-noise ratio (S/N) of the He II line (O3-S-HeII).

4.3.1 Morphology and kinematics

The middle panel in Fig. 4.1 shows the distribution of [O III] $\lambda 5008$ SB around J1000+0234. As expected, significant emission was detected in O3-N and O3-S, but also on C01 and the DSFG. Moreover, the global [O III] emission seems to be spatially extended and low SB

³The equivalent width values presented here consider only the 5008 Å line of the [O III] doublet.

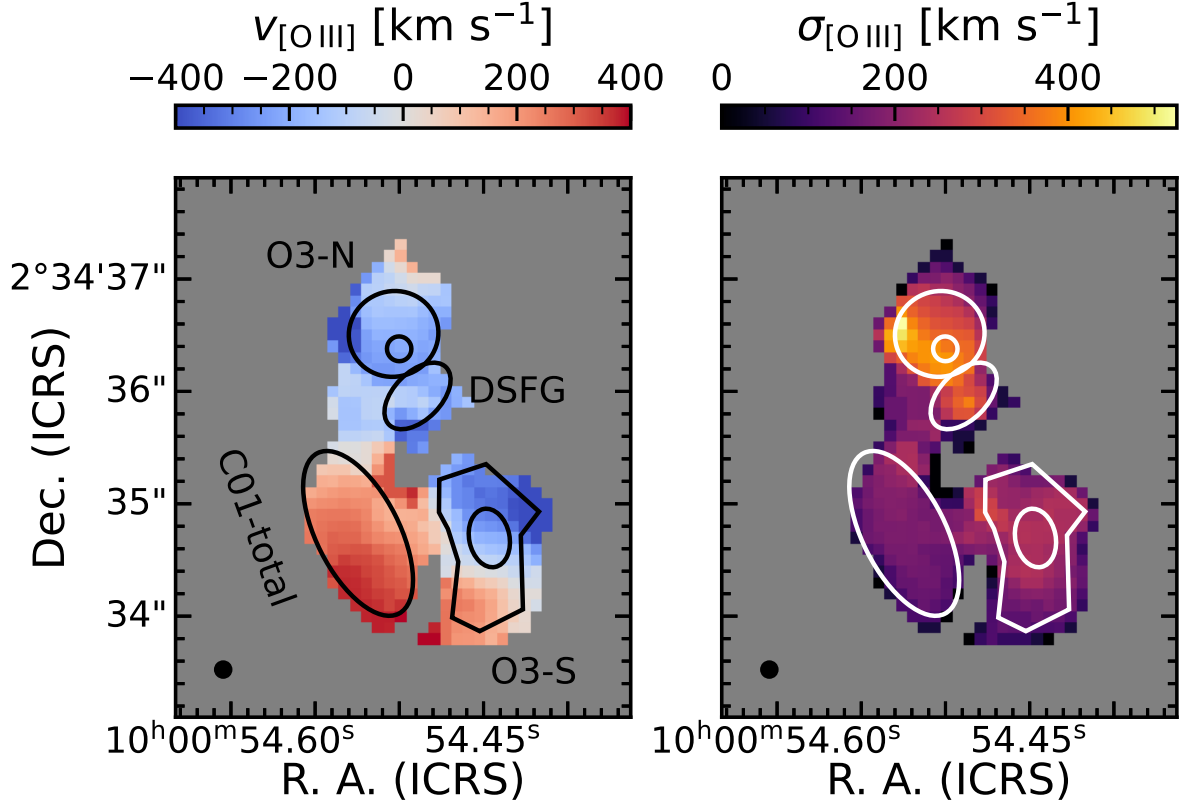


Figure 4.2: Resolved [O III] kinematics of J1000+0234. Velocity field (left) and velocity dispersion (right) maps. The reference velocity is defined at $z = 4.5471$.

emission connects nearly all of the objects in the scene.

Figure 4.2 features the velocity field and velocity dispersion maps of the [O III] emission line in the system. These maps were created following Solimano et al. (2024), with a spatial and spectral Gaussian convolution kernel applied to the continuum-subtracted cube. The spatial kernel has $\sigma = 1$ spaxel, whereas the spectral kernel has $\sigma = \sigma_{LSF}$ at the wavelength of the line. The moments were created by masking out all the voxels with $S/N < 3$ in the convolved cube. In the velocity field map we see the DSFG and O3-N share similar velocities, with an offset of $\approx 500 \text{ km s}^{-1}$ with respect to C01. In turn, O3-S shows a large velocity gradient north-to-south, with a velocity span of almost $\sim 800 \text{ km s}^{-1}$ from end to end. If we were to interpret this gradient as a signature of virialized rotation, a rough calculation would yield a dynamical mass on the order of $Rv^2/G = (4.3 \text{ kpc})(400 \text{ km s}^{-1})^2/G \approx 1.6 \times 10^{11} M_{\odot}$. This value is comparable to the dy-

namical mass of the DSFG (Fraternali et al. 2021), but since O3-S lacks significant stellar or dust emission, we deem unlikely that O3-S is a massive rotator. Instead, O3-S could be tidal debris from an ongoing interaction between the members of the system. In particular, the presence of a low-SB bridge between O3-S and C01, together with matching line-of-sight velocities in the southern end of both sources, already hints at a tidal origin. Further discussion of this scenario is presented in § 4.5.

Additionally, the velocity dispersion map of the [O III] emission shows a fairly uniform structure at 200 km s^{-1} in most of the system except for O3-N. The velocity dispersion in O3-N reaches 500 km s^{-1} , indicating a higher dynamical mass, increased turbulence, or additional kinematic components.

4.3.2 Broad velocity component in O3-N

Inspection of the [O III] and $H\alpha$ line profiles in the O3-N aperture reveal the presence of broad velocity wings. In the case of [O III], we model both lines in the doublet simultaneously but tie their wavelengths and amplitudes to the expected ratios (e.g., [O III] $\lambda 5008$ /[O III] $\lambda 4960 = 2.98$, Storey & Zeippen 2000). For $H\alpha$, we also fit the N II doublet with the [N II] $\lambda 6585$ /[N II] $\lambda 6550$ ratio fixed to 2.8.

We set up the models within the probabilistic programming framework PyAutoFit (version 2024.1.27.4, Nightingale et al. 2021), and use the DYNESTY (Speagle 2020; Koposov et al. 2022) backend to sample the posterior probability distribution and estimate the Bayesian evidence log (Z). The width of the line spread function (LSF) is taken from the dispersion curves available in the JWST documentation⁴.

The results of our fits are shown in Fig. 4.3. The double Gaussian model is preferred over the single one based on its higher Bayesian evidence score, and lower Akaike Information Criterion (AIC; e.g., Cavanaugh 1997) and Bayesian Information Criterion (BIC; e.g., Schwarz 1978) scores.

The [O III] broad component of O3-N displays a full width at half maximum (FWHM) of $1266^{+36}_{-47} \text{ km s}^{-1}$, and is blueshifted by $(158 \pm 24) \text{ km s}^{-1}$ from the central velocity of the

⁴NIRSpec Dispersers and Filters

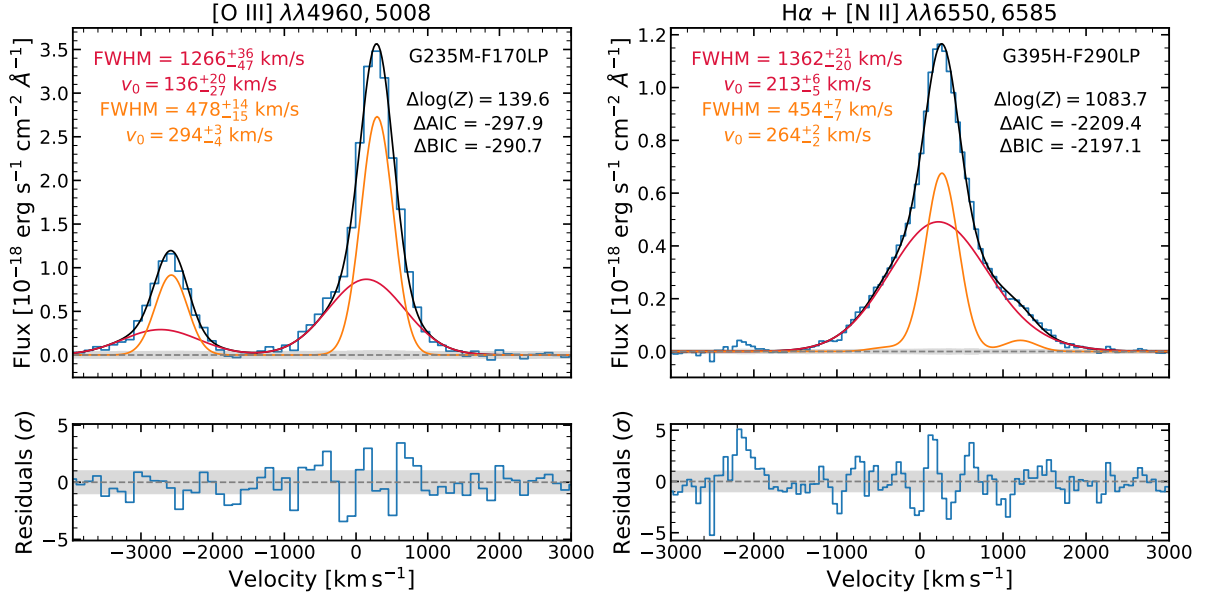


Figure 4.3: Evidence of a broad velocity component in the strongest emission lines from O3-N, namely [O III] $\lambda\lambda 4960, 5008$ (left) and H α + [N II] $\lambda\lambda 6550, 6585$ (right). In both lines, a double Gaussian profile is preferred over a single Gaussian fit (not shown), based on the former having a larger $\log(Z)$, and lower AIC and BIC scores (see upper right legends). The bottom panels show the residuals of the subtraction of the best-fit model from the data, in units of σ .

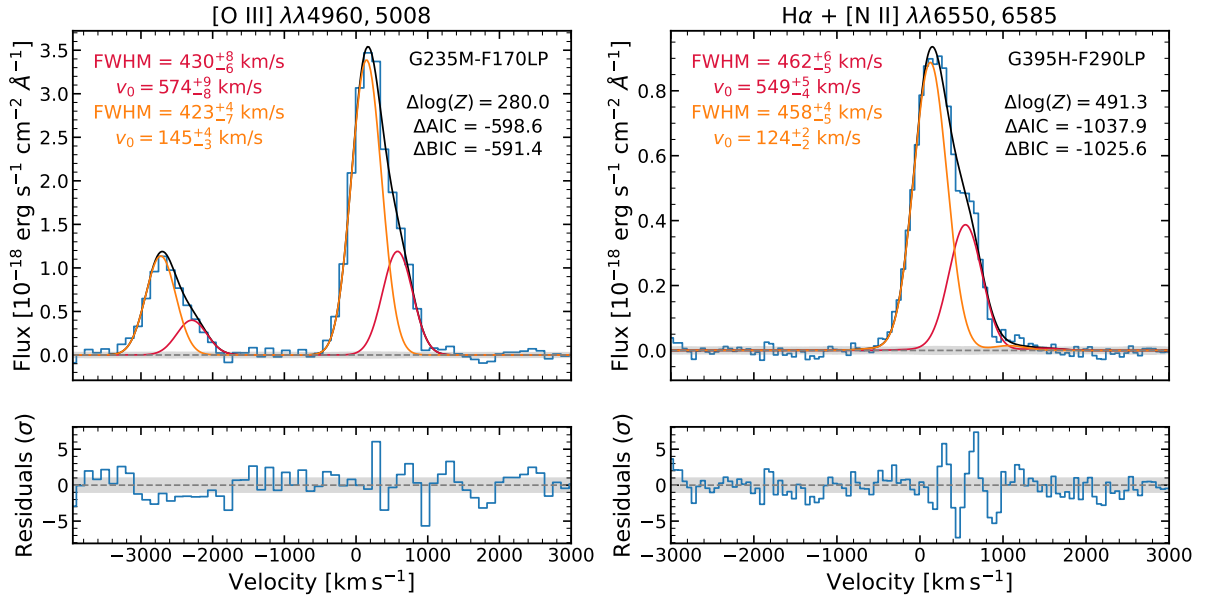


Figure 4.4: Same as Fig. 4.3 but for O3-S. Here, both components have similar line width, in contrast with the expectations for an outflow.

narrow component. Such a profile of the [O III] line (broad and blueshifted) typically points to the existence of strong ionized outflows projected onto the line of sight. H α shows an even broader but less blueshifted profile.

Notably, since O3-N sits at the base of the [C II] plume (see left panel of Fig. 4.1) and has a broad [O III] component at the same velocity ($v_0 \approx 150 \text{ km s}^{-1}$) as the corresponding [C II] 158 μm line, the outflow scenario proposed by Solimano et al. (2024) emerges as a natural explanation. A detailed assessment of this possibility will be presented in a forthcoming paper.

The spectrum of O3-S (Fig. 4.4) also shows a secondary velocity component, but this likely arises from the large velocity gradient (cf. Fig. 4.2) contained within the aperture, or by the superposition of two nebulae separated by roughly 400 km s^{-1} . An outflow origin for O3-S seems less plausible because the two components have the same velocity width.

4.4 Line fitting with pPXF

We use the template-fitting software pPXF (version 9.2.1; Cappellari 2017, 2023) to simultaneously model the continuum and the emission lines of our aperture-extracted spectra in the full wavelength range covered by a single grating. We start with the G395H grating since it provides better spectral resolution than G235M. For each spectrum, we perform fits with one and two velocity components for the emission lines, but a single component for the stars, which is tied to the narrow gas component. We include the following lines in the fit: He I $\lambda 5877$, [O I] $\lambda\lambda 6303, 6365$, [N II] $\lambda\lambda 6550, 6585$, H I $\lambda 6565$ (H α), [S II] $\lambda\lambda 6718, 6732$, He I $\lambda 7065$, [Ar III] $\lambda 7138$, and [S III] $\lambda 9071$, where the [O I] and [N II] doublet ratios have been fixed to their theoretical values. The continuum is fitted against a grid of Stellar Population Synthesis (SPS) spectra computed with `fsps` v3.2 (Conroy et al. 2009; Conroy & Gunn 2010), but restricted to ages younger than the age of the Universe at $z = 4.54$. In most cases, the continuum has $S/N \lesssim 1$ per resolution element and no stellar absorption features can be identified, hence we refrain from interpreting any of the SPS output parameters. We find, nevertheless, that these templates provide a good representation of the continuum slope, and naturally incorporate the stellar absorption

correction for the Balmer emission lines, even though this correction always stays below 1%.

We then compute the AIC and BIC scores of both single and double component fits, and require the score difference to be larger than five to keep the double component fit as the preferred model. This criterion is only met for O3-N and O3-N-core.

Next, we model the G235M spectrum using the velocity and velocity dispersion best fit values from the G395H fit as starting values. Here, we fit the continuum with the same libraries as above, and include the following list of emission lines: [Ne v] $\lambda 3427$, [O II] $\lambda\lambda 3727, 3730$, [Ne III] $\lambda 3870$, [Ne III] $\lambda 3969$, [O III] $\lambda 4364$, He II $\lambda 4687$, [O III] $\lambda\lambda 4960, 5008$, and the Balmer series from H I $\lambda 3799$ (H10) to H I $\lambda 4863$ (H β). The relative intensities of the [O III] doublet are fixed to their theoretical ratio.

Throughout the chapter, we use the line fluxes and uncertainties measured by pPXF to compute line ratios. The values are presented in [Table 4.1](#) and represent model fluxes from the single Gaussian component fits, except for O3-N and O3-N-core, where we use the sum of the narrow and broad components. This is because in most lines of the broad component have too low a S/N to provide a meaningful ratio on their own. We also quote fluxes and ratios without correction by reddening unless otherwise noted.

4.4.1 Line ratio diagnostics and high-ionization species

We measured all line fluxes and errors using pPXF ([Cappellari 2017, 2023](#)) as detailed in [§ 4.4](#). From these, we computed the five line ratios presented in [Fig. 4.5](#). The bottom panels of [Fig. 4.5](#) show three diagrams displaying the $R3=[\text{O III}] \lambda 5008/\text{H}\beta$ ratio against three different line ratios, namely $N2=[\text{N II}] \lambda 6583/\text{H}\alpha$ ([Baldwin, Phillips & Terlevich 1981](#), the “BPT” diagram), $S2=[\text{S II}] \lambda\lambda 6716, 6731/\text{H}\alpha$, and $O1=[\text{O I}] \lambda 6302/\text{H}\alpha$ (also known as the [Veilleux & Osterbrock 1987](#), or VO87 diagrams). In each of them we plotted the theoretical boundary between star-formation (SF) and AGN photoionization models from [Kewley et al. \(2001\)](#) and [Kewley et al. \(2006\)](#). In the BPT diagram we also plotted the boundary between AGN and low-ionization nuclear emission regions (LINERs; [Schawinski et al. 2007](#)). Recent JWST observations have found that these classical boundary lines are not reliable

Table 4.1: Line fluxes for the different apertures used in this paper.

Aperture	O3-N	O3-N-core	O3-S	O3-S-Hell	C01-total	C01-NE	C01-SW	DSFG
R. A. (deg)	150.227 098	150.227 084	150.226 878	150.226 861	150.227 185	150.227 227	150.227 145	150.227 038
Dec. (deg)	2.576 809	2.576 772	2.576 298	2.576 304	2.576 316	2.576 378	2.576 221	2.576 655
[O III] redshift	4.5433(1)	4.5418(1)	4.5448(3)	4.5516(1)	4.5527(2)	4.5521(1)	4.5414(1)	4.5445(1)
[Ne V] λ 3427	< 15.4	2.3 ± 0.3	6 ± 2	< 2.2	< 3.7	< 2.3	< 1.5	< 2.7
[O II] λ 3727, 30	35 ± 2^a	6 ± 2	35 ± 9	13 ± 3	30 ± 6	11.3 ± 1.4^a	13 ± 2	7.0 ± 0.7^a
[Ne III] λ 3870	19 ± 3.4	4.6 ± 0.2	15.9 ± 1.2	5.1 ± 0.5	6.7 ± 1.0	< 2.0	3.3 ± 0.4	2.4 ± 0.6
Hy λ 4342	13 ± 3	2.6 ± 0.2	8 ± 1	3.7 ± 0.4	4.9 ± 0.9	2.2 ± 0.5	2.0 ± 0.3	1.9 ± 0.5
[O III] λ 4364	< 8.5	1.0 ± 0.2	< 3.1	1.3 ± 0.4	< 2.6	< 1.7	< 1.0	< 1.6
He II λ 4687	< 8.4	0.6 ± 0.2	5 ± 1	2.4 ± 0.5	< 2.5	< 1.7	< 0.9	1.9 ± 0.5
H β λ 4863	25 ± 3	6.0 ± 0.2	25 ± 1	8.5 ± 0.5	12.0 ± 0.9	4.6 ± 0.6	5.2 ± 0.3	3.5 ± 0.5
[O III] λ 5008	251 ± 4	60.0 ± 0.5	223 ± 2	87.4 ± 0.9	79 ± 1	29.0 ± 0.8	35.1 ± 0.5	31.8 ± 0.6
[O I] λ 6302, 66	6.4 ± 0.6	1.22 ± 0.05	4.2 ± 0.4	0.97 ± 0.09	< 0.6	< 0.3	0.76 ± 0.09	1.3 ± 0.1
H α λ 6565	122.5 ± 0.8	26.9 ± 0.1	78.5 ± 0.4	23.0 ± 0.1	45.1 ± 0.2	18.2 ± 0.1	18.4 ± 0.1	17.4 ± 0.1
[N II] λ 6550, 85	15.0 ± 0.8	5.0 ± 0.1	2.4 ± 0.4	0.9 ± 0.1	4.6 ± 0.2	2.2 ± 0.1	0.78 ± 0.09	20.9 ± 0.2
[S II] λ 6718, 33	14 ± 3	2.3 ± 0.3	11 ± 1	2.5 ± 0.3	5.9 ± 0.7	1.8 ± 0.3	2.4 ± 0.2	5.2 ± 0.6

All fluxes are given in units of $10^{-18} \text{ ergs}^{-1} \text{ cm}^{-2}$ and are not corrected for dust reddening. Upper limits are quoted at the 3σ level.

^a Measured in standalone single-component fit to avoid unrealistically large uncertainty.

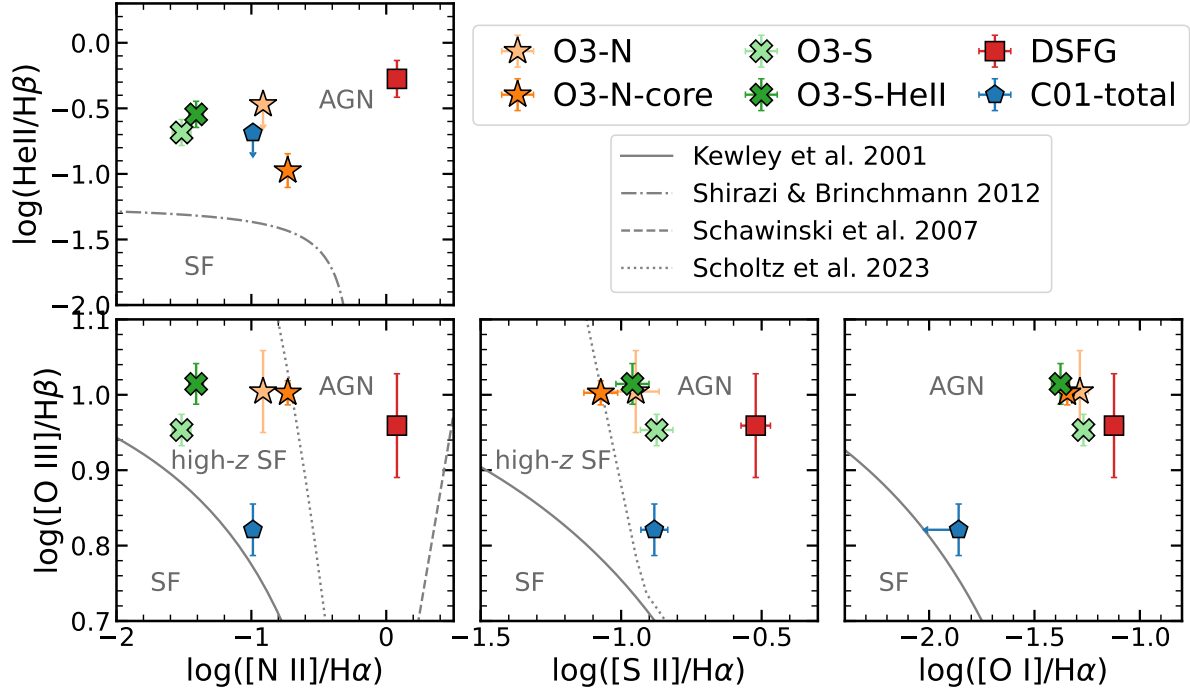


Figure 4.5: Diagnostic line ratio diagrams for the relevant regions of the J1000+0234 system. *Bottom left:* Standard BPT R3 vs N2 diagram. The solid curved lines represent the maximum starburst line of Kewley et al. (2001), while the straight dashed line on the lower right-hand side divides AGN from LINERs according to Schawinski et al. (2007). The dotted line is the separation from SF and AGN adapted for high- z galaxies by Scholtz et al. (2023). *Bottom center:* R3 vs S2 VO87 diagram. Again, the solid line is from Kewley et al. (2001) and the dotted line is the high- z SF/AGN separation from Scholtz et al. (2023). *Bottom right:* R3 vs O1 VO87 diagram. The solid line separates SF from AGN according to Kewley et al. (2001). *Top left:* He2 vs N2 diagram. The division line between AGN and SF is taken from Shirazi & Brinchmann (2012).

at the low metallicities and high-ionization conditions typically found at high redshifts, which make SFGs and AGN overlap in these diagrams (e.g., Harikane et al. 2023; Maiolino et al. 2024; Scholtz et al. 2023). Hence, we also plotted the more conservative boundary line proposed by Scholtz et al. (2023) to account for this issue. In addition, we show in Fig. 4.5 the He2-N2 diagram (Shirazi & Brinchmann 2012), featuring $\text{He2} = \text{He II } \lambda 4686 / \text{H}\beta$ vs N2. This diagnostic diagram has been cited as a more robust way to select AGN than the classical BPT and VO87 diagrams (e.g., Scholtz et al. 2023), although the $\text{He II } \lambda 4686$ is often too faint to be detected.

Despite these caveats, we see in Fig. 4.5 that only C01 appears to be consistent with pure SF, while the rest can be explained at least partially by AGN excitation. On the other hand, the DSFG is the only source showing AGN-like ratios in all diagrams.

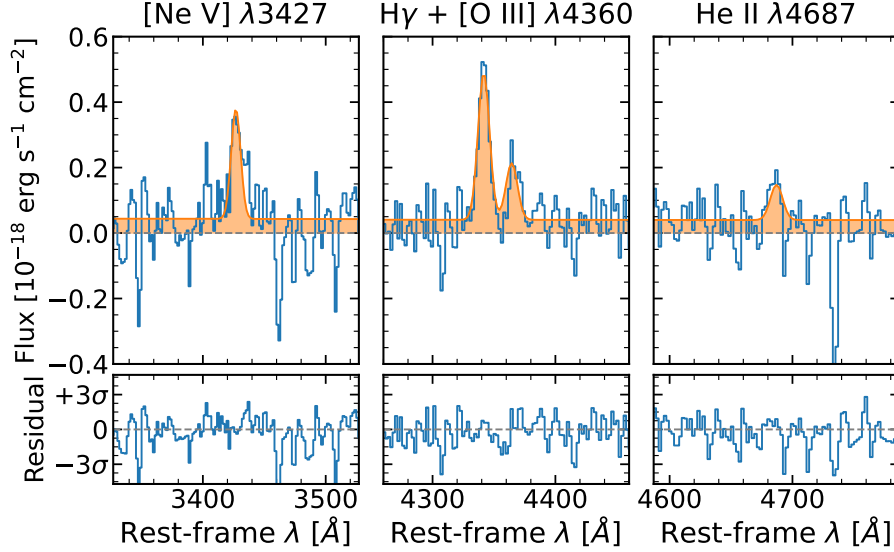


Figure 4.6: Zoom-in to high-ionization lines detected in O3-N-core. The orange filled curve denotes the pPXF best fit stellar plus gaseous template.

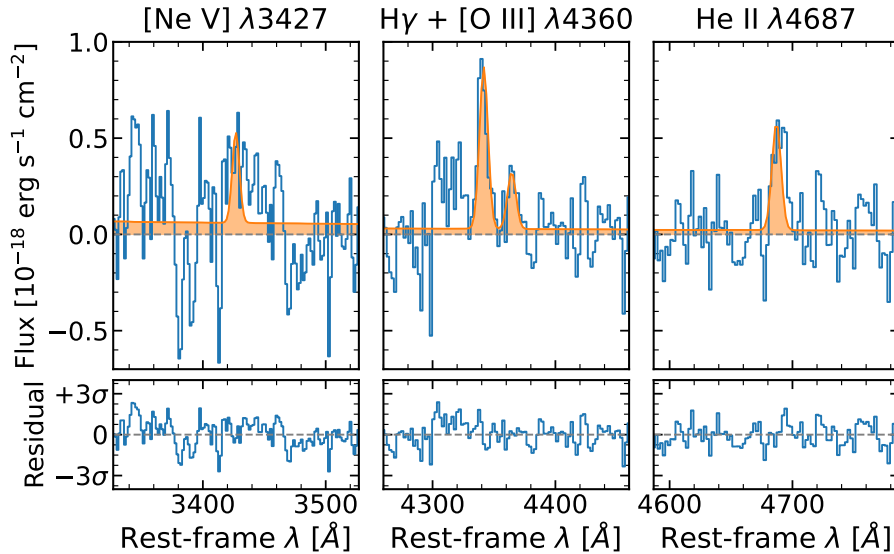


Figure 4.7: Same as Fig. 4.6 but for O3-S-HeII. Here, the detection of the [Ne v] line is only tentative.

The possible presence of an AGN has already been proposed by Jiménez-Andrade et al.

(2023) based on the radio detection, and the $\text{He II } \lambda 1640/\text{Ly}\alpha$ and $\text{C IV } \lambda 1551/\text{Ly}\alpha$ ratios. Additional support to this idea comes from the detection of the $[\text{Ne v}] \lambda 3427$ line toward O3-N-core (see Fig. 4.6), since $[\text{Ne v}]$ requires photons with $E > 97.11$ eV. Such high energies are most easily attainable with AGN activity, either in the form of photoionization or fast shocks (e.g., Gilli et al. 2010; Mignoli et al. 2013; Leung et al. 2021; Cleri et al. 2023).

In O3-S and O3-S-HeII, at the other side of the DSFG, we did not detect $[\text{Ne v}] \lambda 3427$, but only $\text{He II } \lambda 4686$ (see Fig. 4.7). Due to the lower ionization energy of helium ($E > 54.42$ eV), this line is not as clean an indicator of AGN as the $[\text{Ne v}]$ line, and can indeed be excited by X-ray binaries (e.g., Schaerer et al. 2019), Wolf-Rayet stars (e.g., Shirazi & Brinchmann 2012), and shocks (Izotov et al. 2012), among others. Nevertheless, its location on the He2-N2 diagram is well above the SF boundary line.

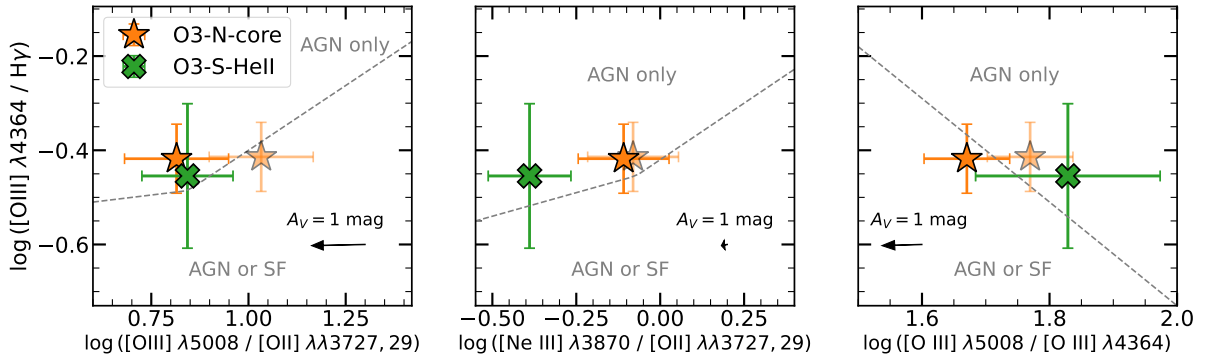


Figure 4.8: Diagnostic line-ratio diagrams based on $[\text{O III}] \lambda 4364$ emission. In all three panels the dashed line is the empirical demarcation between pure AGN and AGN/SF mixtures proposed by Mazzolari et al. (2024). The faded markers with error bars are determined from our pPXF fits to the spectra without reddening correction. The bold markers show the values after reddening correction, with $A_V = 1.58 \pm 0.16$ mag for O3-N-core and $A_V = 0$ for O3-S-HeII. The black arrows denote the dereddening vector for an attenuation of $A_V = 1$ mag with the Calzetti et al. (2000) attenuation law.

Finally, we also detected the temperature-sensitive $[\text{O III}] \lambda 4364$ auroral line toward O3-N-core and O3-S-HeII (see Fig. 4.6 and Fig. 4.7). A high ratio between $[\text{O III}] \lambda 4364$ and the $\text{H}\gamma$ line was recently proposed as an alternative indicator of AGN photoionization (e.g., Übler et al. 2024). In Fig. 4.8, we plot the position of O3-N-core and O3-S-HeII in the three diagnostic diagrams developed by Mazzolari et al. (2024) based on $[\text{O III}] \lambda 4364$ emission. We applied a reddening correction of $A_V = 1.58 \pm 0.16$ mag to O3-N-core based

on its Balmer decrement (see § 4.5.2), while O3-S-HeII is consistent with zero dust. Our points nominally fall in the AGN-only region in two out of three diagrams, but they cross the boundary lines within the uncertainties. Therefore, we are unable to make any firm conclusions regarding the AGN nature of O3-N-core and O3-S-HeII based on the Mazzolari et al. (2024) diagrams.

4.4.2 Oxygen abundance

We measured gas-phase oxygen abundances in the spectra of the different apertures using the indirect indicator proposed by Dopita et al. (2016). This indicator is calibrated as

$$12 + \log(\text{O}/\text{H}) = 8.77 + \log(\text{NII}/\text{SII}) + 0.264 \log(\text{NII}/\text{H}\alpha). \quad (4.1)$$

We chose this indicator because it uses lines from a single grating/filter combination (G395H), thus avoiding possible systematic effects from the combination of the two datasets, and also because it is fairly robust to dust attenuation effects (which are significant at least in the case of the DSFG). The main caveat is that it relies on the assumption of a specific relation between N/O and O/H abundances.

Figure 4.9 shows the values obtained for all the apertures considered in this chapter, including dedicated apertures for the two clumps C01-SW and C01-NE. As expected, the DSFG shows the highest (even supersolar) oxygen abundance. The rest of the apertures are distributed throughout the abundance scale, with O3-S showing the lowest abundance. We also report a large difference (~ 0.8 dex) between C01-SW and C01-NE, with the latter dominating the integrated value (C01-total).

4.5 Discussion

We found in the previous section that the two strongest [O III] nebulae in the system are likely related to AGN activity. In the following subsections, we explore the possibility of radiative shocks, provide an estimate of AGN luminosity and obscuring column density given the current constraints, and then discuss the physical scenario for the origin of the

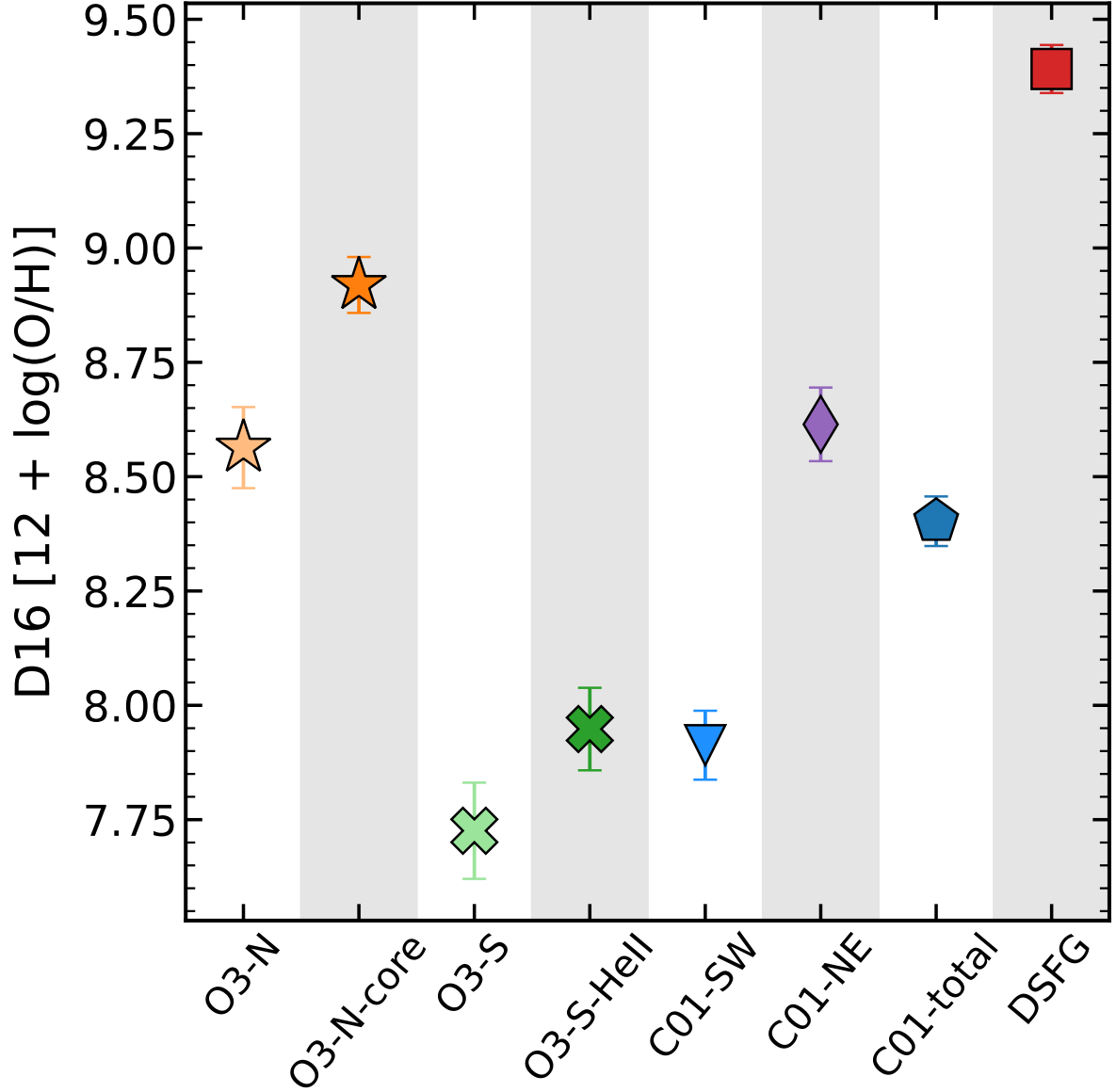


Figure 4.9: Oxygen abundances of the sources in the J1000+0234 system according to the [Dopita et al. \(2016\)](#) calibration. Markers are the same as in [Fig. 4.5](#), except we also show C01-NE and C01-SW.

[O III] nebulae.

4.5.1 No evidence of shocks

The detection of radio emission at the positions of O3-N and O3-S suggests the presence of shocks produced by a radio jet. This might explain, for example, the enhanced velocity dispersion observed even in the “narrow” component of the emission lines ($\sigma \gtrsim 100 \text{ km s}^{-1}$). However, the observed line ratios (see Fig. 4.5) do not resemble those expected in fast radiative shocks, in contrast to those observed in the “Ulema” galaxy, a low-mass radio-detected AGN at $z = 4.6$ (D’Eugenio et al. 2025). In particular, shock models assuming solar abundances predict N2, S2 and O1 ratios that are typically above -0.5 dex, -0.5 dex, and -1.2 dex, respectively (e.g., Allen et al. 2008; Alarie & Morisset 2019). At lower metallicities, these ratios can approach the values we observe in our data, but the R3 ratio decreases as well.

These results indicate that shocks play a negligible role in the ionization of the O3-N and O3-S nebulae. To further test this idea, we explored the relationship between the shock-sensitive N2 ratio and the line width. In shocked gas, a positive correlation has been found between N2 and velocity dispersion (e.g., Rich et al. 2011; Ho et al. 2014; Rich et al. 2015), indicating a coupling between the gas ionization and kinematics, which is not predicted in pure photoionization models (Kewley et al. 2019).

We thus took advantage of JWST NIRSpec IFU’s spatial resolution to measure the resolved N2 ratio within O3-N and O3-S. We extracted spectra from the 30 and 39 spaxels contained in O3-N and O3-S apertures (see Fig. 4.1), respectively. We then fitted each spectrum with single and double Gaussians using the method described in § 4.3.2. Finally, we removed all fits where the posterior error on $\log([\text{N II}] \lambda 6585/\text{H}\alpha)$ is larger than 0.3 dex.

Obtained values of N2 and velocity dispersion (σ) where the best fit is a single Gaussian component are shown with green markers in Fig. 4.10, while the results where a double component is preferred are shown in orange and blue markers for the narrow and broad components, respectively.

We computed the Spearman’s rank correlation coefficient independently for each set

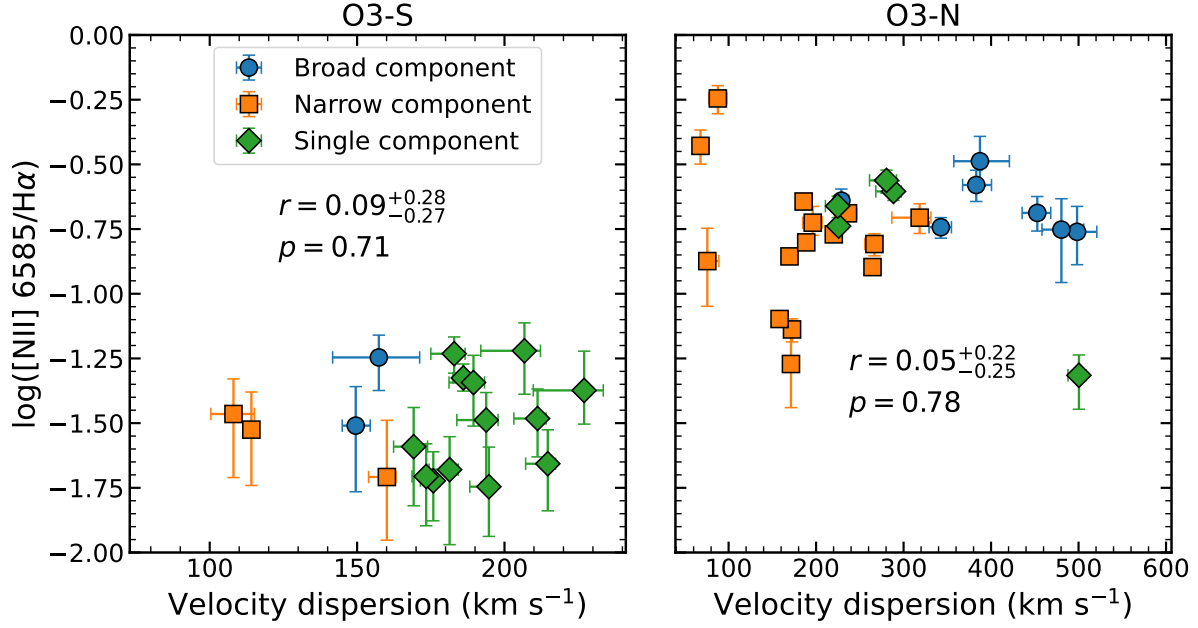


Figure 4.10: Resolved N2 ratio as a function of line velocity dispersion in O3-S (left) and O3-N (right). The inset text displays the Spearman’s rank correlation coefficient r and its corresponding p -value. No significant correlation is present in either panel.

of spaxels, and estimated the uncertainties from 600 bootstrap samples. We find no significant correlation between the line ratio and the velocity dispersion in either O3-N ($r = 0.05^{+0.22}_{-0.25}$, $p = 0.78$) or O3-S ($r = 0.09^{+0.28}_{-0.27}$, $p = 0.71$). Instead, the N2 ratio remains relatively uniform across the dispersion axis, with a median value of -0.74 dex in O3-N and -1.5 dex in O3-S. The different median ratio between the two nebulae could be explained by different metallicities (see § 4.4.2).

4.5.2 Constraints on AGN luminosity and obscuration

As pointed out by several authors (e.g., Capak et al. 2008; Smolčić et al. 2015; Jiménez-Andrade et al. 2023), J1000+0234 was undetected in *Chandra*’s 80 ks observations in the 0.5 keV to 2 keV band (Elvis et al. 2009), leading to a flux upper limit of $3 \times 10^{-16} \text{ erg s}^{-1} \text{ cm}^{-2}$ (Capak et al. 2008). Assuming a Galactic foreground column density of $N_H = 2.6 \times 10^{20} \text{ cm}^{-2}$ and a power-law source with a photon index of $\Gamma = 1.4$, this upper limit translates to a rest-frame hard X-ray luminosity of $L_{2-10\text{keV}} < 6.8 \times 10^{43} \text{ erg s}^{-1}$ (Solimano et al. 2024).

We then tried to determine whether such an AGN can explain the observed narrow-

line luminosities. To address this question, we used the scaling relations of [Berney et al. \(2015\)](#) based on a sample of nearby, hard X-ray-selected AGN for [O III] and other optical lines as a function of $L_{2-10\text{keV}}$. In O3-N, we measured an [O III] $\lambda 5008$ flux of $(2.51 \pm 0.04) \times 10^{16} \text{ erg s}^{-1} \text{ cm}^{-2}$, and a Balmer decrement of $H\alpha/H\beta = 4.9 \pm 0.6$. Assuming case B recombination with an intrinsic ratio of $H\alpha/H\beta = 2.86$ and a [Calzetti et al. \(2000\)](#) attenuation law, we derived $A_V = 1.9 \pm 0.4 \text{ mag}$. We thus inferred a reddening-corrected [O III] $\lambda 5008$ luminosity of $(2.7 \pm 0.5) \times 10^{44} \text{ erg s}^{-1}$.

The [Berney et al. \(2015\)](#) relation predicts that at an intrinsic 2 – 10 keV luminosity of $6.8 \times 10^{43} \text{ erg s}^{-1}$, the [O III] luminosity reaches $\log(L_{[\text{O III}]} / [\text{erg s}^{-1}]) = 42 \pm 0.6$. Despite the large scatter of the [Berney et al.](#) relation, our measured [O III] luminosity exceeds the prediction as a 4σ outlier. This means that either (1) the X-ray source is heavily obscured and thus the intrinsic X-ray luminosity is much larger, (2) the [O III] emission is not only excited by the AGN but is rather mainly excited by SF, (3), the [Berney et al. \(2015\)](#) relation is not applicable at this redshift, or indeed (4) a combination of all of the above.

At face value, the measured [O III] luminosity would correspond to an intrinsic X-ray luminosity of $L_{2-10\text{keV}} = 10^{46} \text{ erg s}^{-1}$, after extrapolating the range of the [Berney et al. \(2015\)](#) relation, and assuming no contribution from SF. We used the simple absorbed power-law model with $\Gamma = 1.4$ within the Chandra PIMMS tool⁵ (version 4.12d) to infer a column density of $N_H > 3.9 \times 10^{24} \text{ cm}^{-2}$ to produce the observed 2-10 keV luminosity. Increasing the photon index to $\Gamma = 2$ would raise the column density to $N_H > 4.7 \times 10^{24} \text{ cm}^{-2}$. In other words, the AGN needs to be Compton-thick along the line of sight to explain the non-detection of X-rays. However, at the same time, there must be an optically thin path for the ionizing radiation to escape and produce the observed [O III] emission.

We repeated the exercise using the [Ne v] $\lambda 3427$ detection. Given the extremely high energies needed to produce the Ne^{4+} ion, the contribution from SF is null or negligible. In the O3-N-core aperture, we measured a [Ne v] $\lambda 3427$ flux of $(2.25 \pm 0.33) \times 10^{-18} \text{ erg s}^{-1} \text{ cm}^{-2}$ and a Balmer decrement of $H\alpha/H\beta = 4.52 \pm 0.16$. Assuming case B recombination with an intrinsic ratio of $H\alpha/H\beta = 2.86$ and a [\(Calzetti et al. 2000\)](#) attenuation law, we derive $A_V = 1.58 \pm 0.16 \text{ mag}$. We thus inferred a reddening-corrected [Ne v] $\lambda 3427$ luminosity

⁵<https://asc.harvard.edu/toolkit/pimms.jsp>

of $(4.8 \pm 1.2) \times 10^{42} \text{ erg s}^{-1}$. [Berney et al. \(2015\)](#) also provide a relation for [Ne v] luminosity versus X-ray luminosity, although it is derived from a smaller sample and has a larger scatter than the [O III] relation. According to this latter relation, the intrinsic X-ray luminosity should be $2.4 \times 10^{45} \text{ erg s}^{-1}$. Using the same model as before, the column density needed to obscure that X-ray output is $N_{\text{H}} > 2 \times 10^{24} \text{ cm}^{-2}$, which is just above the Compton-thick limit.

Assuming the AGN is buried at the center of the DSFG, we now ask how much of the inferred obscuration can be accounted for by the ISM alone. This is motivated by the recent results of [Andonie et al. \(2024\)](#) who find that infrared-quasar host galaxies with $\text{SFR} \gtrsim 300 \text{ M}_{\odot} \text{ yr}^{-1}$ have submillimeter sizes as compact as those of DSFGs, implying a very dense ISM with column densities potentially exceeding the Compton limit. Following [Andonie et al. \(2024\)](#), we estimated the average column density by uniformly distributing the total gas mass (here $M_{\text{gas}} = 1.5 \times 10^{11} \text{ M}_{\odot}$, [Fraternali et al. 2021](#)) over a sphere with a radius equal to the Sérsic effective radius ($r_{\text{eff}} = 0.74 \text{ kpc}$, measured from a fit to the rest-frame $158 \mu\text{m}$ ALMA image, [Solimano et al. 2024](#)), finding $\langle N_{\text{H}} \rangle_{\text{ISM}} \approx 2.5 \times 10^{24} \text{ cm}^{-2}$. Therefore, we conclude that the ISM of the DSFG has enough material to obscure the X-rays. However, some of it must be located very close to the AGN; otherwise, we would detect the broad line region in the spectrum of the DSFG.

The results discussed above again suggest that the AGN is heavily obscured toward our line of sight, yet is powerful enough to produce luminous [O III] (and even [Ne v] emission) along unobscured sightlines. Such sightlines can be the result of a radio jet that has cleared them of obscuring material; we discuss this explanation in § 4.5.3.

4.5.3 Proposed scenario and implications

Here, we put forward a scenario that explains the observed emission. First, we assume that an AGN resides in the very center of the DSFG. This is motivated by the fact that the DSFG occupies the AGN loci of all the diagnostic diagrams we have considered (see § 4.4.1). In addition, given the $M_{\text{SMBH}} - M_{\star}$ relation (e.g., [Reines & Volonteri 2015](#); [Pacucci et al. 2023](#)), the DSFG is the most likely to host a massive SMBH, and thus an AGN. Moreover, its

location between the two radio detections makes it the potential launching site of a jet, as proposed by [Jiménez-Andrade et al. \(2023\)](#).

An alternative explanation has O3-N as a separate galaxy altogether; presumably a lower-mass AGN host currently being accreted by the DSFG (see scenarios 3 and 4 of [Solimano et al. 2024, Fig. 3.7](#)). This would mean that the J1000+0234 system hosts either a dual AGN (if both the DSFG and O3-N are active) or an offset AGN (if only O3-N is active). Dual and offset AGN have been extensively reported in the literature, with examples in both the local (e.g., [Barth et al. 2008](#); [Mazzarella et al. 2012](#); [Koss et al. 2012](#); [Barrows et al. 2017](#); [Secrest et al. 2017](#)) and distant Universe (e.g., [Gerke et al. 2007](#); [Comerford et al. 2015](#); [Perna et al. 2023](#); [Übler et al. 2024](#)). These phenomena are strongly linked to galaxy mergers, making J1000+0234 a plausible candidate. However, an investigation of the 3D geometry of the system to decipher whether O3-N is behind or in front of the DSFG is required to provide further insight into the offset/dual AGN scenario. We defer such an analysis to a future paper.

For simplicity, we return to our fiducial scenario where the AGN is at the nucleus of the DSFG. In this picture, O3-N traces an extended emission-line region (EELR; e.g., [Stockton, Fu & Canalizo 2006](#)) and an outflow driven by the AGN, as evidenced by the line ratios and broad velocity component, respectively.

Regarding O3-S, one could presume it represents the bipolar counterpart of O3-N (i.e., the receding side of the outflow). However, the observed kinematics, morphology, and spectral properties suggest otherwise. In particular, the large velocity gradient, narrower line width, lower SB, lower metallicity (see § 4.4.2), and more elongated structure make O3-S fundamentally different from O3-N. As suggested in § 4.3.1, O3-S is unlikely to be a separate galaxy with $M_{\text{dyn}} \approx 10^{11} M_{\odot}$, but rather a stream of tidal debris. The connection (both spatial and spectral) between C01 and O3-S then suggests that the gas might have been tidally stripped from C01. This is supported by the finding that O3-S has a very similar oxygen abundance to the southern clump of C01 (C01-SW, see [Fig. 4.9](#)).

Finally, due to the high ionization implied by the strong [O III] and He II lines, and its location along the jet axis, we propose that O3-S is being externally illuminated by the AGN. In other words, O3-S is an EELR analog to the famous Hanny’s Voorwerp ([Lintott](#)

et al. 2009). The Voorwerp is characterized by extended, high-equivalent-width [O III] emission at a far projected distance from the galaxy IC 2497. The leading explanation for the nature of the Voorwerp is that a portion of an otherwise-invisible gas tidal tail was exposed to ionizing radiation from the now-faded AGN in the center of IC 2497. Moreover, the escape path of the ionizing photons was carved by a past jet, as evidenced by the detection of a steep-spectrum extended radio relic (Józsa et al. 2009; Smith et al. 2022).

It could be that we are witnessing a similar situation in J1000+0234, although we cannot say whether the AGN in the DSFG is currently switched off or is simply obscured along the line of sight. However, the radio luminosity in J1000+0234 is approximately 100 times lower than the power of typical radio-selected HzRGs ($L_{1.4\text{ GHz}} \gtrsim 10^{27} \text{ W Hz}^{-1}$, Miley & De Breuck 2008), but at the same time is approximately 500 times higher than that of the Voorwerp ($L_{1.4\text{ GHz}} \approx 10^{23} \text{ W Hz}^{-1}$, Józsa et al. 2009). Therefore, the observed emission is more likely explained by a moderate luminosity jet, rather than a relic. Therefore, when considering the alignment of the radio sources along the axis that connects O3-N and O3-S, the idea of a jet carving an unobscured sightline in the polar direction becomes more compelling.

It is important to emphasize that J1000+0234 was selected because of its bright submillimeter emission and associated Ly α blob, as this could uncover a common trend among DSFG groups or protoclusters. For example, Vito et al. (2020) find a powerful ($L_{2-10\text{ keV}} \approx 3 \times 10^{45} \text{ erg s}^{-1}$) Compton-thick QSO hiding in the most gas-rich and submillimeter-bright member of the $z = 4$ protocluster known as DRC (Oteo et al. 2018). This system also hosts a LAB with emission of the high-ionization He II and C IV lines. A second example is that of the SPT2349-56 protocluster, a $z = 4.3$ structure hosting at least 21 DSFGs (Miller et al. 2018; Hill et al. 2020) and a faint LAB (Apostolovski et al. 2024). Recently, deep X-ray and radio observations revealed the presence of two AGN within SPT2349-56 (Vito et al. 2024; Chapman et al. 2024). Vito et al. (2024) then argue that SPT2349-56 and DRC together provide evidence of an enhanced AGN fraction within gas-rich protoclusters.

J1000+0234 is certainly less massive and extreme than either DRC or SPT2349-56, yet our detection of a Compton-thick AGN in it may be related to the same mechanisms that trigger obscured SMBH accretion in these two protoclusters. In theoretical frameworks

of galaxy–SMBH coevolution (e.g., [Hopkins et al. 2008](#)), it is expected that the conditions (e.g., those created in gas-rich mergers) that give rise to extreme dusty starbursts also favor (obscured) SMBH accretion. Observationally, the DSFG-AGN connection is stronger in dense environments, which is possibly due to the higher rate of merger and interaction ([Monson et al. 2023](#); [Vito et al. 2024](#)). A more systematic investigation of the obscured AGN fraction as a function of overdensity and SFR is needed to consolidate these trends.

While rest-frame hard X-rays will remain the gold standard for selecting obscured AGN, current facilities need to spend several tens of hours on source to produce detections at high z . In this context, our results suggest that a search for EELRs with the JWST NIRCam and NIRSpec might provide an alternative way to select high- z AGN.

4.6 Summary and conclusions

We present the discovery and characterization of two bright [O III] nebulae, O3-N and O3-S, around the J1000+0234 DSFG. Using JWST/NIRCam and JWST/NIRSpec, we characterized the morpho-kinematic structure of the nebulae, as well as their potential sources of ionization. Our results can be summarized as follows:

- O3-N, the brightest [O III] nebula in the system, shows a broad and blueshifted velocity component with $\text{FWHM} \gtrsim 1200 \text{ km s}^{-1}$, as measured in both [O III] and $\text{H}\alpha$ lines. We interpret this as evidence of ionized outflows, with a potential link to the [C II] plume of [Solimano et al. \(2024\)](#).
- While fainter than O3-N, O3-S is more extended and shows an elongated but irregular morphology. Moreover, the resolved [O III] velocity field reveals a 800 km s^{-1} gradient roughly aligned with the major axis of O3-S, but without a peaked velocity dispersion profile. Also, the lack of emission from stars, cold gas or dust from O3-S disfavors its identification as a massive rotating galaxy. Instead, given the low-SB bridge between O3-S and C01, in addition to their similar oxygen abundances, we deem it more likely that O3-S is a tidal feature stemming from C01.
- Nebular line ratio diagrams suggest at least some degree of AGN ionization in all the

sources considered in this chapter (except for C01). The DSFG, in particular, shows line ratios consistent with AGN in all the diagrams considered.

- We detect the temperature-sensitive [O III] $\lambda 4634$ auroral line in the central regions of O3-N and O3-S. However, these sources fall very close to the boundary line between pure AGN and an AGN–SF mixture in the [O III] $\lambda 4634$ -based diagrams proposed by [Mazzolari et al. \(2024\)](#).
- The central region of O3-N also shows a significant detection of the high-ionization [Ne V] $\lambda 3427$ line ($E > 97.1$ eV), an almost univocal tracer of AGN activity. Paired with the non-detection of rest-frame hard X-rays, we derive low $L_X/L_{[\text{O III}]}$ and $L_X/L_{[\text{Ne V}]}$ ratios that imply Compton-thick levels of obscuration. Interestingly, if the AGN is at the nucleus of the DSFG, the inferred column densities ($N_{\text{H}} \gtrsim 2 - 5 \times 10^{24} \text{ cm}^{-2}$) are consistent with arising from the ISM alone, as suggested by its dense and compact morphology, as derived in previous ALMA imaging.
- We tested whether or not shocks could be responsible for the emission in O3-N and O3-S by measuring the [N II] $\lambda 6850/\text{H}\alpha$ ratio on a spaxel-by-spaxel basis. We find no correlation between the ratio and the velocity dispersion, thus disfavoring a shock scenario.

We propose a scenario where both nebulae are EELRs powered by an AGN deeply buried within the DSFG. While O3-N shows a prominent outflow, O3-S belongs to a tidal tail of C01. This scenario makes O3-S a plausible high- z analog of Hanny’s Voorwerp, a residual ionized nebula excited by a faded AGN. In this picture, the action of the radio jets might have opened a path along the polar direction for the AGN ionizing radiation to reach O3-S and O3-N. We discuss our findings in the context of the enhanced AGN fraction found in massive, gas-rich protocluster cores at similar redshifts. Our results suggest that the processes that drive obscured SMBH accretion in these structures (e.g., mergers) might also be at play in the less massive J1000+0234 group. Finally, we highlight the ability of JWST to uncover hidden AGN at high redshifts, in a regime where current X-ray facilities lack the required sensitivity.

Chapter 5

Concluding Remarks

In this thesis, I presented three detailed studies on two particular high redshift objects: SGASJ1226 and J1000+0234. As pointed out in [Chapter 1](#), this work was limited to two objects because of the cost of acquiring the high-quality, state-of-the-art data used here. The two objects belong to different cosmic epochs and mass regimes, but the two of them exhibit extended Ly α emission that was detected with MUSE, and therefore represent a starting point for the investigation of larger samples of galaxies with extended emission. In this chapter, I look back at the questions posed in [§ 1.3](#) and review the contribution of this thesis ([§ 5.1](#)). Then, I present the latest progress of the ongoing work on new ALMA and JWST data ([§ 5.2](#)). Finally, I outline a few ideas for future extension of this thesis ([§ 5.3](#)).

5.1 Key Findings

What is the relative contribution of each mechanism to the origin of LAHs?

As discussed in [§ 1.2.1](#), there are at least four proposed main mechanisms to explain extended Ly α emission, namely resonant scattering, fluorescence, gravitational cooling, and unresolved satellites. In [Chapter 2](#) I presented spatially-resolved observations of the Ly α line of a gravitationally-lensed LAH at $z = 2.9$. Using MUSE observations, I explored the variations in the Ly α line profile to try to understand which mechanisms were at

play. While my collaborators and I were unable to provide a quantitative answer to the contribution of each mechanism, some important advancements were made.

First, we found clear indications of extended emission due to resonant scattering. The line exhibited a redshifted and red-asymmetric profile all across the LAH. Such profile is easily attributed to the effect of resonant scattering in an expanding medium. Moreover, we find that the line is wider and more redshifted in bins further away from the central galaxies. In a resonant scattering scenario, this behavior is expected since photons that escaped further away from the source probably suffered a larger amount of scatterings and probed a wider range of velocities, thus leading to a wider line profile relative to photons escaping closer to the source.

Second, we found evidence of satellite emission contributing to the emergence of the LAH. This finding was likely enabled by a fortuitous superposition of a lensing caustic on top of a dwarf satellite of the system. Nevertheless, it confirmed the existence of ultra-faint Ly α emitters that blend in the SB profile of a LAH that were previously predicted in the literature.

Unfortunately, not much can be said regarding the other two mechanisms. On one hand, gravitational cooling requires gas to be infalling, and we did not find evidence of that neither in the Ly α profile nor in the low-ionization UV metal absorption lines. On the other hand, fluorescence requires other indicators of photoionization to be ruled out. Based on the observed far-UV, non-ionizing emission, the galaxies could produce enough ionizing photons to power a fluorescent LAH. However, this estimate depends on the highly uncertain escape fraction of ionizing photons. Observations of extended H α emission around SGASJ1226 with JWST are currently being analyzed to quantify the possible contribution from fluorescence.

Finally, while we consider SGASJ1226 to be a benchmark LAH given the amount of attention that has been given to the central galaxies in the literature, we must stress the fact that it is only one object and therefore it may not be representative of the entire population of LAHs. The main caveat here is that SGASJ1226 is an interacting pair, and thus dynamical effects might introduce additional complexities that are not taken into account in the basic four mechanisms presented in § 1.2.1.

Regarding J1000+0234, the question of the LAH (in this case, LAB) mechanism was not directly addressed in this thesis. The analysis of the extended Ly α emission was instead presented by another team (Jiménez-Andrade et al. 2023). In their paper, they also report extended emission from C IV λ 1551 and He II λ 1640, tracers of high energy photons, which led them to suggest that an obscured AGN was photoionizing the entire LAB (i.e. fluorescent mechanism).

In Chapter 4, the new JWST NIRSpec data allowed us to give additional support to this scenario. The presence of an obscured AGN was confirmed by the detections of He II λ 4686 and [Ne v] λ 3427 toward large [O III] nebulae discovered in the proximity of the central galaxy. Furthermore, strong-line ratio diagnostics also suggest AGN photoionization in these nebulae. But the location of the [O III] nebulae is significantly offset (both spatially and spectrally) from the surface brightness peak of the LAB. This indicates that the Ly α line is still undergoing substantial scattering before escaping toward the observer. Further analysis and modeling is required to track the path of Ly α photons out of the J1000+0234 system and assess the contribution of each mechanism.

What is the nature of extended [C II] emission?

The phenomenon of extended [C II] emission at high redshifts has been linked to both normal, main-sequence galaxies, and to interacting groups, as mentioned in § 1.2.2. In the former case, the emission takes the form of extended disks (or halos in the terminology of Fujimoto et al. 2019) with sizes that exceed those of the rest-frame UV emission. Characterizing these objects at higher angular resolution than what was achieved by ALPINE was one of the primary goals of the CRISTAL survey.

My role within CRISTAL was to explore in detail the case of CRISTAL-01 (DC-842313), a $z = 4.5$ source selected from the ALPINE survey. While Fujimoto et al. (2020) did not classify this source as a [C II] halo due to the low S/N of the ALPINE data and multi-component UV morphology, the improved size measurements presented in Chapter 3 and in Ikeda et al. (2025, of which I am coauthor) reveal that [C II] is about three times as extended as the UV, similar to the average of the CRISTAL sample. CRISTAL-01b, a serendipitous [C II]-emitter in the CRISTAL-01 field, shows an even larger [C II]-to-UV size ratio of 3.8 ± 1.5

(Ikeda et al. 2025).

However, as discussed in [Chapter 3](#), the most striking feature of the CRISTAL-01 field is the narrow 15 kpc [C II] plume extending north of the massive DSFG J1000+0234 at the center of the system. Rather than tracing an isotropic [C II] disk or halo, the plume traces an elongated structure in the CGM of the DSFG. Therefore, the plume falls in the second regime of extended [C II] emission, along with the bridges and tidal features seen in other dense groups in the literature (e.g., [Carilli et al. 2013](#); [Riechers et al. 2014](#); [Peterson et al. 2018](#); [Ginolfi et al. 2020b](#)).

Despite the similarities to other examples of extended [C II] emission, the tidal nature of the [C II] plume in J1000+0234 is far from obvious. In fact, three other scenarios are considered in our discussion ([§ 3.5](#)), namely inflows, outflows, and ram pressure stripping. None of the proposed scenarios—including the tidal stripping—fits perfectly with the observed properties of the plume. After a careful comparison of each scenario under the information provided by the [C II] data, ram pressure stripping was deemed the least likely, but ultimately no scenario was discarded.

In [Chapter 4](#) we introduced new JWST data of the J1000+0234 system. The clear detection of a broad velocity component in O3-N strongly suggests a powerful ionized outflow located at the base of the [C II] plume. This finding naturally tilts the balance toward the outflow scenario, although the question of the decreasing [C II] FWHM and increasing [C II] velocity along the plume remains perplexing.

Interestingly, the G395H NIRSpec data provides additional information not discussed in this thesis. For example, it shows a clear H α counterpart to the [C II] plume that closely follows its shape and kinematics. Also, the faint UV continuum source located close to the center of the plume (see [Fig. 3.3](#)) turns out to be an H α emitter at the same redshift as the plume. These findings lend credence to the tidal scenario where the stripped dwarf galaxy displays a symmetric pair of tails. A detailed analysis of these observations and their implications for the origin of the [C II] plume will be presented in an upcoming paper.

How do feedback and dynamical interactions shape the close environments of SFGs?

According to the baryon cycle framework, feedback from star formation and AGN has important effects on the ISM, the CGM, and even the IGM around galaxies. Gravitational interactions, on the other hand, are also expected to leave an imprint on the surroundings of galaxies. Besides the potential to boost the SFR and AGN activity, these interactions (and ultimately mergers) are capable of stripping off gas from the ISM and distribute it as debris in the CGM.

In this thesis, I studied two high redshift objects that other than being highly active in terms of star formation, they are part of pairs or groups of galaxies and are therefore subject to gravitational interactions. In other words, the effects of feedback and interactions are superimposed.

In SGASJ1226, galaxies A and B have similar masses and SFR (see [Chapter 2](#)) and given their proximity in the sky and velocity space they might be on the brink of a major merger. The LAH surrounding both galaxies traces outflowing gas, with properties that are remarkably coherent across its full extent. This coherence is also seen in the low-ionization UV metal absorption lines toward the continuum of both galaxies. As mentioned briefly in [§ 2.4.1](#), the coherence could either mean that the two galaxies are launching similar outflows independently, or that the apparent outflow arises from large-scale streaming motions from the gravitational interaction. Observations of the outflow in emission using a non-resonant tracer are needed to distinguish between these two possibilities.

In J1000+0234, we have discovered three CGM-scale structures in addition to the LAB: the [C II] plume of currently uncertain origin ([Chapter 3](#)), and the two [O III] nebulae or EELRs that are powered by AGN activity ([Chapter 4](#)). The kinematics of the [C II] plume can be explained by either by feedback or gravitational interactions, but the [C II] emission (and specially the H α emission) that traces the structure is likely powered by feedback from star formation (even if the FIR continuum is not detectable). A similar statement can be said of the [O III] nebulae, in particular O3-S: while the emission is powered by AGN photoionization, the morphology and kinematics resemble a tidal tail connected to CRISTAL-01a. In [§ 4.5.3](#) we drew a parallel between the J1000+0234 system and Hanny's

Voorwerp, where a similar configuration has been observed.

A possible–albeit speculative–conclusion from the two case studies presented in this thesis, is that radiative feedback can illuminate gas structure produced by gravitational interactions. Gravity sets the shape and motions, while feedback makes it possible for us to observe.

5.2 Ongoing work

In this section I present the next steps to follow the research carried out in this thesis, along with the partial progress in completing these steps.

5.2.1 Analysis of ALMA and JWST data of SGASJ1226

In ALMA’s Cycle 8 I was awarded A-ranked observing time (program id 2021.1.01337.S) to image the [C II] 158 μm line in SGASJ1226 at the MUSE-matching resolution of $0''.7$. The program included observations in Band 8 of both the 12m array and the 7m array. The addition of the latter was intended to capture potentially extended [C II] emission from SGASJ1226. [C II] was detected in both arcs A.1 and B (see [Fig. 5.1](#)). Notably, the SB is higher in the latter, with a barely resolved region in between UV clumps dominating the emission. This region is also robustly detected in the underlying continuum and has the largest velocity dispersion. Interestingly, ALMA also detects the [C II] line in a region co-spatial with a foreground galaxy of known redshift ($z = 0.77$, [Tejos et al. 2021](#)) After ruling out a line interloper, we conclude this emission comes from an additional member of the SGASJ1226 system at $z = 2.9$ or a previously undetected lensed image of either A or B.

The global properties of [C II] in SGASJ1226 were presented in a paper led by a Master student I co-advised [Catán et al. \(2024\)](#), with the goal of giving an alternative measurement of the molecular gas in these galaxies. Using a $\text{H}_2/[\text{C II}]$ mass-to-light ratio of $30 \text{ M}_\odot \text{ L}_\odot^{-1}$ (e.g., [Zanella et al. 2018](#)), we find delensed molecular gas masses of $(4.9 \pm 1.1) \times 10^8 \text{ M}_\odot$ and $(1.2 \pm 0.2) \times 10^{10} \text{ M}_\odot$, in galaxies A and B, respectively. These results suggest that despite the similar masses, SFR, and UV colors of SGASJ1226-A and SGASJ1226-B, they

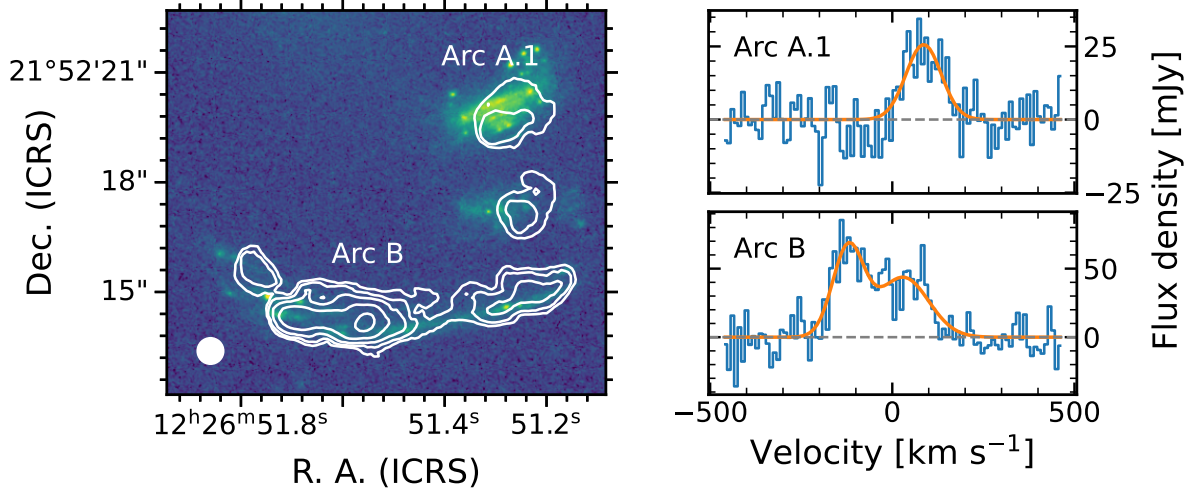


Figure 5.1: ALMA Band 8 observations of SGASJ1226. Figure reproduced from [Catán et al. \(2024\)](#). *Left:* HST ACS/F606W image of the SGASJ1226 field with white contours showing the ALMA [C II] emission. The ALMA beam is shown as a white circle in the bottom left corner. The first contour traces a SB level of $0.21 \text{ Jy km s}^{-1} \text{ beam}^{-1}$, corresponding to $S/N \approx 3$. Subsequent levels increase as powers of $\sqrt{3}$. *Right:* Extracted [C II] spectra from the arc A.1 (top) and arc B (bottom) is shown in blue. The orange line shows the best-fit single and double Gaussian models for A.1 and B, respectively.

seem to differ substantially in their cold ISM properties.

Another remarkable feature of the ALMA data is the velocity gradient in the arc B, with a span of roughly 400 km s^{-1} from end to end. This gradient suggests that galaxy B may be a rotating galaxy, but this remains speculative. Proper modeling of the kinematics and lensing is necessary to understand the dynamical state of this galaxy.

Finally, a pending task is to measure the spatial extent of the [C II] emission in the source plane and compare with other tracers such as UV continuum and $\text{Ly}\alpha$. Just by visual inspection, [C II] does not seem to extend much further out than the UV continuum, in other words, we find no [C II] halo around SGASJ1226. Anyway, proper forward modeling is needed to quantify the [C II] morphology and extent. If the result is confirmed, the connection between [C II] halos and $\text{Ly}\alpha$ halos might be more elusive than previously thought.

The obvious next step toward disentangling the mechanism that create the LAH around SGASJ1226 is the analysis of JWST observations. JWST data was obtained from two differ-

ent programs. The first batch came from the TEMPLATES Early Release Science program (id 1355, [Rigby et al. 2025](#)) and included NIRC*am* imaging in six broadband filters (see left panel of [Fig. 5.2](#)) and NIRS*pec* IFS observations toward arc A.1, with the G235H grating covering important lines such as [O III] $\lambda\lambda 4960, 5008$ and $H\alpha$ at a resolving power of $R \approx 2700$. The second batch was obtained through my own program in Cycle 2 (id 3777), and consists of a 4-pointing mosaic of NIRS*pec* IFU apertures targeting arc B to complete the G235H coverage of the SGASJ1226 system (see right panel of [Fig. 5.2](#)) The proposal was motivated by two main questions:

1. What are the mechanisms driving the SGASJ1226 LAH?
2. What is the origin of the outflow detected in $Ly\alpha$ and low-ionization absorption?

By combining data from programs #1355 and #3777 we obtained a uniform NIRS*pec* IFS coverage of the main components of the SGASJ1226 system. Coverage of the arc B was relevant since ALMA had already revealed it is the most active galaxy of the pair, and hence the most probable source of the outflow.

By looking at [Fig. 5.2](#), we see some striking differences between the lensed morphology of the nebular emission and that of the rest-frame UV and optical. For example, nebular emission in arc B is mostly limited to the southern rim, away from the red diffuse starlight revealed in the NIRC*am* image. Also there are a handful of clumps showing nebular emission but almost no stellar counterpart, and viceversa. For example, the two green clumps in arc B around $\Delta RA = -3''$ are bright continuum emitters, but have almost no ongoing star formation. In arc A.1 the situation is even more contrasting. Almost all visible UV/optical clumps have faint or undetected emission lines. Instead, most of the nebular emission seems to come from in between the clumps. Qualitatively, this implies that galaxy A has generally older clumps and less ongoing star formation relative to galaxy B. Resolved SED fitting of the clumps could help us understand the formation history of these two galaxies.

Returning to question #1, the first thing would be to measure and compare the size of the $H\alpha$ emission in the source plane. If it extends well beyond the UV, it could be

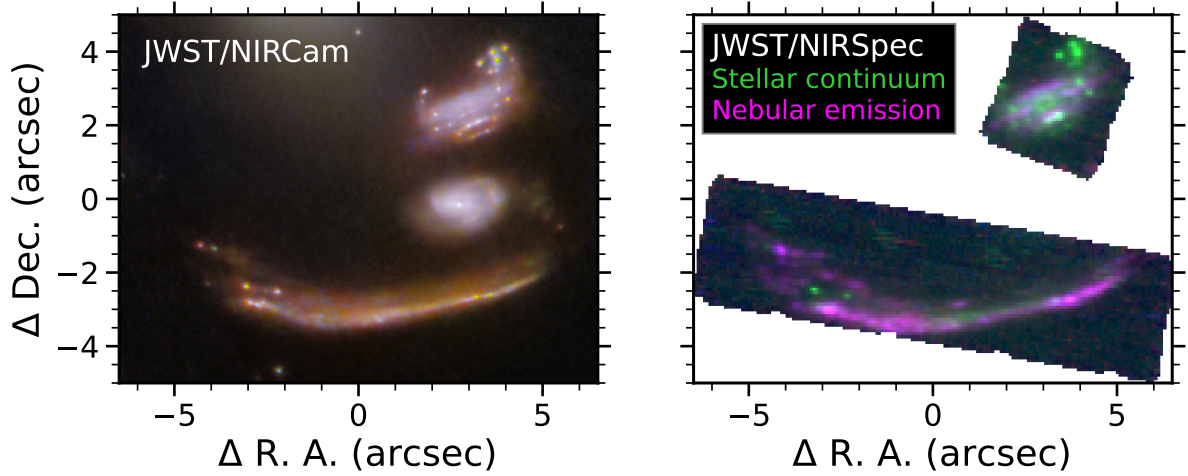


Figure 5.2: JWST view of the SGASJ1226 system. *Left:* RGB cutout of NIRCам data from TEMPLATES, reproduced from the [ESA public image release](#). This view combines images taken with six different broadband filters from F115W to F444W. Image credit: ESA/Webb, NASA & CSA, J. Rigby and the JWST TEMPLATES team. *Right:* RGB composite showcasing the NIRSpec data from programs ERS-1355 (top right) and GO-3777 (bottom). The blue and red channels are mapped to pseudo-narrowband images of [O III] and H α emission, respectively. Therefore, nebular emission dominated by [O III] and H α emission appear as magenta. The green channel is mapped to a pseudo-broadband image of a line-free section of the spectrum around rest-frame 5500 Å. Continuum-only emission thus appears green in the image.

taken as evidence of CGM-scale photoionization and thus Ly α fluorescence. Otherwise, Ly α resonant scattering will remain the preferred scenario.

Relatively more progress has been made toward answering question #2. I have conducted a search of outflow candidates in the resolved spectra of both arcs. To this end, I fitted single and double Gaussian kinematic components to the H α + [N II] line complex. The spectra was extracted from each of 78 bins of a Voronoi tessellation of the image plane, constructed to keep the peak H α S/N close to 100. The H β line was fitted simultaneously with free flux but the velocity centroid and FWHM were tied to the H α fit. In this way, we tracked the Balmer decrement in a self-consistent way, and we were able to infer dust attenuation and dust-corrected quantities with proper treatment of errors. Each spectrum was classified as an outflow candidate if the double component fit (broad plus narrow) performed better than the single component fit in terms of Bayesian evidence

and a set of similar criteria.

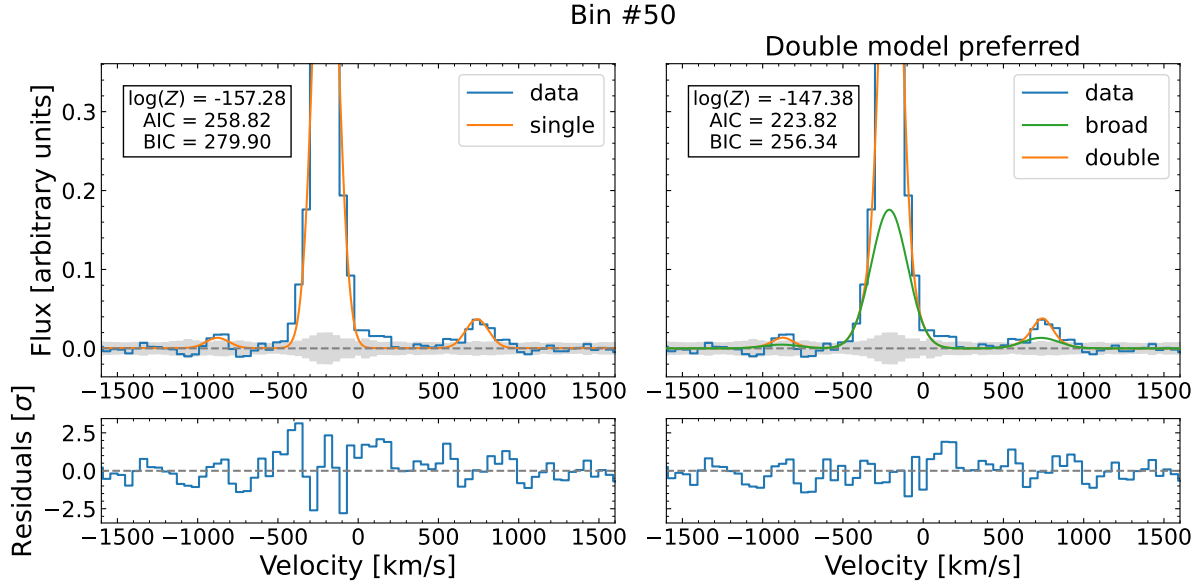


Figure 5.3: Example fit to the $H\alpha$ spectrum of one of the Voronoi bins belonging to arc B. *Left:* Single Gaussian model fit (top) and residuals (bottom). *Right:* Double Gaussian model fit (top) and residuals (bottom). The Bayesian evidence ($\log Z$), Bayesian (BIC), and Akaike (AIC) information criteria scores are shown in the inset legends. In this case, the double Gaussian model is preferred over the single model.

We found that 40 out of the 78 spectra display evidence of a broad velocity component (7 out of 14 in arc A.1, 33 out of 64 in arc B). This result suggests that both galaxies are simultaneously hosting ionized gas outflows. The next question is how much mass and energy are these outflows carrying, and whether they are capable of producing the large-scale motions observed in $Ly\alpha$. This is currently work in progress.

5.2.2 J1000+0234's $H\alpha$ revival: the origin of the plume

In [Chapter 4](#) I characterized the newly-found [O III] nebulae in J1000+0234 using data mainly from NIRSpect IFS program GO-3045 (PI: Faisst). While the analysis was complemented with data from program GO-4256 (PI: González-López, co-PI: Aravena), the main results were derived from GO-3045's data, which covered the blue side of the rest-frame optical spectrum of J1000+0234 with the G235M grating. However, IFU data from GO-4256

are deeper, use more dither positions, have better spectral resolution, and their observation was designed explicitly to cover the [C II] plume, unlike the G235M cube in which the plume falls outside the field of view. In this section, I will describe recent findings from the continued analysis of the G395H cube.

An adaptive pseudo-NB image of the $H\alpha$ emission around $z = 4.54$ shows a clear counterpart of the [C II] plume (see Fig. 5.4). Moreover, visual inspection of the G395H cube revealed five new $H\alpha$ emitters (HAEs) at redshifts close to $z = 4.54$, and three additional HAEs at $z = 4.42$. HAE-01 is cospatial with one of the faint UV continuum sources we had detected at the center of the plume in the HST stack (§ 3.4.3), thus confirming its membership to the J1000+0234 system. The other continuum source, located near the north end of the plume, is also detected in $H\alpha$ (HAE-06) but at $z = 4.4218$ or 7747 km s^{-1} away from J1000+0234, along with two other sources (HAE-07 and HAE-08, see Fig. 5.4e). The large velocity offset makes a physical connection to J1000+0234 very unlikely. These three sources might instead belong to an unrelated group in the foreground, or a continuing filamentary structure connected to J1000+0234.

The confirmation of HAE-01 as a member of the group with consistent velocity and position as the center of the [C II] plume strongly suggests a physical association with the latter. As discussed in § 3.5.2 in the context of the inflow scenario, the presence of dwarf galaxies forming stars along accretion filaments is not unexpected. Therefore, the existence of HAE-01 is consistent with the inflow scenario. However, the diffuse $H\alpha$ emission associated with the plume might not support it, unless there are even fainter dwarfs forming stars all across the plume, or the UV emission from HAE-01 itself and perhaps O3-N are capable of sustaining ionization along the plume.

An alternative option is that HAE-01 is being tidally stripped by the system's gravitational well. This scenario was briefly discussed in § 3.5.4 with O3-N as the candidate stripped galaxy, but HAE-01 is a better candidate since it lies in the middle of the plume. Therefore, HAE-01 will have the expected pair of approaching and receding tidal tails. However, the asymmetry of SB and line FWHM observed in the [C II] data would remain unexplained. Further analysis is currently underway to fully exploit the G395H dataset and finally understand the origin of the [C II] plume.

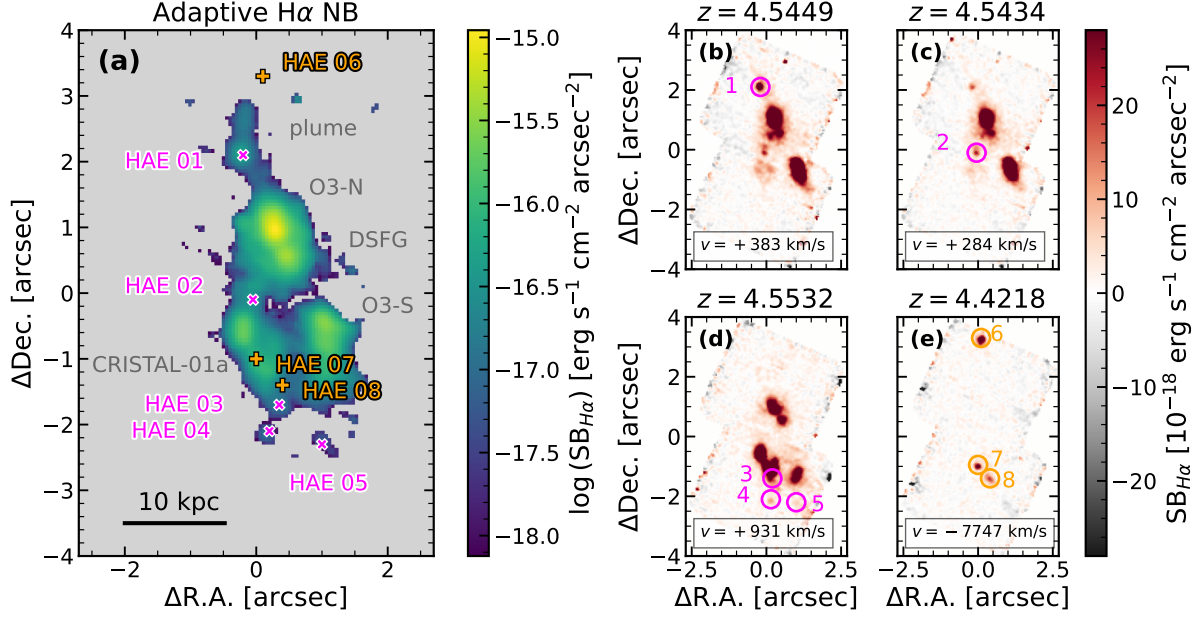


Figure 5.4: Extended H α and H α emitters in J1000+0234. **(a)** Adaptive pseudo-NB image of the H α emission in the J1000+0234 field at $z = 4.54$ spanning 2000 km s^{-1} . This panel shows the main members of the J1000+0234 system (labeled in gray) plus the positions of newly detected HAEs at $z \approx 4.54$ (magenta) and $z \approx 4.42$ (orange). **(b-e)** Pseudo-NB H α images of width 300 km s^{-1} at different redshifts. The label at the bottom of each panel indicates the velocity difference with respect to the systemic redshift $z_{\text{sys}} = 4.5391$.

5.3 Future directions

One of the main limitations of the results presented in this thesis is the focus on two specific objects rather than a statistical sample, so the conclusions will not necessarily apply to the wider population of galaxies. A possible avenue for the extension of this work would rely on the construction of samples of high-redshift galaxies with observations of resolved CGM gas emission.

In the case of Ly α , this can already be done by exploiting the ESO public archive. Existing samples of LAHs observed with MUSE have already been collected from deep exposures of blank (Leclercq et al. 2017) and lensed fields (Claeyssens et al. 2022). Interestingly, the current size of the ESO MUSE archive enables an extensive search of LAHs in random positions of the sky, amounting to a survey volume that is roughly ten times larger than MUSE-Wide (Urrutia et al. 2019), the largest area MUSE-based Ly α survey con-

ducted so far. A systematic mining of the MUSE archive for serendipitous Ly α would be comparable to a wide-area narrowband photometric survey, but with the added value of the spectral and spatial resolution of MUSE. Moreover, the multiplicity of non-contiguous pointings will help mitigate the effects of cosmic variance, while the large total volume will help discover rare and bright objects. With a catalog of all the untargeted LAHs and LABs in the MUSE archive, it will be possible to confirm trends in key parameters such as halo size, line width, offset with the UV, etc., and learn about their potential evolution as a function of redshift.

Regarding rest-frame optical lines, the continuation of the JWST mission in the 2020s and possibly into the 2030s provides a lot of opportunities. In light of the fact that we first identified the EELRs around J1000+0234 in the NIRCam images ([Chapter 4](#)), large imaging surveys with JWST could be used to perform a census of EELRs at high redshifts. The idea of using broadband imaging to identify extreme line emitters is not new, but the superb sensitivity and angular resolution of JWST are really a game changer at $z > 2$. For example, [Chen et al. \(2025\)](#) exploit deep NIRCam imaging from the JWST Advanced Deep Extragalactic Survey (JADES) to look for extreme [O III] emitters at $z \approx 2.2$ selected as candidates with a strong excess in the F150W filter. While they focus on reporting a sample of 128 compact emitters (therein dubbed as “Green Seeds”), they also find a handful of EELRs. Similarly, [Lebowitz et al. \(2025\)](#) present a new method for selecting EELRs, specifically AGN ionization cones, in galaxies at Cosmic Noon using NIRCam’s medium band filters. They apply the method to a sample of 27 previously identified AGN in the GOODS-S field and find 17 to be either extended or cone-shaped. These works confirm the feasibility of performing a more ambitious search for EELRs using existing NIRCam imaging and build a list of candidates to confirm with JWST spectroscopy. If EELRs at high redshift turn out to be as rare as in the local Universe, the small field of view of NIRCam may not supply sufficient counts. In that case, ongoing and future missions such as Euclid or Roman will be crucial, as they will unlock unprecedented statistics with their huge survey volumes.

List of Figures

1.1	Artistic representation of the CGM.	3
1.3	$\text{Ly}\alpha$ size versus $\text{Ly}\alpha$ luminosity for different types of $\text{Ly}\alpha$ nebulae.	12
1.4	Visual summary of the CGM and its extended $\text{Ly}\alpha$ emission.	13
1.5	Stacked [C II] emission around distant star-forming galaxies.	19
1.6	CRISTAL “family picture”	22
2.1	Subtraction of the BCG light model from the MUSE cube.	29
2.2	Overview and details of the image plane morphology of the SGASJ1226 system.	32
2.3	Continuum-subtracted pseudo narrowband image of the lensed $\text{Ly}\alpha$ halo at $z = 2.92$	38
2.4	Example of asymmetric Gaussian fit to one of the extracted spectra.	39
2.5	$\text{Ly}\alpha$ profiles extracted from global apertures.	42
2.6	Image plane $\text{Ly}\alpha$ equivalent width map displaying arcs A.1, B and the counterimage A.2	45
2.7	Source plane modeling of the UV emission from the central galaxies.	48
2.8	Source plane modeling of the LAH and the central galaxies.	49
2.9	Source plane tessellation and extracted spectra.	50
2.10	Source plane map of asymmetric Gaussian fitted parameters for the 50-bin tessellation.	51
2.11	Resolved correlations of the $\text{Ly}\alpha$ line profile parameters	54
2.12	Best fit FLAREON GW models for the integrated spectra of galaxies A and B.	56
2.13	Source plane map of FLAREON GW fitted parameters.	57
2.14	Spatially integrated Al II $\lambda 1670$ absorption spectra of galaxies A and B	60

3.1	HST, Ly α , and [C II] morphologies.	76
3.2	Results from parametric 2D modeling with PYAUTOGALAXY.	82
3.3	Stack of HST/WFC3-IR imaging of J1000+0234 with the outline of the [C II] emission in red.	83
3.4	Selected channel maps from the low-resolution [C II] datacube binned to 40 km s ⁻¹	85
3.5	Spatial variation of spectral properties of the [C II] plume.	89
3.6	Symmetric difference analysis for aperture #1.	91
3.7	Cartoon representations of the four possible scenarios to explain the [C II] plume.	108
4.1	Multiwavelength view of the J1000+0234 system at $z = 4.54$	112
4.2	Resolved [O III] kinematics of J1000+0234.	115
4.3	Evidence of a broad velocity component in the strongest emission lines from O3-N.	117
4.4	Double Gaussian fit to [O III] and H α spectra of O3-S.	117
4.5	Diagnostic line ratio diagrams for the relevant regions of the J1000+0234 system.	121
4.6	Zoom-in to high-ionization lines detected in O3-N-core.	122
4.7	Same as Fig. 4.6 but for O3-S-HeII.	122
4.8	Diagnostic line-ratio diagrams based on [O III] $\lambda 4364$ emission.	123
4.9	Oxygen abundances of the sources in the J1000+0234 system according to the Dopita et al. (2016) calibration.	125
4.10	Resolved N2 ratio as a function of line velocity dispersion in O3-S and O3-N.	127
5.1	ALMA Band 8 observations of SGASJ1226.	141
5.2	JWST view of the SGASJ1226 system.	143
5.4	Extended H α and H α emitters in J1000+0234.	146

List of Tables

2.1	HST aperture photometry of the $z = 2.92$ lensed arcs of the SGASJ1226 system.	31
2.2	Properties of the two largest member galaxies	35
3.1	Global properties of the two main galaxies in the J1000+0234 system. . . .	71
3.2	Results of the parametric 2D fitting of exponential profiles to the $160\,\mu\text{m}$ continuum and [C II] line maps of the DSFG.	80
3.3	Results of the parametric 2D fitting to the [C II] line map of CRISTAL-01a. .	84
3.4	Extracted quantities from the apertures in Fig. 3.5.	88
4.1	Line fluxes for the different apertures used in this paper.	120

Bibliography

Aalto S., et al., 2020, [A&A](#), **640**, A104

Adams J. J., et al., 2011, [ApJS](#), **192**, 5

Ahn S.-H., 2004, [ApJ](#), **601**, L25

Akins H. B., et al., 2022, [ApJ](#), **934**, 64

Alarie A., Morisset C., 2019, [Rev. Mexicana Astron. Astrofis.](#), **55**, 377

Alexander D. M., Hickox R. C., 2012, [New A Rev.](#), **56**, 93

Allen M. G., Groves B. A., Dopita M. A., Sutherland R. S., Kewley L. J., 2008, [ApJS](#), **178**, 20

Andonie C., et al., 2024, [MNRAS](#), **527**, L144

Anglés-Alcázar D., Faucher-Giguère C.-A., Kereš D., Hopkins P. F., Quataert E., Murray N.,
2017, [MNRAS](#), **470**, 4698

Apostolovski Y., et al., 2024, [A&A](#), **683**, A64

Appleton P. N., et al., 2013, [ApJ](#), **777**, 66

Arata S., Yajima H., Nagamine K., Abe M., Khochfar S., 2020, [MNRAS](#), **498**, 5541

Aravena M., et al., 2024, [A&A](#), **682**, A24

Aretxaga I., et al., 2011, [MNRAS](#), **415**, 3831

- Bacon R., et al., 2010, in McLean I. S., Ramsay S. K., Takami H., eds, Society of Photo-Optical Instrumentation Engineers (SPIE) Conference Series Vol. 7735, Ground-based and Airborne Instrumentation for Astronomy III. p. 773508 ([arXiv:2211.16795](#)), [doi:10.1117/12.856027](#)
- Bacon R., et al., 2017, [A&A](#), **608**, A1
- Bacon R., et al., 2021, [A&A](#), **647**, A107
- Bacon R., et al., 2023, [A&A](#), **670**, A4
- Bagley M. B., et al., 2023, [ApJ](#), **946**, L12
- Baldwin J. A., Phillips M. M., Terlevich R., 1981, [PASP](#), **93**, 5
- Bao M., Chen Y.-m., Yuan Q.-r., Shi Y., Bizyaev D., Yu X.-l., Gu Q.-s., Yu Y., 2019, [MNRAS](#), **490**, 3830
- Barrows R. S., Comerford J. M., Greene J. E., Pooley D., 2017, [ApJ](#), **838**, 129
- Barth A. J., Bentz M. C., Greene J. E., Ho L. C., 2008, [ApJ](#), **683**, L119
- Bastian N., Covey K. R., Meyer M. R., 2010, [ARA&A](#), **48**, 339
- Baugh C. M., Cole S., Frenk C. S., Lacey C. G., 1998, [ApJ](#), **498**, 504
- Bayliss M. B., Hennawi J. F., Gladders M. D., Koester B. P., Sharon K., Dahle H., Oguri M., 2011, [ApJS](#), **193**, 8
- Behrens C., Pallottini A., Ferrara A., Gallerani S., Vallini L., 2019, [MNRAS](#), **486**, 2197
- Bekki K., 2009, [MNRAS](#), **399**, 2221
- Bekki K., Koribalski B. S., Kilborn V. A., 2005, [MNRAS](#), **363**, L21
- Berney S., et al., 2015, [MNRAS](#), **454**, 3622
- Bertin E., Arnouts S., 1996, [A&AS](#), **117**, 393

- Béthermin M., Wang L., Doré O., Lagache G., Sargent M., Daddi E., Cousin M., Aussel H., 2013, [A&A](#), **557**, A66
- Béthermin M., et al., 2020, [A&A](#), **643**, A2
- Bian F., et al., 2013, [ApJ](#), **774**, 28
- Bischetti M., Maiolino R., Carniani S., Fiore F., Piconcelli E., Fluetsch A., 2019, [A&A](#), **630**, A59
- Bland J., Tully B., 1988, [Nature](#), **334**, 43
- Böker T., et al., 2023, [PASP](#), **135**, 038001
- Borisova E., et al., 2016, [ApJ](#), **831**, 39
- Boselli A., Fossati M., Sun M., 2022, [A&A Rev.](#), **30**, 3
- Bouchet P., Lequeux J., Maurice E., Prevot L., Prevot-Burnichon M. L., 1985, [A&A](#), **149**, 330
- Bournaud F., et al., 2011, [ApJ](#), **730**, 4
- Bouwens R. J., et al., 2022, [ApJ](#), **931**, 160
- Bradač M., et al., 2017, [ApJ](#), **836**, L2
- Brammer G., 2023, grizli, [doi:10.5281/zenodo.1146904](https://doi.org/10.5281/zenodo.1146904)
- Brinchmann J., Charlot S., White S. D. M., Tremonti C., Kauffmann G., Heckman T., Brinkmann J., 2004, [MNRAS](#), **351**, 1151
- Bullock J. S., Johnston K. V., 2005, [ApJ](#), **635**, 931
- Bunker A. J., et al., 2023, [A&A](#), **677**, A88
- Byrohl C., et al., 2021, [MNRAS](#), **506**, 5129
- CASA Team et al., 2022, [PASP](#), **134**, 114501
- Cai Z., et al., 2016, [ApJ](#), **833**, 135

- Cai Z., et al., 2017, [ApJ](#), **837**, 71
- Calzetti D., Armus L., Bohlin R. C., Kinney A. L., Koornneef J., Storchi-Bergmann T., 2000, [ApJ](#), **533**, 682
- Caminha G. B., et al., 2016, [A&A](#), **595**, A100
- Cantalupo S., Arrigoni-Battaia F., Prochaska J. X., Hennawi J. F., Madau P., 2014, [Nature](#), **506**, 63
- Capak P., et al., 2008, [ApJ](#), **681**, L53
- Cappellari M., 2017, [MNRAS](#), **466**, 798
- Cappellari M., 2023, [MNRAS](#), **526**, 3273
- Cappellari M., Copin Y., 2003, [MNRAS](#), **342**, 345
- Carilli C. L., Walter F., 2013, [ARA&A](#), **51**, 105
- Carilli C. L., et al., 2008, [ApJ](#), **689**, 883
- Carilli C. L., Riechers D., Walter F., Maiolino R., Wagg J., Lentati L., McMahon R., Wolfe A., 2013, [ApJ](#), **763**, 120
- Carniani S., et al., 2024, [Nature](#), **633**, 318
- Casey C. M., 2016, [ApJ](#), **824**, 36
- Casey C. M., Narayanan D., Cooray A., 2014, [Phys. Rep.](#), **541**, 45
- Casey C. M., et al., 2023, [ApJ](#), **954**, 31
- Catán V., et al., 2024, [A&A](#), **692**, A215
- Cavanaugh J. E., 1997, *Statistics & Probability Letters*, **33**, 201
- Ceverino D., Dekel A., Bournaud F., 2010, [MNRAS](#), **404**, 2151
- Chabrier G., 2003, [PASP](#), **115**, 763

- Chapman S. C., et al., 2024, [ApJ](#), **961**, 120
- Chartas G., et al., 2021, [ApJ](#), **920**, 24
- Chen H.-W., Zahedy F. S., 2024, [arXiv e-prints](#), p. [arXiv:2412.10579](#)
- Chen M. C., Chen H.-W., Gronke M., Rauch M., Broadhurst T., 2021a, [MNRAS](#), **504**, 2629
- Chen Y., et al., 2021b, [MNRAS](#), **508**, 19
- Chen N., Motohara K., Spitler L., Malkan M. A., 2025, [ApJ](#), **981**, 96
- Chisholm J., Rigby J. R., Bayliss M., Berg D. A., Dahle H., Gladders M., Sharon K., 2019, [ApJ](#), **882**, 182
- Chisholm J., et al., 2024, [MNRAS](#), **534**, 2633
- Chung A., van Gorkom J. H., Kenney J. D. P., Crawl H., Vollmer B., 2009, [AJ](#), **138**, 1741
- Claeyssens A., et al., 2019, [MNRAS](#), **489**, 5022
- Claeyssens A., et al., 2022, [A&A](#), **666**, A78
- Cleri N. J., et al., 2023, [ApJ](#), **953**, 10
- Comerford J. M., Pooley D., Barrows R. S., Greene J. E., Zakamska N. L., Madejski G. M., Cooper M. C., 2015, [ApJ](#), **806**, 219
- Conroy C., Gunn J. E., 2010, [ApJ](#), **712**, 833
- Conroy C., Gunn J. E., White M., 2009, [ApJ](#), **699**, 486
- Conselice C. J., Mortlock A., Bluck A. F. L., Grützbauch R., Duncan K., 2013, [MNRAS](#), **430**, 1051
- Contursi A., et al., 2013, [A&A](#), **549**, A118
- Cooper J. L., Bicknell G. V., Sutherland R. S., Bland-Hawthorn J., 2008, [ApJ](#), **674**, 157
- Cormier D., et al., 2012, [A&A](#), **548**, A20

- Cowie L. L., Hu E. M., 1998, [AJ](#), **115**, 1319
- Cox T. J., Dutta S. N., Di Matteo T., Hernquist L., Hopkins P. F., Robertson B., Springel V., 2006, [ApJ](#), **650**, 791
- Curti M., et al., 2023, [MNRAS](#), **518**, 425
- Curtis-Lake E., et al., 2023, [Nature Astronomy](#), **7**, 622
- Czekala I., et al., 2021, [ApJS](#), **257**, 2
- D'Eugenio F., et al., 2025, [MNRAS](#), **536**, 51
- Daddi E., et al., 2007, [ApJ](#), **670**, 156
- Dai L., et al., 2020, [MNRAS](#), **495**, 3192
- Danovich M., Dekel A., Hahn O., Ceverino D., Primack J., 2015, [MNRAS](#), **449**, 2087
- Darg D. W., et al., 2010, [MNRAS](#), **401**, 1043
- Davies R. L., et al., 2019, [ApJ](#), **873**, 122
- Decarli R., et al., 2019, [A&A](#), **631**, L10
- Decarli R., et al., 2024, [A&A](#), **689**, A219
- Dekel A., Birnboim Y., 2006, [MNRAS](#), **368**, 2
- Dekel A., et al., 2009, [Nature](#), **457**, 451
- Dessauges-Zavadsky M., et al., 2020, [A&A](#), **643**, A5
- Di Cesare C., Ginolfi M., Graziani L., Schneider R., Romano M., Popping G., 2024, [A&A](#), **690**, A255
- Dijkstra M., Haiman Z., Spaans M., 2006, [ApJ](#), **649**, 37
- Dopita M. A., Kewley L. J., Sutherland R. S., Nicholls D. C., 2016, [Ap&SS](#), **361**, 61
- Draine B. T., 2011, *Physics of the Interstellar and Intergalactic Medium*

- Drake A. B., et al., 2020, [ApJ](#), **902**, 37
- Duc P.-A., Bournaud F., 2008, [ApJ](#), **673**, 787
- Duc P.-A., Renaud F., 2013, in Souchay J., Mathis S., Tokieda T., eds., , Vol. 861, Lecture Notes in Physics, Berlin Springer Verlag. p. 327, [doi:10.1007/978-3-642-32961-6_9](#)
- ESO CPL Development Team 2015, EsoRex: ESO Recipe Execution Tool, Astrophysics Source Code Library, record ascl:1504.003
- Ebeling H., Stephenson L. N., Edge A. C., 2014, [ApJ](#), **781**, L40
- Elbaz D., et al., 2007, [A&A](#), **468**, 33
- Elvis M., et al., 2009, [ApJS](#), **184**, 158
- Emonts B. H. C., et al., 2018, [MNRAS](#), **477**, L60
- Emonts B. H. C., et al., 2023, [Science](#), **379**, 1323
- Endsley R., et al., 2023, [MNRAS](#), **520**, 4609
- Endsley R., et al., 2024, [MNRAS](#), **533**, 1111
- Erb D. K., Steidel C. C., Chen Y., 2018, [ApJ](#), **862**, L10
- Erb D. K., Berg D. A., Auger M. W., Kaplan D. L., Brammer G., Pettini M., 2019, [ApJ](#), **884**, 7
- Faisst A. L., et al., 2020, [ApJS](#), **247**, 61
- Faucher-Giguère C.-A., Oh S. P., 2023, [ARA&A](#), **61**, 131
- Fielding D. B., Bryan G. L., 2022, [ApJ](#), **924**, 82
- Fiore F., et al., 2017, [A&A](#), **601**, A143
- Foreman-Mackey D., Hogg D. W., Lang D., Goodman J., 2013, [PASP](#), **125**, 306
- Förster Schreiber N. M., Genzel R., Lutz D., Sternberg A., 2003, [ApJ](#), **599**, 193

- Fraternali F., 2017, in Fox A., Davé R., eds, *Astrophysics and Space Science Library* Vol. 430, *Gas Accretion onto Galaxies*. p. 323 ([arXiv:1612.00477](#)), [doi:10.1007/978-3-319-52512-9_14](#)
- Fraternali F., Binney J. J., 2008, [MNRAS](#), **386**, 935
- Fraternali F., Karim A., Magnelli B., Gómez-Guijarro C., Jiménez-Andrade E. F., Posses A. C., 2021, [A&A](#), **647**, A194
- Fujimoto S., et al., 2019, [ApJ](#), **887**, 107
- Fujimoto S., et al., 2020, [ApJ](#), **900**, 1
- Fujimoto S., et al., 2024, [arXiv e-prints](#), p. [arXiv:2402.18543](#)
- Fumagalli M., Prochaska J. X., Kasen D., Dekel A., Ceverino D., Primack J. R., 2011, [MNRAS](#), **418**, 1796
- Gaia Collaboration et al., 2018, [A&A](#), **616**, A1
- Gallego S. G., et al., 2021, [MNRAS](#), **504**, 16
- Gallerani S., Pallottini A., Feruglio C., Ferrara A., Maiolino R., Vallini L., Riechers D. A., Pavesi R., 2018, [MNRAS](#), **473**, 1909
- Galliano F., Galametz M., Jones A. P., 2018, [ARA&A](#), **56**, 673
- Gardner J. P., et al., 2006, [Space Sci. Rev.](#), **123**, 485
- Gawiser E., et al., 2007, [ApJ](#), **671**, 278
- Gazagnes S., Chisholm J., Schaerer D., Verhamme A., Rigby J. R., Bayliss M., 2018, [A&A](#), **616**, A29
- Genel S., et al., 2008, [ApJ](#), **688**, 789
- Genzel R., et al., 2011, [ApJ](#), **733**, 101
- Gerke B. F., et al., 2007, [ApJ](#), **660**, L23

- Gilli R., Vignali C., Mignoli M., Iwasawa K., Comastri A., Zamorani G., 2010, [A&A](#), **519**, A92
- Ginolfi M., et al., 2020a, [A&A](#), **633**, A90
- Ginolfi M., et al., 2020b, [A&A](#), **643**, A7
- Goerdt T., Ceverino D., 2015, [MNRAS](#), **450**, 3359
- Gómez-Guijarro C., et al., 2018, [ApJ](#), **856**, 121
- Goto H., et al., 2021, [ApJ](#), **923**, 229
- Gould A., Weinberg D. H., 1996, [ApJ](#), **468**, 462
- Grand R. J. J., et al., 2019, [MNRAS](#), **490**, 4786
- Gronke M., Dijkstra M., McCourt M., Oh S. P., 2016, [ApJ](#), **833**, L26
- Guaïta L., et al., 2022, [A&A](#), **660**, A137
- Gunn J. E., Gott III J. R., 1972, [ApJ](#), **176**, 1
- Gurung-López S., Orsi Á. A., Bonoli S., 2019, [MNRAS](#), **490**, 733
- Hack W. J., et al., 2021, spacetelescope/drizzlepac: Drizzlepac v3.3.0, [doi:10.5281/zenodo.5534751](https://doi.org/10.5281/zenodo.5534751)
- Hagen A., et al., 2014, [ApJ](#), **786**, 59
- Haiman Z., Spaans M., Quataert E., 2000, [ApJ](#), **537**, L5
- Hani M. H., Sparre M., Ellison S. L., Torrey P., Vogelsberger M., 2018, [MNRAS](#), **475**, 1160
- Harikane Y., et al., 2018, [ApJ](#), **859**, 84
- Harikane Y., et al., 2023, [ApJ](#), **959**, 39
- Hashimoto T., et al., 2018, [Nature](#), **557**, 392
- Hasinger G., et al., 2018, [ApJ](#), **858**, 77

- Häußler B., et al., 2013, [MNRAS](#), **430**, 330
- Hayashino T., et al., 2004, [AJ](#), **128**, 2073
- Heiles C., 1994, [ApJ](#), **436**, 720
- Heintz K. E., et al., 2022, [ApJ](#), **934**, L27
- Hennawi J. F., Prochaska J. X., Cantalupo S., Arrigoni-Battaia F., 2015, [Science](#), **348**, 779
- Herenz E. C., Wisotzki L., 2017, [A&A](#), **602**, A111
- Herenz E. C., et al., 2023, [A&A](#), **670**, A121
- Herrera-Camus R., et al., 2015, [ApJ](#), **800**, 1
- Herrera-Camus R., et al., 2018, [ApJ](#), **861**, 94
- Herrera-Camus R., et al., 2021, [A&A](#), **649**, A31
- Herrera-Camus R., et al., 2022, [A&A](#), **665**, L8
- Herrera-Camus R., et al., 2025, [arXiv e-prints](#), p. [arXiv:2505.06340](#)
- Herrero Alonso Y., Wisotzki L., Miyaji T., Schaye J., Pharo J., Krumpe M., 2023, [A&A](#), **677**, A125
- Hill R., et al., 2020, [MNRAS](#), **495**, 3124
- Hjelm M., Lindblad P. O., 1996, [A&A](#), **305**, 727
- Ho I. T., et al., 2014, [MNRAS](#), **444**, 3894
- Hodge J. A., da Cunha E., 2020, [Royal Society Open Science](#), **7**, 200556
- Hopkins P. F., Hernquist L., Cox T. J., Kereš D., 2008, [ApJS](#), **175**, 356
- Hopkins P. F., Cox T. J., Hernquist L., Narayanan D., Hayward C. C., Murray N., 2013, [MNRAS](#), **430**, 1901
- Howard S., Keel W. C., Byrd G., Burkey J., 1993, [ApJ](#), **417**, 502

- Ikeda R., et al., 2025, [A&A](#), **693**, A237
- Izotov Y. I., Thuan T. X., Privon G., 2012, [MNRAS](#), **427**, 1229
- Jiménez-Andrade E. F., et al., 2023, [MNRAS](#), **521**, 2326
- Johnston E. J., et al., 2017, [MNRAS](#), **465**, 2317
- Jones G. C., et al., 2017, [ApJ](#), **850**, 180
- Jorsater S., van Moorsel G. A., 1995, [AJ](#), **110**, 2037
- Józsa G. I. G., et al., 2009, [A&A](#), **500**, L33
- Jullo E., Kneib J. P., 2009, [MNRAS](#), **395**, 1319
- Kageura Y., et al., 2025, [arXiv e-prints](#), p. arXiv:2501.05834
- Karman W., et al., 2015, [A&A](#), **574**, A11
- Kennicutt Jr. R. C., 1998, [ARA&A](#), **36**, 189
- Kennicutt R. C., et al., 2011, [PASP](#), **123**, 1347
- Kereš D., Katz N., Weinberg D. H., Davé R., 2005, [MNRAS](#), **363**, 2
- Kewley L. J., Dopita M. A., Sutherland R. S., Heisler C. A., Trevena J., 2001, [ApJ](#), **556**, 121
- Kewley L. J., Groves B., Kauffmann G., Heckman T., 2006, [MNRAS](#), **372**, 961
- Kewley L. J., Nicholls D. C., Sutherland R. S., 2019, [ARA&A](#), **57**, 511
- Khrykin I. S., et al., 2024, [ApJ](#), **973**, 151
- Kikuta S., et al., 2019, [PASJ](#), **71**, L2
- Kim C.-G., et al., 2020, [ApJ](#), **903**, L34
- Koester B. P., Gladders M. D., Hennawi J. F., Sharon K., Wuyts E., Rigby J. R., Bayliss M. B., Dahle H., 2010, [ApJ](#), **723**, L73

- Kojima T., Ouchi M., Nakajima K., Shibuya T., Harikane Y., Ono Y., 2017, [PASJ](#), **69**, 44
- Koposov S., et al., 2022, joshspeagle/dynesty: v2.0.3, [doi:10.5281/zenodo.7388523](https://doi.org/10.5281/zenodo.7388523)
- Kornei K. A., Shapley A. E., Erb D. K., Steidel C. C., Reddy N. A., Pettini M., Bogosavljević M., 2010, [ApJ](#), **711**, 693
- Koss M., Mushotzky R., Treister E., Veilleux S., Vasudevan R., Trippe M., 2012, [ApJ](#), **746**, L22
- Kusakabe H., et al., 2020, [A&A](#), **638**, A12
- Lambert T. S., et al., 2023, [MNRAS](#), **518**, 3183
- Laursen P., Sommer-Larsen J., Razoumov A. O., 2011, [ApJ](#), **728**, 52
- Law D. R., Steidel C. C., Erb D. K., Larkin J. E., Pettini M., Shapley A. E., Wright S. A., 2009, [ApJ](#), **697**, 2057
- Le Fèvre O., et al., 2020, [A&A](#), **643**, A1
- Lebowitz S., Hainline K., Juneau S., Lyu J., Williams C. C., Alberts S., Fan X., Rieke M., 2025, [ApJ](#), **984**, 13
- Leclercq F., et al., 2017, [A&A](#), **608**, A8
- Leclercq F., et al., 2020, [A&A](#), **635**, A82
- Leibler C. N., Cantalupo S., Holden B. P., Madau P., 2018, [MNRAS](#), **480**, 2094
- Lemaux B. C., et al., 2018, [A&A](#), **615**, A77
- Leung G. C. K., Coil A. L., Rupke D. S. N., Perrotta S., 2021, [ApJ](#), **914**, 17
- Li Y., Luo R., Fossati M., Sun M., Jáchym P., 2023, [MNRAS](#), **521**, 4785
- Li J., et al., 2024, [ApJ](#), **976**, 70
- Lin H.-N., Zou R., 2023, [MNRAS](#), **520**, 6237

- Lines N. E. P., et al., 2025, [MNRAS](#), **539**, 2685
- Lintott C. J., et al., 2009, [MNRAS](#), **399**, 129
- Litke K. C., et al., 2019, [ApJ](#), **870**, 80
- Loiacono F., et al., 2021, [A&A](#), **646**, A76
- Luo R., et al., 2023, [MNRAS](#), **521**, 6266
- Madden S. C., Geis N., Genzel R., Herrmann F., Jackson J., Poglitsch A., Stacey G. J., Townes C. H., 1993, [ApJ](#), **407**, 579
- Maiolino R., et al., 2015, [MNRAS](#), **452**, 54
- Maiolino R., et al., 2024, [A&A](#), **691**, A145
- Malhan K., Ibata R. A., Martin N. F., 2018, [MNRAS](#), **481**, 3442
- Malhotra S., et al., 2017, [ApJ](#), **835**, 110
- Mandelker N., Padnos D., Dekel A., Birnboim Y., Burkert A., Krumholz M. R., Steinberg E., 2016, [MNRAS](#), **463**, 3921
- Mandelker N., van Dokkum P. G., Brodie J. P., van den Bosch F. C., Ceverino D., 2018, [ApJ](#), **861**, 148
- Martínez-Delgado D., et al., 2010, [AJ](#), **140**, 962
- Martínez-Delgado D., et al., 2023, [A&A](#), **671**, A141
- Mas-Ribas L., Dijkstra M., Hennawi J. F., Trenti M., Momose R., Ouchi M., 2017, [ApJ](#), **841**, 19
- Maseda M. V., et al., 2018, [ApJ](#), **865**, L1
- Mason C. A., Chen Z., Stark D. P., Lu T.-Y., Topping M., Tang M., 2025, [arXiv e-prints](#), p. [arXiv:2501.11702](#)

- Matsuda Y., et al., 2004, [AJ](#), **128**, 569
- Matsuda Y., et al., 2011, [MNRAS](#), **410**, L13
- Matthee J., Sobral D., Gronke M., Paulino-Afonso A., Stefanon M., Röttgering H., 2018, [A&A](#), **619**, A136
- Matthee J., et al., 2020, [MNRAS](#), **498**, 3043
- Matthee J., et al., 2024, [ApJ](#), **963**, 129
- Mazzarella J. M., et al., 2012, [AJ](#), **144**, 125
- Mazzolari G., et al., 2024, [A&A](#), **691**, A345
- McCarthy P. J., Spinrad H., Djorgovski S., Strauss M. A., van Breugel W., Liebert J., 1987, [ApJ](#), **319**, L39
- McPherson D. K., et al., 2023, [MNRAS](#), **525**, 6170
- Mehta V., et al., 2017, [ApJ](#), **838**, 29
- Menzel M., et al., 2023, [PASP](#), **135**, 058002
- Meurer G. R., Heckman T. M., Calzetti D., 1999, [ApJ](#), **521**, 64
- Mignoli M., et al., 2013, [A&A](#), **556**, A29
- Miley G., De Breuck C., 2008, [A&A Rev.](#), **15**, 67
- Miller T. B., et al., 2018, [Nature](#), **556**, 469
- Mitchell P. D., Blaizot J., Devriendt J., Kimm T., Michel-Dansac L., Rosdahl J., Slyz A., 2018, [MNRAS](#), **474**, 4279
- Mitchell P. D., Blaizot J., Cadiou C., Dubois Y., Garel T., Rosdahl J., 2021, [MNRAS](#), **501**, 5757
- Mitsuhashi I., et al., 2024, [A&A](#), **690**, A197
- Molyneux S. J., et al., 2022, [MNRAS](#), **512**, 535

- Momose R., et al., 2014, [MNRAS](#), **442**, 110
- Momose R., et al., 2016, [MNRAS](#), **457**, 2318
- Monson E. B., et al., 2023, [ApJ](#), **951**, 15
- Morales A. M., Mason C. A., Bruton S., Gronke M., Haardt F., Scarlata C., 2021, [ApJ](#), **919**, 120
- Mortensen K., Keerthi Vasan G. C., Jones T., Faucher-Giguère C.-A., Sanders R. L., Ellis R. S., Leethochawalit N., Stark D. P., 2021, [ApJ](#), **914**, 92
- Muñoz-Elgueta N., Arrigoni Battaia F., Kauffmann G., Pakmor R., Walch S., Obreja A., Buhlmann L., 2024, [A&A](#), **690**, A392
- Nakajima K., et al., 2012, [ApJ](#), **745**, 12
- Neeleman M., Prochaska J. X., Kanekar N., Rafelski M., 2020, [Nature](#), **581**, 269
- Neeleman M., et al., 2021, [ApJ](#), **911**, 141
- Neeleman M., Walter F., Decarli R., Drake A. B., Eilers A.-C., Meyer R. A., Venemans B. P., 2023, [ApJ](#), **958**, 132
- Nelson D., Genel S., Vogelsberger M., Springel V., Sijacki D., Torrey P., Hernquist L., 2015, [MNRAS](#), **448**, 59
- Nelson D., et al., 2019, [MNRAS](#), **490**, 3234
- Nesvadba N. P. H., De Breuck C., Lehnert M. D., Best P. N., Collet C., 2017, [A&A](#), **599**, A123
- Nightingale J., Hayes R., Griffiths M., 2021, [The Journal of Open Source Software](#), **6**, 2550
- Nightingale J., et al., 2023, [The Journal of Open Source Software](#), **8**, 4475
- Noeske K. G., et al., 2007, [ApJ](#), **660**, L43
- Noirot G., et al., 2018, [ApJ](#), **859**, 38
- O’Connell R. W., Gallagher III J. S., Hunter D. A., Colley W. N., 1995, [ApJ](#), **446**, L1

- Oesch P. A., et al., 2023, [MNRAS](#), **525**, 2864
- Olsen K., Greve T. R., Narayanan D., Thompson R., Davé R., Niebla Rios L., Stawinski S., 2017, [ApJ](#), **846**, 105
- Ono Y., et al., 2010, [MNRAS](#), **402**, 1580
- Orsi A., Lacey C. G., Baugh C. M., 2012, [MNRAS](#), **425**, 87
- Osterbrock D. E., Ferland G. J., 2006, Astrophysics of gaseous nebulae and active galactic nuclei
- Oteo I., et al., 2018, [ApJ](#), **856**, 72
- Ouchi M., et al., 2003, [ApJ](#), **582**, 60
- Ouchi M., et al., 2008, [ApJS](#), **176**, 301
- Ouchi M., Ono Y., Shibuya T., 2020, [ARA&A](#), **58**, 617
- Overzier R. A., 2016, [A&A Rev.](#), **24**, 14
- Overzier R. A., Nesvadba N. P. H., Dijkstra M., Hatch N. A., Lehnert M. D., Villar-Martín M., Wilman R. J., Zirm A. W., 2013, [ApJ](#), **771**, 89
- Pacucci F., Nguyen B., Carniani S., Maiolino R., Fan X., 2023, [ApJ](#), **957**, L3
- Padnos D., Mandelker N., Birnboim Y., Dekel A., Krumholz M. R., Steinberg E., 2018, [MNRAS](#), **477**, 3293
- Paltani S., et al., 2007, [A&A](#), **463**, 873
- Patrício V., et al., 2016, [MNRAS](#), **456**, 4191
- Pavesi R., et al., 2018, [ApJ](#), **861**, 43
- Peng C. Y., Ho L. C., Impey C. D., Rix H.-W., 2002, [AJ](#), **124**, 266
- Peng C. Y., Ho L. C., Impey C. D., Rix H.-W., 2010, [AJ](#), **139**, 2097

- Pereira-Santaella M., et al., 2016, [A&A](#), 594, A81
- Pereira-Santaella M., et al., 2018, [A&A](#), 616, A171
- Pérez-González P. G., et al., 2024, [arXiv e-prints](#), p. [arXiv:2405.03744](#)
- Perna M., et al., 2023, [A&A](#), 679, A89
- Péroux C., Howk J. C., 2020, [ARA&A](#), 58, 363
- Peschken N., Łokas E. L., Athanassoula E., 2020, [MNRAS](#), 493, 1375
- Peterson B. W., et al., 2018, [ApJ](#), 855, 141
- Pineda J. L., Langer W. D., Velusamy T., Goldsmith P. F., 2013, [A&A](#), 554, A103
- Pizzati E., Ferrara A., Pallottini A., Gallerani S., Vallini L., Decataldo D., Fujimoto S., 2020, [MNRAS](#), 495, 160
- Pizzati E., Ferrara A., Pallottini A., Sommovigo L., Kohandel M., Carniani S., 2023, [MNRAS](#), 519, 4608
- Poggianti B. M., et al., 2017, [ApJ](#), 844, 48
- Posses A. C., et al., 2023, [A&A](#), 669, A46
- Posses A., et al., 2024, [arXiv e-prints](#), p. [arXiv:2403.03379](#)
- Qin Y., et al., 2024, [arXiv e-prints](#), p. [arXiv:2412.00799](#)
- Raney C. A., Keeton C. R., Brennan S., Fan H., 2020, [MNRAS](#), 494, 4771
- Rauch M., 1998, [ARA&A](#), 36, 267
- Reddy N. A., Steidel C. C., Pettini M., Adelberger K. L., Shapley A. E., Erb D. K., Dickinson M., 2008, [ApJS](#), 175, 48
- Reddy N. A., Steidel C. C., Pettini M., Bogosavljević M., 2016, [ApJ](#), 828, 107
- Reines A. E., Volonteri M., 2015, [ApJ](#), 813, 82

- Reuland M., et al., 2003, [ApJ](#), **592**, 755
- Rhoads J. E., Malhotra S., Dey A., Stern D., Spinrad H., Jannuzi B. T., 2000, [ApJ](#), **545**, L85
- Rich J. A., Kewley L. J., Dopita M. A., 2011, [ApJ](#), **734**, 87
- Rich J. A., Kewley L. J., Dopita M. A., 2015, [ApJS](#), **221**, 28
- Richard J., et al., 2021, [A&A](#), **646**, A83
- Riechers D. A., et al., 2014, [ApJ](#), **796**, 84
- Rieke M. J., et al., 2023, [PASP](#), **135**, 028001
- Rigby J. R., et al., 2017, TEMPLATES: Targeting Extremely Magnified Panchromatic Lensed Arcs and Their Extended Star Formation, JWST Proposal ID 1355. Cycle 0 Early Release Science
- Rigby J. R., et al., 2018, [AJ](#), **155**, 104
- Rigby J., et al., 2023, [PASP](#), **135**, 048001
- Rigby J. R., et al., 2025, [ApJ](#), **978**, 108
- Rizzo F., Vegetti S., Powell D., Fraternali F., McKean J. P., Stacey H. R., White S. D. M., 2020, [Nature](#), **584**, 201
- Rizzo F., Vegetti S., Fraternali F., Stacey H. R., Powell D., 2021, [MNRAS](#), **507**, 3952
- Roediger E., Brüggen M., 2008, [MNRAS](#), **388**, 465
- Roman-Oliveira F., Fraternali F., Rizzo F., 2023, [MNRAS](#), **521**, 1045
- Rose T., et al., 2024, [MNRAS](#), **528**, 3441
- Rowland L. E., et al., 2024, [MNRAS](#), **535**, 2068
- Roy N., et al., 2024, [ApJ](#), **970**, 69

- Rubin K. H. R., Prochaska J. X., Koo D. C., Phillips A. C., Martin C. L., Winstrom L. O., 2014, [ApJ](#), **794**, 156
- Rupke D. S. N., et al., 2019, [Nature](#), **574**, 643
- Ruschel-Dutra D., et al., 2021, [MNRAS](#), **507**, 74
- STSCI Development Team 2012, DrizzlePac: HST image software, Astrophysics Source Code Library, record ascl:1212.011
- Saintonge A., et al., 2013, [ApJ](#), **778**, 2
- Sakamoto K., Aalto S., Combes F., Evans A., Peck A., 2014, [ApJ](#), **797**, 90
- Salpeter E. E., 1955, [ApJ](#), **121**, 161
- Sanders D. B., Soifer B. T., Elias J. H., Madore B. F., Matthews K., Neugebauer G., Scoville N. Z., 1988, [ApJ](#), **325**, 74
- Sanders R. L., Shapley A. E., Topping M. W., Reddy N. A., Brammer G. B., 2024, [ApJ](#), **962**, 24
- Sarazin C. L., 1986, [Reviews of Modern Physics](#), **58**, 1
- Saxena A., et al., 2024, [MNRAS](#), **531**, 4391
- Schaerer D., Hayes M., Verhamme A., Teyssier R., 2011, [A&A](#), **531**, A12
- Schaerer D., Fragos T., Izotov Y. I., 2019, [A&A](#), **622**, L10
- Schaerer D., et al., 2020, [A&A](#), **643**, A3
- Schawinski K., Thomas D., Sarzi M., Maraston C., Kaviraj S., Joo S.-J., Yi S. K., Silk J., 2007, [MNRAS](#), **382**, 1415
- Schinnerer E., et al., 2008, [ApJ](#), **689**, L5
- Schlafly E. F., Finkbeiner D. P., 2011, [ApJ](#), **737**, 103
- Schmitt H. R., Donley J. L., Antonucci R. R. J., Hutchings J. B., Kinney A. L., Pringle J. E., 2003, [ApJ](#), **597**, 768

- Schneider E. E., Ostriker E. C., Robertson B. E., Thompson T. A., 2020, [ApJ](#), **895**, 43
- Scholtz J., et al., 2023, [arXiv e-prints](#), p. [arXiv:2311.18731](#)
- Scholtz J., et al., 2024, [A&A](#), **687**, A283
- Schwarz G., 1978, *Annals of Statistics*, **6**, 461
- Scoville N., et al., 2017, [ApJ](#), **837**, 150
- Seaquist E. R., Clark J., 2001, [ApJ](#), **552**, 133
- Secrest N. J., Schmitt H. R., Blecha L., Rothberg B., Fischer J., 2017, [ApJ](#), **836**, 183
- Sersic J. L., 1968, *Atlas de Galaxias Australes*
- Shapley A. E., Steidel C. C., Pettini M., Adelberger K. L., 2003, [ApJ](#), **588**, 65
- Sharon K., et al., 2020, [ApJS](#), **247**, 12
- Shen Y., et al., 2007, [AJ](#), **133**, 2222
- Shibuya T., et al., 2014, [ApJ](#), **788**, 74
- Shibuya T., et al., 2018, [PASJ](#), **70**, S14
- Shirazi M., Brinchmann J., 2012, [MNRAS](#), **421**, 1043
- Shopbell P. L., Bland-Hawthorn J., 1998, [ApJ](#), **493**, 129
- Smit R., Swinbank A. M., Massey R., Richard J., Smail I., Kneib J. P., 2017, [MNRAS](#), **467**, 3306
- Smith L. J., Norris R. P. F., Crowther P. A., 2002, [MNRAS](#), **337**, 1309
- Smith R. J., et al., 2010, [MNRAS](#), **408**, 1417
- Smith A., Ma X., Bromm V., Finkelstein S. L., Hopkins P. F., Faucher-Giguère C.-A., Kereš D., 2019, [MNRAS](#), **484**, 39
- Smith D. J. B., Krause M. G., Hardcastle M. J., Drake A. B., 2022, [MNRAS](#), **514**, 3879

- Smolčić V., et al., 2015, [A&A](#), 576, A127
- Smolčić V., et al., 2017a, [A&A](#), 597, A4
- Smolčić V., et al., 2017b, [A&A](#), 602, A6
- Sobral D., Matthee J., 2019, [A&A](#), 623, A157
- Solimano M., et al., 2021, [A&A](#), 655, A42
- Solimano M., et al., 2022, [ApJ](#), 935, 17
- Solimano M., et al., 2024, [A&A](#), 689, A145
- Solimano M., et al., 2025, [A&A](#), 693, A70
- Sommovigo L., Ferrara A., Carniani S., Zanella A., Pallottini A., Gallerani S., Vallini L., 2021, [MNRAS](#), 503, 4878
- Song H., Seon K.-I., Hwang H. S., 2020, [ApJ](#), 901, 41
- Soto K. T., Lilly S. J., Bacon R., Richard J., Conseil S., 2016, [MNRAS](#), 458, 3210
- Sparre M., Whittingham J., Damle M., Hani M. H., Richter P., Ellison S. L., Pfrommer C., Vogelsberger M., 2022, [MNRAS](#), 509, 2720
- Speagle J. S., 2020, [MNRAS](#), 493, 3132
- Spilker J. S., et al., 2020, [ApJ](#), 905, 85
- Spitzer L., 1978, Physical processes in the interstellar medium, [doi:10.1002/9783527617722](#).
- Springel V., Hernquist L., 2005, [ApJ](#), 622, L9
- Staab P., et al., 2024, [MNRAS](#), 528, 6934
- Stacey G. J., Geis N., Genzel R., Lugten J. B., Poglitsch A., Sternberg A., Townes C. H., 1991, [ApJ](#), 373, 423

- Stacey G. J., Hailey-Dunsheath S., Ferkinhoff C., Nikola T., Parshley S. C., Benford D. J., Staguhn J. G., Fiolet N., 2010, [ApJ](#), **724**, 957
- Stark D. P., Ellis R. S., Chiu K., Ouchi M., Bunker A., 2010, [MNRAS](#), **408**, 1628
- Steidel C. C., Adelberger K. L., Shapley A. E., Pettini M., Dickinson M., Giavalisco M., 2000, [ApJ](#), **532**, 170
- Steidel C. C., Pettini M., Adelberger K. L., 2001, [ApJ](#), **546**, 665
- Steidel C. C., Adelberger K. L., Shapley A. E., Pettini M., Dickinson M., Giavalisco M., 2003, [ApJ](#), **592**, 728
- Steidel C. C., Bogosavljević M., Shapley A. E., Kollmeier J. A., Reddy N. A., Erb D. K., Pettini M., 2011, [ApJ](#), **736**, 160
- Stockton A., Fu H., Canalizo G., 2006, [New A Rev.](#), **50**, 694
- Storey P. J., Zeppen C. J., 2000, [MNRAS](#), **312**, 813
- Strickland D. K., Heckman T. M., Colbert E. J. M., Hoopes C. G., Weaver K. A., 2004, [ApJ](#), **606**, 829
- Sun M., Donahue M., Voit G. M., 2007, [ApJ](#), **671**, 190
- Swinbank A. M., Bower R. G., Smith G. P., Wilman R. J., Smail I., Ellis R. S., Morris S. L., Kneib J. P., 2007, [MNRAS](#), **376**, 479
- Swinbank A. M., et al., 2012, [MNRAS](#), **427**, 1066
- Swinbank A. M., et al., 2015, [MNRAS](#), **449**, 1298
- Szokoly G. P., et al., 2004, [ApJS](#), **155**, 271
- Tacconi L. J., et al., 2013, [ApJ](#), **768**, 74
- Tacconi L. J., et al., 2018, [ApJ](#), **853**, 179
- Tejos N., et al., 2021, [MNRAS](#), **507**, 663

- Telikova K., et al., 2024, [arXiv e-prints](#), p. [arXiv:2411.09033](#)
- Tielens A. G. G. M., Hollenbach D., 1985, [ApJ](#), **291**, 722
- Tonnesen S., Bryan G. L., 2010, [ApJ](#), **709**, 1203
- Tonnesen S., Stone J., 2014, [ApJ](#), **795**, 148
- Toomre A., Toomre J., 1972, [ApJ](#), **178**, 623
- Topping M. W., et al., 2022, [MNRAS](#), **516**, 975
- Tsukui T., Iguchi S., Mitsuhashi I., Tadaki K., 2023a, ESSENCE: Evaluate spatially correlated noise in interferometric images, Astrophysics Source Code Library, record [ascl:2306.055](#)
- Tsukui T., Iguchi S., Mitsuhashi I., Tadaki K., 2023b, [Journal of Astronomical Telescopes, Instruments, and Systems](#), **9**, 018001
- Tumlinson J., Peebles M. S., Werk J. K., 2017, [ARA&A](#), **55**, 389
- Übler H., et al., 2024, [MNRAS](#), **531**, 355
- Umehata H., et al., 2021, [ApJ](#), **918**, 69
- Urrutia T., et al., 2019, [A&A](#), **624**, A141
- Valentino F., et al., 2016, [ApJ](#), **829**, 53
- Vasudevan R. V., Fabian A. C., 2007, [MNRAS](#), **381**, 1235
- Vayner A., et al., 2024a, [arXiv e-prints](#), p. [arXiv:2412.02862](#)
- Vayner A., et al., 2024b, [ApJ](#), **960**, 126
- Veilleux S., Osterbrock D. E., 1987, [ApJS](#), **63**, 295
- Veilleux S., Rupke D. S., 2002, [ApJ](#), **565**, L63
- Veilleux S., Shopbell P. L., Miller S. T., 2001, [AJ](#), **121**, 198

- Veilleux S., Cecil G., Bland-Hawthorn J., 2005, [ARA&A](#), **43**, 769
- Veilleux S., Maiolino R., Bolatto A. D., Aalto S., 2020, [A&A Rev.](#), **28**, 2
- Venemans B. P., et al., 2007, [A&A](#), **461**, 823
- Venkateshwaran A., et al., 2024, [ApJ](#), **977**, 161
- Venturi G., Marconi A., Mingozi M., Carniani S., Cresci G., Risaliti G., Mannucci F., 2017, [Frontiers in Astronomy and Space Sciences](#), **4**, 46
- Venturi G., et al., 2018, [A&A](#), **619**, A74
- Verhamme A., Schaerer D., Maselli A., 2006, [A&A](#), **460**, 397
- Verhamme A., et al., 2018, [MNRAS](#), **478**, L60
- Villanueva V., et al., 2024, [A&A](#), **691**, A133
- Vito F., et al., 2020, [A&A](#), **642**, A149
- Vito F., et al., 2024, [A&A](#), **689**, A130
- Vizgan D., et al., 2022, [ApJ](#), **929**, 92
- Walter F., et al., 2020, [ApJ](#), **902**, 111
- Wang G. C. P., et al., 2021, [MNRAS](#), **508**, 3754
- Wang W., et al., 2024, [A&A](#), **683**, A169
- Weaver J. R., et al., 2022, [ApJS](#), **258**, 11
- Weilbacher P. M., Streicher O., Urrutia T., Jarno A., Pécontal-Rousset A., Bacon R., Böhm P., 2012, in Radziwill N. M., Chiozzi G., eds, Society of Photo-Optical Instrumentation Engineers (SPIE) Conference Series Vol. 8451, Software and Cyberinfrastructure for Astronomy II. p. 84510B, [doi:10.1117/12.925114](#)
- Weilbacher P. M., et al., 2020, [A&A](#), **641**, A28

- Westmoquette M. S., Smith L. J., Gallagher III J. S., 2011, [MNRAS](#), **414**, 3719
- Wisotzki L., et al., 2016, [A&A](#), **587**, A98
- Wisotzki L., et al., 2018, [Nature](#), **562**, 229
- Witstok J., et al., 2025a, [MNRAS](#), **536**, 27
- Witstok J., et al., 2025b, [Nature](#), **639**, 897
- Wolfire M. G., Tielens A. G. G. M., Hollenbach D., 1990, [ApJ](#), **358**, 116
- Wuyts E., Rigby J. R., Gladders M. D., Gilbank D. G., Sharon K., Gralla M. B., Bayliss M. B., 2012, [ApJ](#), **745**, 86
- Wylezalek D., et al., 2013, [ApJ](#), **769**, 79
- Wylezalek D., et al., 2022, [ApJ](#), **940**, L7
- Xue R., et al., 2017, [ApJ](#), **837**, 172
- Yajima H., Li Y., Zhu Q., 2013, [ApJ](#), **773**, 151
- Zanella A., et al., 2018, [MNRAS](#), **481**, 1976
- Zheng Z., Wallace J., 2014, [ApJ](#), **794**, 116
- Zitrin A., et al., 2015, [ApJ](#), **810**, L12
- da Cunha E., Charlot S., Elbaz D., 2008, [MNRAS](#), **388**, 1595
- da Cunha E., et al., 2015, [ApJ](#), **806**, 110